

**A MICROSCALE STUDY OF SMALL CRACK PROPAGATION
IN MULTIAXIAL FATIGUE**

A Thesis
Presented to
The Academic Faculty

by

Valerie P. Bennett

In Partial Fulfillment
of the Requirements for the Degree
Doctor of Philosophy in Mechanical Engineering

Georgia Institute of Technology

Atlanta, Georgia
July 1999

**A MICROSCALE STUDY OF SMALL CRACK PROPAGATION
IN MULTIAXIAL FATIGUE**

Approved:

David L. McDowell, Chairman

Richard Neu

Jianmin Qu

Steve Johnson

Ashok Saxena

Date Approved _____

DEDICATION

This thesis is dedicated to those who have given their time, love, encouragement and support in making this a reality, namely my husband, Harold and my son, Quinton for always bringing a smile to my face. I am also especially grateful for my parents, John and Lola Poindexter, for their sacrifices and patience over the years. This work reflects the efforts of all persons mentioned and would not be a reality without their support.

ACKNOWLEDGEMENTS

As this project comes to a close, it is challenging to fully express the gratitude and thankfulness to so many people that have made this part of my journey possible. To my advisor, Dr. David L. McDowell, whose patience, patience, and more patience have been such a significant part of the completion of this degree. Your talent and tremendous technical insight are only a few of the qualities that I hope to have obtained by studying under your direction. To my committee, Dr. Qu, Dr. Neu, Dr. Saxena, and Dr. Johnson, thank you for sharing your thoughts and ideas from various discussions which have helped to shape this project. I would also like to thank the Office of Naval Research MURI program in Integrated Diagnostics (ONR N00149510539) for sponsoring this research.

The following persons have been instrumental in enabling me to complete this degree: Robert McGinty, Dr. Yibin Xue, Joyce, Keith Miller, Samuel Graham, Tom Lacy, Mark Horstemeyer, Alicia Thomas, Nona Tindall, Dean Carolyn Williams, Willie Ford, and Dr. Veronique Ferney.

TABLE OF CONTENTS

	<u>Page</u>
List of Tables	
List of Figures	
List of Abbreviations, Nomenclature	
Summary	
Chapter I Introduction	1
I.1 Definitions of Small Cracks and Length Scales.	5
I.2 Critical Plane Multiaxial Theories for Fatigue Crack Initiation.	8
I.3 Small Fatigue Crack Growth.	15
I.3.1 Transition from Stage I to Stage II Crack Growth.	16
I.3.2 Fatigue Limits.	18
I.3.3 Roughness and Plasticity-Induced Crack Closure.	21
I.3.4 The Role of the Free Surface.	23
I.3.5 Small Crack Interactions with Microstructure.	25
I.3.6 Small Crack Propagation Approaches.	27
I.4 McDowell-Berard Small Crack Propagation Law.	29
I.5 Three-Dimensional Effects for Small Cracks.	36
I.6 Outstanding Issues to Be Addressed In This Work.	40
Chapter II Crystal Plasticity and Modeling Objectives	45
II.1 Planar Double Slip.	45
II.2 Rate Dependent and Rate Independent Crystal Plasticity.	49
II.3 Structure of the Crystal Plasticity Algorithm.	50
II.4 Finite Element Model Based on Crystal Plasticity.	59
II.5 Crystal Plasticity and Cyclic Deformation.	61
II.6 Crystal Plasticity and Cracked Body Analysis.	62
II.7 Application of Computational Crystal Plasticity: 2-D Analyses.	63

TABLE OF CONTENTS (continued)

	<u>Page</u>
Chapter III Polycrystal Orientation Distribution Effects on Microslip	70
III.1 Fatigue Crack Initiation Parameters.	71
III.1.1 Normalized Cyclic Microplasticity Parameter.	71
III.1.2 Mohr-Coulomb Parameter.	72
III.1.3 Fatemi-Socie Parameter.	73
III.2 Distribution of Cyclic Microplasticity	74
III.2.1 Completely Reversed Cyclic Tension-Compression	78
III.2.1.1 Normalized Cyclic Microplasticity (N-CM).	78
III.2.1.2 Normalized Mohr-Coulomb Parameter (MC).	80
III.2.1.3 Normalized Fatemi-Socie (F-S) Parameter.	80
III.2.2 Cyclic Shear.	81
III.2.2.1 Normalized Cyclic Microplasticity (N-CM).	81
III.2.2.2 Normalized Mohr-Coulomb Parameter (MC).	82
III.2.2.3 Normalized Fatemi-Socie (F-S) Parameter.	83
III.2.3 Cyclic Tension-Compression with Tensile Mean Stress	83
III.2.4 Combined Cyclic Tension-Compression and Shear.	84
III.2.4.1 Normalized Cyclic Microplasticity (N-CM).	85
III.2.4.2 Normalized Mohr-Coulomb Parameter (MC).	86
III.2.4.3 Normalized Fatemi-Socie (F-S) Parameter.	86
III.3 Fatigue Initiation Parameters: Implications.	87
 Chapter IV Analysis of Microstructurally Small Fatigue Cracks	 95
IV.1 Use of Planar Double Slip for Determining CTOD and CTSD for Microstructurally Small Cracks.	 96
IV.2 CTD as Driving Force for Microstructurally Small Fatigue Cracks.	97
IV.3 Model Description for Crack Analysis.	100
IV.3.1 Description of Mesh and Location of Driving Force Measurements.	 101
IV.3.2 Crack Geometries.	103
IV.3.3 Loading Conditions.	105
IV.4 Results for Monotonic Loading.	106
IV.4.1 Remote Tensile Loading.	106
IV.4.2 Remote Shear Loading.	114
IV.4.3 Implications for Small Crack Behavior.	117

TABLE OF CONTENTS (continued)

	<u>Page</u>
IV.5 Results for Cyclic Loading.	118
IV.5.1 Cyclic Tension-Compression.	120
IV.5.2 Cyclic Shear.	126
IV.5.3 Implications for Understanding Small Crack Behavior.	129
Chapter V Implications for Small Crack Models	159
V.1 Shakedown Limits for Cyclic Microplasticity.	160
V.2 Evaluation of $ CTSD/CTOD $, ΔCTD , $\Delta CTSD/\Delta CTOD$, and $\Delta CTOD$	162
V.2.1 Ratio of $ CTSD/CTOD $	163
V.2.1.1 Cyclic Tension-Compression.	163
V.2.1.2 Cyclic Shear.	164
V.2.2 ΔCTD	166
V.2.2.1 Cyclic Tension-Compression.	167
V.2.2.2 Cyclic Shear.	168
V.2.3 $\Delta CTSD/\Delta CTOD$	169
V.2.3.1 Cyclic Tension-Compression.	170
V.2.3.2 Cyclic Shear. ... $\frac{\Delta \tau_n}{2} \cdot \frac{\Delta \gamma_n}{2}$	171
V.3 ΔCTD as a Function of Parameter $\frac{\Delta \tau_n}{2} \cdot \frac{\Delta \gamma_n}{2}$	171
V.3.1 Cyclic Tension-Compression.	172
V.3.2 Cyclic Shear.	173
V.4 Conclusions.	174
Chapter VI Conclusions and Recommendations	192
VI.1 Conclusions.	192
VI.2 Recommendations	198
VI.2.1 Slip Intensification.	199
VI.2.2 Remeshing with Growing Small Crack.	200
VI.2.3 Frictional Contact along the Crack Face.	201
VI.2.3.1 Cyclic Tension-Compression.	201
VI.2.3.2 Cyclic Shear.	201
VI.2.4 Numerical Simulations of Small Crack Growth.	202
References	212
Vita	226

LIST OF TABLES

<u>Table</u>	<u>Page</u>
IV.1a Assignment of Nearest-Neighbor Grain Misorientation for Remote Tension-Compression	157
IV.1b Assignment of Nearest-Neighbor Grain Misorientation for Remote Shear.	158
V.1 Estimates of Shakedown Limits based on Micromechanical Solutions for 4340 Steel	190
V.2a Relationship between the Applied Strain Amplitude and the Initial Slope of the Δ CTD vs. a/d for $a/d < 1$ for Cyclic Tension-Compression.	190
V.2b Relationship between the Applied Strain Amplitude and the Initial Slope of the Δ CTD vs. a/d for $a/d < 1$ for Cyclic Shear	190
V.3a Slope, l , for Cyclic Tension-Compression for different crack length ratios.	191
V.3b Slope, l , for Cyclic Shear for different crack length ratios.	191

LIST OF FIGURES

<u>Figure</u>	<u>Page</u>
I.1 (a) Upper plate of rotor hubs (b) and sites of crack formation (17).	41
I.2 Small crack sizes and characteristic dimensions - (a) microstructurally small, (b) mechanically small, and (c) physically small.	42
I.3 Schematic of Stage I and Stage II crack growth behavior for cyclic tensile loading	42
I.4 Case A and Case B - under general multiaxial cyclic strains (6).	43
I.5 Γ - planes for 1Cr-Mo-V steel at 20°C showing Case A and Case B (6).	43
I.6 Kitagawa diagram for a low carbon steel with a ferrite grain size of 55 μm (12)	44
I.7 Predicted interaction behavior for completely reversed torsion followed by cyclic tensile sequences for three different constant amplitude fatigue lives for 1045 steel; in each case, N_f corresponds to $a_f = 1\text{mm}$ (20)	44
II.1 (a) Two of the four unique $\{111\}$ planes are shown together with the four $\langle 110 \rangle$ slip directions that would be activated in $(1\bar{1}0)$ planar plastic flow. The top dashed arrow corresponds to the slip direction for the "effective slip system" that represents the $(111)[\bar{1}01]$ and $(111)[0\bar{1}1]$, whereas the bottom dashed arrow represents the $(11\bar{1})[0\bar{1}\bar{1}]$ and $(11\bar{1})[\bar{1}0\bar{1}]$ slip systems, and (b) effective slip systems for 2-D planar double slip idealization.	66
II.2 Modeling options for modeling a polycrystal using crystal plasticity within a finite element context: (a) one finite element with each gauss point representing several grains, and (b) finite element mesh with each element representing a grain or multiple elements within each grain.	67
II.3 Kinematics of elastic-plastic deformation showing undeformed (reference), intermediate, and deformed configurations.	67
II.4 Illustration of incremental line search algorithm showing how the optimal value of the plastic shearing rate is obtained.	68

LIST OF FIGURES (continued)

<u>Figure</u>	<u>Page</u>
II.5 Illustration of time step subincrementation scheme used to assure convergence of Newton-Raphson procedure.	68
II.6 Illustration of primary and secondary slip designations for adjacent grain orientation for a surface grain containing crack under remote (a) tension-compression in the x_2 direction (σ_{22}) and (b) shear (τ_{12}) loading	69
III.1 Finite element model of polycrystal aggregate used in crystal plasticity analysis with surface grains indicated by arrows.	89
III.2 Hysteresis loops for cyclic tension-compression in the 2-D simulation.	89
III.3 Contour plots of equivalent plastic strain for (a) cyclic tension-compression at strain amplitude of $0.7 \epsilon_y$ with bands along $\pm 45^\circ$ directions, (b) cyclic shear at strain amplitude of $0.7 \gamma_y$ with bands principally along 0° and 90° directions, and (c) cyclic tension-compression ($0.7 \epsilon_y$) and cyclic shear ($0.7 \gamma_y$) with proportional loading with bands along oblique directions.	90
III.4 Cyclic Tension-Compression - (a) Normalized Cyclic Microplasticity, (b) Mohr-Coulomb, (c) Fatemi-Socie Parameters.	91
III.5 Cyclic Shear - (a) Normalized Cyclic Microplasticity, (b) Mohr-Coulomb, (c) Fatemi-Socie Parameters	92
III.6 Characteristic hysteresis loops for cyclic tension-compression with mean stress of 400 MPa ($R = 0$) in the 2-D simulation	93
III.7 Cyclic Tension-Compression with Mean Stress - (a) Normalized Cyclic Microplasticity, (b) Mohr-Coulomb, (c) Fatemi-Socie Parameters	93
III.8 Cyclic Tension-Compression and Shear - (a) Normalized Cyclic Microplasticity, (b) Mohr-Coulomb, (c) Fatemi-Socie Parameters	94
IV.1 Illustration of (a) Stage I growth (CTD vector along primary slip plane only) in the first grain with transition to Stage II over a few grains, (b) extended Stage II CTD components and (c) Stage II conjugate slip.	133

LIST OF FIGURES (continued)

<u>Figure</u>	<u>Page</u>
IV.2 Crack tip geometry for finite element mesh.	134
IV.3 Three cases considered for modeling the cracked polycrystalline aggregate (a) cracked grain and adjacent grain modeled with crystal plasticity with remaining mesh modeled with anisotropic plasticity, (b) cracked grain and adjacent grain with 'three rings' of surrounding grains modeled with crystal plasticity, remaining grains modeled with anisotropic plasticity, and (c) entire aggregate modeled with crystal plasticity.	135
IV.4 Schematic of mesh configuration with nearest neighbor Grain A and finite element mesh	136
IV.5 CTSD and CTOD as a function of applied polycrystal tensile strain for a surface crack ($a/d = 0.25$) in a favorably oriented grain with a range of nearest neighbor (Grain A) orientations given in Table IV.1a, evaluated (a) $2\ \mu\text{m}$ and (b) $18\ \mu\text{m}$ behind the crack tip.	137
IV.6 Contour plots of effective plastic strain for an applied tensile strain of $0.9\epsilon_y$ for (a) single slip and (b) conjugate slip in Table IV.1a, $a/d = 0.25$; the peak strain intensity (red) has a threshold of 1% plastic strain, which is at least twice the polycrystal average applied strain.	137
IV.7 CTSD and CTOD as a function of applied polycrystal tensile strain for a surface crack ($a/d = 0.5$) in a favorably oriented grain with a range of nearest neighbor (Grain A) orientations given in Table IV.1a, evaluated (a) $2\ \mu\text{m}$ and (b) $25\ \mu\text{m}$ behind the crack tip.	138
IV.8 CTSD and CTOD as a function of applied polycrystal tensile strain for a surface crack ($a/d = 0.97$) in a favorably oriented grain for the nearest neighbor (Grain A) orientations given in Table IV.1a, evaluated (a) $2\ \mu\text{m}$ and (b) $25\ \mu\text{m}$ behind the crack tip.	138
IV.9 CTSD and CTOD as a function of applied polycrystal tensile strain for a surface crack ($a/d = 1.25$) in a favorably oriented grain for the nearest neighbor (Grain A) orientations given in Table IV.1a, evaluated (a) $2\ \mu\text{m}$ and (b) $25\ \mu\text{m}$ behind the crack tip.	139

LIST OF FIGURES (continued)

<u>Figure</u>	<u>Page</u>
IV.10 CTSD and CTOD as a function of applied polycrystal tensile strain for a surface crack ($a/d = 1.97$) in a favorably oriented grain for the nearest neighbor (Grain A) orientations given in Table IV.1a, evaluated (a) $2\ \mu\text{m}$ and (b) $25\ \mu\text{m}$ behind the crack tip.	139
IV.11 CTSD and CTOD as a function of applied polycrystal tensile strain for a surface crack ($a/d = 2.5$) in a favorably oriented grain for the nearest neighbor (Grain A) orientations given in Table IV.1a, evaluated (a) $2\ \mu\text{m}$ and (b) $25\ \mu\text{m}$ behind the crack tip.	140
IV.12 Schematic of kinked-up (KU) and kinked-down (KD) crack.	140
IV.13 CTSD and CTOD as a function of applied polycrystal tensile strain for a surface crack ($a/d = 2.5$ - KD) in a favorably oriented grain for the nearest neighbor (Grain A) orientations given in Table IV.1a, evaluated (a) $2\ \mu\text{m}$ and (b) $25\ \mu\text{m}$ behind the crack tip.	141
IV.14 CTSD and CTOD as a function of applied polycrystal tensile strain for a surface crack ($a/d = 2.5$ - KU) in a favorably oriented grain for the nearest neighbor (Grain A) orientations given in Table IV.1a, evaluated (a) $2\ \mu\text{m}$ and (b) $25\ \mu\text{m}$ behind the crack tip.	141
IV.15 CTSD and CTOD as a function of applied polycrystal shear strain for a surface crack ($a/d = 0.25$) in a favorably oriented grain with a range of nearest neighbor (Grain A) orientations given in Table IV.1b, evaluated (a) $2\ \mu\text{m}$ and (b) $18\ \mu\text{m}$ behind the crack tip.	142
IV.16 CTSD and CTOD as a function of applied polycrystal shear strain for a surface crack ($a/d = 0.5$) in a favorably oriented grain with a range of nearest neighbor (Grain A) orientations given in Table IV.1b, evaluated (a) $2\ \mu\text{m}$ and (b) $25\ \mu\text{m}$ behind the crack tip.	142
IV.17 Contour plots of effective plastic strain for an applied shear strain of $0.9\gamma_y$ for the two cases in Table IV.1b, $a/d = 0.5$; the peak strain intensity (red) has a threshold of 0.5% plastic strain.	143

LIST OF FIGURES (continued)

<u>Figure</u>	<u>Page</u>
IV.18 CTSD and CTOD as a function of applied polycrystal shear strain for a surface crack ($a/d = 0.97$) in a favorably oriented grain for the nearest neighbor (Grain A) orientations given in Table IV.1b, evaluated (a) $2\ \mu\text{m}$ and (b) $25\ \mu\text{m}$ behind the crack tip.	143
IV.19 CTSD and CTOD as a function of applied polycrystal shear strain for a surface crack ($a/d = 1.25$) in a favorably oriented grain with a range of nearest neighbor (Grain A) orientations given in Table IV.1b, evaluated (a) $2\ \mu\text{m}$ and (b) $25\ \mu\text{m}$ behind the crack tip.	144
IV.20 CTSD and CTOD as a function of applied polycrystal shear strain for a surface crack ($a/d = 1.97$) in a favorably oriented grain for the nearest neighbor (Grain A) orientations given in Table IV.1b, evaluated (a) $2\ \mu\text{m}$ and (b) $25\ \mu\text{m}$ behind the crack tip.	144
IV.21 CTSD and CTOD as a function of applied polycrystal shear strain for a surface crack ($a/d = 2.5$) in a favorably oriented grain for the nearest neighbor (Grain A) orientations given in Table IV.1b, evaluated (a) $2\ \mu\text{m}$ and (b) $25\ \mu\text{m}$ behind the crack tip.	145
IV.22 CTSD and CTOD for the tensile loading case as a function of crack length ratio at $2\ \mu\text{m}$ behind the crack tip for strain amplitudes of (a) $0.3\ \epsilon_y$, (b) $0.6\ \epsilon_y$, and (c) $0.9\ \epsilon_y$	146
IV.23 CTSD and CTOD for the shear loading case as a function of crack length ratio at $2\ \mu\text{m}$ behind the crack tip for strain amplitudes of (a) $0.3\ \gamma_y$, (b) $0.6\ \gamma_y$, and (c) $0.9\ \gamma_y$	147
IV.24 Cyclic CTSD and CTOD for cyclic tension-compression loading for a crack oriented at 45° with respect to the tensile axis for $a/d = 0.25$ for strain amplitudes of $0.3\ \epsilon_y$, $0.6\ \epsilon_y$, and $0.9\ \epsilon_y$ at distances of $2\ \mu\text{m}$ and $18\ \mu\text{m}$ behind the crack tip.	148

LIST OF FIGURES (continued)

<u>Figure</u>	<u>Page</u>
IV.25 Cyclic CTSD and CTOD for tension-compression loading for a crack oriented at 45° with respect to the tensile axis for $a/d = 0.25$ for strain amplitudes of $0.3 \epsilon_y$ and $0.9 \epsilon_y$ at a distance of $2 \mu\text{m}$ behind the crack tip showing differences in the effective stress range due to closure effects.	149
IV.26 Cyclic CTSD and CTOD for cyclic tension-compression loading for a crack oriented at 45° with respect to the tensile axis for $a/d = 0.5$ for strain amplitudes of $0.3 \epsilon_y$, $0.6 \epsilon_y$, and $0.9 \epsilon_y$ at distances of $2 \mu\text{m}$ and $25 \mu\text{m}$ behind the crack tip.	150
IV.27 Contour plots of effective plastic strain for an cyclic tension-compression with tensile strain of $0.9\epsilon_y$ for the two cases in Table IV.1a, (a) single slip and (b) conjugate slip $a/d = 0.5$; the peak strain intensity (red) has a threshold of 1% plastic strain after 3 cycles and at the maximum load.	151
IV.28 Cyclic CTSD and CTOD for cyclic tension-compression loading for a crack oriented at 45° with respect to the tensile axis for $a/d = 0.97$ for strain amplitudes of $0.3 \epsilon_y$, $0.6 \epsilon_y$, and $0.9 \epsilon_y$ at distances of $2 \mu\text{m}$ and $25 \mu\text{m}$ behind the crack tip.	152
IV.29 Cyclic CTSD and CTOD for cyclic tension-compression loading for a crack oriented at 45° with respect to the tensile axis for $a/d = 1.25$ for strain amplitudes of $0.3 \epsilon_y$, $0.6 \epsilon_y$, and $0.9 \epsilon_y$ at distances of $2 \mu\text{m}$ and $25 \mu\text{m}$ behind the crack tip.	153
IV.30 Cyclic CTSD and CTOD for cyclic shear loading for a crack oriented at 90° with respect to the tensile axis for $a/d = 0.25$ for strain amplitudes of $0.3 \gamma_y$ and $0.9 \gamma_y$ at distances of $2 \mu\text{m}$ and $18 \mu\text{m}$ behind the crack tip.	154
IV.31 Cyclic CTSD and CTOD for cyclic shear loading for a crack oriented at 90° with respect to the tensile axis for $a/d = 0.97$ for strain amplitudes of $0.3 \gamma_y$ and $0.9 \gamma_y$ at distances of $2 \mu\text{m}$ and $25 \mu\text{m}$ behind the crack tip.	155
IV.32 Cyclic CTSD and CTOD for cyclic shear loading for a crack oriented at 90° with respect to the tensile axis for $a/d = 1.97$ for strain amplitudes of $0.3 \gamma_y$ and $0.9 \gamma_y$ at distances of $2 \mu\text{m}$ and $25 \mu\text{m}$ behind the crack tip.	156

LIST OF FIGURES (continued)

<u>Figure</u>	<u>Page</u>
V.1 Comparison of the maximum shear strain amplitude on a slip system and the maximum plastic shear strain amplitude (averaged over all grains) as a function of the average amplitude of the maximum shear stress for (a) cyclic tension-compression and (b) cyclic shear.	175
V.2 Relationship between the amplitude of the maximum average shear stress and the shear strain amplitudes showing relative intensity between the maximum shear strain on a slip system and the maximum plastic shear strain for (a) cyclic tension-compression and (b) cyclic shear.	176
V.3 Ratio of $ CTSD/CTOD $ for cyclic tension-compression loading for a crack oriented at 45° with respect to the tensile axis with $a/d = 0.25$ for strain amplitudes of (a) $0.3 \epsilon_y$, (b) $0.6 \epsilon_y$, and (c) $0.9 \epsilon_y$ at a distance of $2 \mu\text{m}$ behind the crack tip.	177
V.4 Ratio of $ CTSD/CTOD $ for cyclic tension-compression loading for crack oriented at 45° with respect to the tensile axis with $a/d = 0.5$ for strain amplitudes of (a) $0.3 \epsilon_y$, (b) $0.6 \epsilon_y$, and (c) $0.9 \epsilon_y$ at a distance of $2 \mu\text{m}$ behind the crack tip	178
V.5 Ratio of $ CTSD/CTOD $ for cyclic tension-compression loading for crack oriented at 45° with respect to the tensile axis with $a/d = 0.97$ for strain amplitudes of (a) $0.3 \epsilon_y$, (b) $0.6 \epsilon_y$, and (c) $0.9 \epsilon_y$ at a distance of $2 \mu\text{m}$ behind the crack tip	179
V.6 Ratio of $ CTSD/CTOD $ for cyclic tension-compression loading for crack oriented at 45° with respect to the tensile axis with $a/d = 1.25$ for strain amplitudes of (a) $0.3 \epsilon_y$, (b) $0.6 \epsilon_y$, and (c) $0.9 \epsilon_y$ at a distance of $2 \mu\text{m}$ behind the crack tip	180
V.7 Ratio of $ CTSD/CTOD $ for cyclic shear loading for crack oriented at 90° with respect to the tensile axis with $a/d = 0.25$ for strain amplitudes of (a) $0.3 \gamma_y$ and (b) $0.9 \gamma_y$ at a distance of $2 \mu\text{m}$ behind the crack tip.	181

LIST OF FIGURES (continued)

<u>Figure</u>	<u>Page</u>
V.8 Ratio of $ CTSD/CTOD $ for cyclic shear loading for crack oriented at 90° with respect to the tensile axis with $a/d = 0.97$ for strain amplitudes of (a) $0.3 \gamma_y$ and (b) $0.9 \gamma_y$ at a distance of $2 \mu\text{m}$ behind the crack tip	182
V.9 Ratio of $ CTSD/CTOD $ for cyclic shear loading for crack oriented at 90° with respect to the tensile axis with $a/d = 1.97$ for strain amplitudes of (a) $0.3 \gamma_y$ and (b) $0.9 \gamma_y$ at a distance of $2 \mu\text{m}$ behind the crack tip.	183
V.10 ΔCTD as a function of crack length ratio at a distance of $2 \mu\text{m}$ behind the crack tip after 3 cycles of loading for (a) cyclic tension-compression and (b) cyclic shear	184
V.11 $\Delta CTSD/\Delta CTOD$ as a function of crack length ratio for cyclic tension-compression and at $2 \mu\text{m}$ behind the crack tip over the 3 rd cycle of loading for applied strain amplitudes of (a) $0.3 \epsilon_y$, (b) $0.6 \epsilon_y$, and (c) $0.9 \epsilon_y$	185
V.12 $\Delta CTSD/\Delta CTOD$ as a function of crack length ratio for cyclic shear and at $2 \mu\text{m}$ behind the crack tip over the 3 rd cycle of loading for applied strain amplitudes of (a) $0.3 \epsilon_y$, (b) $0.6 \epsilon_y$, and (c) $0.9 \epsilon_y$	186
V.13 $\Delta CTOD$ as a function of product $\Delta \tau_n/2$ (amplitude of shear stress on the plane of maximum range of shear strain) and $\Delta \gamma_n/2$ (amplitude of shear strain acting on the plane of maximum range of shear strain) for cyclic tension-compression at $2 \mu\text{m}$ behind the crack tip over the 3 rd cycle of loading for crack length ratios of (a) 0.25, (b) 0.5, (c) 0.97, (d) 1.25, and (e) 1.97.	187
V.14 $\Delta CTOD$ as a function of product $\Delta \tau_n/2$ (amplitude of shear stress on the plane of maximum range of shear strain) and $\Delta \gamma_n/2$ (amplitude of shear strain acting on the plane of maximum range of shear strain) for cyclic shear at $2 \mu\text{m}$ behind the crack tip over the 3 rd cycle of loading for crack length ratios of (a) 0.25, (b) 0.5, (c) 0.97, (d) 1.25, and (e) 1.97.	189

LIST OF FIGURES (continued)

<u>Figure</u>	<u>Page</u>
VI.1 Cyclic CTOD and CTSD for cyclic tension-compression loading for a crack oriented at 45° with $a/d = 0.25$ for strain amplitudes of $0.9 \epsilon_y$ with preferential softening of $0.8 \cdot g_1$ (along slip direction aligned with the crack plane) at a distance of $2 \mu\text{m}$ behind the crack tip for (a) single and (b) conjugate slip.	203
VI.2 Cyclic CTOD and CTSD for cyclic tension-compression loading for a crack oriented at 45° with $a/d = 0.25$ for strain amplitudes of $0.9 \epsilon_y$ with preferential softening of $0.8 \cdot g_1$ (along slip direction aligned with the crack plane) at a distance of $18 \mu\text{m}$ behind the crack tip for (a) single and (b) conjugate slip.	204
VI.3 Cyclic CTOD and CTSD for cyclic tension-compression loading for a crack oriented at 90° with $a/d = 0.25$ for strain amplitudes of $0.9 \gamma_y$ with preferential softening of $0.8 \cdot g_1$ (along slip direction aligned with the crack plane) at a distance of $2 \mu\text{m}$ behind the crack tip for (a) single and (b) conjugate slip.	205
VI.4 Cyclic CTOD and CTSD for cyclic tension-compression loading for a crack oriented at 90° with $a/d = 0.97$ for strain amplitudes of $0.9 \gamma_y$ with preferential softening of $0.8 \cdot g_1$ (along slip direction aligned with the crack plane) at a distance of $2 \mu\text{m}$ behind the crack tip for (a) single and (b) conjugate slip.	206
VI.5 Cyclic CTOD and CTSD for cyclic tension-compression loading for a crack oriented at 90° with $a/d = 1.97$ for strain amplitudes of $0.9 \gamma_y$ with preferential softening of $0.8 \cdot g_1$ (along slip direction aligned with the crack plane) at a distance of $2 \mu\text{m}$ behind the crack tip for (a) single and (b) conjugate slip.	207
VI.7 Cyclic CTSD and CTOD for cyclic tension-compression loading for a crack oriented at 45° with $a/d = 0.25$ for strain amplitudes of $0.9 \epsilon_y$ with a coefficient of friction of 0.4 on the crack faces at a distance of $2 \mu\text{m}$ behind the crack tip (a) for all three cycles and (b) exploded view of first two cycles	208
VI.8 Cyclic CTSD and CTOD for cyclic tension-compression loading for a crack oriented at 45° with $a/d = 0.97$ for strain amplitudes of $0.9 \epsilon_y$ with a coefficient of friction of 0.4 on the crack faces at a distance of $2 \mu\text{m}$ behind the crack tip (a) for all three cycles and (b) exploded view of first two cycles	209

LIST OF FIGURES (continued)

Figure

Page

VI.9 Cyclic CTSD and CTOD for cyclic tension-compression loading for a crack oriented at 90° with $a/d = 0.25$ for strain amplitudes of $0.9 \gamma_y$ with a coefficient of friction of 0.4 on the crack faces at a distance of $2 \mu\text{m}$ behind the crack tip (a) for all three cycles and (b) exploded view of first two cycles210

VI.10 Cyclic CTSD and CTOD for cyclic tension-compression loading for a crack oriented at 90° with $a/d = 0.97$ for strain amplitudes of $0.9 \gamma_y$ with a coefficient of friction of 0.4 on the crack faces at a distance of $2 \mu\text{m}$ behind the crack tip (a) for all three cycles and (b) exploded view of first two cycles211

LIST OF ABBREVIATIONS AND NOMENCLATURE

Abbreviations

CSS	Crystallographic slip system
CTD	Crack tip displacement
CTOD	Crack tip opening displacement
CTSD	Crack tip sliding displacement
EPFM	Elastic plastic fracture mechanics
FCC	Face-centered cubic
FIP	Fatigue initiation parameter
F-S	Fatemi-Socie
HCF	High cycle fatigue
HSLA	High strength low alloy
KD	Kinked down
KU	Kinked up
LCF	Low cycle fatigue
LEFM	Linear elastic fracture mechanics
MC	Mohr-Coulomb
MFM	Microstructural fracture mechanics
N-CM	Normalized cyclic microplasticity
PDF	Probability distribution function
PSB	Persistent slip band

RDCP	Rate dependent crystal plasticity
SS	Stainless steel

Nomenclature

α, β	constants
β_e, β_p	biaxiality functions for fully elastic and plastic cases, respectively
$\Delta\gamma$	range of shear strain
$\Delta\gamma_{\max}$	maximum shear strain range
$\Delta\gamma_{\max}^{\alpha}$	maximum range of shear strain on either of the two slip systems
$\Delta\gamma_{\max}^e$	elastic part of $\Delta\gamma_{\max}$
$\Delta\gamma_{\max}^p$	plastic part of $\Delta\gamma_{\max}$
$\Delta\epsilon^e, \Delta\epsilon^p$	ranges of uniaxial elastic and plastic strain, respectively
ΔJ	cyclic J-Integral based on a range of stress and strain fields
ΔK	cyclic stress intensity factor based on a range of stress and strain fields
ΔK_{CPA}	cyclic range of stress intensity factor for shear dominated growth
$\Delta K_{th\infty}$	long crack threshold
$\Delta\sigma_n, \Delta\tau_n$	normal and shear stress ranges, respectively, acting on the plane of maximum shear strain range
$\Delta\sigma$	range of axial stress
Δs_{wo}	smooth specimen fatigue limit

$\Delta\tau_c$	range of maximum resolved shear stress in the grain
$\Delta\epsilon_{an}$	strain amplitude normal to the plane of maximum shear strain amplitude
ϕ	defines crystallographic close-packed planes relative to bisector angle
$\dot{\gamma}_o$	reference plastic slip strain rate
$\lambda_\sigma, \xi_\sigma$	stress ratios τ/σ_{yy} and σ_{xx}/σ_{yy} , respectively
μ	constraint coefficient
ρ	constraint parameter
θ	bisector angle between slip systems
σ_{an}	stress amplitude normal to the plane of maximum shear strain amplitude
σ_{max}	maximum stress
σ_{min}	minimum stress
σ_n^{max}	maximum normal stress on the plane of critical alternating shear stress
σ_{op}	opening stress
σ_{xx}	direct stress parallel to the crack plane
σ_y	yield stress
σ_{yy}	far field normal stresses
τ	far field shear stress acting on the crack plane
τ_{an}	allowable alternating shear stress
τ_a	amplitude of the maximum shear stress
τ^a	resolved shear stress on a th slip system

Ψ_e, Ψ_p	driving force parameters in fully elastic and plastic microcrack propagation laws, respectively
a	crack length
a_i	initial crack length
a_f	final crack length
a_0	crack length corresponding to the long crack threshold, $\Delta K_{th\infty}$
A_0, B	constants
C_e, C_p	fully elastic and plastic microcrack propagation law coefficients, respectively
C'_p	fully plastic microcrack propagation law coefficient
C, C^*, C_J	constants
C	elastic stiffness
$\bar{\mathbf{C}}$	elastic right Cauchy stretch tensor
D_{aN}	
D	threshold growth rate
d	grain size
E, G	Young's modulus and shear modulus, respectively
$\bar{\mathbf{E}}'$	elastic Lagrangian strain tensor with respect to intermediate configuration
g^a	reference strength of the a^{th} slip system
H	fatigue limit for shakedown

k, k^*	constants
k_d	transition crack length, where k is the scaling factor
K_{open}	stress intensity factor at crack opening load
K_{max}	stress intensity factor at maximum load
M, m	exponents for fully elastic and plastic terms in da/dN , respectively
M_ϵ	strain rate sensitivity
$m^{(\alpha)}$	unit vector along direction normal to the α^{th} slip system
m_γ	crack length exponent in da/dN law
m_J, n	constants
N_f	number of cycles to fatigue crack of prescribed length considered as "failure"
P	hydrostatic stress
q	parameter which characterizes hardening behavior
R	ratio $\Delta\sigma_{min}/\Delta\sigma_{max}$
R_e	ratio $\Delta\gamma_{max}^e/\Delta\gamma_{max}$
R_n	ratio $\Delta\sigma_n/\Delta\tau_n$
r_p	plastic zone size
$s^{(\alpha)}$	unit vector along the α^{th} slip system
$\bar{\tilde{S}}$	2nd Piola-Kirchoff stress tensor with respect to the intermediate configuration

SUMMARY

The problem of estimating the remaining life in components under HCF conditions is to properly assess and small crack regime, which may account for 50-90% of the total life ($N_f = 1$ mm). With many of the factors that affect small crack behavior, such as interactions with grain boundaries, material inhomogeneity, and surface roughness, incorporating these effects into growth models which account for microstructurally small cracks to long cracks has been a challenge. This work is an effort to assess these features and to understand amplitude and stress state dependencies which enable more precise incorporation of these factors into growth models. This was achieved through the use of a crystal plasticity micromechanical model which was embedded within a finite element context. Plasticity effects are primarily accounted for in this model.

For the uncracked cases considered on polycrystalline aggregate, it was found that when assessing three candidate fatigue initiation parameters, the Fatemi-Socie parameter produced the most descriptive assessment of the damage because it showed both amplitude and stress state dependencies from the distribution plots. This results also correlates with its ability to predict fatigue damage from components under multiaxial fatigue.

For the cracked analyses performed, the local microplasticity which develops behind the crack under cyclic loading has a tremendous impact on the crack tip opening and sliding

displacements which are produced. With proportional, reversed loading applied macroscopically, a local, nonproportionality develops at the crack tip. This nonproportional develops at smaller crack length ratios for cyclic tension-compression as compared to cyclic shear. It also develops at lower strain amplitudes for the cyclic tension-compression case than for the cyclic shear case. Plasticity induced-closure was found to have an influence on this development. These computations have shown that the opening displacements for small cracks account for a large proportion of the driving forces which attribute to crack growth. Small crack behavior has been previously viewed as being dominated by sliding displacements along the crack plane. The increased opening displacements are primarily caused by the lack of constraint from the surface and the surrounding microstructure has an influence for increased crack lengths. This work quantified the influences of the free surface and the surrounding microstructure through the utilization of the crystal plasticity micromechanical model.

CHAPTER I

INTRODUCTION

A major challenge in estimating the high cycle fatigue (HCF) life of components is proper characterization of the small crack regime. This regime refers to the initial part of the crack growth rate versus crack length curve wherein the crack growth rate is not correlated by linear elastic fracture mechanics (LEFM) concepts based on long crack solutions for ΔK in homogeneous materials and long crack growth rate data. The growth of sufficiently small cracks is controlled by the local microstructure (grain boundaries, inclusions), and exhibit growth rates higher than long cracks at the same apparent applied stress intensity fatigue range based on long crack solutions (1). Under primarily HCF conditions and for the small crack regime, long crack LEFM concepts have been used, although they lead to an overestimation of fatigue life. Within the past few decades, critical plane approaches have gained increasing support for correlation of fatigue crack "initiation" lives and character of small crack propagation under predominantly low cycle fatigue (LCF) conditions for various stress states (2-7).

In addition, experimental studies of the propagation of microstructurally and physically small cracks under both LCF and HCF conditions (8-15) have revealed that elastic-plastic fracture mechanics (EPFM) concepts may be used to correlate the growth of

small fatigue cracks for various alloys. However, due to the persistent influence of microstructural anisotropy and periodicity, complex mixed-mode loading conditions and crack opening/closure behavior of small cracks, EPFM solutions and concepts for long cracks do not uniquely carry over to small cracks. Small fatigue cracks show anomalously high, irregular (oscillatory) growth rates in the early stage of crack propagation when compared to large cracks at the same nominal ΔK based on long crack solutions. This high crack growth rate occurs even under nominally elastic conditions, i.e. even when no macroplasticity is involved. The irregular growth rate, in turn, is caused by interactions with microstructural inhomogeneities. This is considered as a major contributing factor to the so-called "small crack problem" involving inapplicability of long crack LEFM ΔK solutions and data.

It is important to incorporate small crack growth behavior into life assessment of components limited by HCF performance. Examples include rotor hubs in helicopters, such as the US Navy H-46 and H-53 platforms. The H-46 helicopter will be required to satisfy the Navy and Marine corps mission requirements for the foreseeable future. Service life extension of the aircraft is, therefore, dependent upon valid analysis of the useful life of the aircraft's components such as the rotor hub which must withstand several cyclic loading modes - tension, compression, twisting, as well as corrosive environments. One of the most prominent modes of loading is low amplitude cycling with high tensile mean stress. Due to these types of loading conditions, detectable small cracks were found on the tie bar of rotor

hubs (16) and in the upper hub plate (17) (in Fig. I.1). In this case, a redesign of the tie bar was required. Premature cracks in the titanium H-53 main rotor hub upper plate spawned an investigation into the adequacy of inspection intervals of 10 flight hours (17). Analytical and experimental tests were performed and it was recommended that the inspection interval increase to 30 flight hours, assuming reliable ultrasonic detection of a 0.030 inch (762 μm) flaw. It is evident that loading conditions, flaw size detection, and correlative models all play a major role in fatigue life assessment.

Comprehensive and robust models for the growth of cracks from a length on the order of a grain size (or below) to reliably detectable dimensions (approximately 500 μm to 1000 μm) do not currently exist, especially under general multiaxial loading conditions. Such models would provide a fundamental advance relative to the current cyclic stress- and strain-based crack initiation models. In addition, they should provide a consistent treatment of the growth of fatigue cracks ranging in length from microstructurally small to mechanically long cracks. The key goal of this research is to explore the effects of material inhomogeneity on the driving forces for fatigue crack formation and small fatigue crack growth, as well as conditions for the transition from crystallographic Stage I to Stage II growth. Using computational models which incorporate planar double slip crystal plasticity, qualitative forms for driving force parameters are examined that are consistent with critical plane concepts and local mixed-mode crystallographic growth concepts for the 2-D case. This research also considers the effects of the free surface, surrounding grains, and local plasticity

on crack tip opening and sliding displacements (CTOD and CTSD, respectively), which are central to the crack propagation relation. In addition to computing CTOD and CTSD for monotonic loading of cracks which are oriented on favorable crystallographic planes in surface grains subjected to either remote tensile or shear loading, these parameters are also determined for fatigue loading cases.

These results assist the development of small crack propagation models which respect stress state, stress amplitude, and stress state sequence effects (cf. McDowell and Bennett (18)). To verify the model's capability for complex loading, baseline constant amplitude, amplitude sequence, as well as stress state sequence experiments were performed on 304 SS and 1045 steel. These materials were selected because they have two different cracking mechanisms - shear stress-dominated versus normal stress-dominated - and were previously well-documented in the work of Socie (4) for uniaxial and torsional loading conditions on thin-walled tubular specimens.

This introductory chapter provides background for the thesis by: (i) defining small cracks and related length scales; (ii) reviewing multiaxial theories with an emphasis on critical plane approaches for fatigue crack formation and early growth; (iii) summarizing the status of small fatigue crack growth laws; and (iv) outlining the outstanding issues to be addressed in this work.

I.1 Definitions of Small Cracks and Length Scales

Three categories of small fatigue cracks may be defined. The first category is microstructurally small fatigue cracks. These cracks are characterized as having all dimensions on the order of a characteristic microstructural dimension, e.g. the grain size (19). Cracks of this type often exhibit crystallographic crack growth, that is, crack growth dominated by shear along crystallographic slip planes. If the applied stress is not high enough, the crack growth rate decreases or the cracks even arrest as the crack tip encounters a grain boundary or other material inhomogeneity. The microstructurally small crack and its crack tip cyclic plastic zone may be completely embedded within a single grain. Microstructural Fracture Mechanics (MFM) (11) is a label that has been introduced for models that treat the distinct growth behavior of these cracks. MFM is a material-structure sensitive approach that is characterized by the consideration of material attributes, e.g., grain boundaries, inclusions, and persistent slip bands (PSBs).

The next category is that of mechanically small fatigue cracks (11). These cracks have dimensions that are small compared to a characteristic dimension, such as the scale of plasticity at the root of some mechanical discontinuity (19) or a crack tip cyclic plastic zone. Such cracks may be fully embedded within the cyclic plastic zone of a notch, or the cyclic plastic zone size may simply be a large fraction of the crack size. A variant of EPFM, which was termed EPFM_p, has been suggested for cracks of this category (18).

Finally, fatigue cracks are considered physically small (11) when the crack size is

small compared to the scale of the characteristic physical dimension. This term includes mechanically small cracks as well, but generally applies to cracks that are small but still larger than 5 to 10 grain diameters such that LEFM or EPFM applies (20). Such cracks may exhibit anomalous behavior if analyzed based on LEFM because of the physical smallness of the crack (21) relative to the cyclic plastic and damage process zones at the crack tip. Physically small cracks eventually become long cracks which are described by LEFM. Figure I.2 illustrates these different crack sizes along with the characteristic dimensions. It is emphasized that these categorizations depend on both crack geometry and load level.

These characterizations of small cracks are presented within a context of stages of growth. In ductile metallic materials, small cracks initiate on crystallographic planes of intensified slip, a process which occurs on planes of maximum shear. Stage I cracks propagate on these shear planes, due to slip processes and decohesion ahead of the crack tip. Typically, microstructurally and mechanically small cracks are in this stage of crack growth. Stage II propagation occurs by processes of slip and decohesion in the plastic shear zone at the crack tip. Figure I.3 shows a schematic of Stage I and Stage II crack growth behavior. The slip and decohesion is again controlled by the maximum shear strain and the growth increment depends on slip irreversibility. Another important effect is the tensile stress across the maximum shear-strain plane, which influences dislocation mobility and the decohesion associated with the slip process (22). Li (23) examined the effect of the normal stress on extended Stage I growth, wherein it acts to offset the dominate crystallographic slip at the crack tip by causing a balance of slip mechanisms. Long crack propagation in initially

isotropic polycrystals is almost always observed to follow Stage II growth, corresponding to macroscopic Mode I dominance.

Attempting to apply a correlation for small cracks by using da/dN versus ΔK (as in showing the ΔK solution and LEFM precepts of mechanically long cracks), i.e.

$$\frac{da}{dN} = C (\Delta K)^n \quad (I.1)$$

has resulted in the so-called anomalous behavior of microstructurally small cracks, first reported by Pearson (24). In particular, the cyclic crack growth rate of small cracks may significantly exceed that of long cracks at the same level of ΔK . One of the reasons for the nonconformity of small crack behavior with that of mechanically long cracks has to do with the violation of validity limits of LEFM. These limits are violated due to the lack of self-similarity of growth and a cyclic plastic zone/process zone size which is on the order of crack length. As small cracks grow further into the bulk material and away from the surface, the crack is increasingly constrained by surrounding grains and statistically has more available slip systems upon which to grow and local crack paths to choose. From a statistical viewpoint, the small crack front samples an increasing number of microstructural barriers with extension (e.g. grain boundaries, inclusions, etc.) (54) leading to a reduction of the growth rate and to a decrease in the scatter of the growth rate (1). As the crack increases in length, it must maintain a coherent crack front across a growing number of grains. As the

number of grains sampled along the crack front increases, the probability of encountering retarding grain orientations along the crack front increases (24). This change in 'environment' that the small crack undergoes accounts for such breakdowns of the applicability of simple, homogeneous, self-similar LEFM and EPFM concepts to small cracks. Furthermore, application of simple plasticity-induced or obstruction-induced closure laws can only partially explain these microstructurally small crack effects.

I.2 Critical Plane Multiaxial Theories for Fatigue Crack Initiation

The local conditions at the tip of a Stage I small fatigue crack are mixed-mode regardless of mixity of the remote loading due to crystallographic growth, local anisotropy, and constraint of neighboring grains. Therefore, multiaxial behavior with multiaxial fatigue crack initiation mechanics is an inseparable feature of the small crack problem. Various approaches have been developed to model the small crack "initiation" regime under multiaxial fatigue loading conditions. These approaches include equivalent stress-strain (26), energy (27), damage mechanics/cumulative damage (28-33), and critical plane (34). Early developments of multiaxial fatigue theories were based on static yield theories (von Mises, Tresca, Rankine) but were later extended to more address complex states of stress (26). Early LCF theories were based on parameters such as the maximum principal strain range, maximum shear strain range, and maximum octahedral shear strain range (34). A more

detailed review of these approaches is given elsewhere (35). In these approaches there is no distinction between nucleation, small crack propagation, and transition to mechanically long crack growth. There is simply an effective stress or strain range quantity which was correlated to “fatigue life.” These theories did not incorporate the effects of orientation of the crack in relation to the 3-D stress/strain field - a crucial factor when assessing multiaxial behavior.

Critical plane approaches are of most relevance to the present research because of their more intimate connection to mixed-mode driving forces. In the early 1970's, critical plane multiaxial fatigue theories were first formally introduced. These approaches are based on observations that cracks form and grow on specific shear planes during the early stages of fatigue; the approach considers the macroscopic stress and strain resolved onto such ‘critical’ planes as most directly influential in the nucleation and growth of cracks. Critical planes refer to those planes within a material which undergo the most extensive range of shear strain. From early multiaxial HCF fatigue research by Stulen and Cummings (36), Findley *et al.* (37) and Findley (38), critical plane approaches have sought to include more detailed information regarding the fatigue cracking process. Based on physical observations of the orientation of evolving fatigue cracks in steel and aluminum, Findley *et al.* (37) discussed the influence of the normal stress acting on the maximum shear stress plane. The earliest critical plane model was then introduced (38) for HCF, i.e.

$$\tau_{an} + k \sigma_{an} = C \quad (1.2)$$

for a given fatigue life, where the allowable alternating shear stress amplitude on the shear stress plane, τ_{an} , decreases with an increase in the maximum normal stress amplitude, σ_{an} , to this plane. Constant k is used to correlate experimental data and C is constant for a given life. Equation (I.2) is discussed here to demonstrate the general philosophy of critical plane approaches. Some combination of the shear and normal stresses that act on a certain 'critical' plane establishes a level function for a given life. The major advantage of critical plane approaches is that they offer a two-parameter correlation to relate predicted fatigue life to experimentally observed cracking behavior. As a result, this approach provides good correlation with experimental results, a physical interpretation of the theory of small crack initiation/growth, and the ability to predict the plane on which cracks occur. An analogy can be drawn to two parameter approaches in elastic-plastic fracture, such as including both the singularity strength and the triaxiality factor ahead of the notch root. In the EPFM case, the two-parameter approach is used to describe geometry effects on the R-curve. In fatigue, equations of this form help describe stress state dependence and planes of crack formation along with the primary cyclic driving force.

In 1973, Brown and Miller (6) proposed an expression similar to that in Equation (I.2) for LCF. They proposed that cracks initiated on the planes of maximum shear strain range. They hypothesized that the amplitude of maximum shear strain, $\Delta\gamma_{max}$, and the strain amplitude normal to the plane of maximum shear strain amplitude, $\Delta\epsilon_n$, were the critical parameters governing damage. Brown and Miller (6) also developed the Γ -plane

representation for LCF as a means to obtain an empirical fit to experimental data. A so-called Γ -plane plot is a locus of points of constant fatigue life to a given crack length in the space of $\Delta\epsilon_n$ versus $\Delta\gamma_{max}$. Brown and Miller (6) found that data from all types of biaxial and multiaxial fatigue tests can be plotted on such Γ -planes, i.e within the “wedge” formed by uniaxial and equibiaxial test conditions (cf. Figure I.4). When obtaining $\Delta\epsilon_n$ and $\Delta\gamma_{max}$ for several different types of tests, it is possible to draw contours of constant fatigue life to a given crack length which separate out the torsion test, with its Case A type cracking system, from the plane strain and equibiaxial tests, which produce Case B cracks. These two types of cracking systems, illustrated in Figure I.5, are indicated by the planes of maximum shear and the directions of Stage I and Stage II crack growth. In this Figure, ϵ_1 , ϵ_2 , and ϵ_3 are the principal strains. Case A cracks propagate along the surface of the specimen, whereas Case B cracks propagate inwards and away from the surface. In a uniaxial test, there are equal proportions of Case A and Case B propagation modes, which consequently produces a nearly circular crack front. In a torsion test, cracks propagate predominantly in the Case A mode, giving long shallow Stage I cracks along the surface.

Socie *et al.* (39) added a term to Equation I.2 which would account for the effect of mean normal stress on the γ_{max} plane. Fatemi and Socie (40) were able to incorporate nonproportional loading effects into the earlier model. This was significant because it was found that shear-based approaches would not be applicable to all multiaxial fatigue situations as had already been demonstrated under HCF conditions in the work of Gough *et al.* (41) and

Findley (38). The increased damage during out-of-phase loading was attributed to the extra cyclic hardening due to the rotation of the principal axes. Kurath and Fatemi (42) introduced the parameter

$$\Delta\gamma_{\max} \left(1 + k^* \frac{\sigma_n^{\max}}{\sigma_y} \right) = C^* \quad (I.3)$$

for a given life, where σ_n^{\max} is the maximum normal stress to the plane of maximum shear strain range, $\Delta\gamma_{\max}$; here, k^* is used to correlate experimental data, C^* is constant for a given life, and σ_y is the cyclic yield strength.

A most recent development in critical plane formulations is incorporating the effects of the transverse strain - the normal strain in the crack-line direction. Wang and Pan (43) examined the effects of the transverse strain on the near-tip fields of small Case A cracks in power-law hardening materials under mixed mode I and II conditions. For their finite element analyses on a 2-D center cracked panel subjected to biaxial normal and shear strains, they found that in addition to the cyclic plastic zone ahead of the crack tip, a second concentration of plastic straining occurred directly below the crack tip. This result indicated that the presence of a tensile transverse strain produced increased opening stress ahead of the crack tip. From their computational results, they suggest that the transverse strain be included in critical plane formulations. Therefore, an additional normal (stress) strain term

would be added in Equation (I.3). Clearly, more experimental and computational analyses are required to properly determine how the transverse strain should be incorporated into critical plane formulations in order to reflect increased opening stresses ahead of the crack tip.

Even with these significant advances in LCF correlations, additional work is needed to model the evolution of the crack length with increments of cycle under multiaxial fatigue, and to address the HCF regime. Propagation analyses, often treated using either LEFM or EPFM, should be combined with critical plane concepts outlined above. Critical plane approaches, to some degree, have been extended (2-3,20) to small crack propagation formulations because of their ability to reflect the physical observations of crack growth behavior. Such a physically-based approach is attractive in that modeling parameters can be directly attributed to features of cracking mechanisms on the microscale; other empirical approaches do not directly reflect such observations.

Small crack propagation formulations consistent with critical plane concepts were introduced by McDowell and Berard (2-3) and Reddy and Fatemi (44). Reddy and Fatemi (44) used a combination of ΔK and critical plane concepts for the propagation of cracks. Since the two-parameter approach in Equation (I.3) correlated fatigue life to a 1 mm surface crack under a wide variety of multiaxial loading conditions, Reddy and Fatemi (44) postulated that these parameters can represent the driving force for crack propagation. They defined a pseudo- ΔK as

$$\Delta K_{CPA} = G \Delta \gamma_{\max} \left(1 + k^* \frac{\sigma_n^{\max}}{\sigma_y} \right) (\pi a)^{1/2} \quad (I.4)$$

to correlate with da/dN . This parameter takes the form of an effective strain-based ΔK_{CPA} , where G is the shear modulus, and a is half the surface crack length. Here, ΔK_{CPA} is used for materials for which crack nucleation and small crack propagation occur along the planes of maximum shear strain amplitude. The constant k^* is determined by collapsing the fully reversed uniaxial fatigue data to the fully reversed torsional fatigue data. It was found that this formulation gave promising results for both nonproportional and proportional tests, but there was still significant scatter for low ΔK_{CPA} when comparing to experimental data.

Indeed there are problems in using LEFM concepts/parameters to characterize small crack growth. Dowling and Begley (44) first introduced the ΔJ -Integral for fatigue crack growth in an elastic-plastic cyclic deformation field. This parameter is perhaps a more appropriate candidate than ΔK to be combined with critical plane concepts because ΔJ can be applied to problems involving elastic-plastic deformation, and small fatigue cracks are often characterized by substantial crack tip plasticity. Small crack propagation under predominately LCF conditions has been treated within the framework of EPFM by a number of researchers (13-14,46-48). The cyclic J-Integral (45,49-51), ΔJ , has been frequently applied to correlate small crack propagation rate using the power-law relation

$$\frac{da}{dN} = C_J (\Delta J)^{m_J} \quad (I.5)$$

Hoshide and Socie (8) extended the J-Integral form presented by Shih and Hutchinson (52) (pure Mode I loading) to include mixed-mode loading. One of the shortcomings of Equation (I.5) is that both the elastic and plastic components of the ΔJ -Integral have the same linear dependence on crack length. Results of various studies (cf. (19,53-54)) conflicted with the notion that the dependencies were the same for microstructurally small fatigue cracks. Such cracks grow by traversing and re-encountering grain boundaries. Their growth depends on microstructure, which renders the rate of growth of small cracks highly nonlinear, even oscillatory. Once the small crack has extended over more grains and has become mechanically small, the crack tends toward the applicability of Equation (I.5).

I.3 Small Fatigue Crack Growth

By establishing physical attributes of small crack behavior under HCF, a growth equation which respects many of these attributes can be proposed. A primary goal of establishing a crack growth law which traverses multiple regimes of crack growth is to provide better estimates of the remaining life of components in fatigue. Naive treatments of propagation have led to overestimations of fatigue life. A distinguishing feature of HCF is

the high degree of heterogeneity of local cyclic slip processes. Under LCF conditions, PSBs and small cracks are fairly uniformly distributed among grains, leading to low variability of fatigue crack nucleation and propagation processes. There is a regime of crystallographic growth of small cracks roughly coincident with the orientation of maximum shear planes, termed by Forsyth (55) as Stage I growth. For HCF conditions, the cyclic plastic slip processes are highly heterogeneously distributed among grains and the surface crack density is sparse (56). For these conditions, there may also be an early transition to Stage II behavior, characterized by propagation normal to the direction of the maximum principal stress range. The following sections discuss in more detail the transition between stages of small crack growth, intrinsic material resistance ahead of the crack, fatigue limits, the role of the free surface and crack closure issues.

I.3.1 Transition from Stage I to Stage II Crack Growth

Early assessments of the transition from Stage I to Stage II crack propagation were made by Cox and Field (57) in 1952. They found that this occurred when the ratio of local tensile stress to shear stress was about 1.6. Swenson (58) established that the transition for FCC metals that exhibit disassociation into partial dislocations occurs when the separation of partial dislocations is reduced to the order of the Burger's vector. This disassociation is influenced by the crack tip stress field and the materials' stacking fault energy. In 1972, Plumbridge (22) stated that the transition occurred when the ratio of tensile stress to shear

stress at the crack tip reached a critical value. Miller (11) established that Stage I crystallographic (shear-dominated) small crack growth is typically observed to transition to the Stage II growth (normal/tensile dominated) regime for crack lengths on the order of 5-10 grains, depending on the strength of the material. The strength of the material itself is a function of grain size and texture (11).

Li (23) studied the small crack transition behavior for aluminum alloys. The transition condition was quantitatively proposed to occur when the CTSD of Stage I cracks was equivalent to the CTOD of a Stage II crack. A physical basis of the transition crack size can be interpreted as the point where the dislocation pile-up reaches a level sufficiently high due to grain boundary blocking at the transition until new dislocation sources are activated. The plastic zone then extends right through the grain boundary to re-develop in the next grain. In Li's (23) interpretation, the transition is not related to the grain size or several grain sizes; rather the transition is closely related to the local stress level. His dislocation-based micromechanical model predicted both the crack growth transition and growth rates for small fatigue cracks. Both the local stress level *and* local microstructure control the transition from Stage I and Stage II. This transition depends on stress amplitude and stress state as well. Precise conditions for the transition are not yet established, in general. Certainly, no comprehensive models of cracks in polycrystals have been developed or studied to understand effects of heterogeneity due to lattice misorientation on a broad scale rather than single, planar bicrystal boundaries.

I.3.2 Fatigue Limits

One method to represent thresholds for small crack growth in HCF is to plot a Kitagawa diagram which represents a locus of points of non-propagating crack length versus stress amplitude. An example for a low carbon steel with a ferrite grain size of $55\text{ }\mu\text{m}$ is shown in Fig. I.6 (12). Three regimes are labeled. In Regime I, small cracks do not propagate. Regime I is bounded from above at very small crack lengths by the smooth specimen fatigue limit, $\Delta\sigma_{wo}$. In reality, microstructurally small cracks have complex oscillatory growth rates below $\Delta\sigma_{wo}$ (cf. Fig. I.6), but these cracks arrest if the applied stress amplitude lies below $\Delta\sigma_{wo}$ (10-11,59). In Regime II, cracks propagate at stress amplitudes greater than $\Delta\sigma_{wo}$, or at crack lengths that exceed a_o , defined as the crack length corresponding to the long crack threshold, ΔK_{th} , at an applied stress of $\Delta\sigma_{wo}$. The dashed line between Regimes II and III corresponds to the asymptotic long crack threshold of LEFM for $a > a_o$. Crack length $a_o' = 20.3\text{ }\mu\text{m}$ represents the non-propagating limit for microstructurally small cracks for this material; for $a > a_o'$ and at stress levels below $\Delta\sigma_{wo}$, small cracks propagate at crack lengths below that of the long crack threshold. This has been attributed to decreased plasticity-induced closure effects for small cracks relative to long cracks in the vicinity of threshold conditions, accounting for the gradual transition from microstructurally small to long crack regimes (54). Cracks in Regime III grow until arrested at the boundary of Regimes II and III, subject to EPFM, a plasticity-induced closure transient

that develops with propagation.

The Kitagawa diagram has considerable relevance to threshold fatigue design approaches for HCF because it distinguishes between thresholds for small and long cracks. To a limited extent, the diagram also shows the change in fatigue crack growth mechanisms as a function of stress amplitude and crack length. Such diagrams, however, are applicable only to constant amplitude fatigue and may not be applied to overload conditions or sequences of amplitudes (54). Detailed incremental models for crack propagation and arrest are therefore crucially important to treat history effects and multiaxial loading conditions.

Riemelmoser *et al.* (60) utilized dislocation arguments to describe fatigue limits for an aluminum alloy (Al 7075-T6) and a steel (Steel A533). They assert that if the discrete nature of plasticity is taken into account by a dislocation model, the conditions for the fatigue threshold may be established. They found that this demarcation between applying a continuum versus a discrete (or cycle-by-cycle) analysis occurred at when the $\Delta CTOD$ was smaller than 150 Burgers vectors per cycle. Although their model neglected the influence of microstructure, the existence of a threshold was expressed in terms of the discrete nature and development of plasticity.

In addition to the fatigue limit for nonpropagating cracks, shakedown may also lead to a fatigue limit in HCF. The shakedown stress amplitude refers to the level at which microplasticity within and among grains is suppressed. The elastic shakedown limit of the heterogeneous cyclic microplasticity response may, in general, be lower than that associated with grain boundary blockage of small cracks. An elastic-plastic shakedown limit may also

exist which reflects an insufficient degree of cyclic microplasticity to nucleate cracks. In both instances, the consideration of heterogeneity of the polycrystal is essential. The model of Dang-Van (61), for example, accounts for the orientation distribution of grains, employing a polycrystal plasticity analysis to assess the intensity of cyclic plasticity and constraint between grains. A local critical slip plane failure criterion of Mohr-type, similar to Equation (I.2), is given by

$$\frac{\Delta\tau_c}{2} + k P = H \quad (I.6)$$

to assess whether the fatigue limit (arrest threshold) of individual grains, H , is breached. Here, $\Delta\tau_c$ is the range of the maximum resolved shear stress in the grain, and P is the peak hydrostatic stress. Shakedown of cyclic microplasticity is explicitly taken into account, although a crack length dependency is not included. Such local approaches recognize that the description of threshold behavior of local mixed Mode I-II nucleation/propagation behavior of Stage I small cracks must consider a combination of maximum shear stress range and some measure of normal stress to this plane (62). This method has successfully correlated HCF life for high strength components such as bearings.

From the discussions above, it is apparent that some combined approach which utilizes stress state, crack length dependencies, and shakedown limits of cyclic microplasticity would provide a more complete method for determining fatigue limits for

small cracks. Chapter III presents a micromechanical analysis on the distribution of microplasticity in polycrystals. This serves in establishing the nature of the transfer function between macroscopically applied stress to microcracking within an aggregate. Analyses of this type enables one to comprehend the distribution and intensity of cyclic microplasticity as a function of stress state and amplitude. Chapter V details a three-regime model which accounts for the full range of growth from microstructurally small to long cracks, including small crack threshold limits.

I.3.3 Roughness and Plasticity-Induced Crack Closure

There are other important mechanisms that affect the propagation of small cracks in HCF, including roughness-induced (crack face asperity interactions) and plasticity-induced closure. Faceted crystallographic crack growth promotes crack surface roughness-induced interference effects, particularly in low stacking fault energy FCC alloys and for coarse grained metals (63). Roughness-induced crack closure is promoted by a tortuous crack path associated with a mixed-mode crack growth mechanism and mismatch between the fatigue crack face asperities (64). This is particularly important for small cracks in HCF since the distribution of crack-like defects in cyclic plasticity is much less uniform than under LCF conditions (54). Asperities form on surfaces of growing small cracks, and these asperities may either bridge or wedge cracks open, leading to local shielding or enhancement. Tong *et al.* (63) addressed modeling sliding mode crack closure effects due to faceted fracture

surfaces which may prevail in the propagation of small crystallographic cracks. They performed analytical and finite element analyses to parametrically show the effects of asperity height, friction coefficient and crack length on the near threshold propagation rate in pure remote mode II loading. The model revealed that the faceted crack surface generated a local wedging mode I displacement, while the frictional attenuation tended to decrease the mode II displacements. Consequently, both the macroscopic mode II and local mode I ΔK were reduced at the same time. In view of actual small crack profiles, an ideal mode II loading condition may not be achieved due to the inevitable local mixed-mode loading conditions at the crack tip. Stage I crack tips inherently involve mode mixity because of local anisotropy and heterogeneity (54) ahead of the crack.

This behavior contrasts to plasticity-induced closure of small cracks under constant amplitude loading. Plasticity-induced closure is caused by residual plastic deformation left in the wake of an advancing crack. Small cracks generally have a smaller plastic wake behind the crack tip for the same crack tip driving force and decreases with decreasing crack size (65). As the crack lengthens, interactions between the crack and microstructural features (such as asperity height) may diminish relative to plasticity-induced closure, particularly for fine grain alloys. Effects of plasticity-induced closure on small crack behavior are explored in the computational analyses in Chapter IV.

1.3.4 The Role of the Free Surface

Proximity of the small crack to the free surface has several implications. One aspect of surface proximity is its effect on dislocation accumulation near the surface. Harvey *et al.* (66) used atomic force microscope images of slip band emergence at the free surface in both HSLA steel and Ti to confirm their model for crack nucleation based on cumulative slip offset which incorporates grain size and other factors. Dislocation models by Tanaka and Mura (67) and Venkataraman *et al.* (68-70) assume that the forward and reverse (irreversible) plastic flow within a PSB is modeled by dislocations with different signs moving on two closely spaced layers. The theory of continuously distributed dislocations is used to account for the monotonic buildup of dislocation dipoles piled up within the PSB. This buildup is associated with the development of extrusions or intrusions which are crack nucleation sites. These models, however, do not consider the effect of surrounding grains and the spread of cyclic plastic strain into those grains. This is a significant consideration, particularly for the growth of cracks. The role of the dislocation density gradient near the surface in the propagation of small cracks in HCF has not been studied.

A second factor which influences small cracks growing from the surface is the lack of constraint on crack opening/sliding. Constraint refers to the buildup of stress around a crack front due to the restraint against in-plane and out of plane deformation (71). The in-plane constraint has been associated with the closeness of the crack front to external boundaries whereas the out-of-plane constraint is mainly influenced by plate (or specimen)

thickness. Quantifying the level of constraint, therefore, is an important factor in modeling fatigue crack growth of small cracks. This lack of constraint also leads to initially high crack growth rates for small cracks until they grow into the surface where they experience more constraint from surrounding grains and more available slip systems upon which to grow (72-73). Keller and Gerberich (74) and Lin and Lin (75) made observations on the surface versus bulk behavior of a HSLA steel and single and polycrystalline aluminum under cyclic loadings, respectively. Keller and Gerberich (74) measured the surface layer to be approximately 300 μm or 6-7 grain diameters and found that after an accumulated bulk strain of 5% for high strength, low alloy (HSLA) steel, the surface experienced approximately three times as much accumulated strain as the bulk of the material. Additional studies by Chen *et al.* (76) reproduce similar results for single crystals of Fe-3wt%Si. Chen *et al.* (76) explain that this type of surface effect is due to the activation of multiple slip systems on the surface which causes a higher strain level on the surface, thereby affecting the crystal orientation locally. They found that the strain gradient disappeared after approximately 100 μm below the surface. This dimension is very crucial to small cracks because their dimension is on the order of this surface layer. These observations have tremendous bearing as to why they grow so rapidly in the MSC regime relative to long cracks with the same applied ΔK .

I.3.5 Small Crack Interactions with Microstructure

Grain boundaries and second phase particles are the primary microstructural barriers to small crack growth. The grain boundary is an amorphous interface where two single crystals of different orientation are joined. Because of the plastic incompatibility due to misorientation at the grain boundary, it is an effective barrier to dislocation glide. Likewise, interphase boundaries resist dislocation motion in the softer phase unless the hard particles are fractured or sheared, or the interface is decohered. Three observed small crack behaviors provide evidence for interaction of the small crack tip with grain boundaries. First, small fatigue crack propagation may slow down upon approaching a grain boundary due to interaction of the plastic zone with the grain boundary. Deceleration of the growth rate is the result of interaction of the crack tip cyclic plasticity with local barriers to plastic flow. Secondly, due to misorientation between two neighboring grains, a small crack front may deviate after penetrating the grain boundary. The deflection of the crack front is the result of an orientation change of newly activated slip bands. Thirdly, the very first grain boundary does not always lead to a severe drop of growth rate when a small fatigue crack penetrates it, although it usually controls the scale of nonpropagating cracks of the fatigue limit (cf. Miller (11), Li (23)). Some grain boundaries provide less blockage to small fatigue crack propagation due to their orientation (22). The adjacent grain may have a favorable orientation that promotes continuous slip without enhancing dislocation pile-ups and related stress concentrations. After penetrating the grain boundary, the small fatigue crack

propagates with reference to this preferred grain orientation.

Through the periodic measurement of plastic zone size (and shape) of growing small fatigue cracks, Zhang and Edwards (77) found that cracks begin to decelerate when their relatively large cyclic plastic zones (not the crack tips), were blocked by grain boundaries. Further propagation of the crack required that the plastic zone extend in the next grain, suggesting that the initiation of plasticity in the next grain controls the fatigue limit and growth rate in the small crack regime. This is a similar description of the small crack behavior as given by Li (23).

There is a subtle distinction of the interaction of the local lattice orientation of a long crack tip and a small crack tip with barriers. In the long crack case, it may be said that the crack tip *field* is influenced by barriers since it represents a bounded singular domain enclosing a statistically significant set of barriers. For microstructurally small crystallographic cracks, it is not clear that the tip obeys a singularity of long crack type since the scale of inelastic deformation, surface roughness, and damage process zone in the vicinity of the crack may be on the order of the crack length itself. Certainly, the embryonic stages of crack nucleation along PSBs suggests that such cracks embark on growth with the scale of cyclic plasticity and/or distributed damage as the dominant feature. Hence, there is a significant perturbation of the stress and strain fields in the vicinity of the crack due to interaction with microstructural obstacles. For long cracks, interaction with barriers along the crack front tend to average out, leading to less variability in the crack growth rate and therefore an apparent insensitivity to microstructural detail.

1.3.6 Small Crack Propagation Approaches

Identification of the potential limitations of LEFM/EPFM and direct experimental observations have led to alternative small crack propagation approaches. Tomkins (78) proposed a small crack propagation law for LCF based on shear decohesion along conjugate slip planes ahead of a Stage II crack, resulting in linear dependence of da/dN on crack length. In the transition from microstructurally small to long crack behavior, da/dN is often observed to be approximately linear with crack length in LCF. Many of the applications of the ΔJ -Integral have been reported for physically small cracks in LCF. Additional approaches for microstructurally and physically small cracks may be found in articles by Miller (10-11). Of particular interest for this research are those approaches which address many of the details of microstructural barrier interactions in Stage I and early Stage II propagation. Hobson *et al.* (79) developed empirical laws for deceleration of small fatigue cracks approaching a microstructural barrier located at $a = d$, i.e.

$$\frac{da}{dN} = A_o \tau_a^\alpha (d - a) \quad (I.7)$$

for $a < d$, where τ_a is the amplitude of maximum shear stress, α and A_o are constants (for a given mean stress), and d is fitted by regression analysis of data. Often, d is on the order of

a few mean grain diameters. The crack growth rate relation in Equation (I.7) averages oscillatory behavior at individual grain boundaries. For mechanically small cracks, the relation

$$\frac{da}{dN} = B \tau_a^\beta a - D \quad (\text{I.8})$$

was proposed by Miller (10), where D is a threshold growth rate, and B is a constant for a given mean stress. This relation assumes that cracks on the order of 3-10 grain diameters must be treated with an EPFM-type relation due to local large scale yielding effects. The highest rate from Equations (I.7) or (I.8) is assumed to apply. Arrest may occur if the two curves do not intersect prior to $a = d$.

In work by Hussain *et al.* (80), models of the small crack growth process were based on dislocation blockage and slip transfer solutions that display significant microstructural sensitivity and oscillatory growth behavior predicted over the first several grains. Tanaka *et al.* (81) provide detailed solutions for crack tip sliding and opening displacements which consider grain boundary blockage and slip transfer for Stage I and Stage II small cracks. They show that in addition to grain boundary blockage, large scale yielding and lower effective yield strength near the surface contribute to higher growth rates for cracks on the order of grain size. Depending on the degree of misorientation with nearest neighboring

grains, the first grain boundary may serve as the most effective barrier against arrest, similar to the assumptions of the Hobson *et al.* (79) and Navarro and de los Rios (83-84) models. Local crack closure effects associated with discrete slip bands and crack path fluctuations can also alter the local crack tip opening displacements in Stage II. While distributed dislocation theory-based approaches offer predictive capability, they are limited in addressing other important effects such as crack branching, lack of constraint associated with the free surface, effects of surrounding grains, and roughness-induced crack face interference. In short, they are highly idealized.

I.4 McDowell-Berard Small Crack Propagation Law

To properly assess and provide correlative models for the small crack regime, stress state, stress amplitude and crack length dependencies must be incorporated. McDowell and Berard (2-3) introduced a growth law that addressed these dependencies by proposing distinct growth laws for LCF and HCF. Under LCF conditions, McDowell and Berard (2-3) assumed mixed mode I and II crack growth in the plane of the crack, associated with crystallographic Stage I shear growth. They extended the ΔJ -Integral by analogy in the form

$$\frac{da}{dN} = C'_p (1 + \mu \rho)^m (\beta_p (\lambda_\sigma, \xi_\sigma) R_n + 1)^m \left(\frac{\Delta \tau_n}{2} \frac{\Delta \gamma_{\max}^p}{2} \right)^m a^m = D_{aN} C_p (\Psi_p)^m a^m \quad (I.9)$$

for completely reversed loading, where Ψ_p is defined as

$$\Psi_p = (1 + \mu\rho) (\beta_p(\lambda_\sigma, \xi_\sigma)R_n + 1) \left(\frac{\Delta\tau_n}{2} \frac{\Delta\gamma_{max}^p}{2} \right) \quad (I.10)$$

Equation (I.9) applies in the limit as the plastic strains dominate the elastic strains, i.e. the fully plastic case. Parameter β_p introduces dependence of the crack tip fields and/or crack tip opening and sliding displacements on stress biaxiality ratios λ_σ and ξ_σ , where $\lambda_\sigma = \tau/\sigma_{yy}$ and $\xi_\sigma = \sigma_{xx}/\sigma_{yy}$ (τ and σ_{yy} are the far field shear and normal stresses, respectively; σ_{xx} is the direct stress parallel to the crack). The constraint parameter, ρ , is nonzero only when multiple normal stress components are operative as in biaxial loading. It is defined as

$$\rho = \frac{\Delta\sigma_{kk}/2}{2 \Delta\tau_n/2} - R_n \quad (I.11)$$

and introduces additional dependence of the small crack propagation rate on $R_n = (\Delta\sigma_n/2)/(\Delta\tau_n/2)$. Here, R_n is a biaxiality factor which varies from zero for completely reversed torsional fatigue to unity for uniaxial or biaxial loading conditions. Also, $\Delta\sigma_n$, $\Delta\tau_n$, and $\Delta\gamma_{max}^p$ are the ranges of normal stress, shear stress, and maximum plastic shear strain,

respectively, on the plane of maximum range of plastic shear strain. Constants μ and m control the influence of constraint and nonlinearity of small crack growth; C'_p is a fully plastic coefficient which recovers the independent LCF Coffin-Manson and cyclic stress-plastic strain laws for completely reversed loading in torsional and uniaxial fatigue.

The McDowell and Berard (2-3) law showed qualitative agreement with LCF experimental results based on Γ -plane plots (6-7) for completely reversed loading of both Case A and Case B (6-7) histories for Stage I shear-dominated small cracks. Again, Case A (e.g. torsion or combined axial-torsion or tubes) cracks grow along the surface and Case B (e.g. equibiaxial loading) cracks grow into the surface depending on the orientation of the 3-D strain field with respect to the surface. Their proposed law was able to correlate fatigue life (to a 1 mm crack) to within a factor of two on life for a wide range of multiaxial loading conditions. From these results and others (4-7), consideration of (i) the range of shear strain and (ii) the stress or strain normal to the plane of maximum shear strain seem essential to correlate fatigue life.

Although separate forms for LCF and HCF small crack propagation were developed (2-3), a unified law is desirable. Considering that the McDowell-Berard approach (i) provided agreement with LCF experimental behavior in the Γ -plane, (ii) correlated the fatigue life (1 mm crack) to within a factor of two for a wide range of multiaxial loading conditions, and (iii) included distinct small crack growth laws for LCF and HCF, it is a viable candidate for extension to multiple regimes of small fatigue crack growth, especially

with an enhancement of its treatment of the MSC regimes.

As a first step, McDowell and Poindexter (aka Bennett) (20) extended the McDowell-Berard model into a unified law for both LCF and HCF. In this case, the possibility of a fatigue limit was neglected. The treatment of detailed nucleation and MFM growth concepts for $a < d$ (10-11,84) were not addressed, where a is the crack length and d is on the order of the grain size. For this engineering model, the complexities of microstructural influence on small cracks below the transition crack length, kd , were taken into account in an average sense by assigning a nonlinear dependence on crack length, amplitude and stress state, rather than considering the vagaries of oscillatory growth past barriers. For $a > kd$, a linear dependence of da/dN on crack length was assumed up to validity of LEFM.

To represent the MFM and EPFM_μ regimes of small crack propagation, the McDowell-Berard small crack propagation law was modified as

$$\frac{da}{dN} = D_{aN} [R_e C_e (\Psi_e)^M + (1 - R_e) C_p (\Psi_p)^m] \left(\frac{a}{kd} \right)^{m_\gamma} \quad (\text{I.12})$$

where

$$\Psi_p = (1 + \mu\rho) (\beta_p R_n + 1) \left(\frac{\Delta\tau_n}{2} \frac{\Delta\gamma_p^{\text{max}}}{2} \right) \quad (\text{I.13})$$

$$\Psi_e = (1 + \mu\rho) (\beta_e R_n + 1) \left(\frac{\Delta\tau_n}{2} \frac{\Delta\gamma_{\max}^e}{2} \right) \quad (\text{I.14})$$

and R_e is a non-dimensional ratio, $0 < R_e \leq 1$, representative of the relative degree of macroscopic elastic straining

$$R_e = \frac{\Delta\gamma_{\max}^e}{\Delta\gamma_{\max}} \quad (\text{I.15})$$

The effective crack length exponent, m_γ , is of a different form for each of two regimes of propagation, i.e.

$$m_\gamma = m_\gamma(R_e, R_n, \Delta\gamma_{\max}^e) \text{ for } \frac{a}{kd} < 1 \quad ; \quad m_\gamma = 1 \text{ for } \frac{a}{kd} \geq 1 \quad (\text{I.16})$$

In Equation (I.12), the coefficient D_{aN} is determined by integrating the expression for constant amplitude loading conditions between given initial and final crack lengths, i.e.

$$D_{aN} = 2 \int_{a_i}^{a_f} \left(\frac{a}{kd} \right)^{m_\gamma} da = 2 kd \ln \left(\frac{a_f}{kd} \right) + 2 \frac{a_i \left(\frac{kd}{a_i} \right)^{m_\gamma} - kd}{m_\gamma - 1} \quad (I.17)$$

where it is understood that m_γ in the second term on the right-hand-side corresponds to the regime $a < kd$. The decomposition into MFM ($a < kd$) and EPFM _{μ} ($a > kd$) regimes is clearly reflected by the two terms of equation above. Since m_γ is a function of stress amplitude and stress state, it is apparent that D_{aN} depends on both stress state and amplitude. The adoption of a constant kd in Equation (I.12) is purely empirical in nature, intended to reflect experimental evidence. Likewise, the forms of Ψ_e and Ψ_p in Equation (I.12) are based on the McDowell-Berard model from MFM concepts/solutions and micromechanical models. Improvements in the forms of kd and m_γ are desired in order to reflect the changing driving forces for small cracks.

Equation (I.12) compared well to experiments performed by Socie (4) on 1045 steel and Inconel 718 concerning the growth of small cracks under completely reversed tension and torsion. There are fundamental differences between propagation of small cracks in cyclic torsion and tension-compression. For lives on the order of 10^6 cycles under tension-compression, most of the "initiation" life is spent in propagating cracks with lengths on the order of the grain size. However, in torsion for $N_f = 10^6$ cycles, most of the life is devoted to propagation of cracks with lengths in excess of the grain size. At increasing lives, the

fraction of life spent in growing cracks with lengths less than 100 μm in length increases, to a much greater extent in uniaxial fatigue than in torsional fatigue. The crack growth behavior is quite nonlinear with respect to crack length for cracks shorter than 100 μm under HCF conditions, particularly for uniaxial fatigue at longer lives. The point of departure from Stage I shear-dominated crack growth to Stage II normal stress-dominated growth occurs at higher strain amplitudes for uniaxial fatigue, likely due to the influence of the normal stress across the Stage I crack in promoting secondary slip band formation and crack branching at the crack tip. Torsional fatigue appears to promote Stage I behavior at long lives for a given crack length, perhaps associated with low symmetry slip (lower Taylor factor and more primary slip) at the local level. This likely points to an enhanced microstructural roughness-induced shielding effect in uniaxial HCF relative to torsion when the crack opening displacement is on the scale of crack surface roughness.

Iso-crack length contours similar to those of Socie (4) were constructed for 1045 steel. Consistent and similar differences are exhibited by the model for torsional and uniaxial behavior. A major reason for writing Equation (I.12) in that form is to account for sequence effects. Sequences of torsional fatigue followed by uniaxial fatigue for three different loading levels are shown in Fig. I.7, with N_f corresponding to $a_f = 1 \text{ mm}$. The law predicts relatively strong sequence effects for the case of decreasing stress amplitude (11). The interaction curves plotted from stress state sequence effects exhibit a nearly bilinear character, similar to the double-damage curve analysis introduced by Manson and Halford

(32), especially for cyclic tension. The McDowell-Poindexter (20) law more adequately correlates experimentally observed damage accumulation and interaction than a single power-law description based on nonlinear cycle fraction summation. This 'bilinear' form is a natural consequence of the decomposition of the crack growth process into two regimes with different operative mechanisms. Even with the advances offered by this form of the small crack propagation law, improvements are needed for the current empirical forms for kd , Ψ_e , Ψ_p , and crack length dependencies.

I.5 Three-Dimensional Effects for Small Cracks

After small cracks initiate on the surface, they grow along the surface and into the bulk material. By growing into the bulk, the small crack experience more constraint from the surrounding material which can be characterized as a three-dimensional (3-D) effect. A 3-D description of small fatigue crack closure would be another factor that would improve the predictive capabilities of remaining life. To predict the fatigue crack growth patterns and fatigue lives for surface cracks, and 3-D crack geometries such as surface cracks at holes and corner cracks at holes, Newman and Raju (85) used LEFM concepts that were modified to account for crack closure behavior. They examined two aluminum alloys (7075-T651 and 7050-T73). Under constant amplitude loading, the cracks geometries were assumed to grow in either a semi-elliptical or quarter-elliptical shape and points at the surface and at the

maximum depth point were monitored. They found that for $R = 0$ loading, small semicircular surface cracks tended to grow in a self-similar fashion, although the stress-intensity factor at the surface was 10% higher than at the maximum depth. Although a constraint factor was introduced to account for these differences in K , growth rates and fatigue lives were only correlated within 30%. In addition, the shape of the crack front was not predicted well because the closure parameter did not account for residual stresses at the surface. Work by Trantina *et al.* (86) found that the K value was only 4% higher at the surface than in the depth. Their finite element analyses on 3-D small surface cracks provided stress-intensity factors for 3-D crack geometries and effective K values for 3-D elastic-plastic conditions. As found in the previous work by Newman and Raju (85), these changes in K along the surface was attributed to the lack of plane-strain constraint at the surface, therefore, self-similarity of small cracks in 3-D bodies cannot be assumed.

In 1990, Dawicke *et al.* (87) experimentally quantified the three-dimensional closure effect for an aluminum alloy (2024-T351). Indeed, the global and surface crack opening load measurements only provide a 2-D view of a 3-D problem. With the exception of very thin sheets, where the constraint is entirely plane stress, a 3-D variation in plasticity-induced closure behavior exists along the crack front. This variation is due to the change in constraint from plane stress at the surface to plane strain in the interior. The shape changes are due to a combination of the 3-D variation of both fatigue crack closure and stress intensity factor along the crack perimeter and cannot be predicted with 2-D models. The crack opening loads (K_{open}/K_{max}) were found to range from 0.35 to 0.4 near the surface while values of less than

0.2 were observed in the interior. Newman *et al.* (71) also performed 3-D elastic plastic finite element analyses to quantify these constraints in order to incorporate 3-D effects in 2-D crack analyses. They suggest a global constraint factor to account for three “local” constraint parameters along the crack front and are based on the normal, tangential, and hydrostatic stresses along the crack front. Although these results are mainly for cracks on the order of physically small cracks, including this influence improved the model’s ability to predict fatigue crack growth data within 15%. This is a significant improvement to the initial model by Newman and Raju (85). Later studies by Newman (88) and Wu *et al.* (89) incorporated this constraint concept to better correlate fatigue data.

Carlson *et al.* (90) present experimental studies of the fatigue growth of small corner crack emanating from small flaws in an aluminum alloy. A three-point bending state of loading was used and by virtue of the square cross-section of the specimen, the maximum tensile stress developed at the middle of the gage section and on a corner edge. For this geometry, grain boundaries were effective in curtailing crack growth; this is in line with 2-D assessments of small crack growth in that grains barriers are one of the barriers to continuing growth. However, it is more descriptive to visualize a 3-D geometry in which the advancing crack encounters a ‘grain boundary wall’ which introduces local barriers to continuing growth. In addition, since small thumbnail cracks, for the same crack depth, can be expected to have about twice as many grains along their fronts as small corner cracks, their growth behaviors may differ. The usual stress intensity factors which assume homogeneity, however, are insensitive to these differences. The anomalous growth rate of small cracks

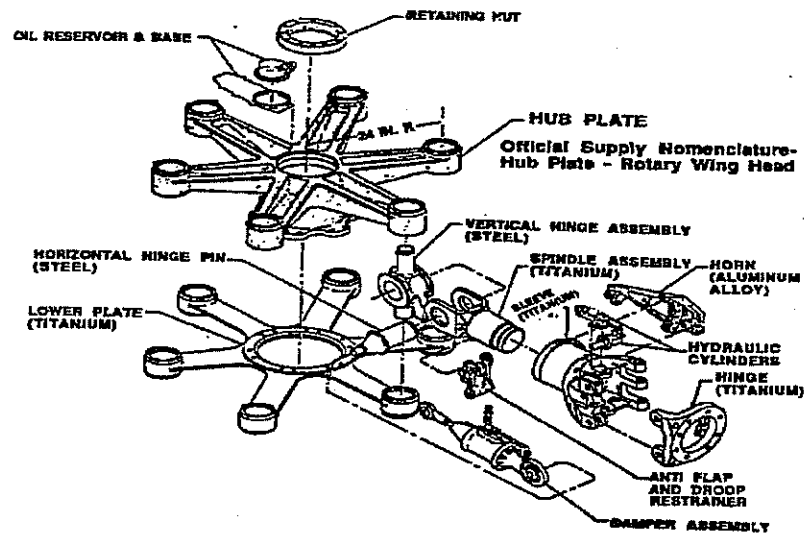
may be due in part to the fact that surface grains, which are a large fraction of the total number of grains along the crack front of a small crack, are not subjected to the level of interior grains.

In an effort to further bridge experimental and computational analyses, Zhang *et al.* (64) used in-situ SEM measurements and finite element analyses to determine the magnitude of fatigue crack closure due to the effect of plasticity- and roughness-induced closure. They found that the fatigue crack closure stress levels from the finite element analyses were lower than those from SEM data because roughness was not accounted for in the finite element model. This was due to the contact of asperities on the fatigue crack surfaces which was not accounted for in the finite element analysis. When a model was developed which accounted for both plasticity and roughness effects, it correlated well with experimental fatigue life data for Al 2024-T351.

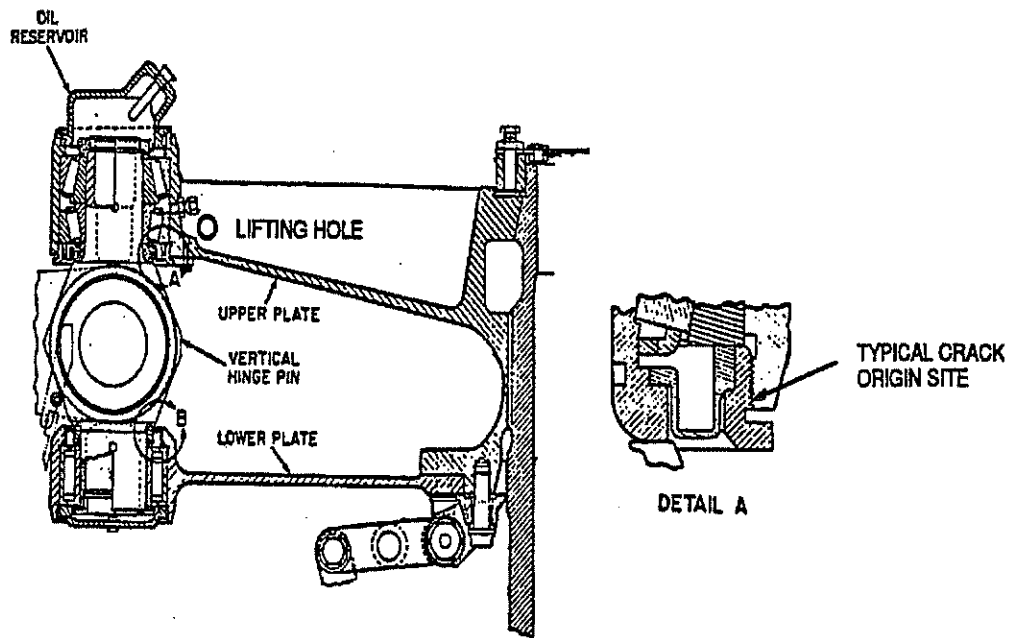
Most recently, Newman *et al.* (91) used a plasticity-induced closure model to predict fatigue lives of using 'small-crack theory' for various materials (aluminum alloys and steels) and loading conditions. The model included a 3-D constraint factor which accounted for the elevated flow stress at the crack tip and the influence of stress state. A distinguishing feature of this work is that smaller initial crack sizes were considered (2 μm to 10 μm) as well as microstructural features, such as inclusion-particles which served as crack initiation sites.

L.6 Outstanding Issues to Be Addressed In This Work

At present, small crack propagation laws are largely qualitative in nature due to the complexity of the local problem of propagation in heterogeneous microstructure and EPFM conditions. The current small crack growth laws have not fully incorporated the effects of periodic barrier interactions, non-propagating crack limits, and shakedown of microplasticity. Detailed micromechanical approaches that recognize local anisotropy and heterogeneity effects, such as crystal plasticity, can shed light on more appropriate and specific forms for such small crack propagation laws. While distributed dislocation theory-based approaches offer predictive capability, they are limited in addressing realistic, first order effects such as lack of constraint associated with the free surface, effects of surrounding grains, and crack face interference. The computational micromechanical approach used in this work will address these first order effects and will foster the development of improved forms of small fatigue crack growth laws. Although 3-D effects which account for additional constraints for small crack growth are potentially important, they will not be explicitly addressed in this work.



(a)



(b)

Figure I.1 (a) Upper plate of rotor hubs (b) and sites of crack formation (17).

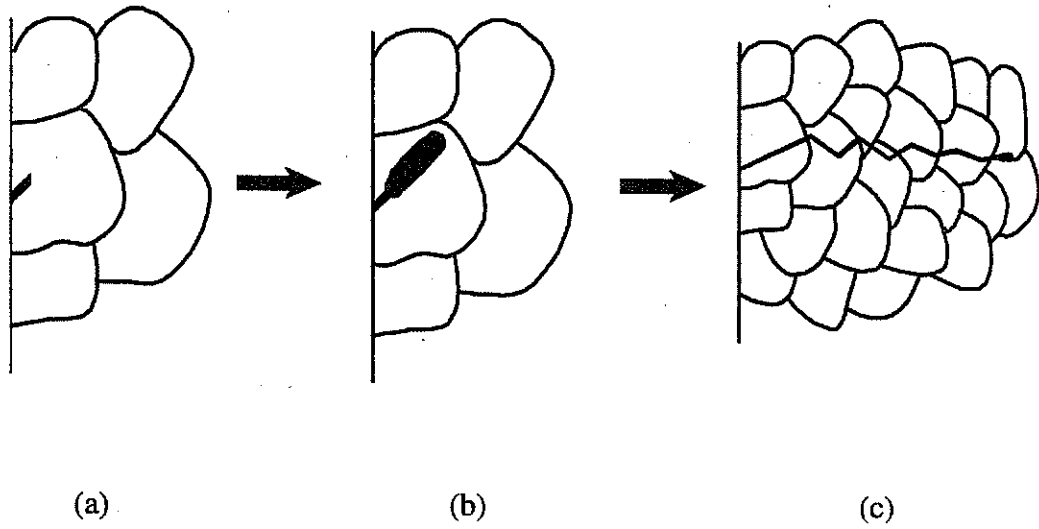


Figure I.2 Small crack sizes and characteristic dimensions (a) microstructurally small, (b) mechanically small, and (c) physically small.

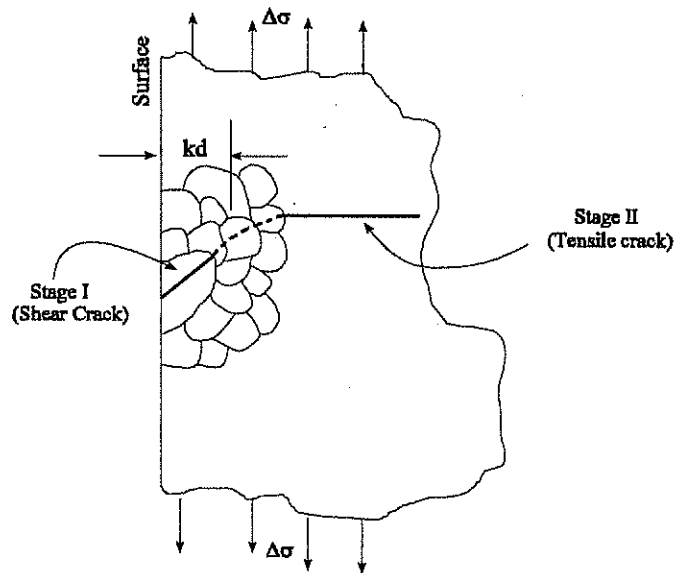


Figure I.3 Schematic of Stage I and Stage II crack growth behavior for cyclic tensile loading.

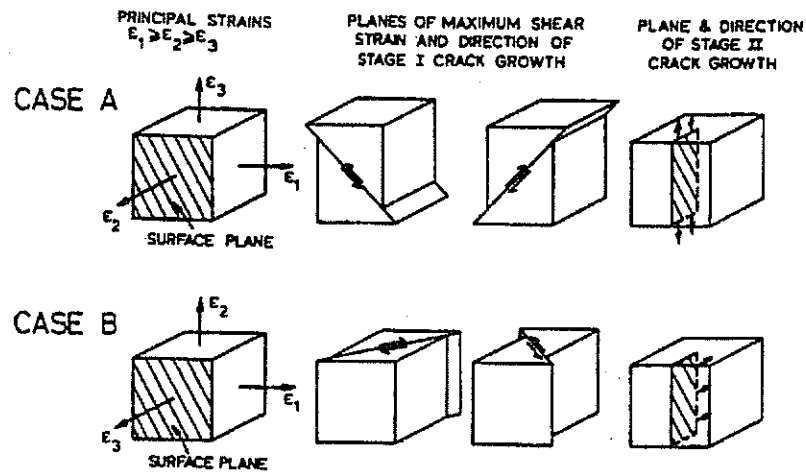


Figure I.4 Case A and Case B - under general multiaxial cyclic strain (6).

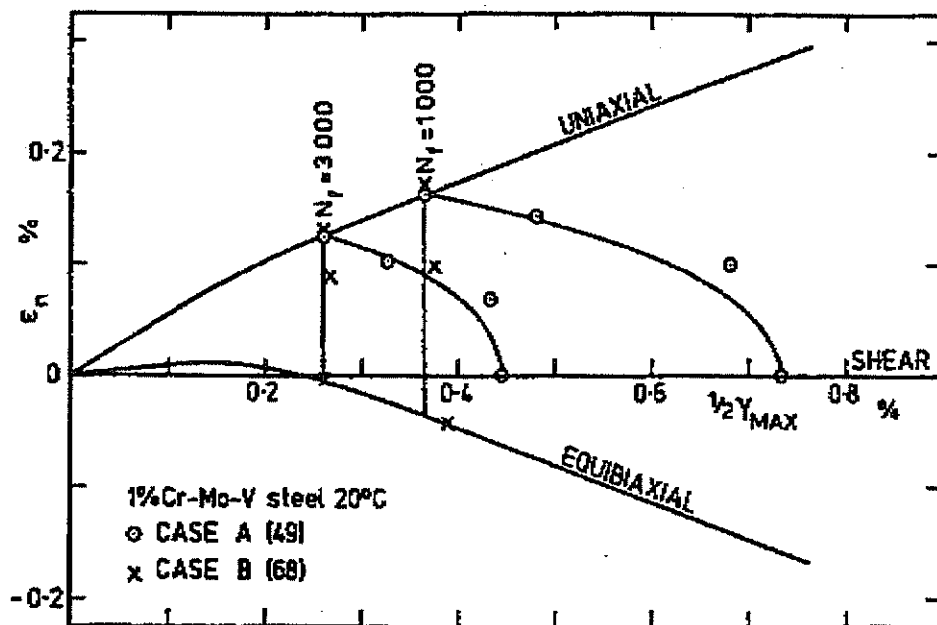


Figure I.5 Γ - planes for 1Cr-Mo-V steel at 20°C showing Case A and Case B (6).

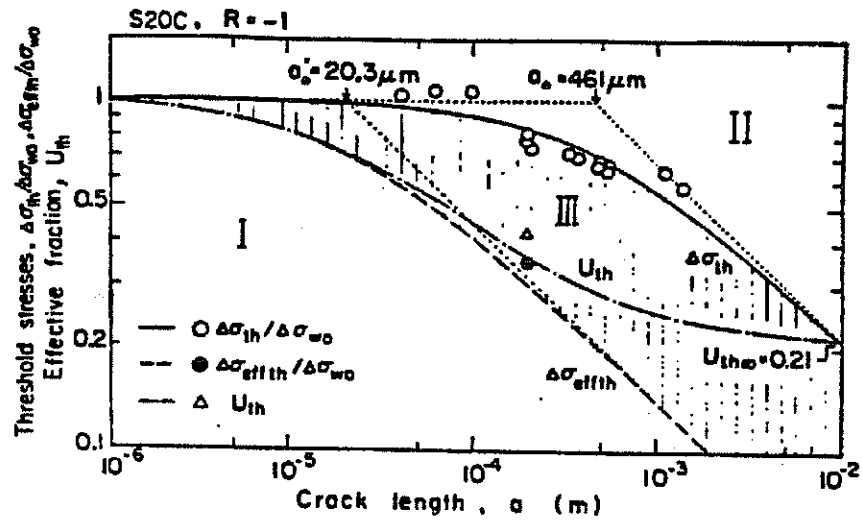


Figure I.6 Kitagawa diagram for a low carbon steel with ferrite grain size of 55 μm (12).

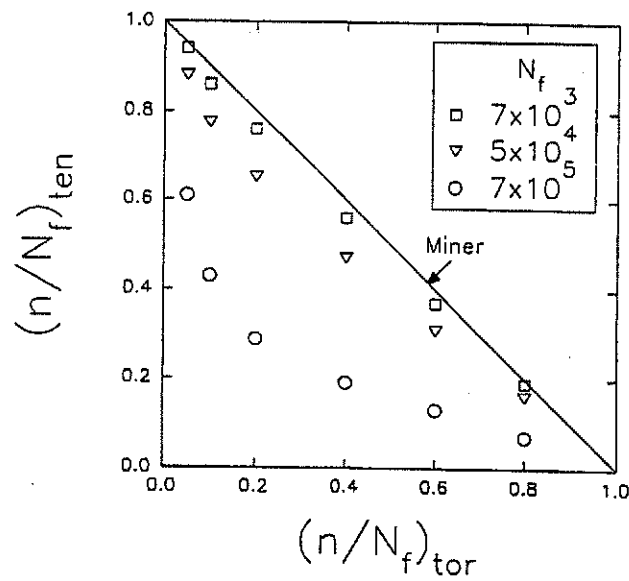


Figure I.7 Predicted interaction behavior for completely reversed torsion followed by cyclic tensile sequences for three different constant amplitude fatigue lives for 1045 steel; in each case, N_f corresponds to $a_f = 1 \text{ mm}$ (20).

CHAPTER II

CRYSTAL PLASTICITY AND MODELING OBJECTIVES

To facilitate necessary improvements in small fatigue crack growth models, micromechanical calculations based on computational cyclic crystal plasticity can provide a better understanding of the influence of microstructure. Since crystal plasticity models relate the macroscopically applied stress to the microscopic crystallographic slip response, they are appropriate to study heterogeneity and interactions across grains. Given that small crack growth is highly dependent on microstructure and the interaction of cyclic microplasticity among grains, a continuum slip idealization for response of grains seems appropriate. Models of this type can provide useful, quantitative information which serve as an important vehicle to study local behavior of microstructurally small cracks. This Chapter reviews the essential details and implementation of a continuum crystal plasticity model.

II.1 Planar Double Slip

The continuum theory of single crystal plasticity can be used to model the behavior

of FCC metallic crystals, which are known to plastically deform by slip on the close-packed $\{111\}$ planes, and in the close-packed $\langle 110 \rangle$ directions. FCC crystals possess 12 separate slip systems (three possible $\langle 110 \rangle$ slip directions on four $\{111\}$ planes). Figure II.1a gives a slip system representation of the planar double slip idealization. Two of the four unique $\{111\}$ planes are shown together with the four $\langle 110 \rangle$ slip directions that would be activated in $(1\bar{1}0)$ planar plastic flow defined by a condition of zero plastic strain rate normal to the plane. The top dashed arrow corresponds to the slip direction for the “effective slip system” that represents the $(111)[\bar{1}01]$ and $(111)[0\bar{1}1]$, whereas the bottom dashed arrow represents the $(1\bar{1}\bar{1})[0\bar{1}\bar{1}]$ and $(1\bar{1}\bar{1})[\bar{1}0\bar{1}]$ slip systems (92). These four slip systems can therefore be characterized by two effective slip systems separated by 70.2 degrees in the crystal lattice (93-94). Figure II.1b illustrates the effective slip systems for the 2-D planar double slip idealization.

The slip geometry for a 2-D plastic deformation can therefore be represented by a planar-double slip idealization in which all grains share a common plane of deformation. These effective slip systems in 2-D (plane-strain assumption) maintain a fixed orientation with respect to each other and rotate with respect to the continuum (94). Figure II.1b shows the geometry for the two effective slip systems and how they may be oriented. The bisector angle, θ , orients the slip system pair relative to the fixed specimen axis. The angle ϕ defines the crystallographic close-packed planes in relation to the bisector angle, and ϕ equals 35.1° for an FCC crystal.

Of course, such a planar double slip model is always an idealization because it only accounts for deformation by crystallographic dislocation slip alone. In reality, inelastic deformation is not only a result of crystallographic slip, it may also occur via twinning, diffusion, and grain boundary sliding (95). Planar double slip only accounts for deformation by crystallographic dislocation slide alone. The basic premise of the analysis is that with the decomposition of the deformation gradient, $\mathbf{F} = \mathbf{F}^e \cdot \mathbf{F}^p$, material flows through the crystal lattice via dislocation motion, whereas the lattice itself, with the material embedded on it, undergoes elastic deformation and rotations. The deformation gradient remaining after elastic unloading and upon returning the lattice to its orientation in the reference state is $\mathbf{F}^{e-1} \mathbf{F} = \mathbf{F}^p$. Of course, in real processes, removal of the loads alone will not return the lattice to its original state and thus what remains as a residual \mathbf{F} after slip is more than just \mathbf{F}^p ; the lattice may be permanently reoriented, for example, as well as placed in a state of residual deformation. A 2-D model should be regarded as giving results of more qualitative value.

Another limitation of \mathbf{F}^p is that it represents the collective effect of dislocation glide and is a continuously distributed field quantity. Therefore, it is not well-suited to describe localized plasticity and does not produce a 'banded' effect along slip systems representing preferential softening along a slip direction. For cracked body analyses from which crack tip sliding and opening displacements are obtained, the initially equal probability of slip of the two system for the planar double slip idealization likely yields an underestimation of the sliding displacement quantities. The issue of equal probability of slip is briefly investigated in Chapter VI where one slip system has reduced hardening in order to simulate the effect

of a less resistant slip direction which might represent slip band behavior.

Glide of dislocations occurs along crystallographic slip planes and directions (96). The first quantitative description of plastic flow by crystallographic slip was made early this century by Taylor (97). With the introduction of computers, the use of incremental crystal plasticity theory has become more tractable. The rate of dislocation motion, or the rate of viscoplastic shearing, has often been represented by the phenomenological equation

$$\dot{\gamma}^{\alpha} = \dot{\gamma}_o \left(\frac{\tau^{\alpha}}{g^{\alpha}} \right)^{M_e} \quad (\text{II.1})$$

where $\dot{\gamma}_o$ is the reference viscoplastic shear rate, τ^{α} is the resolved shear stress on slip system α , g^{α} is the hardening or resistance to flow on the α^{th} slip system, and M_e represents the material strain rate sensitivity exponent (95, 98). Since the finest scale of microstructure processes considered in the present model is at the scale of the crystallographic slip system (CSS), it is assumed that all phenomena which are related to length scales below the grain level (e.g., atoms, molecules, discrete lattice defects) are modeled at the CSS level using this phenomenological approach. There are, however, two options when implementing crystal plasticity into continuum slip models to solve deformation problems - rate dependent and rate independent flow rules.

II.2 Rate Dependent and Rate Independent Crystal Plasticity

Initial crystal plasticity models, intended for plastic flow at low homologous temperatures, idealized the crystallographic slip as rate independent (9). Rate independent models, however, suffer an inherent deficiency in that the combination of active slip systems necessary to accommodate an arbitrary deformation is not unique. Active slip systems refer to those slip systems for which the resolved shear stress, τ^α , equals g^α , the resistance. An additional hypothesis is necessary in order to unambiguously specify which slip systems are active. The minimum work principle proposed by Taylor (97) resolves this deficiency, but replaces it with a new one - prohibitively expensive computational times. Anand and Kothari (99) and Schröder and Miehe (100) have addressed this issue by introducing iterative numerical procedures that substantially reduce the computational requirements.

Rate dependent crystallographic slip was introduced to resolve the numerical challenges of rate independent crystal plasticity theory and to represent more realistic flow kinetics at higher homologous temperatures (cf. Pierce *et al.* (98) and Asaro and Needleman (101)). In this approach, there typically is no yield condition and no loading/unloading criterion is applied. Instead, all slip systems are assumed active with their shearing rates being related to the resolved shear stress by the flow rule given in Equation (II.1), for example. Rate dependent crystal plasticity (RDCP) also introduces computational complexities in the form of very stiff differential equations that must be integrated numerically. RDCP formulations must, in turn, employ time steps in numerical integration

that remain very small to obtain accurate results (cf. Cuitiño and Ortiz (102)), especially when there is low rate sensitivity and hardening rate.

II.3 Structure of the Crystal Plasticity Algorithm

In modeling a polycrystalline aggregate with crystal plasticity, there are a few options regarding the structure of the crystal plasticity algorithm. The first is within a finite element context for cases where each integration point in an element represents the behavior of a number of grains. For this case, it is usually necessary to make an assumption regarding grain-to-grain constraints and interactions. The second option is for the aggregate to be modeled with discrete grains, where each element or several elements represents a grain or part of a grain. Figure II.2 gives examples of these modeling options.

In this work, the second method is used. For uncracked cases, each grain is represented by one element. The advantage of using this option is that both compatibility and equilibrium are well-approximated. Each element deforms according to continuity with neighboring grains. A distribution of plastic strain is obtained within each grain by using higher order elements. For the cracked cases, the second method is also used, but instead of each grain being represented by one element, the grain is subdivided into numerous (2-400) elements. The variation in number of elements in each grain depends on the grain's proximity to the small crack tip - those grains which are closer to the crack tip have a finer

mesh, whereas those grains further from the crack tip are less refined. Each grain is given an orientation, θ , which orients the slip system pair relative to the fixed specimen axis. However, a constraint is imposed on the nearest neighbor orientation in that the misorientation cannot exceed 15° (103).

The crystal plasticity algorithm begins with the kinematics of deformation by assuming a multiplicative decomposition (92, 95, 104) of the deformation gradient, $\mathbf{F} = \mathbf{F}^e \cdot \mathbf{F}^p$. Here, \mathbf{F} is the total deformation gradient; \mathbf{F}^e is the elastic deformation gradient which represents the the elastic distortion of the lattice and the rigid rotation; \mathbf{F}^p , the plastic deformation gradient, defines the cumulative effect of dislocation glide that leaves the lattice undisturbed. As discussed earlier, component \mathbf{F}^p represents the collective effect of dislocation glide along crystallographic slip planes. It is assumed that slip is a continuously distributed field quantity in this approach, which is a limitation in describing localized cyclic plastic strain, for example in PSBs. Three configurations of the deformation are defined: undeformed (reference), intermediate, and deformed. Figure II.3 shows the kinematics of elastic-plastic deformation of a crystalline solid deforming purely by crystallographic slip and elastic deformation of the lattice. The resolved shear stress (RSS) on the α^{th} slip system is given by $\tau^\alpha = \boldsymbol{\sigma} : (\mathbf{s}^\alpha \otimes \mathbf{m}^\alpha)$, where $\boldsymbol{\sigma}$ is the Cauchy stress, \mathbf{s}^α is the vector along the direction of slip, and \mathbf{m}^α is the vector normal to the slip direction, all expressed in the current configuration. The RSS or Schmid stress is the component of shear stress resolved in the slip plane and in the slip direction.

The slip system level constitutive framework essentially follows that of Cailletaud *et al.* (105) and Jordan and Walker (106). Pure nonlinear kinematic hardening is employed to describe cyclically stable response. The rate of viscoplastic shear strain, $\dot{\gamma}^\alpha$, for the α^{th} slip system is given by

$$\dot{\gamma}^\alpha = \dot{\gamma}_o \left| \frac{\tau^\alpha - x^\alpha}{G} \right|^{M_\epsilon} \text{sgn} (\tau^\alpha - x^\alpha) \quad (\text{II.2})$$

where G represents isotropic strengthening and $\dot{\gamma}_o$ is the reference shearing rate. Isotropic hardening is held constant to represent cyclically stable behavior and pure nonlinear kinematic hardening is employed according to the Armstrong-Frederick form

$$\dot{x}^\alpha = C \dot{\gamma}^\alpha - d x^\alpha |\dot{\gamma}^\alpha| \quad (\text{II.3})$$

The backstress, x^α , relates to dislocation interactions with, for example, dislocation walls produced by cyclic loading which serve to resist deformation. Equation (II.3) represents the nonlinear kinematic evolution of x^α , where C and d are direct hardening and dynamic recovery coefficients, respectively.

Given some known deformation history, one must determine the stress, crystal

orientation, and updated state variables for the entire deformation history, as in Ref (102). The numerical integration must solve a set of equations which enables \mathbf{F}^p to be determined from the history of deformation. An iterative technique, the Newton-Raphson (N-R) method (107), is used to solve for the system of coupled algebraic equations which arise in the course of this integration. A Fortran subroutine, UMAT (User MATerial), integrates the constitutive equations within the ABAQUS (108) finite element code. At each loading increment and gauss point within the finite element code, UMAT is called. It must provide updated stress and state variables at the end of the time step, given the updated deformation gradient. The N-R iteration technique was used to iteratively obtain the plastic shear strain rate, $\dot{\gamma}^\alpha$, for each slip system. The state variable update is reduced to a system of nonlinear equations for the increment of the plastic shear strain rate, $\Delta\dot{\gamma}^\alpha$, for each slip system. A backward Euler, fully implicit integration scheme was employed for the numerical integration. An incremental line search algorithm (110) and a time step subincrementation scheme (111) were both used to assist the rate of convergence (94) on $\Delta\dot{\gamma}^\alpha$. Convergence conditions are satisfied within 2-3 iterations. Global equilibrium and compatibility are enforced at the end of each time step based on the variational principle of virtual work in ABAQUS (108). The incremental line search algorithm on the N-R step does the following: the increment of the plastic shear strain rate, $\Delta\dot{\gamma}^\alpha$, is halved until an optimal value is reached such that the sum of the squares of the error in the estimate is minimized. This is necessary if the initial estimate of $\dot{\gamma}^\alpha$ is not a 'good' estimate - such that a minimum error results. The N-R iteration is again pursued towards the local minima. Figure II.4 illustrates the line

search algorithm. If the N-R procedure does not converge, the time step, Δt , is repetitively halved until convergence. The deformation gradient is also linearly interpolated during time step subincrementation (shown in Figure II.5).

The algorithm assumes small elastic strains and is comprised of four main components: (1) determine initial guess of $\dot{\gamma}^a$, (2) perform N-R to solve for $\Delta\dot{\gamma}^a$, (3) perform line search and time step subincrementation (if necessary) for convergence criteria, (4) obtain converged $\dot{\gamma}^a$, and (5) calculate the Jacobian for ABAQUS. An outline is given below to illustrate the algorithm:

- Variables passed into UMAT from ABAQUS at the beginning of the current time step: \tilde{F}_n , \tilde{F}_{n+1} , $\tilde{\sigma}_n$ where n is the current time step

- Define the elastic stiffness, C_{ijkl} , $C_{ijkl} = \lambda\delta_{ij}\delta_{kl} + \mu(\delta_{ik}\delta_{jl} + \delta_{il}\delta_{kj})$

(1) Determine initial guess of $\dot{\gamma}^a$ by the following steps:

$$\tilde{F}_n^e = \tilde{F}_n \cdot \tilde{F}_n^{p-1}$$

\tilde{F}_n^p is assumed to be the Identity tensor for the very first time step, based on the fact that there is initially no plastic deformation at the beginning of the first time step.

- Calculate the Elastic Green strain, \tilde{E}_n^e , from

$$\tilde{C}_n^e = \tilde{F}_n^{eT} \cdot \tilde{F}_n^e$$

$$\bar{\tilde{E}}^e_n = \frac{1}{2} \left(\bar{\tilde{C}}^e_n - I \right)$$

- Calculate 2nd Piola-Kirchoff Stress, $\bar{\tilde{S}}_n$, with respect to the intermediate configuration

$$\bar{\tilde{S}}_n = \bar{\tilde{C}} : \bar{\tilde{E}}^e_n$$

- Calculate resolved shear stress on α^{th} slip system

$$\tau_n^\alpha = \underline{\sigma} : (\underline{s}^\alpha \otimes \underline{m}^\alpha)$$

$$\underline{\sigma} = \frac{\underline{\sigma}^*}{\det \left| \bar{\tilde{F}}^e_n \right|}, \quad \text{where} \quad \underline{\sigma}^* = \bar{\tilde{F}}^e_n \bar{\tilde{S}}_n \bar{\tilde{F}}^e_n{}^T$$

Here, \underline{s}^α and \underline{m}^α are the vectors along the slip direction and normal to the slip plane, respectively, in the current configuration.

- Determine an estimate of the shearing rate,

$$\dot{\gamma}^\alpha = \dot{\gamma}_o \left| \frac{\tau_n^\alpha - x_o^\alpha}{G} \right|^{M_\epsilon} \text{sgn} (\tau_n^\alpha - x_o^\alpha)$$

where x_o^α is the initial value of the backstress

(2) Perform N-R to solve for $\dot{\gamma}^\alpha$. Given $\dot{\gamma}^\alpha$, find \tilde{F}_{n+1}^p , $\tilde{\sigma}_{n+1}$, $\tilde{\tau}_{n+1}^\alpha$, \tilde{x}_{n+1}^α , and \tilde{f}_{n+1}^α by solving simultaneous equations for $\Delta\dot{\gamma}^\alpha$

- Find \tilde{F}_{n+1}^p by

$$\tilde{F}_{n+1}^p = \exp \left(\tilde{\bar{L}}_{n+1}^p * \Delta t \right) \tilde{F}_n^p$$

where $\tilde{\bar{L}}_{n+1}^p$ is the plastic part of the velocity gradient in the intermediate configuration and is calculated by

$$\tilde{\bar{L}}_{n+1}^p = \sum_{\alpha} \dot{\gamma}^\alpha \left(\tilde{\bar{s}}^\alpha \otimes \tilde{\bar{m}}^\alpha \right)$$

Here, $\tilde{\bar{s}}^\alpha$ and $\tilde{\bar{m}}^\alpha$ are the vectors along the slip direction and normal to the slip plane, respectively, in the intermediate configuration.

- Continue with calculations for

$$\tilde{F}_{n+1}^e = \tilde{F}_{n+1} \cdot \tilde{F}_{n+1}^p{}^{-1}$$

$$\bar{\underline{C}}_{n+1}^e = \underline{F}_{n+1}^e{}^T \cdot \underline{F}_{n+1}^e$$

$$\bar{\underline{E}}_{n+1}^e = \frac{1}{2} \left(\bar{\underline{C}}_{n+1}^e - \underline{I} \right)$$

$$\bar{\underline{S}}_{n+1} = \underline{C} : \bar{\underline{E}}_{n+1}^e$$

$$\tau_{n+1}^\alpha = \underline{\sigma} : (\underline{s}^\alpha \otimes \underline{m}^\alpha)$$

$$x_{n+1}^\alpha = \frac{x_n^\alpha + C \Delta t \dot{\gamma}^\alpha}{1 + d \Delta t |\dot{\gamma}^\alpha|}$$

- Begin Newton-Raphson iteration to determine $\Delta\dot{\gamma}^\alpha$ by forming

$$f^\alpha(\dot{\gamma}^\alpha) = \tau_{n+1}^\alpha - x_{n+1}^\alpha - G \left| \frac{\dot{\gamma}^\alpha}{\dot{\gamma}_o} \right| \frac{1}{M_e}$$

- Do a linear expansion of $f^\alpha(\dot{\gamma}^\alpha)$

$$f_{i+1}^\alpha = f_i^\alpha + \sum_\beta \frac{\partial f_i^\alpha}{\partial \dot{\gamma}^\beta} (\Delta\dot{\gamma}^\beta)$$

where i refers to the iteration

- Setting $f_{i+1}^a = 0$ gives

$$- \sum_{\beta} \frac{\partial f_i^a}{\partial \dot{\gamma}^\beta} (\Delta \dot{\gamma}^\beta) = f_i^a$$

or in matrix form

$$- \begin{bmatrix} \frac{\partial f^1}{\partial \dot{\gamma}^1} & \frac{\partial f^1}{\partial \dot{\gamma}^2} \\ \frac{\partial f^2}{\partial \dot{\gamma}^1} & \frac{\partial f^2}{\partial \dot{\gamma}^2} \end{bmatrix} \begin{bmatrix} \Delta \dot{\gamma}^1 \\ \Delta \dot{\gamma}^2 \end{bmatrix} = \begin{bmatrix} f^1 \\ f^2 \end{bmatrix}$$

- Solve simultaneous equation for $\Delta \dot{\gamma}^B$
- Determine $SSE_{ref} \equiv$ reference sum squares error

$$SSE_{ref} = \sum_a [f^a]^2$$

(3) Begin Line Search

- Begin with $\Delta \dot{\gamma}^a = \frac{\Delta \dot{\gamma}^a}{2}$
- Form $\dot{\gamma}_{i+1}^a = \dot{\gamma}_i^a + \Delta \dot{\gamma}^a$ and recalculate

F_{n+1}^{p-1} , σ_{n+1} , τ_{n+1}^a , x_{n+1}^a , f_{n+1}^a , and $SSE_{line\ search}$ by performing N-R to solve for $\Delta \dot{\gamma}^a$.

(4) Check the convergence of the line search by comparing the SSEs.

4A. If $SSE_{line\ search} \leq SSE_{ref}$, $\Delta\dot{\gamma}^a$ has converged and go to Step 5

4B. If $SSE_{line\ search} > SSE_{ref}$ this step has not converged. The time increment is divided into two subincrements and start again at Step 2 with \bar{L}^p .

(5) Calculate global Jacobian matrix, J (tangent stiffness matrix)

$$J = \frac{\partial \Delta \underline{\sigma}}{\partial \Delta \underline{\epsilon}} = \left[\underline{I} + \underline{C} : \frac{\partial \underline{D}^p}{\partial \underline{\sigma}} \Delta t \right]^{-1} : \underline{C}$$

where

$$\underline{D}^p = \sum_a \dot{\gamma}^a \text{sym} \left(\underline{\bar{s}}^a \otimes \underline{\bar{m}}^a \right)$$

II.4 Finite Element Model Based on Crystal Plasticity

A planar double slip idealization (92, 112) of cyclic crystal plasticity was implemented in ABAQUS (108) through UMAT. The 3-D implementation described above, developed and coded by R. M. McGinty (109), was modified for the 2-D case as well as for cyclic behavior. The crystal plasticity model provides a phenomenological description of

crystallographic slip and dislocation interactions at the grain level and offers insight into the nature of heterogeneous cyclic plasticity and driving forces for small crack growth due to intergranular misorientation. This micromechanical model is useful to (1) study the distribution of cyclic microslip amongst a set of grains in a polycrystal, (2) investigate the character of crack tip fields for small cracks in the presence of crystallographic anisotropy and heterogeneity, and (3) better understand the interaction of a crack with microstructural barriers. The 2-D nature of planar double slip renders these calculations of more qualitative value in assessing the influence of microstructure. Only a single phase metal is idealized where grain boundary misorientation is the only source of heterogeneity. Moreover, the effect of shear localization within slip bands is not entirely treated with this model without modification by introduction of bands of lesser resistance to flow. This formulation does, however, offer a more direct treatment of crystallographic dislocation glide and associated plastic anisotropy in order to address the small fatigue crack problem. Isotropic elasticity is assumed within each grain in order to isolate the role of plastic anisotropy due to crystallographic slip.

Cuitiño and Ortiz (102) performed a numerical simulation of cracks in single crystals to assess the near-tip fields for monotonic loading by incorporating crystal plasticity within a finite element context. They computed the isocontours of slip activity in the small strain region ahead of the crack tip as well as dominant slip modes. The significance of the dominant slip modes is that they signify directions of rapid variations of displacements and stresses. These types of calculations are potentially very important for the understanding of small crack

behavior, even under complex loading conditions. The isocontours of slip are directly related to the plastic zones that develop around crack tips. Single crystal plasticity was extended to the polycrystalline realm by several investigators (113-115), enabling them to examine the effects of misorientation among neighboring grains. Analyses of this type provide evidence that the fundamental concepts of crystal plasticity can be extended in a straightforward manner to polycrystalline and crack problems.

II.5 Crystal Plasticity and Cyclic Deformation

The application of crystal plasticity to cyclic deformation problems has been undertaken by Cailletaud *et al.* (105), Jordan *et al.* (101), and Jordan and Walker (116). These studies have provided guidance for modeling with cyclic crystal plasticity. Cailletaud *et al.* (105) performed both microstructural observations and micromechanical modeling of cyclic multiaxial behavior of an austenitic stainless steel using a viscoplastic, rate dependent constitutive framework. Satisfactory correlations with experimental data were obtained for both uniaxial and nonproportional loading. The Cailletaud model predicted extra hardening and the extent to which multiplicity of slip occurred under nonproportional loading. By including the influence of multiple slip using interaction laws for cross hardening of slip systems, the response of the material was more accurately modeled.

Jordan *et al.* (106) and Jordan and Walker (116) also applied crystal plasticity to cyclic

planar double slip crystal plasticity concepts to study the crystallographic behavior of microstructurally small cracks in single crystals. They varied the orientation of the two slip planes with respect to the crack growth direction in order to estimate the variation of growth rate of MSCs. Upper and lower bounds for the growth rate of MSCs as a function of the macroscopic load and the crack opening were obtained based on a linear crack growth rate law (with COD), with implications for variability of the crack growth rate.

II.7 Application of Computational Crystal Plasticity: 2-D Analyses

Two types of analyses are performed in this work. In the first type, the distribution of three different fatigue initiation criteria on uncracked, polycrystalline aggregates are evaluated. This work considers different realizations of grains (aggregates of grains with random orientations of slip systems). By examining different microstructure realizations at different strain amplitudes, statistical information is obtained which provides insight into the dependence of fatigue crack formation and early growth on the heterogeneity inherent in real metal polycrystals.

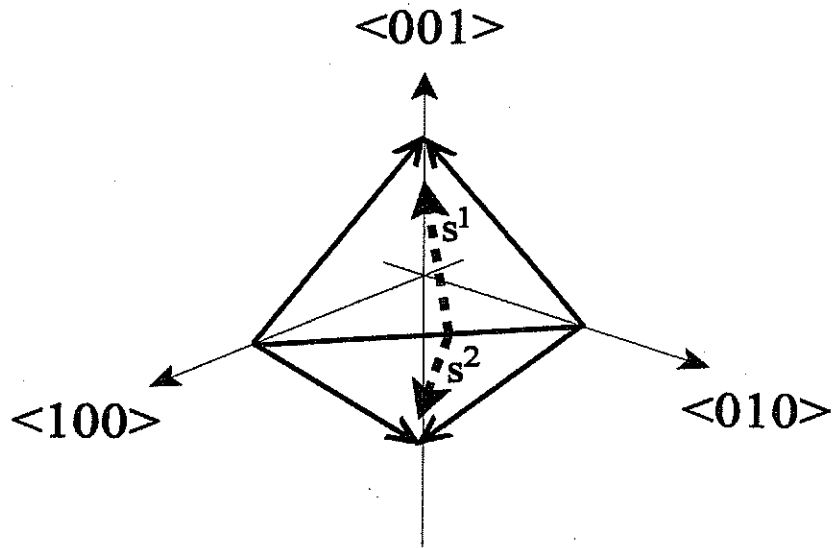
The second type of analysis considers a polycrystalline aggregate with an embedded surface crack. This type of analysis is unique in that cyclic deformation of polycrystalline aggregates using crystal plasticity includes the effect of surrounding (not just adjacent) grains on the distribution of cyclic microplasticity. This work is distinctive from the work of Li

(121) on bi-crystals. Firstly, not only is the influence of the orientation of slip in the cracked grain and adjacent grain studied, but also the effect of surrounding grains on the distribution of cyclic microplasticity and crack tip driving forces. Secondly, the effects of both primary and secondary slip in the grain adjacent to the surface crack are studied. These adjacent grain orientations are selected to either promote primary or conjugate slip at the crack tip and as the crack grows across grain boundaries.

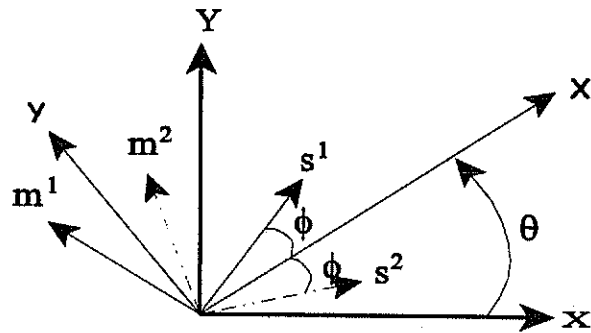
Both conditions of loading and crack orientations are shown in Figure II.6. For the remote tension-compression case (Figure II.6a), a surface grain contains a crack which is oriented at 45° with respect to the tensile axis. The slip system in the surface grain is oriented such that one of the slip system directions is aligned with the crack's orientation. There are two cases for the orientation of slip in the adjacent grain (denoted by the shaded area). One case is where the adjacent grain is modeled with an orientation of the slip system which promotes single (or primary) slip; the other case is for the adjacent grain having an orientation which promotes conjugate (or secondary) slip. In Figure II.6b, the remote shear loading condition has a surface grain that contains a crack which is oriented at 90° with respect to the tensile axis. In a similar manner as the tension-compression case, the remote shear case also has adjacent grains which are modeled with orientations which promote single and conjugate slip. Note that the orientations which promote single and conjugate slip in the adjacent grains differ for each loading condition.

Upper and lower bounds of the driving forces are determined for radically different orientations of the next grain ahead of the crack tip. These calculations are distinctive in that

they provide a direct method for determining what combination and to what extent orientation of adjacent and surrounding grains, crack length, and loading level contribute to driving forces for small surface fatigue cracks. Stationary crack analyses over a range of crack lengths are considered in this work rather than propagating the crack along predetermined crack paths using a nodal release criterion for crack growth. The former method was selected in order to focus more on first order microstructural influences (which are not yet well-characterized) rather than on complex crack paths and history effects which are more relevant to future work.



(a)



(b)

Figure II.1 (a) Two of the four unique $\{111\}$ planes are shown together with the four $\langle 110 \rangle$ slip directions that would be activated in $(1\bar{1}0)$ planar plastic flow. The top dashed arrow corresponds to the slip direction for the “effective slip system” that represents the $(111)[\bar{1}01]$ and $(111)[0\bar{1}1]$, whereas the bottom dashed arrow represents the $(1\bar{1}\bar{1})[0\bar{1}\bar{1}]$ and $(1\bar{1}\bar{1})[\bar{1}0\bar{1}]$ slip systems, and (b) effective slip systems for 2-D planar double slip idealization.

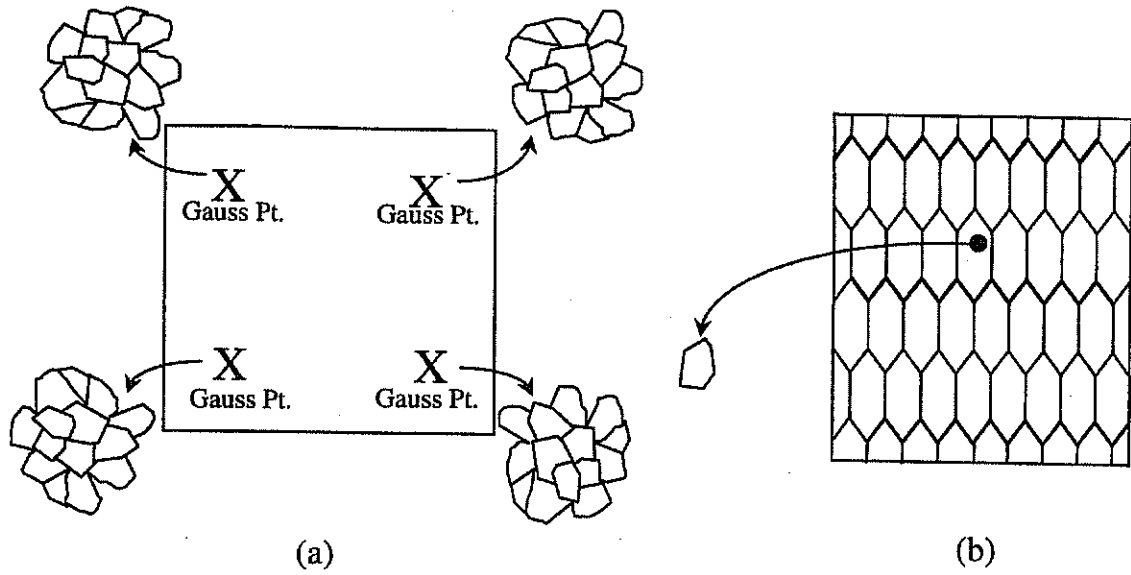


Figure II.2 Modeling options for modeling a polycrystal using crystal plasticity within a finite element context (a) one finite element with each gauss point representing several grains and (b) finite element mesh with each element representing a grain or multiple elements within each grain.

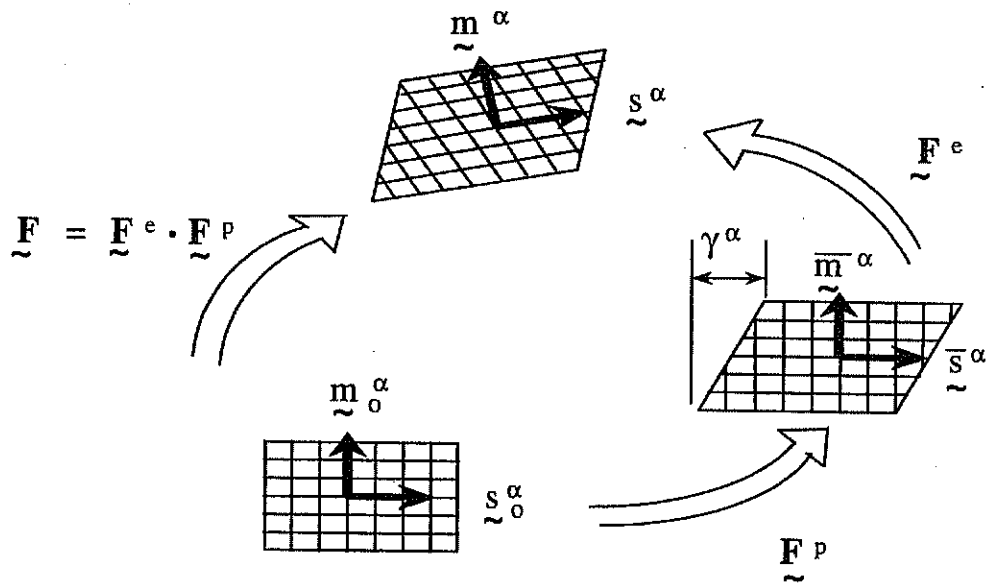


Figure II.3 Kinematics of elastic-plastic deformation showing undeformed (reference), intermediate, and deformed configurations.

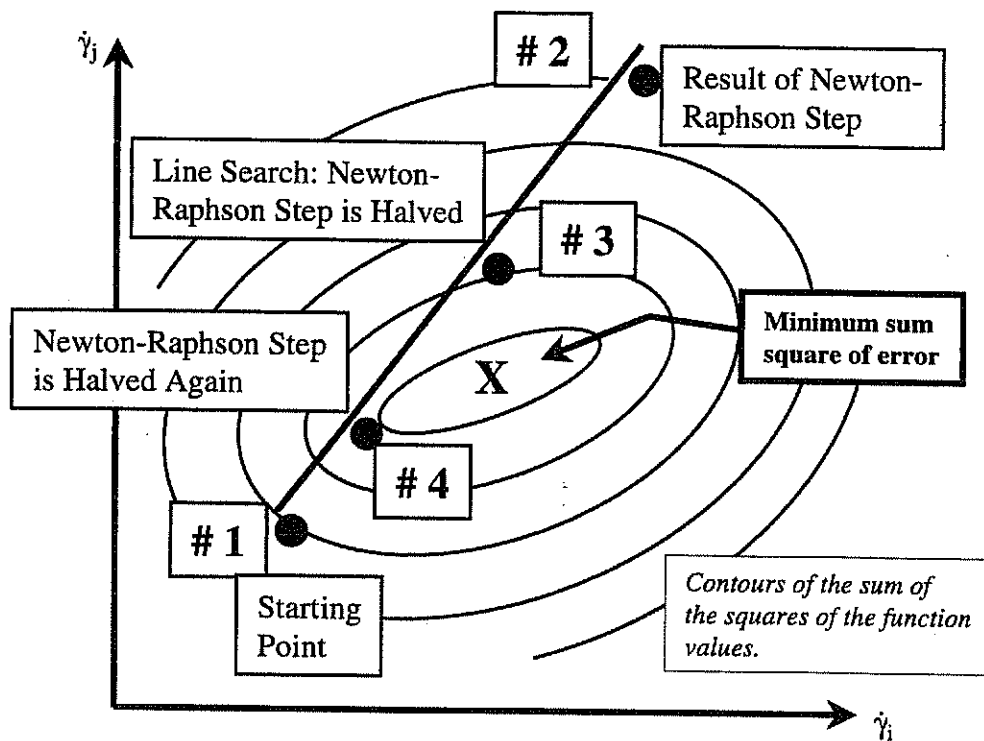


Figure II.4 Line search procedure wherein the Newton-Raphson step is successively halved until an optimum value is reached.

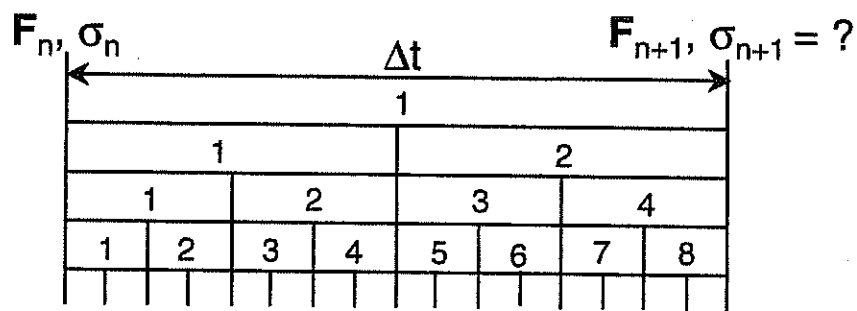


Figure II.5 Time step subincrementation procedure - if the Newton-Raphson procedure does not converge, the time step is repetitively halved until convergence does occur.

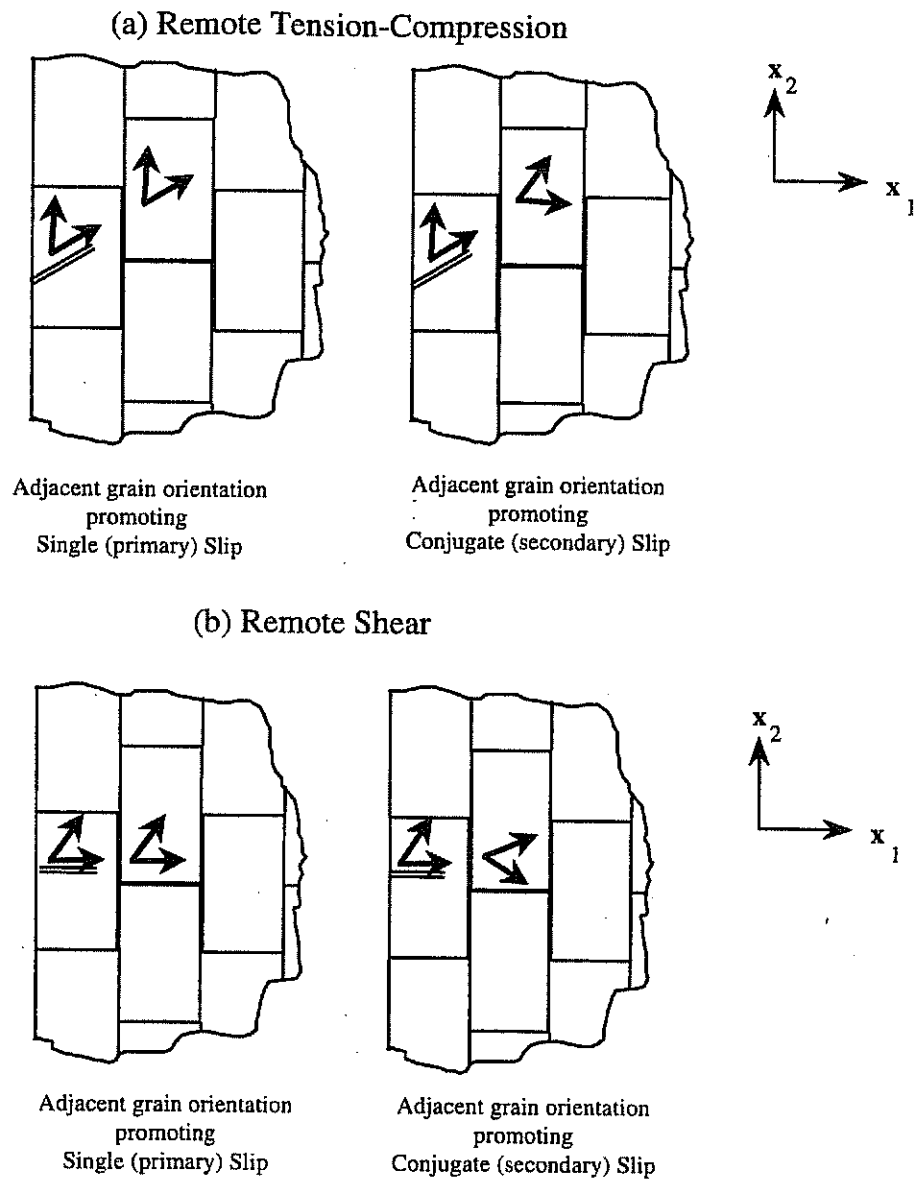


Figure II.6 Illustration of primary and secondary slip designations for adjacent grain orientation for a surface grain containing crack under remote (a) tension-compression in the x_2 (σ_{22}) direction and (b) shear (τ_{12}) loading.

CHAPTER III

POLYCRYSTAL ORIENTATION DISTRIBUTION EFFECTS ON MICROSLIP

In this Chapter, two-dimensional computational cyclic crystal plasticity results are presented for the distribution of cyclic microplastic slip and critical plane-type fatigue parameters among a polycrystalline ensemble. A material is examined with the nominal uniaxial stress-strain response of 4340 steel. Cases of applied cyclic tension-compression, cyclic shear, cyclic tension-compression with a tensile mean stress, and combined cyclic tension-compression and cyclic shear are analyzed at strain amplitudes ranging from well below to macroscopic yielding. Emphasis is placed on stress state and amplitude dependence of the distribution of these parameters among grains. The role of anisotropic plasticity is isolated by assuming that the elastic behavior of grains obeys homogeneous, isotropic linear elasticity.

Studies of this type are significant because small crack formation and growth behavior, whether examined by crack tip displacement (CTD), plastic zone size, or misorientation of adjacent grains, cannot be considered in detail using macroscopic approaches that ignore microstructure. In this Chapter, three candidate fatigue initiation parameters are examined in order to quantify and interpret the distribution of each parameter over an aggregate polycrystal.

III.1 Fatigue Crack Initiation Parameters

Fatigue crack initiation parameters are used as a means for relating macroscopic parameters, such as the applied stresses, to parameters such as the plastic shear strain amplitude on the plane of maximum shear. This permits one to assess the development of the distribution of damage within a material. These parameters are related to the initiation of damage (formation and very early crack growth). This work considers three such parameters and examines how these parameters are distributed throughout the aggregate as a function of stress state and stress amplitude. The HCF regime is the primary focus, and hence applied loading levels are at or below macroscopic yield. This Chapter focuses on fatigue crack initiation criteria and qualitatively compares the criteria with experimental observations.

III.1.1 Normalized Cyclic Microplasticity Parameter

As discussed in Chapter I, the extent and distribution of plasticity among grains is an important factor in fatigue crack formation and early Stage I growth. A direct measure of the cyclic microplasticity is the maximum cyclic plastic shear strain on a slip system normalized by the global cyclic plastic strain averaged over all grains, defined here as the normalized cyclic microplasticity parameter (N-CM), i.e.

$$\frac{\Delta\gamma_{\max}^{\alpha}}{2} \bigg/ \left(\frac{\Delta P}{2} \right)_{\text{avg}} \quad (\text{III.1})$$

where $\Delta\gamma_{\max}^{\alpha}$ is the maximum range of shear strain on either of the two slip systems and $\Delta P = \Delta\epsilon_{22}^p$ for the tension-compression case, and $\Delta P = \Delta\gamma^p = 2\Delta\epsilon_{12}^p$ for cyclic shear.

III.1.2 Mohr-Coulomb Parameter

Another fatigue crack initiation parameter that has been used for the multiaxial HCF case involves a linear combination of the range of maximum resolved shear stress, $\Delta\tau^{\alpha}$, and the peak hydrostatic stress, P_{hyd} . Dang-Van (9) and Papadopoulos (122) have employed the Mohr-Coulomb (MC) parameter within individual grains, i.e.

$$\frac{\Delta\tau_{\max}^{\alpha}}{2} + k P_{\text{hyd}} = C_1 \quad (\text{III.2})$$

where C_1 is a constant for a given fatigue life. They asserted that HCF crack initiation takes place in grains which have local plastic strain within characteristic intracrystalline bounds while the entire aggregate is still macroscopically elastic (shakedown state). Although the MC parameter has often been employed to assess the behavior of soils or granular materials

(123), its extension to fatigue crack initiation in metals is related to the assumed influence of normal stress on decohesion along persistent slip bands, or opening of small Stage I fatigue cracks under predominately shear loading.

III.1.3 Fatemi-Socie Parameter

A macroscopic parameter proposed by Fatemi and Socie (F-S) (40), given by

$$\frac{\Delta\gamma_{\max}^p}{2} \left(1 + k^* \frac{\sigma_n^{\max}}{\sigma_y} \right) = C_2, \quad (\text{III.3})$$

produced correlations very similar in the LCF regime to a corresponding fully plastic form of Equation (III.3) (2-3). Here, C_2 is a constant for a given number of cycles necessary to produce a surface crack length on the order of 0.5 to 1 mm in length. The peak tensile stress, σ_n^{\max} , normal to the plane of maximum shear strain amplitude is normalized by the yield strength, σ_y , to essentially reflect the modifying influence of the normal stress on the crack tip displacement (CTD). The constant k^* value of 0.5 is selected by correlating fully reversed uniaxial and torsional data sets and as being representative of correlations (39). The Fatemi-Socie parameter has been shown to correlate a wide range of multiaxial loading

conditions, including cases involving mean stress for 1045 steel and IN 718 (both extended Stage I-dominant materials) over a range of fatigue lives (10^3 to 10^6 cycles)(41-42).

III.2 Distribution of Cyclic Microplasticity

A phenomenological, micromechanical model based on crystal plasticity is employed to conduct two-dimensional (2-D) finite element analyses to assess the distribution of microslip among grains in a polycrystal. In determining an appropriate aggregate size, the works of Abdul-Latif and Saanouni (124-125) and Hoshide and Socie (126) were examined. Although these studies were not set within a finite element context, they not only serve to guide a selection of the number of grains to use in the analysis, but they also show how crystal plasticity concepts are used to model cyclic behavior and the development of fatigue damage. Abdul-Latif and Saanouni (124-125) quantitatively examined the fatigue life and micro-damage heterogeneity for FCC polycrystalline metals by employing a coupled phenomenological-micromechanical model of the early plastic fatigue damage initiation. Their model is based on slip theory (crystal plasticity) and employs a self-consistent homogenization technique. One of their studies (125) examined the influence of the number of grains (40, 48, 96, 200, 300, 504) in the aggregate on the direction and orientation of damage. They found that in modeling Waspaloy, the number of grains had a considerable effect on the micro-damage heterogeneity, mainly because damage phenomena are governed

by the void nucleation and growth in fatigue. However, between 200 and 504 grains, the predicted damage and resulting fatigue life values converged and one is assured of consistent results. Since their work was done outside the context of finite elements, a transgranular micro-damage variable was employed. This points to one of the advantages of using finite elements coupled with micromechanical concepts - no ad hoc assumptions are made regarding grain-to-grain interactions. Finite elements assure very good approximations of both compatibility and equilibrium.

The model of Hoshide and Socie (126) also considered the driving force for fatigue crack nucleation and microstructurally small crack growth in a distribution of randomly oriented grains. A double primary-conjugate slip system was used with a total of 625 square grains in their analysis. They considered two regimes of shear cracking. The first regime was crack growth by nucleation within individual grains by coalescence. The dislocation model of Tanaka and Mura (67) was used to compute the nucleation of cracks with individual grains. In the second regime, cracks became large enough to generate their own stress fields and grow as a single dominant crack. This regime was analyzed using fracture mechanics concepts with an equivalent strain intensity factor. The model was used to simulate the fatigue behavior of SAE 1045 steel. Both crack distribution and fatigue life estimates were obtained under nominally LCF conditions. They were able to reproduce observed crack patterns reasonably well in addition to predicting fatigue life up to 10^5 cycles for 1045 steel. In their model, the fatigue crack nucleation and growth were assumed to be governed by cyclic microplasticity, with mixed-mode contributions from the cyclic shear

strain and the cyclic normal strain to the microcracks within individual grains. Hoshide and Socie (126) assumed that each grain had the same stress as the surrounding material in the bulk. Their analysis is likely overly-simplistic because stresses vary considerably throughout the microstructure depending on grain orientation.

In this research, 2-D (plane strain) finite element analyses are conducted to assess distribution of microslip and propensity for formation of small fatigue cracks. The grains are modeled as 8-noded quadrilateral, biquadratic elements and planar double slip models the cyclic plasticity. A total of 576 grains are used in the analyses with each grain represented by one element. Grain orientations are randomly assigned to describe an initially isotropic effective medium. Uniform vertical displacements are prescribed at the top and bottom boundaries in the uniaxial loading y-direction, with zero traction in the x-direction; the lateral sides were traction free. In shear, the x-direction displacements on the top and bottom surfaces are specified, with no y-direction traction on the upper surface, and traction free lateral boundaries. For each loading condition (stress state and stress amplitude), a set of three realizations are analyzed, each with a different, but randomly assigned, orientation distribution of grains. Two rings of elements are considered as surface grains, as shown in Figure III.1. Only 16% of the total volume of the mesh are surface grains and were not included in the distribution calculations in order to minimize edge effects. Error bars are shown on plots, indicating differences in distribution of parameters among the various realizations.

The plane strain tension-compression hysteresis loops in the 2-D simulation are

assigned a behavior typical of uniaxial behavior of a 4340 steel for illustrative purposes, as shown in Figure III.2 for a 100 grain polycrystal. Constants for this fit are $E = 175$ GPa, $\nu = 0.3$, $M_e = 10$, $\dot{\gamma}_o = 10^{-8} \text{ s}^{-1}$, $G = 60$ MPa, $C = 100$ MPa and $d = 30$ for a strain rate of $1.5 \times 10^{-3} \text{ s}^{-1}$. Variables M_e , $\dot{\gamma}_o$, G , C , and d were defined in Equations (II.2 - II.3). A constant polycrystal effective strain rate is imposed in all calculations to avoid significant strain rate differences among the various cases evaluated, so the value of M_e was selected more to promote computational stability than to mimic a realistic rate sensitivity. The elastic behavior in all calculations reported here is assumed to be isotropic and linear elastic.

The strain amplitude levels for tension and shear range from well below to the cyclic yield strain of the polycrystal ensemble, corresponding to approximately 0.2% plastic strain (defined as $\epsilon_y = 0.0065$ and $\gamma_y = 0.0042$, respectively) of the polycrystal and are applied at an effective strain rate of $1.5 \times 10^{-3} \text{ s}^{-1}$. Peak strain levels considered are fractions (0.3, 0.5, 0.7, 0.9, and 1.0) of the cyclic total yield strain in each case in order to investigate the cyclic microstrain distributions under predominately HCF conditions. Two completely reversed strain cycles are applied to ensure a numerically repeated path in the simulation during the second cycle. The distribution of parameters among grains arising from microstructural inhomogeneity are assessed by discussion the overall shape of these as a function of stress amplitude and stress state.

III.2.1 Completely Reversed Cyclic Tension-Compression

When using the crystal plasticity model as the constitutive model for the material stress-strain response, the contour plot of equivalent plastic strain for cyclic strain amplitude of $0.7 \epsilon_y$ in Figure III.3a correctly shows bands along $\pm 45^\circ$. It is along these directions (planes of maximum shear) that small cracks develop. This appears to be consistent with experimental results reported by Socie (5) for small cracks which nucleate in surface grains under cyclic tension-compression.

III.2.1.1 Normalized Cyclic Microplasticity (N-CM)

For each strain level, the distribution among grains for the N-CM parameter is shown in Figure III.4a shows two peaks. The first peak is due to a percentage of grains (20-30%) which have a maximum shear strain on the slip system which is a small proportion of the applied plastic strain averaged over all grains. This initial peak decreases with increasing amplitude, but still remains a dominant feature for all distributions. The second peak is more apparent for increasing strain amplitudes. This occurs as an increasing number of grains have a closer proportion of the maximum shear strain on a slip system to the average applied plastic strain. For a strain amplitude of $0.3 \epsilon_y$, this second peak occurs near a N-CM value of 2.4, but with increasing strain, this peak is centered close to 1.0 and has a Gaussian type

distribution. Bars denote the range of the distribution obtained from three realizations of the orientation distribution of grains which show that there is little variation among simulations, except for the highest applied strain amplitude of $0.9 \epsilon_y$. Clearly, only a limited number of grains experience cyclic plastic strains that considerably exceed the average macroscopic plastic strain as evidenced by the narrow right-end tail of the distribution; these grains are expected to control fatigue crack formation and early Stage I growth. This parameter also shows a strong amplitude dependency.

As a part of a study by Roven and Nes (127), quantitative observations were made of the nature of PSBs formed in the cyclic stress saturation condition. The number of PSBs in grains containing at least one PSB were analyzed. From a selection of 26 grains, an average value of 5 PSBs per grain was counted. It was further noted that the number of PSBs per grain, in grains containing at least one PSB, is well described by the Gaussian distribution. However, for the N-CM parameter considered here, the distribution tended more so towards a pseudo-log-normal type distribution for increased amplitudes. For LCF conditions, there are higher concentrations of the plasticity within the aggregate and increased compatibility of plastic deformation from grain-to-grain. The important point here is that a Gaussian type distribution may be more suited to describe LCF conditions, whereas the HCF conditions in this analysis show that there is not a homogeneous distribution of the normalized cyclic microplasticity.

III.2.1.2 Normalized Mohr-Coulomb Parameter (MC)

The MC parameter is normalized by the average applied stress amplitude. A value of the parameter $k = 0.2$ is selected as representative of correlations reported by Dang-Van (9). As seen in Fig. III.4b, the distribution tends towards Gaussian characteristics as general macroscopic yielding is approached. Hydrostatic stresses do not distinguish between stresses normal and parallel to the potential crack, so no amplitude dependency is reflected for this parameter and for this loading case. The peak values and shape of the distributions are quite similar with increasing strain.

III.2.1.3 Normalized Fatemi-Socie (F-S) Parameter

For all strain levels ($0.3 \epsilon_y$ through ϵ_y) shown in Figure III.4c, the distributions show an initial peak for grains which have a small value of the normalized F-S parameter. The distributions are skewed to the left and the shape of the distribution reflects a dependence of strain amplitude, although to a lesser degree as compared to the N-CM parameter. The variability among multiple realizations of orientation distribution is nil. What is also observed is the narrow right-end tail of the distribution which has a small peak which shifts to the left with increasing strain amplitude. In comparison to the N-CM distribution, the distribution for the F-S case consistently has a higher percentage of grains with a higher value of the fatigue initiation parameter; this implies that a higher percentage of grains have

an increased propensity for initiating.

III.2.2 Cyclic Shear

As in the cyclic tension case, the contour plot of equivalent plastic strain for a shear strain amplitude of $0.7 \gamma_y$ is generated. Focusing on the interior grains and away from the boundaries, these bands appear to concentrate along 0° and 90° for cyclic shear, as shown in Figure III.3b. This initial result agrees with experimental results reported by Socie (5) for the orientation of microcracks which nucleate in surface grains under cyclic shear.

III.2.2.1 Normalized Cyclic Microplasticity (N-CM)

The results for normalized cyclic microplasticity (presented in Figure III.5a) are similar for all strain amplitudes, but exhibit a drop in the peak of the distribution with an increase of applied strain level. For all strain amplitudes, the distributions resemble an exponential decaying function which points to a highly inhomogeneous distribution of the cyclic microplasticity. About 50-60% of the grains experience a local maximum shear strain on a slip system that is less than half of the macroscopic plastic shear strain. However, a small percentage of the grains have two to three times the macroscopic plastic shear strain. Even though a significant amount of grains have a very small proportion of the macroscopic plastic shear strain, it is the few grains which have a larger value of the N-CM control the

initiation of small cracks.

Note also that due to the extreme skewness of the distribution, smaller ranges of this parameter (as low as 0.01) were also examined to determine if a different shape of the distribution would become apparent, however, the extreme skewness of the distribution persisted. There is therefore, an assurance that this exponential decaying type of distribution does in fact properly assess this parameter for cyclic shear.

III.2.2.2 Normalized Mohr-Coulomb (MC) Parameter

The distribution for cyclic shear contrasts significantly from the distribution of the MC parameter for cyclic tension-compression. The cyclic tension-compression case showed minimal differences in the distribution as a function of strain amplitude, as given in Fig. III.4b. The MC parameter for cyclic shear in Figure III.5b has lower peak values as compared to the cyclic tension-compression case. This parameter yields a more homogeneous distribution of the damage within the aggregate and shows a strong dependence on amplitude. With increasing applied strain, the peak increases slightly and becomes more distinct, with the parameter centering near a value of 1.0.

III.2.2.3 Normalized Fatemi-Socie (F-S) Parameter

The distribution in Fig. III.5c shows some similarities to the cyclic tension-compression case with both having an initial peak which is skewed to the left. This high initial peak persists for all strain amplitudes. The distribution also resembles an exponential decaying function which points to an inhomogeneous distribution of the damage.

III.2.3 Cyclic Tension-Compression with Tensile Mean Stress

As mentioned in the Introduction, many components are subjected to HCF loading conditions with a superimposed tensile mean stress. The goal of this set of calculations is to simulate this behavior and to identify the differences which arise as compared to the completely reversed tension-compression case. In order to achieve a stress ratio of $R = 0$, the mean stress level is chosen as 400 MPa. A plot of the hysteresis loops for this case, given in Fig. III.6, shows material that has undergone some degree of mean stress relaxation.

The distribution plots of the polycrystal aggregate are given in Figure III.7. These distributions are very similar to the case of completely reversed tension-compression. The distributions for the N-CM and the F-S parameters are very similar to the case with no mean stress. For the MC parameter, the distributions for the case with and without the mean stress are quite similar as well, but the case with mean stress has a smaller range (0.0 - 0.6) as compared to the range (0.0 - 1.0) for the case without a mean stress. This is perhaps due to

the overall increased homogeneity among grains as signified by the lower peaks. There are lower peaks of the distributions for all fatigue initiation parameters (as compared to the completely reversed case).

It is also apparent that these parameters, when normalized, are not especially sensitive to mean stress effects because the distributions were very similar to the completely reversed case. These results appear to correlate with the work of Nisitani (47) who compared the changes of the surface states of 70/30 brass under different R ratios ($R = -1$, $R = 0$, and $R = \infty$). He found that fatigue damage in the crack formation/initiation regime was almost independent of the mean stress value and the damage was primarily controlled by the stress amplitude. This signifies that the crack propagation process, as opposed to crack formation and initiation, was greatly affected by the values of mean stress.

III.2.4 Combined Cyclic Tension-Compression and Shear

For this loading case, a contour plot of equivalent plastic strain in Figure III.3c shows several bands along many oblique directions (from the horizontal axis) for combined loading with strain amplitudes of $0.7 \epsilon_y$ and $0.7 \gamma_y$. Orientations along the outer edge of this figure show one example of an orientation at approximately 20° . Although the darkest bands tend to align with the planes of maximum shear, there are other less intense contours which surface as a result of the combined effect of tension and shear loading. These less intense bands do not appear to align with neither the $\pm 45^\circ$ nor with the 0° (or 90°) directions. It

appears that there are regions of grains which may have developed a 'bandedness' along the $\pm 45^\circ$ direction when loaded in cyclic tension-compression, but when loaded in shear, the 'bandedness' which developed is then smeared by subsequent shear loading. This smearing effectively creates regions within the aggregate which are clearly a combination of the two loading states. The distributions of the fatigue initiation parameters for the combined case are evaluated for three realizations of random orientations of grains. Each parameter is now normalized by an effective stress or strain based on the average stress (or strain) over all grains.

III.2.4.1 Normalized Cyclic Microplasticity (N-CM)

For each strain level, the distribution among grains for the N-CM parameter, shown in Fig. III.8a, resembles an exponential decaying function. With increasing strain, the plots have the same shape, but has decreasing peak values. The distribution for the combined loading case resembles the cyclic shear case. There is increased variability between the three realizations for increasing strain amplitudes as signified by the wider range on the error bars. The log normal PDF is used to fit the distributions for each strain amplitude. At the highest strain levels, however, the PDF did not fit the distributions well due to the dual peaks.

At higher strain amplitudes, a redistribution of normalized cyclic microplasticity occurs such that two values of N-CM dominate. In reality, bimodal grain size distributions have been observed when analyzing materials which have undergone heat treatment (131)

due to the presence of two dominant features of the microstructure. In a different work (132), the statistical distribution of the interfacial strength in ductile metal was also bimodal, showing the presence of both weakly and strongly bonded particles. Although these specific types of studies were not investigated in this work, they do suggest how bimodal distributions arise - two strongly opposing effects wherein one does not overshadow the other. This seems plausible for the case of combined loading since the planes of maximum shear for tension-compression loading ($\pm 45^\circ$) and for cyclic shear loading (0° and 90°) are quite distinct.

III.2.4.2 Normalized Mohr-Coulomb (MC) Parameter

The distribution of the MC parameter appears to have a Gaussian type of distribution with values centered near 0.5. As seen in Fig. III.8b, increasing strain has a minimal effect on the change of the shape and peak values of the distribution. This behavior contrasts with the distributions of the MC parameter for the cyclic shear loading case wherein the peak of the distributions is more distinct with increasing strain.

III.2.4.3 Normalized Fatemi-Socie (F-S) Parameter

For all strain levels, the distributions for this parameter are fit with a three parameter log-normal PDF (in Figure III.8c).

III.3 Fatigue Initiation Parameters: Implications

The Fatemi-Socie critical plane fatigue parameter was previously discussed to have a stronger linkage to cyclic crack tip displacement for microstructurally small cracks (8). The F-S parameter has demonstrated a more direct correlation of mixed-mode, multiaxial fatigue crack formation and early growth than either maximum cyclic plastic shear strain (N-CM) or the MC parameter. Although both the MC and the F-S parameters both provide information regarding the maximum cyclic shear stress and strain, the F-S parameter identifies the plane of maximum plastic shear strain combined with the effects of normal stress on that plane. It is well-known that plastic deformation of metals exhibits very weak dependence on hydrostatic stress. The MC parameter includes the peak hydrostatic stress which may not directly influence crack initiation, as discussed by Socie (4). Even though the hydrostatic stress reflects constraint that may either promote or hinder crack initiation, the directionality of the influence is lacking.

In the computations performed in this research, it was found that the normalized cyclic microplasticity and Fatemi-Socie parameter both showed amplitude dependency for the cyclic tension-compress loading case, whereas the MC parameter showed amplitude dependency for the cyclic shear case. The F-S parameter, however, does show more of a consistent distribution for both stress states, especially at the higher strain amplitudes. It is also well-known that both uniaxial and torsional fatigue cannot be correlated, in general, using only the maximum plastic shear strain parameter (6,35). Socie (4) has effectively

shown that the F-S parameter correlates multiaxial fatigue behavior (small crack regime) that cannot be resolved by the MC parameter. These calculations may offer some understanding of why this is the case. The broadening of the shear distribution among grains for the MC parameter is in accordance with observations of higher surface crack density in cyclic shear relative to tension-compression (4). This suggests a fundamental difference between these two stress states in terms of the driving force for crack formation and early Stage I propagation, which is confirmed experimentally (6,35). Micromechanical FE calculations such as these provide useful information as to the propensity for initiation of small cracks.

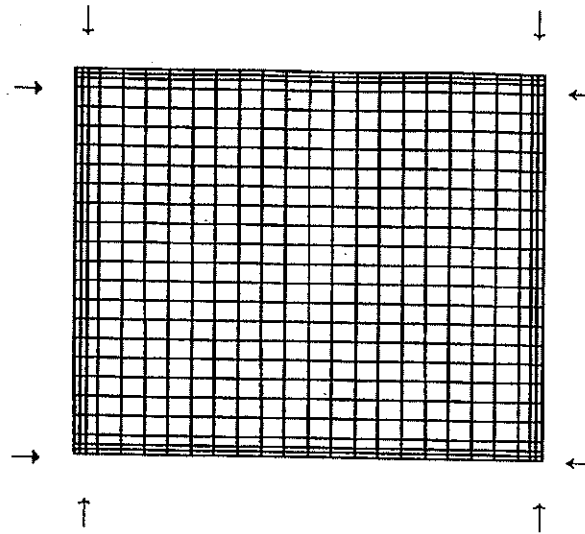


Figure III.1 Finite element model of polycrystal aggregate used in crystal plasticity analysis with surface grains indicated by arrows.

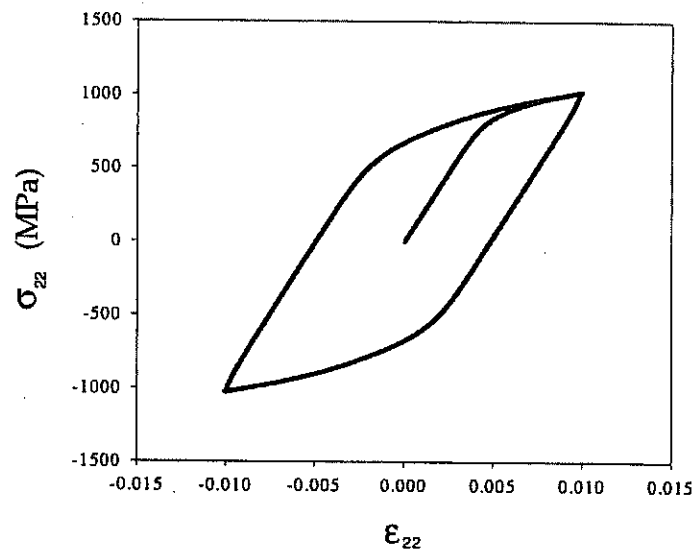


Figure III.2 Hysteresis loops for cyclic tension-compression in the 2-D simulation.

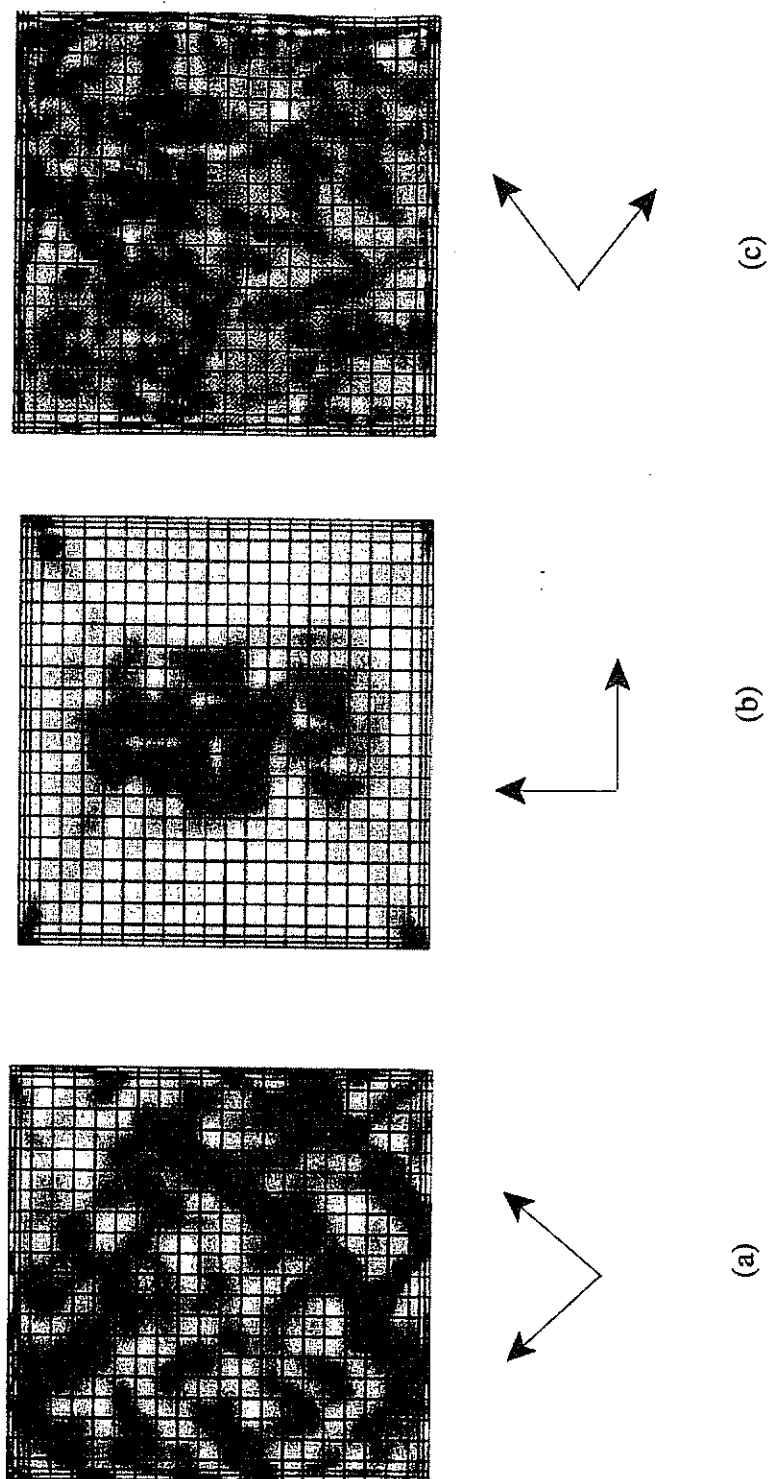


Figure III.3 Contour plots of equivalent plastic strain for (a) cyclic tension-compression at strain amplitude of $0.7 \epsilon_y$ with bands along $\pm 45^\circ$ directions, (b) cyclic shear at strain amplitude of $0.7 \gamma_y$ with bands principally along 0° and 90° directions, and (c) cyclic tension-compression ($0.7 \epsilon_y$) and cyclic shear ($0.7 \gamma_y$) with proportional loading with bands along oblique directions.

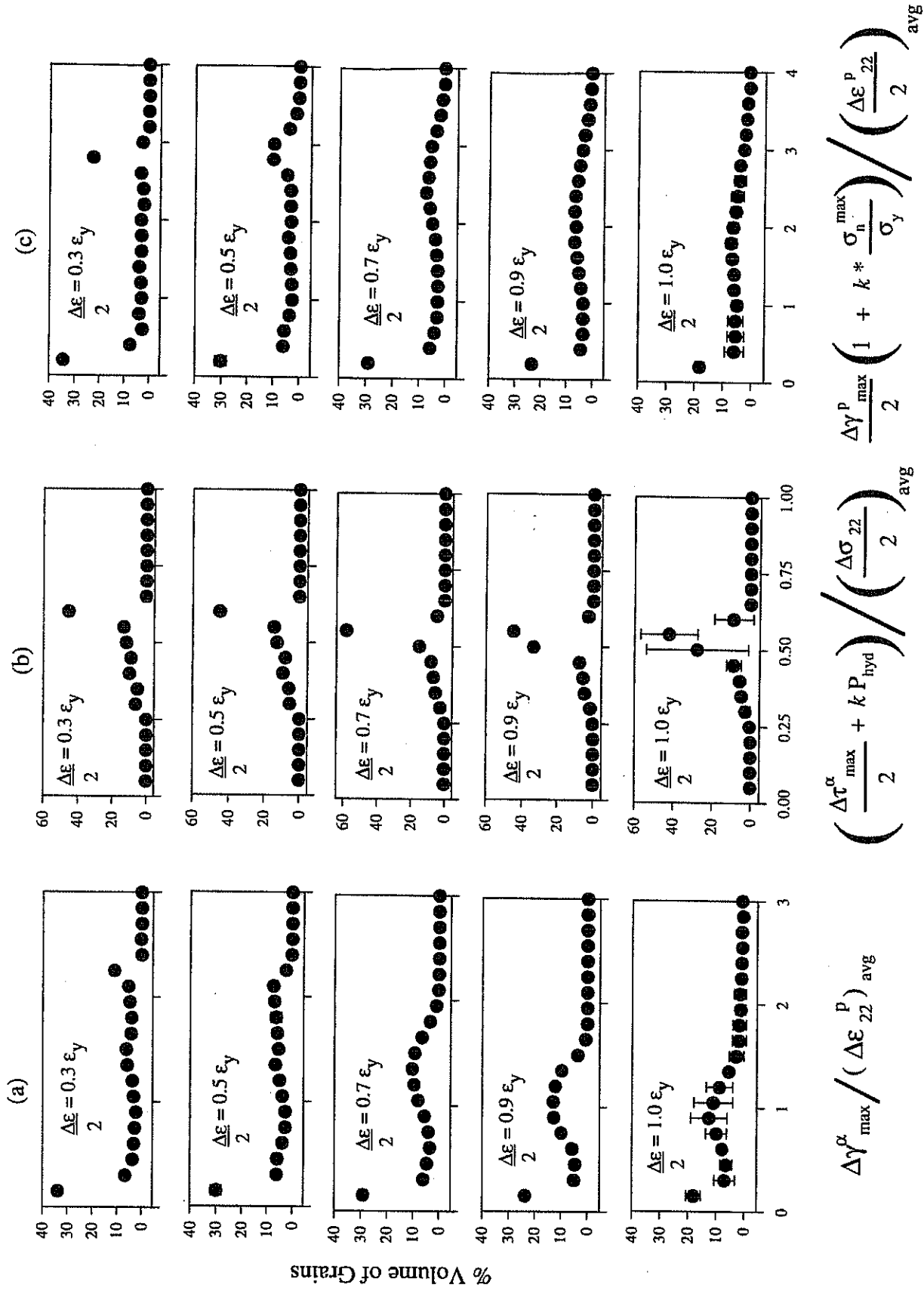


Figure III.4 Cyclic Tension-Compression - (a) Normalized Cyclic Microplasticity, (b) Mohr-Coulomb, (c) Fatemi-Socie.

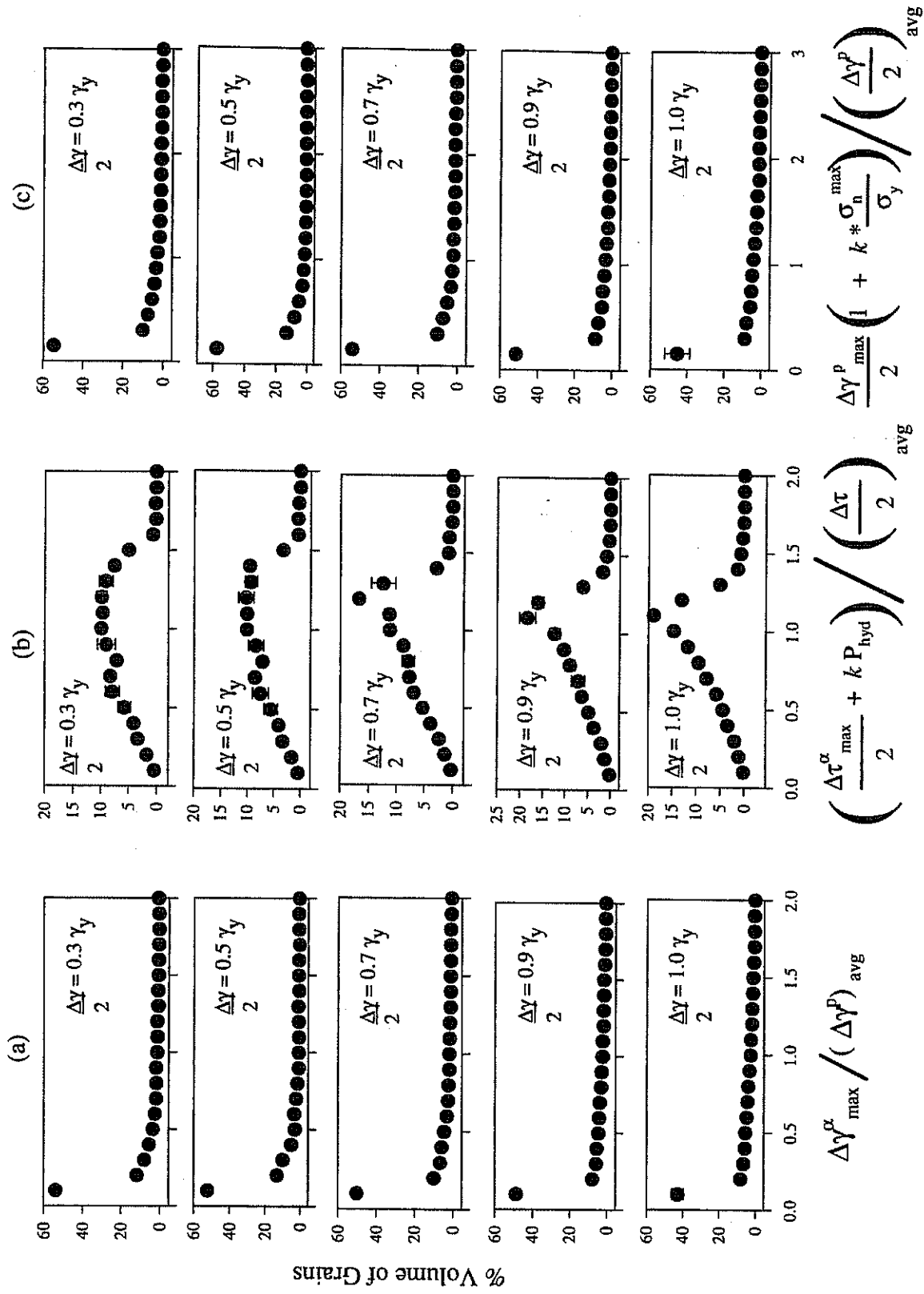


Figure III.5 Cyclic Shear - (a) Normalized Cyclic Microplasticity, (b) Mohr-Coulomb, (c) Fatemi-Socie.

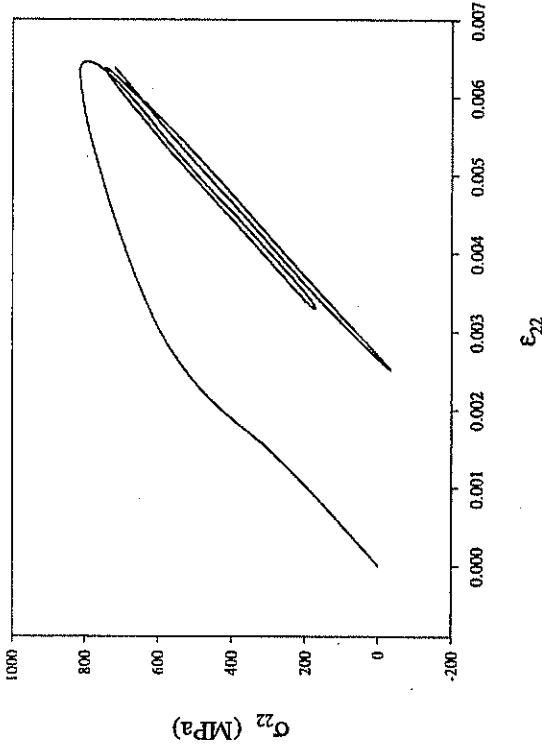


Figure III.6 Characteristic hysteresis loops for cyclic tension-compression with mean stress of 400 MPa ($R = 0$) in the 2-D simulation.

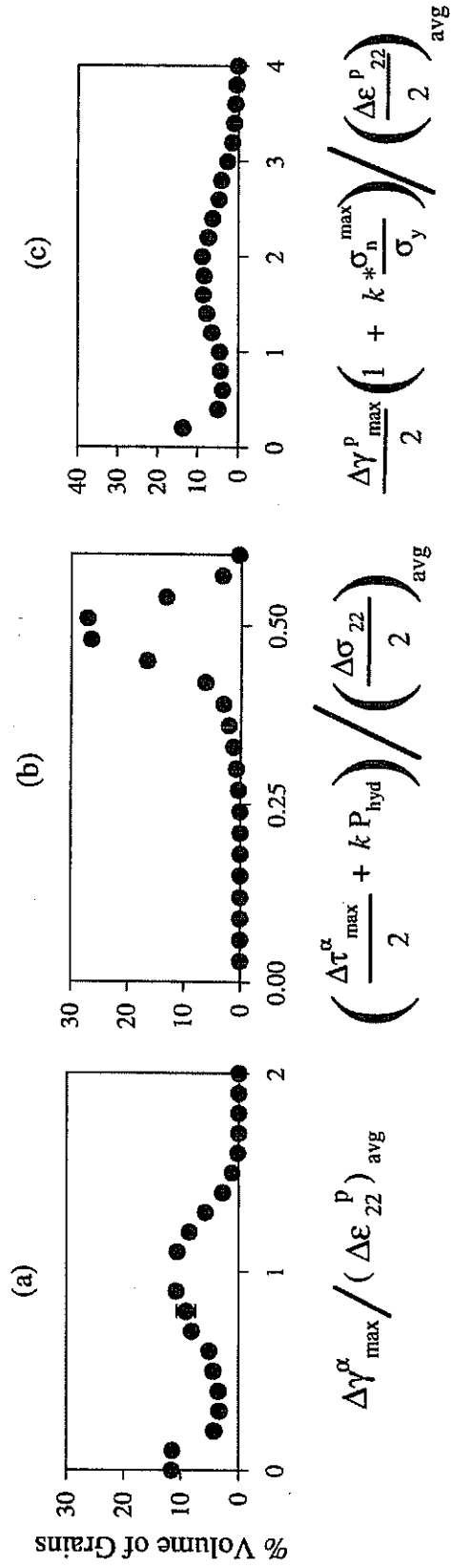
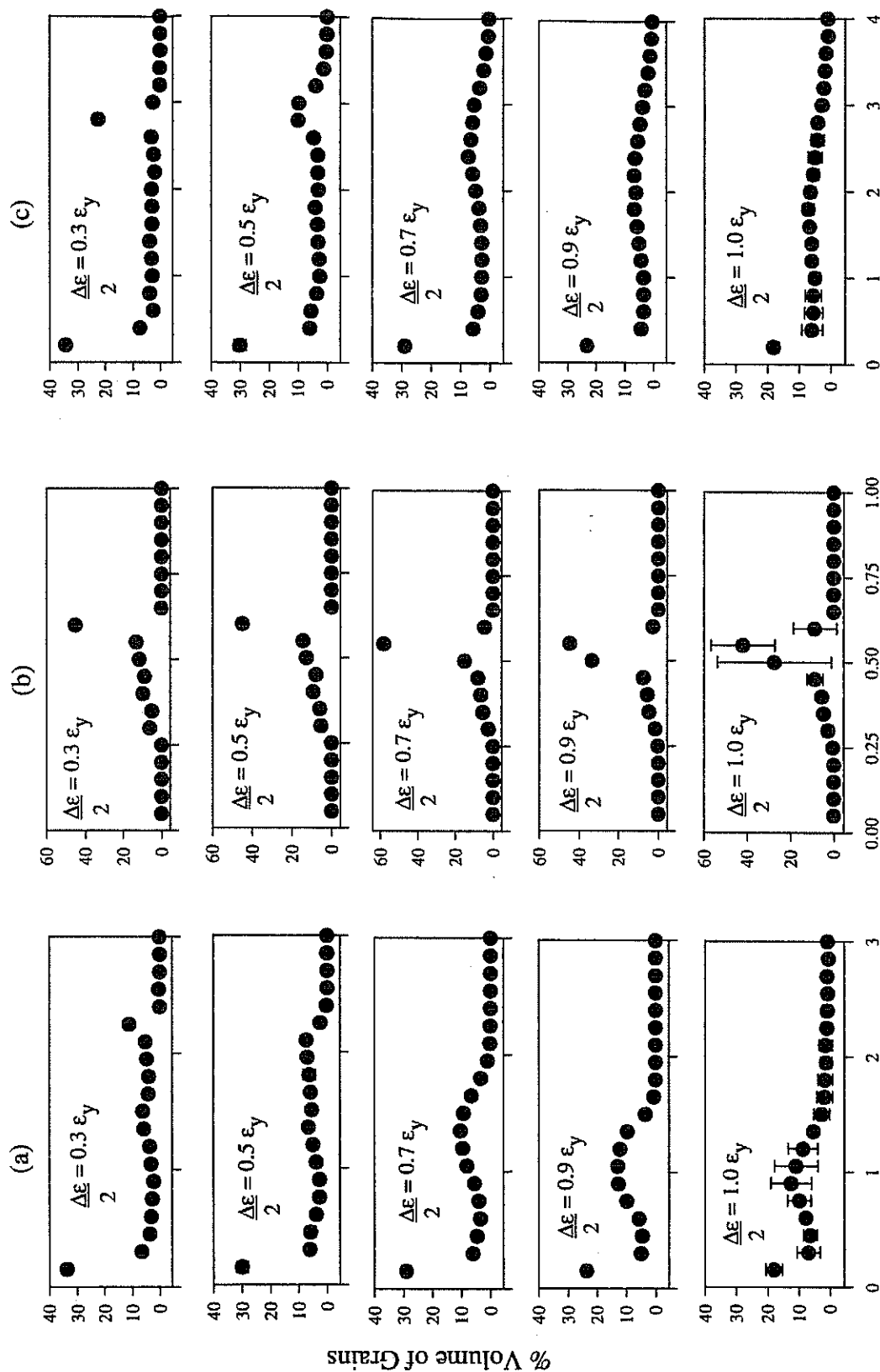


Figure III.7 Cyclic Tension-Compression with Mean Stress - (a) Normalized Cyclic Microplasticity, (b) Mohr-Coulomb, (c) Fatemi-Socie.



$$\frac{\Delta \gamma_{\max}^{\alpha}}{(\Delta \epsilon_{22}^p)_{\text{avg}}} \left(\frac{\Delta \tau_{\max}^{\alpha}}{2} + k P_{\text{hyd}} \right) / \left(\frac{\Delta \sigma_{22}}{2} \right)_{\text{avg}} \quad \frac{\Delta \gamma_{\max}^p}{2} \left(1 + k \frac{\sigma_n^{\max}}{\sigma_y} \right) / \left(\frac{\Delta \epsilon_{22}^p}{2} \right)_{\text{avg}}$$

Figure III.8 Cyclic Tension-Compression and Shear - (a) Normalized Cyclic Microplasticity, (b) Mohr-Coulomb, (c) Fatemi-Socie.

CHAPTER IV

ANALYSIS OF MICROSTRUCTURALLY SMALL FATIGUE CRACKS

One objective of this study is to perform micromechanical computations in order to qualitatively assess the effects of microstructural heterogeneity which contribute to anomalously high growth rates and oscillatory behavior for small cracks. Since the small crack growth regime can account for 50-90% of the total life of components, properly characterizing this regime is essential. One way to quantify the effects of microstructural heterogeneity on small crack behavior is to study the changes in crack tip driving forces as the cracks grow through grains of different orientations. As a first approximation, the changes in crack tip driving forces are examined by considering cracks of different lengths from the free surface with various crystallographic orientations of surrounding grains. Only stationary cracks are considered in this work.

The 2-D micromechanical model used in the uncracked polycrystal analysis is now applied to the evaluation of CTSDs and CTODs for microstructurally small fatigue cracks under both monotonic and cyclic loading. These crack tip driving force parameters relate to the relative motion of the crack faces near the crack tip. A unique feature of these calculations is that these driving force parameters reflect the influence of the free surface as

well as surrounding grains within the microstructure. These two factors have often been neglected in previous continuously distributed dislocation models (82, 128) and slip band models (83). CTSD and CTOD computational results are presented as a function of the applied average strain, ranging from well below to slightly above nominal yielding for tensile and shear loading. The same nominal strain levels that were used in the uncracked polycrystal cases are utilized in these crack analyses. Crack tip displacements for a polycrystal with surface cracks are first evaluated for monotonic loading to understand shielding and redistribution effects, absent of slip band considerations in fatigue. Cyclic loading results are then presented, showing the nature of the crack tip sliding and opening displacements as functions of amplitude and including plasticity-induced closure effects.

IV.1 Use of Planar Double Slip for Determining CTOD and CTSD for Microstructurally Small Cracks

Before discussing the results generated using the micromechanical crystal plasticity model, it is important to briefly review previous work and the results generated from similar models. Gall *et al.* (117) employed a planar double slip crystal plasticity model and compared their results of crack opening displacement (COD) and crack opening stress with initially isotropic elasto-plastic solutions for a plane strain center cracked panel loaded in tension. A range of orientations of the two slip directions with respect to each other and the

orientation of the crack were considered with $R = 0$ loading. Not surprisingly, the initially isotropic plasticity solutions significantly underestimated the COD (up to a factor of two) for many of the orientations considered. The COD measurements were made at a distance x behind the crack tip according to $x/(K_{\max}/\sigma_o)^2 = 0.1$. Crystallographic orientations that promoted predominately single slip near the crack tip resulted in little plasticity-induced closure, while orientations that promoted double (conjugate) slip resulted in closure levels well above that computed with the initially isotropic plasticity theory ($S_{\text{open}}/S_{\text{max}} = 0.37$ rather than 0.17). The implication is that conjugate double slip, typical of Stage II propagation, is conducive to producing substantial plasticity-induced closure effects (18).

IV.2 CTD as Driving Force for Microstructurally Small Fatigue Cracks

In general, small cracks grow along 3-D paths, interacting with multiple barriers along the crack front. Certain segments of the crack front grow sequentially, while on the surface the growth appears intermittent. Idealizing the behavior as principally mixed mode I-II growth in 2-D, it is widely held that the crystallographic fatigue crack growth process is dictated by the local crack opening and sliding displacements. Li (129) proposed a vectorial crack tip displacement (CTD) relation

$$\frac{da}{dN} = A (\Delta CTD)^n, \quad \Delta CTD = |\Delta \delta_s + \Delta \delta_p| \quad (\text{IV.1})$$

where CTD is the magnitude of the vector comprised of all primary (δ_p) and secondary (δ_s) slip vectors or band lengths ahead of the crack tip (see Fig. IV.1). Exponent n is typically on the order of 1 to 2 (128, 130) to capture experimental results for small/short and long cracks. For small cracks in single and polycrystals, a linear dependence of da/dN on crack length has been commonly observed (131), suggesting that $n \approx 1$. The observed crack increment per cycle typically falls far short of the nominal CTD (129), due in part to the fact that the crack front has some segments which actively grow and others that are temporarily pinned by interactions with obstacles such as second phase particles or grain boundaries in a complex 3-D arrangement and in part to partially reversible slip.

According to Li (132), for small crystallographic cracks in Stage I growth predominately under single slip (minimal cross slip or multislip ahead of the crack tip), the growth process is dominated by the CTSD on the primary slip system. The contribution of secondary slip becomes more prominent as the tendency for multislip sets in, or the crack encounters barriers that induce opening displacement. Microstructurally small cracks initially grow along the primary slip plane with little or no contribution from secondary slip (Stage I). Upon encountering constraints on continued propagation in single slip, secondary slip may become relevant to continued propagation. The onset of extended Stage I growth (Fig. IV.1b) is associated with development of secondary slip bands which are constrained by the coplanar primary slip ahead of the crack and hence are quite small compared to the primary slip band length. Li (132) also found that based on solutions by Koss and Chan (133), the ratio of the secondary to primary slip length is on the order of 5% to 10% during

extended Stage I growth. The extent of secondary slip depends upon the stress normal to the crack plane (primary slip plane). This process results in a net curvature of the crack path due to asymmetric slip, resulting in a transition to dual conjugate primary slip systems typical of Stage II growth (normal to the maximum principal stress), as shown in Fig. IV.1c. Even if the slip is not completely balanced each cycle, the net effect is to maintain a crack path which maximizes the CTOD. As the crack lengthens, it may grow either in extended Stage I if the slip is relatively unconstrained (as in planar slip single crystals or coarse grain polycrystals) or may shift to a Stage II alternating primary slip growth mode early if the slip is diffuse or wavy (e.g. Al alloys).

In considering how the CTD is affected by secondary slip through the stages of crack growth, it is instructive to rewrite the CTD in Equation (IV.1) in (18) as

$$CTD = \left(1 + \left(\frac{|\delta_s|}{|\delta_p|} \right)^2 + 2 \frac{|\delta_s|}{|\delta_p|} \cos 2\alpha \right)^{1/2} |\delta_p| \quad (IV.2)$$

where 2α is the angle between the primary and secondary slip systems. Clearly, in coplanar Stage I growth, $|\delta_s|/|\delta_p| = 0$ and $CTD_I = |\delta_p|$. During extended Stage I growth, the ratio $|\delta_s|/|\delta_p|$ may be roughly approximated as $\sigma^2/9\tau^2$, where σ is the stress amplitude normal to the crack plane and τ is the shear stress amplitude on the primary slip plane. Assuming $2\alpha \approx 70.5^\circ$, this leads to $CTD_{II} \approx 1.07 |\delta_p|$. In Stage II growth with symmetric conjugate slip, $CTD_{III} \approx 1.63 |\delta_p|$. The primary slip band length is given, assuming small scale plasticity and

isotropic linear elasticity, as $|\delta_p| = 4(1-\nu^2)\tau^2 a / (E \tau_s)$, where τ_s is the cyclic shear yield stress in the primary slip band. These values establish the magnitude of CTD for different stages of crack growth in terms of the primary slip band length ahead of the crack.

IV.3 Model Description for Crack Analysis

Details of the computational model are given along with discussions of parallels and differences with the work of Li (129, 132) and Gall *et al.* (117). Li's (129, 132) work focuses on the interaction of the crack tip with bi-crystals of varying orientations, whereas Gall *et al.* (117) used planar double slip with varying crystal orientations in a single crystal to assess the CTOD and CTSD. Figure IV.2 shows the crack tip configuration utilized for this work. The CTSD and CTOD are determined by resolving the relative displacements of two nodes occupying the same location in space on the initial crack surface (but attached to upper and lower surfaces) into components along (CTSD) and normal (CTOD) to the original crack plane behind the crack tip.

The grain ahead of the crack tip along the slip plane was assigned two orientations: either identical to that of the surface grain with the crack, or in a conjugate slip orientation with significant misorientation relative to the surface grain, as shown in Figure II.6. The former assignment is to some extent analogous to a crack in a large surface grain and promotes shear localization or slip transfer to the next grain to the greatest extent, while the

latter is expected to produce maximum shielding of the CTD. Results for the CTSD and CTOD are reported at 2 μm and 25 μm behind the crack tip. The mesh at the crack tip is comprised of elements which are 0.5 μm in length; therefore, at the point which displacements are taken at 2 μm , there are four elements behind the crack tip. For the smallest crack length ratio analyzed, $a/d = 0.25$, the CTSD and CTOD are reported at a distance 18 μm behind the crack tip. The values CTOD and CTSD at 18 μm for $a/d = 0.25$ and 25 μm for $a/d = 0.5$ are considered to be more so crack mouth displacement variables rather than crack tip values, but that distinction in nomenclature is not made here.

IV.3.1 Description of Mesh and Location of Driving Force Measurements

In devising an appropriate mesh, three possibilities were considered as shown in Figure IV.3. The first two cases were considered in order to reduce computational times associated with a fairly large mesh in addition to the incorporation of a UMAT subroutine for the material behavior. The polycrystal was initially modeled with crystal plasticity in the grain containing the crack and its adjacent grain, similar to the work of Li (132). This case was motivated by a micromechanics principle advocated by Kocks (134) which assumes that the action of all grains on the surrounding ones is equivalent to the action of an isotropic continuum on the grain. Consequently, only one additional grain was modeled with crystal plasticity ahead of the Stage I small crack tip. The surrounding elements were therefore

modeled initially with isotropic plasticity behavior, with constants selected to fit the macroscale behavior of the material. Second, three 'rings' of grains surrounding the cracked surface grain were modeled with the crystal plasticity model. Finally, the entire aggregate was modeled with crystal plasticity. The first two cases resulted in unacceptably high stresses between the boundaries of the grains having the crystal plasticity model and those which were modeled with macroscale plasticity. In addition, the CTOD and CTSD were not consistent between the first two cases, yielding results which differed by 20-40%. The final configuration produced values of CTOD and CTSD which did not deviate considerably when using another realization of grain orientations for the polycrystal (within 5-10%). Hence, the last option of using crystal plasticity through the entire model was adopted.

The finite element analyses were performed using a two-dimensional, plane strain mesh with a height of 0.9 mm and width of 1 mm. The grains were rectangular with dimensions of $d = 0.1$ mm by $h = 0.15$ mm. Elongated grains were used in order to avoid having a crack at a triple point (crack crosses at a location in the mesh where the nodes of three grains coexist). This was especially a concern for the remote tension-compression loading case where the cracks were oriented at 45° to the tensile axis to lie along the Stage I maximum shear plane. The finite element program ABAQUS (108) was used to perform the analyses employing the UMAT formulation for crystal plasticity described in Chapter II. Two-dimensional, 8-noded quadrilateral, biquadratic (CPE8R) and 6-noded quadratic (CPE6) solid elements were used throughout the mesh. A less refined mesh was used as one progresses from the crack tip to the mouth of the crack. A typical mesh with a surface crack

is shown in Figures IV.4a and IV.4b where considerable mesh refinement was employed in and near this surface grain. The elements surrounding the crack tip were $0.5\ \mu\text{m}$ in dimension to resolve the near tip CTSD and CTOD properly and crack surfaces were assumed to be initially perfectly planar.

Figures IV.4c and IV.4d show the boundary conditions for the remote tension and remote shear loading cases. In tension, uniform vertical displacements were prescribed at the top and bottom boundaries in the uniaxial loading y-direction, with zero traction in the x-direction; the lateral sides were traction free. In shear, the x-direction displacements on the top and bottom surfaces were specified (zero x-direction traction on the bottom, except for one point), with no y-direction traction on the upper surface, and traction free lateral boundaries. In shear, the upper surface was subjected to a multipoint constraint to maintain planarity, and the bottom surface was constrained against y-direction displacement.

IV.3.2 Crack Geometries

The crack was assumed to reside within a surface grain which is favorably oriented for single slip, with one of the two available slip systems aligned with the macroscopic maximum shear plane orientation. For the case of tensile loading, the surface crack is oriented at 45° to the tensile axis. For shear loading, the surface crack is oriented at 90° to the tensile axis. Six a/d ratios were analyzed in this study (0.25, 0.5, 0.97, 1.25, 1.97, and 2.5) where a is defined as the crack length along the crack plane and d is the grain width (0.1

mm). For tensile loading (crack oriented at 45°) a is the length of the crack projected onto the horizontal plane.

All cracks are stationary, i.e. introduced without prior effects of growth history. Stationary cracks were considered instead of allowing the propagation of the crack along a predetermined path because propagating a crack would require the selection of a critical condition for releasing nodes along the crack front. In contrast, the goal of these studies is to determine the dependence of driving forces of the crack tip driving force on microstructure for crack paths that represent typical observations, to within limitations of 2-D analysis.

In the grain adjacent to the cracked surface grain and diagonally along the path of the crack plane (see Fig. II.6), labeled as Grain A, two different orientations of the slip systems are considered. These include an aligned orientation that promotes extended single slip on the plane of the crack and a conjugate slip orientation which promotes slip along both slip directions. Tables IV.1a and IV.1b summarize the two cases. The angle of misorientation, η , is defined as the minimum angle between the primary slip system in the surface grain and the nearest slip system in grain A. The remaining grains are constrained to have no more than a 15 degree difference in θ (orientation of the planar double slip geometry described in Chapter II) relative to their nearest neighboring grain (Bassani (103)), but are otherwise randomly oriented. It should be recognized that while grain A provides the most capacity for orientation blockage, the surrounding grains also contribute, rendering these analyses different from that of a crack interacting with a bicrystal grain boundary (135).

IV.3.3 Loading Conditions

This study considers a range of peak applied strain levels as fractions (0.3, 0.5, 0.7, 0.9, 1.0) of the total strain at yield, $\epsilon_y = 0.0065$ for tensile loading and $\gamma_y = 0.0042$ for shear loading, corresponding to the cyclic curve. In all cases, the applied strain is regarded as the nominal strain corresponding to the displacement controlled boundary conditions shown in Figure IV.4. Combined with the geometry of the overall mesh shown in Figure IV.4, this results in a decreased crack tip driving force relative to the solution for prescribed remote stress. Moreover, since this is a finite body, reference isotropic, homogeneous linear elastic solutions are conducted for each case to compare the behavior.

A set of monotonic analyses were conducted to the end of the first half cycle. The intent was to consider the influence of the free surface, anisotropy and heterogeneity on CTOD and CTSD without effects of crack face interference or stress redistribution associated with cyclic microplasticity. A second set of analyses were conducted for three complete cycles to explore the nature of the Δ CTOD and Δ CTSD, including the influence of the free surface and reversed cyclic plastic strain as a function of crack length ratio, stress state, and applied strain amplitude.

As just mentioned, reference elastic solutions were also performed in each case using precisely the same mesh and boundary conditions, but suppressing the plasticity. Effects of the free surface are reflected in the elastic solutions as well. The elastic behavior in both sets

of simulations is linear, isotropic and homogeneous; hence, there are no weak elastic singularities at junctions of grains. Of course, this is an approximation for crystals, but the intent here is to isolate the effects of anisotropic plasticity.

IV.4 Results for Monotonic Loading

IV.4.1 Remote Tensile Loading

As described earlier, the remote tensile loading case contains a surface crack oriented at 45° to the tensile axis. Two cases are considered. First, the adjacent grain is oriented in a single slip mode, such that the surface grain and the adjacent grain are aligned. Next, the adjacent grain is oriented in a mode of conjugate slip, such that maximum shielding of the CTD is produced. CTODs and CTSDs are taken from nodes which are located $2\ \mu\text{m}$ and $25\ \mu\text{m}$ ($18\ \mu\text{m}$ for $a/d = 0.25$) behind the crack tip. Calculations of this type serve to quantify the CTD as a function of stress state and amplitude.

$a/d = 0.25$: For this case of a small surface crack well-oriented within a surface grain, Figure IV.5 shows plots of CTOD and CTSD for the elastic reference solutions and for the micromechanical model for single and conjugate slip. For both orientations of the adjacent

grain and at both locations behind the crack tip, the CTOD is on the order of two to four times greater than the elastic solution as general yielding is reached. For both distances behind the crack tip, the CTOD in the single slip case is nearly identical to that of the case of the conjugate slip orientation of grain A for applied strains less than $0.25 \epsilon_y$. Above $0.25 \epsilon_y$, the CTSD and CTOD for the single slip case intensifies well above the elastic solution.

This behavior differs considerably from that calculated based on slip band impingement on a grain boundary ahead of the crack as in distributed dislocation (82, 128) or finite element solutions that use a constraint argument to represent slip bands (132). Figure IV.5 clearly shows that the CTOD exceeds the CTSD even in the reference elastic solutions which do not depend in any way on the arrangement of grains or their orientation (due to elastic homogeneity), but does depend on the geometry and boundary conditions imposed. In particular, the CTOD near the tip departs significantly from the elastic solution well below $0.4 \epsilon_y$, and then continues to intensify relative to the elastic solution as general yielding is approached. The intensification of the CTOD is at least that of the CTSD with increased applied strain for both adjacent grain orientations. This illustrates why applying elastic solutions to the analysis of small cracks can yield anomalous results, even in the HCF regime below general yielding, when microplasticity is considered. Surface measurements might not reflect crack tip mode mixity very well, as inferred by the significant differences in the ratios of CTOD and CTSD at $2 \mu\text{m}$ and $18 \mu\text{m}$ behind the crack tip as well as large relative discrepancies in the ratio of the micromechanical solutions to the elastic CTOD and

CTSD values. It is clear that surface measurements would apparently provide little useful information regarding the near tip behavior.

The CTOD solutions appear to be strongly influenced by the crack tip's proximity to the free surface, and to some extent, by the full set of nearest neighbor grains surrounding the cracked grain. This is a feature that has not been brought out in previous analyses by Li (132). Plots of contours of equivalent plastic strain support this assertion, as shown in Figure IV.5. By viewing these contours for each misorientation, η , one can gain perspective on the CTOD and CTSD calculations. For $\eta = 0^\circ$ and 35.1° , it is apparent that there is some transfer of plastic strain into the grain directly below the surface grain, more-or-less along the 45° maximum shear plane. There is multislip on the two systems in the cracked surface grain within this band of localized plastic strain. For $\eta = 0^\circ$, as expected, slip transfer is unhindered. In fact, cyclic plastic slip continues across not only the adjacent grain, but also into its next neighbor. This is an expected result, but it is intriguing that this process begins well below the yield strain (slightly more than $0.3 \epsilon_y$). Therefore, at strain values well below nominal yield, transgranular plastic strain occurs. For the case of conjugate slip in the adjacent grain, $\eta = 35.1^\circ$, there is a suppression of the slip transfer into grain A, but not necessarily into others. It is also recognized that even with the redistribution of the plastic strain into neighboring grains, it does not overshadow the strong influence of the surface on the crack tip displacements. This is manifested by the dominant opening behavior of the crack plotted in Fig. IV.4.

Such effects have been reported in 3-D crystal plasticity analyses and observations of cracks approaching bicrystal interfaces by Li (135). Essentially, the overall dominance of the CTOD reflects the influence of the free surface and the assignment of multislip with equal hardening on the two systems. For materials that exhibit profuse multislip (i.e., pronounced secondary slip in Fig. IV.1c), even weak constraints on primary slip may trigger conjugate slip and early transition to mode I-dominated conditions.

$a/d = 0.5$: Figure IV.7 shows plots of CTOD and CTSD. For both orientations of slip in the adjacent grain, the opening displacements exceed the sliding displacements. At $2\text{ }\mu\text{m}$ behind the crack tip, the sliding displacements are more nearly equal to the opening displacements. Above $0.25\text{ }\epsilon_y$, the elastic-plastic solution starts to deviate from the elastic solution. Indeed the elastic solution is a very conservative estimate of the near tip CTOD, by nearly a factor of ten at the highest strain level of $0.9\text{ }\epsilon_y$. Again, it is observed that the effect of misorientation in the grain ahead of the crack tip plays a notable role at higher strain amplitudes in addition to the apparent loss of constraint on plasticity near the free surface, since the elastic-plastic CTOD is dominant. Multislip in the cracked surface grain is activated by stress redistribution associated with neighboring grains.

At $25\text{ }\mu\text{m}$ behind the crack tip, the opening displacements exceeding the sliding displacements by 2.5 times at $0.9\text{ }\epsilon_y$, whereas at $2\text{ }\mu\text{m}$, the opening displacements are only 1.5 times higher than the sliding displacements. This again indicates the uncertainty of

interpreting surface values as indicative of near tip values. The conjugate slip case promotes a slightly increased opening mode at the crack tip and the single slip mode produces increased sliding displacements. Figure IV.7 also shows that the influence of the orientation of the adjacent grain has an increased effect on the sliding and opening displacements at larger a/d ratios.

$a/d = 0.97$: Figure IV.8 shows plots of CTOD and CTSD computed 2 μm and 25 μm behind the crack tip, along with the elastic reference solutions, as the crack approaches the grain boundary. The near tip (2 μm) CTSD is essentially 4-5 times greater than the elastic solution. The CTOD shows enormous intensification relative to the elastic solution for the single slip case, similar to the smaller crack length ratio solutions; however, the near tip CTSD for the conjugate slip case in the next grain has fallen off to the elastic solution, indicating a constraint of the adjacent grain on the sliding displacement in this case. As the crack approaches the grain boundary, the CTSD and CTOD have very similar magnitudes when the next grain shares the same orientation. There is a shift of the local mode mixity of the crack tip displacements as the crack lengthens. However, for the conjugate slip case, the sliding displacements are tremendously impeded. At 25 μm behind the crack tip, and for the conjugate slip orientation, more sliding displacements are evident as compared to near tip measurements. The influence of surrounding grains appears to relieve the some of the strong constraint caused by the shielding due to the orientation of the adjacent grain.

$a/d = 1.25$ and $a/d = 1.97$: For these a/d ratios, the crack remains oriented at 45° to the tensile axis. The CTOD and CTSD results are presented in Figures IV.9 and IV.10, respectively. As for the previous a/d ratios, the CTOD is greater than the CTSD. At $2\text{ }\mu\text{m}$ behind the crack tip, the CTOD for conjugate slip is greater than the CTOD for the single slip orientation. The conjugate slip case promotes an opening mode that is evidenced at higher amplitudes and crack lengths. The conjugate slip orientation of grain A increases the crack's tendency to open at the crack tip and as pointed out previously, provides an increased influence of the adjacent grain for increasing crack length ratios. At $2\text{ }\mu\text{m}$ behind the crack tip, the opening displacements for the conjugate slip case (at the highest strain amplitude) are 20% higher than the opening displacements for the single slip case. At $25\text{ }\mu\text{m}$ behind the crack tip, the trend is similar. For both a/d ratios and at both locations behind the crack tip, the sliding displacements for the conjugate slip and single slip cases are nearly identical to each other. At $25\text{ }\mu\text{m}$ behind the crack tip, the opening displacements for the single slip case are greater than those of the conjugate slip case. At this location, there is perhaps a decreased effect of the grain just ahead of the crack and an increased influence of the surrounding grains. For both a/d ratios and at both locations behind the crack tip, the sliding displacements are 25% to 40% lower than the opening displacements. Recall that for smaller crack length ratios ($a/d = 0.25$ and 0.5), the opening displacements dominated the behavior. For the a/d ratios of 1.25 and 1.97, the sliding displacements now have values comparable

to the opening displacements.

$a/d = 2.5$: Figure IV.11 shows the CTODs and CTSDs for this a/d ratio. As the crack lengthens, the orientation of the embedded crack is still modeled at 45° , with the adjacent grain being oriented either in single or conjugate slip, the same as in the previous analyses. Again, the opening displacements are greater than the sliding displacements for both locations behind the crack tip. At this a/d ratio, the opening displacements for both the single and conjugate slip cases are nearly identical, with the sliding displacements being approximately 25% lower than the opening displacements. At $25\ \mu\text{m}$ behind the crack tip and for both orientations, the opening displacements are about 1.5 times higher than the sliding displacements. Again, although the opening displacements are still greater than the sliding displacements, the sliding displacements are more comparable to the opening values at these increased a/d ratios.

Also note how the elastic solutions appear to be very similar for a/d ratios of 1.25, 1.97, and 2.5. This is due to the nature of the boundary conditions used for these analyses. As previously discussed, the top face remains planar such that the entire face must have the same vertical displacement. This boundary condition leads to nearly constant CTD for larger a/d ratios.

$a/d = 2.5$ (kinked): At this a/d ratio, the crack was also modeled as a kinked crack, growing along one of the two available conjugate slip directions in the adjacent grain. Figure IV.12

illustrates both cases, labeled as kinked-down (KD) and kinked-up (KU). The computed CTODs and CTSDs for the KD and KU cases are reported in Figures IV.13 and IV.14, respectively. The KD case in Fig. IV.13 shows that the opening displacements dominate the sliding displacements for both the conjugate and single slip cases. In fact, the sliding displacements are only slightly higher than those for the elastic solution. At 25 μm behind the crack tip, the behavior is nearly the same as at 2 μm , but the elastic solution for the opening displacement is closer to the micromechanical calculations as compared to the smaller a/d ratios considered. For the KU case, the opposite behavior occurs - the sliding displacements dominate. Although this case is not actually observed in small crack experiments (129), it is interesting to see why this is the case from the standpoint of a micromechanistic analysis. Newman *et al.* (136) proposed that small cracks grow in a manner such that the opening or sliding mode is maximum. The calculations show that the CTD is much greater for the KD crack due in part to the dominance of the CTOD. This is one possible explanation for the crack to 'select' the path normal to the applied stress. The KD case also more closely resembles a Stage I-Stage II transition crack wherein the crack grows from shear-dominated behavior to one which is normal-stress dominated. This growth mode (change from Stage I to Stage II behavior) may also be associated with maintaining the maximum CTD.

IV.4.2 Remote Shear Loading

The remote shear loading case examines a surface crack oriented at 90° to the longitudinal (vertical) axis. The effects of the two orientations of the adjacent grain are examined by computing the CTOD and CTSD. Table IV.1b shows the misorientation, η , of the adjacent grain for remote shear loading. The case of single slip ($\eta = 0^\circ$) in the adjacent grain allows for relatively unhindered progression of microplasticity into the adjacent grain. The second misorientation, $\eta = 35.1^\circ$, reflects a conjugate slip orientation in the adjacent grain which imposes crack tip shielding. Boundary conditions for this loading case are shown in Figure IV.4d.

$a/d = 0.25$ and 0.5 : Figures IV.15 and IV.16 show the CTOD and CTSD for a/d ratios of 0.25 and 0.5, respectively. For $a/d = 0.25$, the opening displacements are nearly 15 times higher than the sliding displacements. For $a/d = 0.5$ at $25 \mu\text{m}$ behind the crack tip, the opening displacements are about 3 times higher than the sliding displacements. Even for a 90° crack and at these crack lengths, the behavior is dominated by the nature of the imposed boundary conditions as evidenced by the dominance for opening of the elastic solution. Hence, this particular case differs substantially from that of an edge crack in a semi-infinite half-space loaded in shear at infinity. The sliding displacements are nearly the same (for $\Delta\gamma/2 < 0.5 \gamma_y$) as those for the elastic solution. The orientation of the adjacent grain has

minimal effect on the displacements for these crack length ratios.

Contour plots of the effective plastic strain for $a/d = 0.5$ are given in Figure IV.17 for both the single and conjugate slip cases of orientation of the next grain ahead of the crack. For the conjugate slip case, note how the plasticity is concentrated not only ahead of the crack tip, but it is redistributed ahead of the crack tip and along the surface. The surface acts to relieve the stress that is shielded by the adjacent grain. Similar to the contours for $a/d = 0.25$ for the remote tension case, although plasticity is concentrated ahead of the crack tip and into adjacent grains for the single slip case, the effect of the free surface dominates the behavior at the crack tip.

$a/d = 0.97$: The behavior for this ratio is quite different from that observed for a/d of 0.25 and 0.5. Figure IV.18 shows the CTOD and CTSD for the elastic as well as the micromechanical elastic-plastic solutions. For both locations behind the crack tip, the sliding displacements for the elastic solution exceed those of the opening. For single slip, the sliding and opening displacements are nearly the same for all strain amplitudes. The CTODs are greater than the CTSDs for the conjugate slip case after a strain amplitude of $0.7 \gamma_y$. This is an expected result because conjugate slip does promote an opening mode and multislip, although it was not clear when this effect would be manifested in the CTOD and CTSD for the shear loading case.

$a/d = 1.25$: The CTOD and CTSD for this a/d ratio are shown in Fig. IV.19. At $2\text{ }\mu\text{m}$ behind the crack tip, the single slip case promotes sliding displacements which are 40% greater than the opening displacements. For the conjugate slip case, the opening and sliding displacements are nearly the same for both locations behind the crack tip. For the single slip case and at $25\text{ }\mu\text{m}$ behind the crack tip, the sliding and opening displacements are nearly the same. As nominal cyclic yield is approached, both the CTOD and CTSD rapidly increase.

$a/d = 1.97$: Figure IV.20 shows the results for this a/d ratio. At this a/d ratio, there is a complete reversal of the behavior as compared to $a/d = 0.25$. As plotted in Figure IV.20, the sliding displacements dominate in contrast to dominance of the opening displacements for $a/d = 0.25$. Starting from about $0.5\text{ }\gamma_y$ to γ_y , the sliding displacements increase from twice the opening displacements to three times the opening displacements. It is also observed that (for the first time) at $25\text{ }\mu\text{m}$ behind the crack tip, the elastic solution provides a good approximation of the micromechanical sliding and opening displacements.

$a/d = 2.5$: In Figure IV.21, the CTOD and the CTSD are plotted. For both locations behind the crack tip, the sliding displacements dominate the opening displacements by nearly a factor of five for both the single and conjugate slip orientations of the adjacent grain. At this ratio, the behavior of the two cases are nearly the same, suggesting relative insensitivity to local microstructure. As the crack lengthens, the driving forces are high enough such that

the orientation of the adjacent grain or surrounding grain has minimal effect on reducing the CTD for remote shear.

IV.4.3 Implications for Small Crack Behavior

For the remote tensile loading case, the differences in sliding and opening displacements are elucidated in Figure IV.22 which summarizes the behavior as a function of stress amplitude and crack length ratio at 2 μm behind the crack tip. Trend lines are also drawn. This Figure shows two principal features for tensile loading. First, the opening displacements dominate for all crack length ratios and applied strain amplitudes. Second, there appears to be three regimes. The first is a more-or-less linear relationship between both the CTOD and CTSD and applied strain for $a/d < 0.5$. For all strain amplitudes considered and at $a/d = 0.97$, the sliding and opening displacements exhibit sensitivity to the grain boundary, especially for the conjugate slip case. In the second regime ($0.97 < a/d < 1.97$), there appears to be a parabolic increase. In the third regime ($1.97 < a/d < 2.5$), it is clear that the kinked down solution for $a/d = 2.5$ provides a much more consistent extension of the trend for $a/d < 2$ than for the cracked still oriented at 45° (as shown by the dotted line in Figure IV.22).

Figure IV.23 summarizes the behavior of the CTOD and CTSD for remote shear loading. It shows a plot of the sliding and opening displacements for 2 μm behind the crack

tip as a function of crack length ratio and applied strain amplitude. Up to an a/d of 1.25, the sliding and opening displacements are nearly the same for all shear strain amplitudes. For a/d ratios greater than 1.25, the conjugate slip case does effectively promote increased opening displacements as compared to the single slip case. With the increased CTOD, this would increase the propensity for multislip such that the shear cracks might tend to branch towards secondary planes. At a/d ratios of 1.97 and 2.5, the sliding and opening displacements are significantly different, with the sliding displacements dominating the behavior, especially as the nominal yield strain is approached. This contrasts markedly to the tensile loading case where the sliding and opening displacements differ for all a/d ratios and strain amplitudes; for cyclic shear, the larger strain amplitudes and larger a/d ratios produce significant differences in the CTOD and CTSD values. The results for both cases are further discussed in Chapter V regarding their implications for small crack behavior and model development.

IV.5 Results for Cyclic Loading

For the cyclic loading cases, the polycrystal is subjected to strain amplitudes of 30%, 60% and 90% of the cyclic yield strain, where $\epsilon_y = 0.0065$ for tensile loading and $\gamma_y = 0.0042$ for shear loading. Three completely reversed ($R = -1.0$) cycles are applied to determine the behavior of the sliding and opening displacements. Only three cycles of loading are

considered in view of the level of the idealization and necessary computation time. Elastic solutions are also plotted in order to show the relative differences in the crystal plasticity solutions. In the same manner as for the monotonic cases, the surface crack is oriented at 45° with respect to the tensile axis, with two orientations of the adjacent grain - single and conjugate slip. For the cyclic shear case, the surface crack is oriented at 90° to the tensile (vertical) axis. The results for $\Delta CTOD$ and $\Delta CTSD$ are discussed in terms of their dependence on crack length ratio, amplitude of the applied load, stress state, orientation of adjacent grain, degree of local phasing or nonproportionality, and crack closure behavior.

As previously stated, the CTOD and CTSD values are determined by considering two nodes which have initially identical coordinates, but rest on opposite sides of the crack face. As for the monotonic solutions, the displacements are taken at $2\ \mu\text{m}$ and $25\ \mu\text{m}$ behind the crack tip for all a/d ratios, except for $a/d = 0.25$, where the displacements are taken at $2\ \mu\text{m}$ and $18\ \mu\text{m}$ behind the crack tip. The CTODs and CTSDs throughout the loading cycles are found by resolving the coordinates of these nodes into components along (CTSD) and normal (CTOD) to the original crack plane. At the end of the third cycle, the range of the CTSD ($\Delta CTSD$) and CTOD ($\Delta CTOD$) are found from the absolute value of the difference between the maximum and minimum values of the displacements.

The crack surface is assumed as traction free provided the surfaces do not contact. Once the crack faces do come into contact during the compressive part of the load, there are several options within ABAQUS (108) that are able to handle this condition. For these

studies, the option most appropriate for the cases considered is the use of contact elements along the crack face. This formulation allows for both small- and finite-sliding between the two surfaces which interact. For both tensile and shear loading, the crack surfaces are not allowed to ‘overlap’, but they are allowed to move along and normal to the crack plane. Crack face contact friction is not considered in these studies.

The material constants were presented in Chapter II, but it is further noted here that the slip system backstress, x^α , is included in the flow rule to account for the resistance to forward loading due, for example, to dislocation walls produced by cyclic loading. The evolution of x^α is defined as

$$\dot{x}^\alpha = C \dot{\gamma}^\alpha - d x^\alpha |\dot{\gamma}^\alpha| \quad (\text{IV.3})$$

from Cailletaud *et al.* (107), where C and d are direct hardening and dynamic recovery coefficients, respectively. For these studies, $C = 100$ MPa and $d = 30$.

IV.5.1 Cyclic Tension-Compression

a/d = 0.25: For this a/d ratio, the cyclic behaviors of the CTOD and CTSD are shown in Fig. IV.24 for the three strain amplitudes. For $0.3 \epsilon_y$ and at $2 \mu\text{m}$ behind the crack tip, the elastic solution provides a good estimate of the CTOD and the CTSD for the first cycle. However, for increasing numbers of cycles, the crystal plasticity solution deviates from the elastic

solution by exhibiting greater sliding and opening values. After the third cycle, the elastic solution, which maintains the same maximum and minimum amplitudes throughout loading, has only half of the opening displacements as the micromechanical solution. Of course, the elastic solution for the CTOD and CTSD repeat identically regardless of the cycle number. The micromechanical model behaves quite differently, especially for the highest applied strain range. For both the single slip and conjugate slip cases, and for both locations behind the crack tip (at $0.3 \epsilon_y$ and $0.6 \epsilon_y$), the Δ CTOD and Δ CTSD are nearly the same for all cycles. At the highest strain amplitude, the CTOD and more so the CTSD are quite distinct for each η . These differences are also evident at $25 \mu\text{m}$ behind the crack tip.

Another aspect of the cyclic behavior regarding the near crack tip displacements is that crack closure effects decrease with increased strain amplitude(at $2\mu\text{m}$ behind the crack tip and at $0.9 \epsilon_y$). The crack faces are not completely closed at zero load. The crack faces are only completely closed well into the compressive part of the loading cycle. This is evident by comparing the stress level when the crack faces are completely closed during the compressive part of the cycle. Note how for the last cycle, the amplitude of the effective stress increases with increasing amplitude. This is more easily demonstrated in Figure IV.25 with dashed lines comparing the range of the effective stress for cases of applied strain amplitude $0.3 \epsilon_y$ and $0.9 \epsilon_y$. There is also some evidence of complete opening at $18 \mu\text{m}$ behind the crack tip, but only for the highest strain amplitude.

What is also intriguing is the highly nonlinear and nonproportional sliding and

opening displacements for $0.9 \epsilon_y$ with respect to the loading with increasing maximum values of CTOD. This behavior continues for all cycles at this strain amplitude. For $a/d = 0.25$ and for $0.9 \epsilon_y$, the sliding displacements are approximately 60% of the opening displacements for the last two cycles whereas they are nearly the same values in the first half cycle. This indicates that there is perhaps a redistribution of cyclic microplasticity into surrounding grains which allows for more opening and sliding in the vicinity of the crack tip. At $2 \mu\text{m}$ behind the crack tip and for $0.9 \epsilon_y$, the CTSD develops a positive mean displacement. This relates to the amount of irreversible slip which develops due to reversed loading and the amount which contributes to the offset sliding displacement at the crack tip, a kind of cyclic ratchetting effect. In essence, a degree of plasticity-induced closure develops. At both locations behind the crack tip, there are pronounced differences in the sliding displacements for single and conjugate slip cases for $0.9 \epsilon_y$. For this a/d ratio of 0.25, the effect of the orientation of the adjacent is not manifested until the highest strain amplitude is applied. The studies will also show that at increased crack length ratios, the nonproportionality sets in at smaller applied strain amplitudes.

For $a/d = 0.5$ and for all strain amplitudes, the sliding and opening displacements are nonproportional with respect to each other for strain amplitudes of $0.6 \epsilon_y$ and $0.9 \epsilon_y$ (Fig. IV.26). At these strain amplitudes, differences between the single and conjugate slip cases for sliding displacements are more pronounced. For $a/d = 0.25$, these differences are only evidenced at the highest strain amplitude. In fact, there is less crack closure at higher strain

amplitudes for small crack (Tanaka (60)). These computations support this because when comparing the closure behavior as a function of amplitude, Figure IV.24 (at $0.9 \epsilon_y$), shows that the crack is open for nearly the entire loading cycle. With increasing number of cycles, the oscillatory nature of the sliding and opening displacements for the crystal plasticity model is quite nonlinear and unsymmetric as compared to the elastic solution. For the lowest strain amplitude, the oscillatory behavior of the CTOD and CTSD is fairly linear and consistent with loading cycle. Another observation is that the two cases of adjacent grain orientation show greater differences in sliding displacements as compared to the opening displacement for strain amplitudes $0.6 \epsilon_y$ and $0.9 \epsilon_y$. There is almost no closure for $0.6 \epsilon_y$ and $0.9 \epsilon_y$ for the 2nd and 3rd cycles, especially near the crack tip. No closure implies that more of the apparent driving forces are contributing to propagating the crack.

There is also evidence for $a/d = 0.5$ of local ratchetting of the sliding and opening displacements at $2 \mu\text{m}$ behind the crack tip, even though the remote loading is completely reversed. This ratchetting apparently contributes to the decreased effects of crack closure. Whether it is an accurate portrayal of the actual behavior of the crack tip or a manifestation of the nonlinear kinematic hardening law is not completely clear, but these results are the first to suggest this possibility. It is very possibly related to asymmetry of crack tip plasticity induced by the variation of surrounding “hard” and “soft” grains in the microstructure.

Figure IV.27 shows contour plots of the effective plastic strain for $a/d = 0.5$ after three cycles were applied for both the single and conjugate slip cases. These plots are similar

to the case of monotonic loading. For the cyclic case, there is blunting of the crack tip, related to the presence of two plastic zones (lobes) ahead of the crack tip. For the conjugate slip case, the progression of plasticity is blocked from entering the adjacent grain. As pointed out by Zhang and Edwards (77), it is more so the cyclic plastic zone which is blocked by adjacent (or surrounding) grains which causes retardation of crack propagation rather than the blockage of the crack tip at the grain boundary. Due to the constraint of the adjacent grain and the build-up of the cyclic microplasticity which develops, the surface acts to relieve that stress (e. g. by high plastic strain at the surface).

The crack length ratio of 0.97, shown in Figure IV.28, exhibits CTOD and CTSD behaviors similar to those of the $a/d = 0.5$ case. There are, however, two distinguishing features. First, for the lowest strain amplitude, the sliding and opening displacements for the two adjacent grain orientations have different trajectories (or paths), although less ratchetting-like behavior develops. Of course, with the crack just short of the grain boundary, differences in the behavior are readily reflected in the calculations, even at this low strain amplitude. Secondly, the sliding displacements (at $2 \mu\text{m}$) for the single slip case at a strain amplitude of $0.6 \epsilon_y$ are nearly 40% higher than the sliding displacements for the conjugate slip case. With increased cycling, there is a continuous accumulation and progression of plasticity ahead of the crack tip and into surrounding grains which is reflected in the increased sliding along the crack plane. As stated earlier, at longer crack lengths, nonproportionality in sliding and opening displacements sets in at lower strain amplitudes.

At this a/d ratio (0.97), these computations reveal that for the last applied cycle, there is crack closure at the lowest strain amplitude. Note that on the first cycle at $0.6 \epsilon_y$ and at both locations behind the crack tip, the crack faces are completely closed during the entire compressive part of the loading cycle. Close to the crack tip and for the second and third cycles, the crack remains open for a significant fraction of the loading cycle. Further behind the crack tip at 25 mm, subsequent cycling shows that the crack faces close before the crack faces closer to the crack tip which signifies that there is a 'peeling off' or sequential closing of the crack face. Portions of the crack furthest away from the crack tip tend to close first followed by a progressive closing down to the crack tip. Indeed as the applied strain amplitude increases to $0.9 \epsilon_y$, the crack tip exhibits less closure effects whereas farther away from the crack tip, the faces contact upon entering the compressive part of the cycle. These results relative to the sequential closing of the crack face are in line with the computational results by Zhang *et al.* (64).

For an a/d ratio of 1.25 and at a strain amplitude of $0.9 \epsilon_y$ (shown in Figure IV.29), the sliding and opening displacements exhibit differences at 2 μm and 25 μm behind the crack tip. The conjugate slip case produces more symmetric-type sliding displacements as compared to the single slip sliding displacements. Plasticity-induced closure effects develop almost immediately upon cycling near the crack tip for all strain amplitudes. At 25 μm behind the crack tip and for $0.3 \epsilon_y$, the crack faces are closed for the entire compressive part

of the loading cycle. For $0.6 \epsilon_y$, the single slip case produces a positive mean sliding displacement, but the range of the CTSD for the conjugate slip is slightly greater than for the single slip case. This is perhaps due to multislip generated by the conjugate slip orientation in the adjacent grain. For $0.9 \epsilon_y$ and at $2 \mu\text{m}$ behind the crack tip, local nonproportionality of the CTOD and CTSD occurs almost immediately upon the first cycle.

IV.5.2 Cyclic Shear

A limited computational matrix was completed for this case. Ratios of 0.25, 0.97 and 1.97 are used in these analyses with shear strain amplitudes of $0.3 \gamma_y$ and $0.9 \gamma_y$. These cases are used based on the results of the monotonic analysis which showed that there was a linear dependence of CTOD and CTSD with respect to crack length ratio and amplitude for a/d ratios less than 2. The same mesh and crack geometry that was used for the monotonic case are also employed for the cyclic analyses. The crack is oriented at 90° with respect to the tensile axis with boundary conditions shown in Figure IV.4d. The crack faces were allowed to move relative to one another, although they were not allowed to 'overlap' or interpenetrate during cycling.

For $a/d = 0.25$ and for both shear strain amplitudes considered, Figure IV.30 shows the resulting CTODs and CTSDs. In a similar fashion as the monotonic results, the opening displacements are dominant. As stated earlier, the dominant opening behavior at this a/d

ratio is primarily caused by the imposed boundary and free surface conditions. The range of the sliding displacements are nearly the same for all cycles, with symmetric sliding in the forward part and reversed part of the cycle. In addition, single and conjugate slip solutions produce the same sliding and opening displacements. The effect of the adjacent grain has not surfaced at this a/d ratio and for the strain amplitudes of $0.3 \gamma_y$ and $0.9 \gamma_y$.

For $a/d = 0.97$, the behavior of the CTOD and CTSD (in Figure IV.31) begins to reflect an influence of the adjacent and surrounding grains at the highest strain amplitude. At $2 \mu\text{m}$ behind the crack tip and at the highest strain amplitude, there is evidence of the development of a mean or offset sliding displacement. Crack closure also develops at both locations behind the crack tip as shown by the vertical dashed lines superimposed in Figure IV.31. Further down the crack face, the crack moves in more of a symmetric manner.

Figure IV.32 shows the results for $a/d = 1.97$. At $2 \mu\text{m}$ behind the crack tip, the range of the crack tip sliding displacements (ΔCTSD) is nearly 4 times the range of the opening displacement (ΔCTOD) for the conjugate slip case; for the single slip case, the ΔCTSD is nearly 8 times the range of the ΔCTOD . For this a/d ratio, the influence of the adjacent grain is reflected in the displacements. It would seem that the ΔCTSD would be greater for the single slip case as compared to the conjugate slip case. One explanation of this behavior is the increased multislip that is created at the crack tip due to the conjugate orientation of the adjacent grain; since the conjugate slip case promotes the opening mode at the crack tip, the increased opening also allows for additional sliding at the crack tip. Even though the ranges

of the sliding displacements are comparable for both instances of adjacent grain orientation for $0.3 \gamma_y$ and at $2 \mu\text{m}$, the closure levels are quite different. Since there is no misorientation between the cracked grain and adjacent grain for the single slip case, there is minimal unloading at the crack tip. The conjugate slip case does have a closure stress as compared to the single slip case which remains nearly closure free throughout cycling.

At $2 \mu\text{m}$ behind the crack tip and at $0.9 \gamma_y$, the sliding displacements develop a nonproportional response with increased cycling. This points to the increased accumulation of cyclic microplasticity which attributes to the nonproportional sliding and opening displacements. For an amplitude of $0.9 \gamma_y$ and at $2 \mu\text{m}$ behind the crack tip, the range of the sliding displacements for the conjugate and single slip case is nearly 4.5 times greater than the range of the opening displacements. For both cases of adjacent grain orientation, an offset, or mean displacement develops with increased cycling - somewhat of a ratchetting-like behavior. This may be caused by the non-symmetric development of cyclic microplasticity due, in part, to the effect of the different orientations of surrounding grains. Both the single and conjugate slip cases are closure free after the first cycle. Further along the crack front (at $25 \mu\text{m}$), nonproportional CTOD and CTSD are both evident. Just as for the cyclic tension-compression case, the cyclic shear case also shows evidence that there is a 'peeling off' of the crack face, such that the crack tip is the last part of the crack to close upon reversed loading and the first part to open during the forward loading part of the cycle.

IV.5.3 Implications for Understanding Small Crack Behavior

Understanding the trends of the local CTSD and CTOD as a function of crack length and stress amplitude is an important factor in developing models for microstructurally small fatigue cracks. Some insight into these trends may be gained based on the micromechanical analyses from this study. The implications for small fatigue crack growth behavior are discussed in terms of the degree of local nonproportionality, closure behavior, and the influence of the free surface versus local microstructural effects.

For the elastic solutions and for all a/d ratios considered, during the entire compressive part of the cycle for the cyclic tension-compression loading case, the crack faces are completely closed and remain closed until a forward, positive load is applied. This produces proportional CTOD and CTSD throughout the loading cycles. Cyclic shear elastic solutions also show proportional local CTOD and CTSD. Unlike the elastic solutions, the micromechanical analyses reveal a nonproportional variation of the local CTOD and CTSD with $R = -1.0$ and proportional applied loading primarily evidenced at higher strain amplitudes for small a/d at at small strain amplitudes for large a/d . This nonproportionality is a manifestation of many factors: (i) reversed plasticity which translates to restricted motion at the crack tip, (ii) microstructural heterogeneity, and (iii) multislip ahead of the crack tip. For both loading cases, evidence that all three influences have a tremendous impact on the development of local nonproportional CTOD and CTSD. The changing mode-mixity at the crack tip is the source of the nonproportionality. These calculations have provided a

qualitative means to elucidate the effects of stress state, amplitude, and crack length ratio on the development of this nonproportionality. It was found that this phenomenon develops at smaller cracks lengths for cyclic tension-compression as compared to cyclic shear. For cyclic tension-compression, it begins at $a/d = 0.25$ at a strain amplitude of $0.9 \epsilon_y$ and is evidenced for the other crack length ratios for $\Delta\epsilon/2 \geq 0.6 \epsilon_y$. One possible contributing factor to this is the normal stress across the 45° oriented crack plane. In addition, the sliding behavior develops a mean or offset displacement almost immediately ($a/d = 0.25$) for increasing strain amplitudes for cyclic tension-compression. Such complex phasing and ratchetting behavior have not come to light in previous computational studies based on homogeneous elasto-plasticity. Nonproportional local CTOD and CTSD for cyclic shear loading is evidenced at $a/d = 1.97$ at a shear strain amplitude of $0.9 \gamma_y$. Although higher a/d ratios were not considered, it is expected that the local nonproportionality will continue.

These studies point to some possible deficiencies in an understanding of small cracks, such as: (a) surface measurements of CTSD and CTOD may be very misleading and unrepresentative, as also pointed out by Zhang *et al.* (64), (b) plasticity-induced closure need not occur first at the crack tip for initially planar cracks, and (c) sliding and opening displacements ratchet at the crack tip in a manner which appears to maximize the CTD and decrease closure effects.

Some of the same influences which contribute to the nonporportional local CTOD and CTSD also contribute to the development of crack closure. In these computations,

closure is purely a result of plasticity effects. Plasticity-induced closure develops as cracks increase in length and have residual plasticity in the wake of the crack. Since small cracks are not long enough to develop appreciable residual plasticity, it is argued () that small cracks have minimal to nil plasticity-induced closure effects under HCF conditions. These computations show that for cyclic tension-compression (with a crack oriented at 45°), and for a/d ratios of 0.25 and 0.5, the crack faces show evidence of crack closure, primarily due to the cyclic microplasticity which develops and the free surface effect. For larger a/d ratios, closure effects tend to decrease the effective CTD. For cyclic shear loading, there is evidence of plasticity-induced closure at longer crack length ratios ($a/d = 1.97$) with an amplitude dependency as well.

Throughout the discussions in this section, distinctions may be made as to associating the effects of crack closure or local nonproportional CTOD and CTSD with the free surface, the local plasticity or a combination of both. The free surface directly contributes to the high mode I component due to lack of constraint at the surface for small a/d ratios ($a/d = 0.25$ and 0.5) for cyclic tension-compression and for $a/d = 0.25$ for cyclic shear. Local microplasticity is indeed the cause of plasticity-induced closure and local nonproportionality. The dominant CTOD (mode I) for small a/d ratios may actually aid in propagating the small cracks (such that the CTD has a large component of CTOD). These computations reveal that closure and nonproportionality occurs from a combination of factors rather than one single factor. It is important to elucidate the effects of microplasticity and free surface effects by viewing them in terms of their propensity for contributing to the driving forces for small cracks.

Chapter V takes a look at the degree of local plasticity which develops as a function of applied strain amplitude and the implications for elastic shakedown for the uncracked cases. In addition, Chapter V provides a discussion on the merging the computational results for the CTSD and CTOD to critical plane concepts. This connection is key to developing more appropriate forms for the driving forces for small cracks as well as providing a means to enhance the development of a microcrack propagation law which spans the full range of crack growth from microstructurally small to the physically small crack regime.

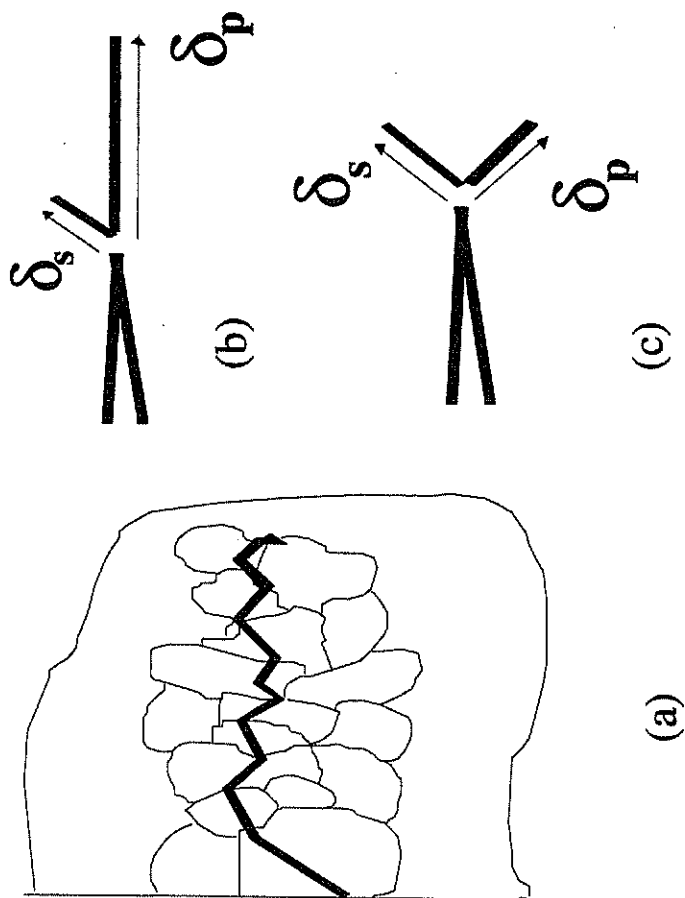


Figure IV.1 Illustration of (a) Stage I growth (CTD vector along primary slip plane only) in the first grain with transition to Stage II over a few grains, (b) extended Stage II CTD components and (c) Stage II conjugate slip.

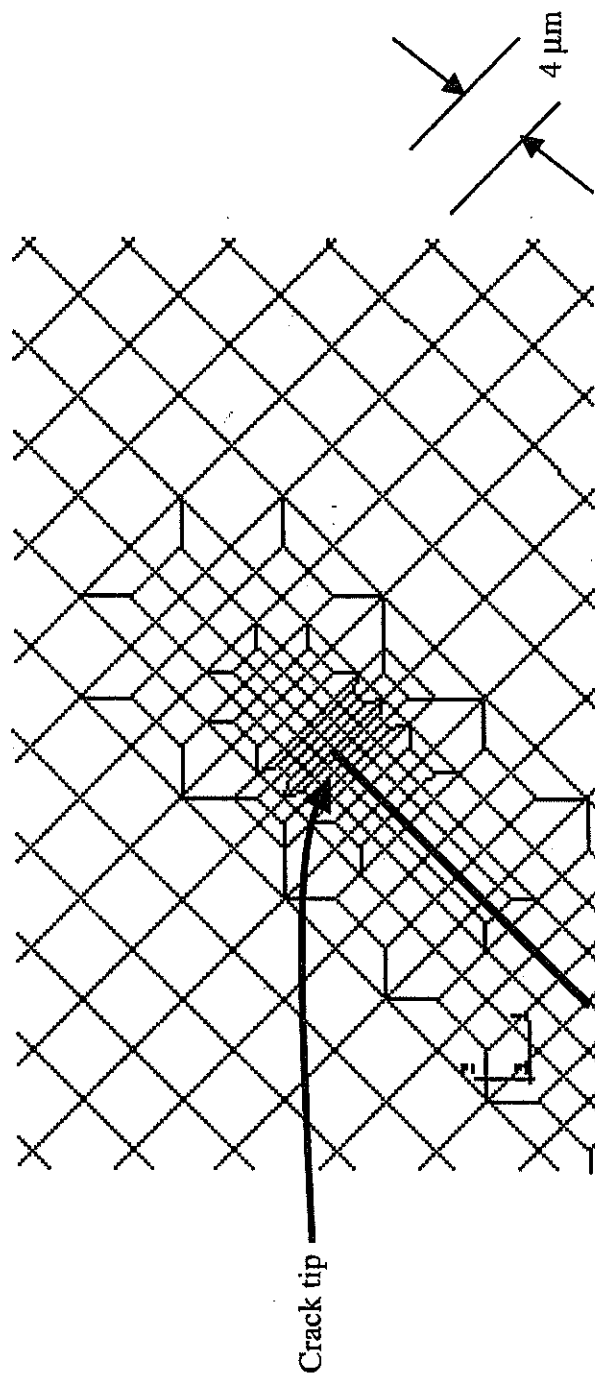


Figure IV.2 Crack tip geometry for finite element mesh.

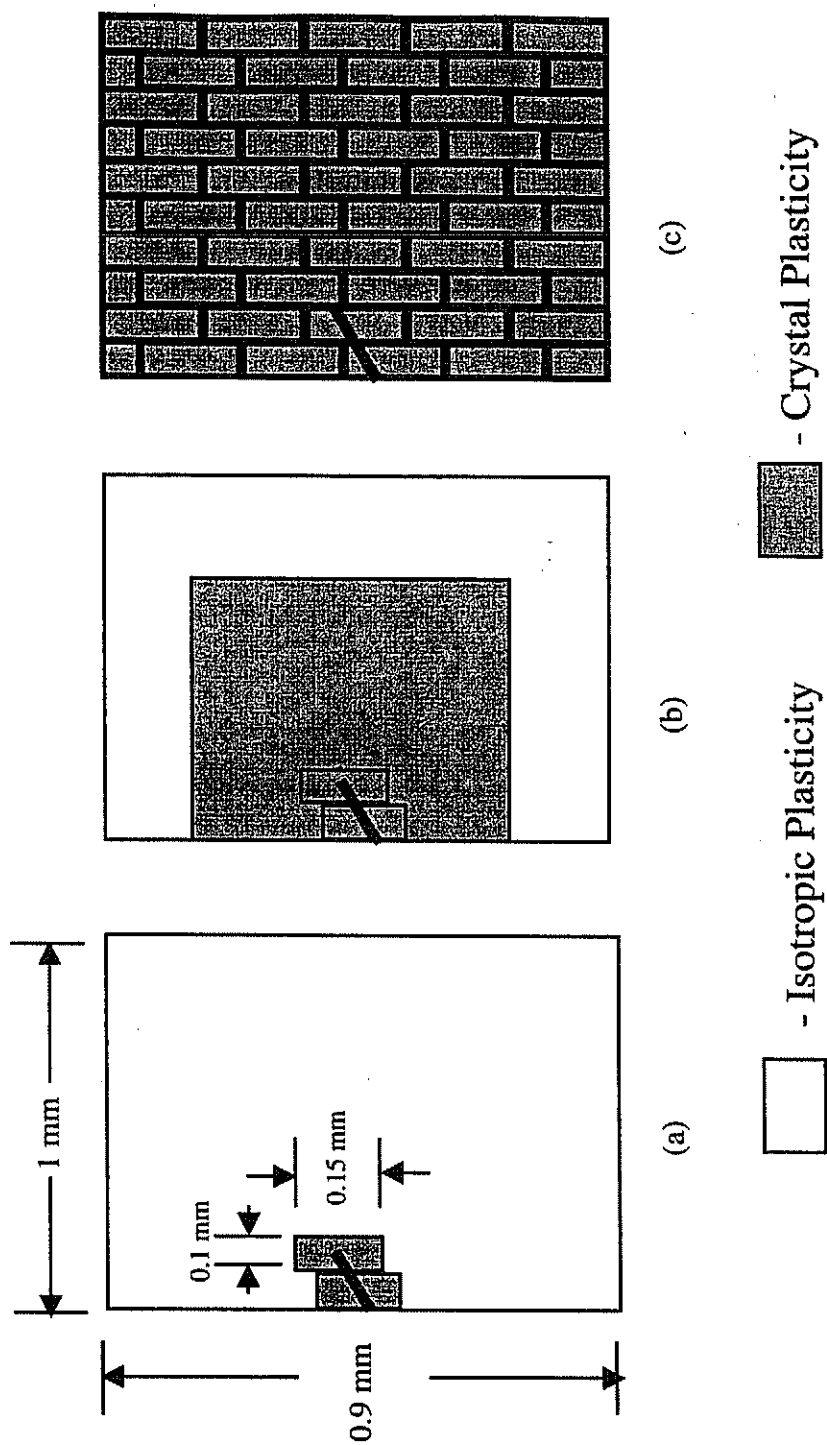


Figure IV.3 Three cases considered for modeling the cracked polycrystalline aggregate (a) cracked grain and adjacent grain modeled with crystal plasticity with remaining mesh modeled with isotropic plasticity, (b) cracked grain and adjacent grain with 'three rings' of surrounding grains modeled with crystal plasticity, remaining grains modeled with isotropic plasticity, and (c) entire aggregate modeled with crystal plasticity.

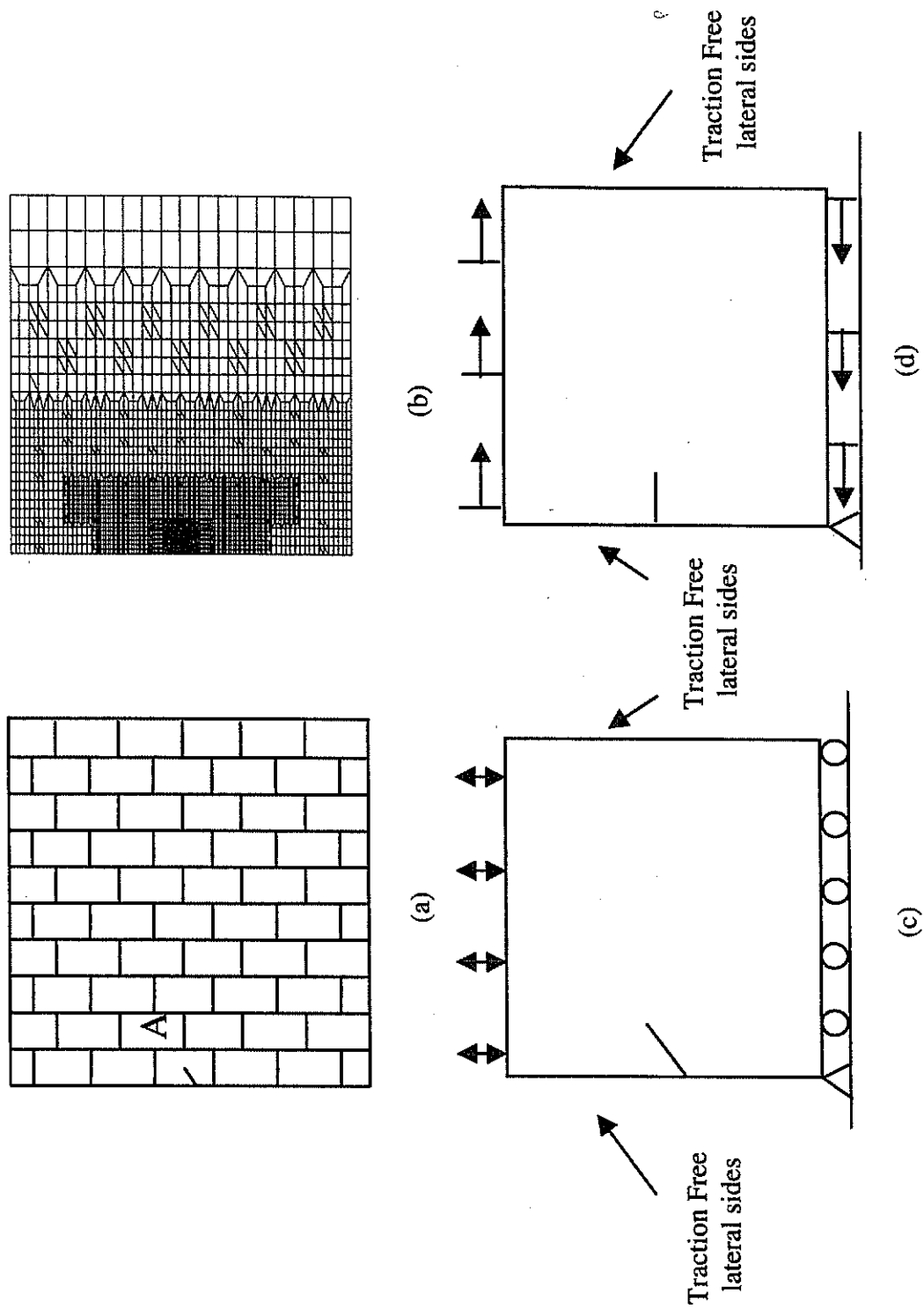


Figure IV.4 (a) Schematic of mesh configuration with nearest neighbor Grain A, (b) finite element mesh, (c) boundary conditions for remote tension-compression and (d) boundary conditions for remote shear loading.

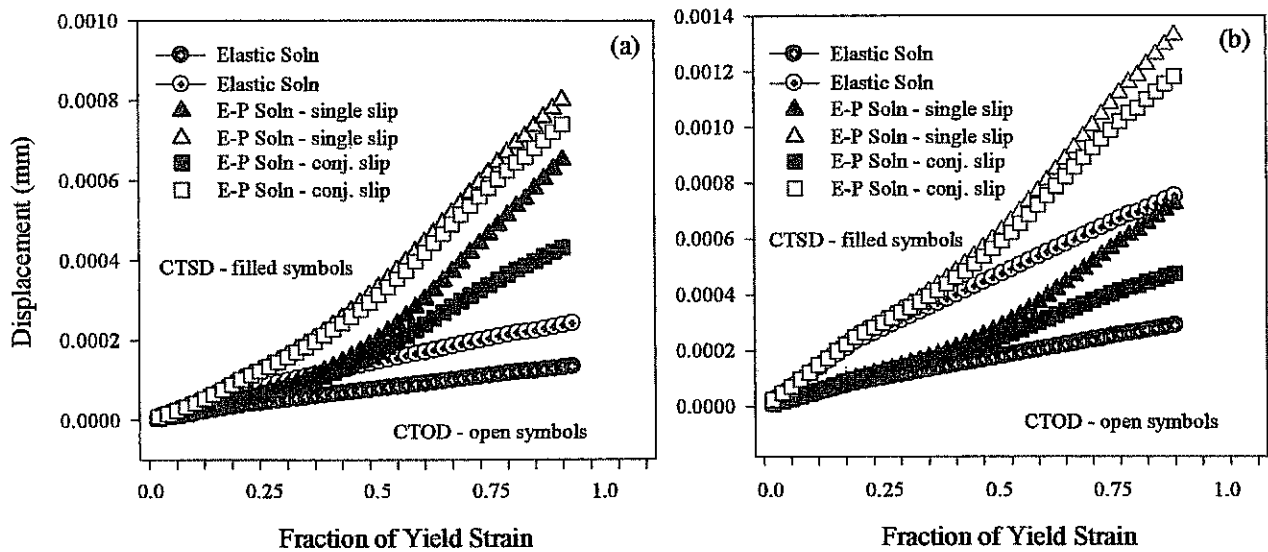


Figure IV.5 CTSD and CTOD as a function of applied polycrystal tensile strain for a surface crack ($a/d = 0.25$) in a favorably oriented grain with a range of nearest neighbor grain (Grain A) orientations given in Table IV.1a, evaluated (a) $2 \mu\text{m}$ and (b) $18 \mu\text{m}$ behind the crack tip.

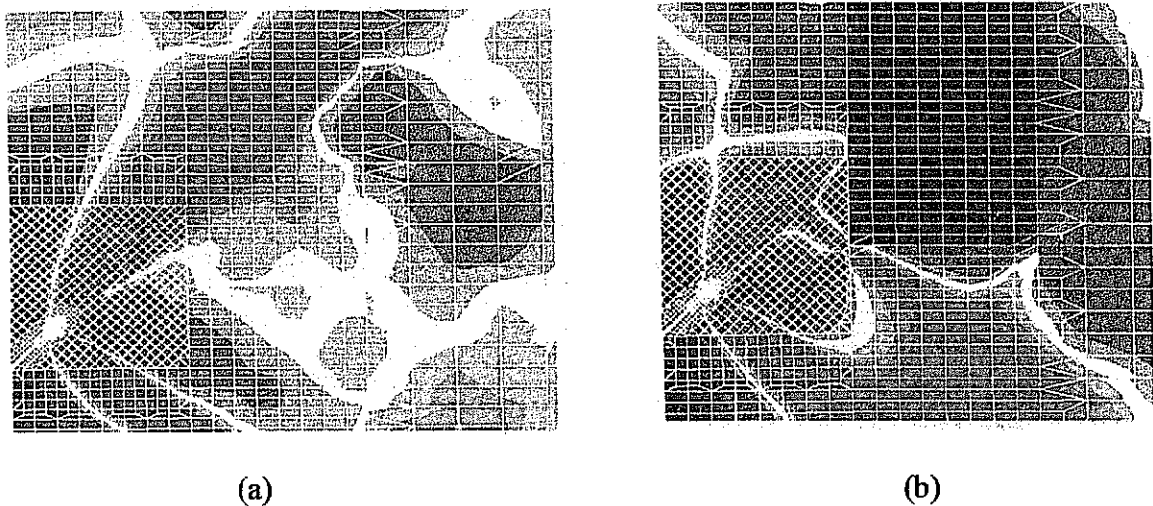


Figure IV.6 Contour plots of effective plastic strain for an applied tensile strain of $0.7 \epsilon_y$ for (a) single slip and (b) conjugate slip in Table IV.1a, $a/d = 0.25$; the peak strain intensity has a threshold of 1% plastic strain, which is at least twice the polycrystal average applied strain.

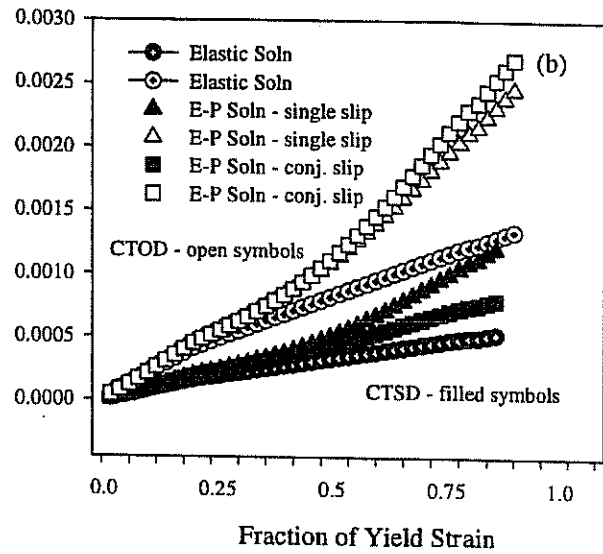
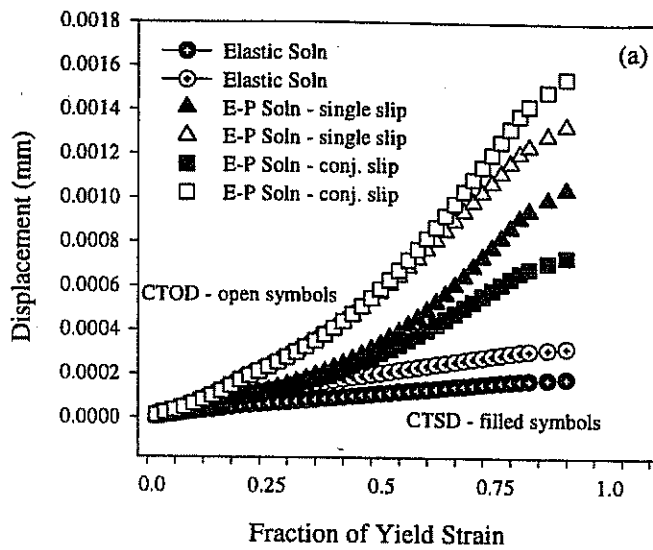


Figure IV.7 CTSD and CTOD as a function of applied polycrystal tensile strain for a surface crack ($a/d = 0.5$) in a favorably oriented grain with a range of nearest neighbor grain (Grain A) orientations given in Table IV.1a, evaluated (a) 2 μm and (b) 25 μm behind the crack tip.

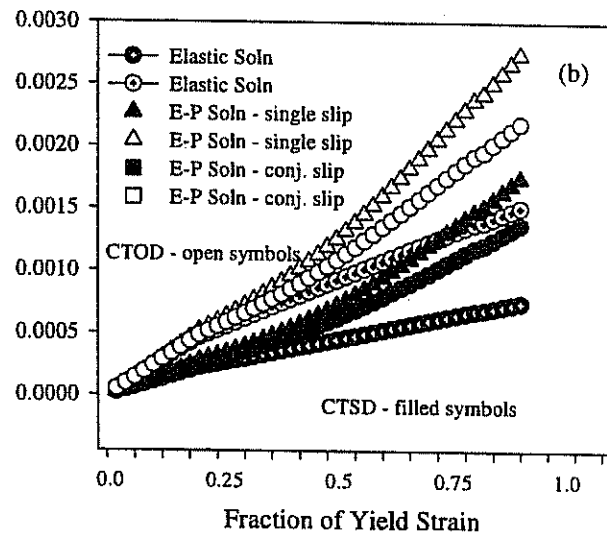
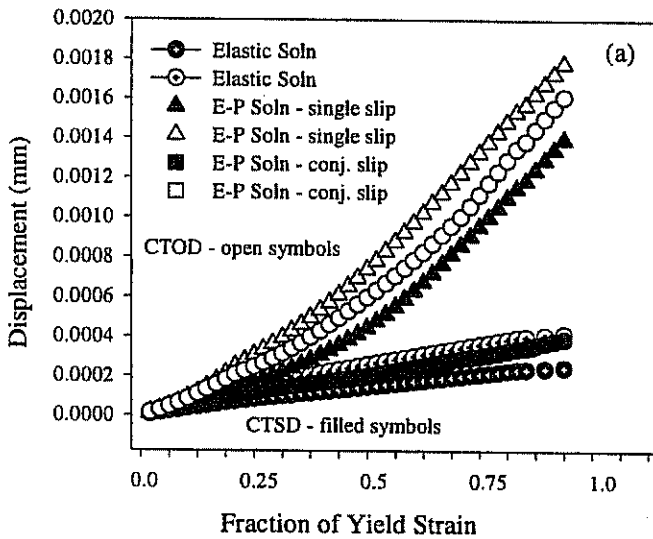


Figure IV.8 CTSD and CTOD as a function of applied polycrystal tensile strain for a surface crack ($a/d = 0.97$) in a favorably oriented grain with a range of nearest neighbor grain (Grain A) orientations given in Table IV.1a, evaluated (a) 2 μm and (b) 25 μm behind the crack tip.

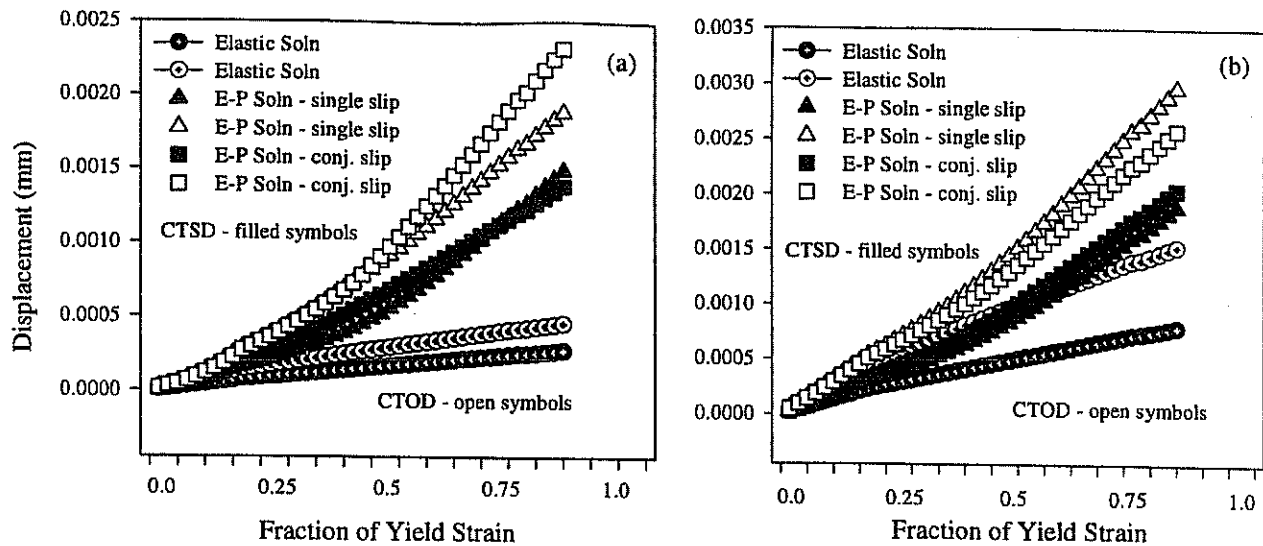


Figure IV.9 CTSD and CTOD as a function of applied polycrystal tensile strain for a surface crack ($a/d = 1.25$) in a favorably oriented grain with a range of nearest neighbor (Grain A) orientations evaluated (a) $2 \mu\text{m}$ and (b) $25 \mu\text{m}$ behind the crack tip.

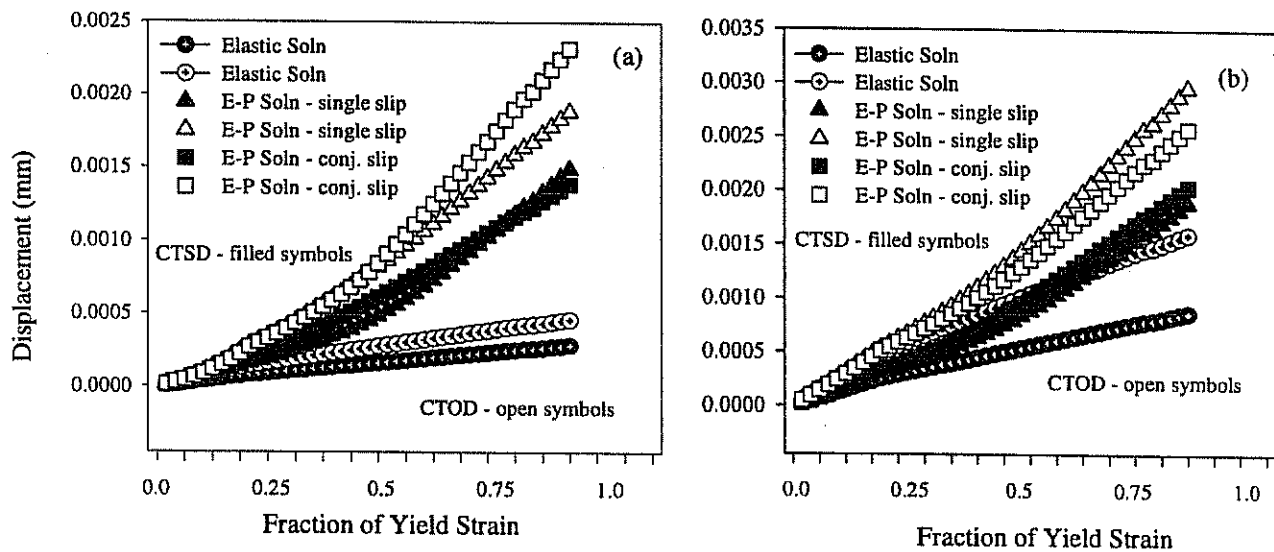


Figure IV.10 CTSD and CTOD as a function of applied polycrystal tensile strain for a surface crack ($a/d = 1.97$) in a favorably oriented grain with a range of nearest neighbor (Grain A) orientations evaluated (a) $2 \mu\text{m}$ and (b) $25 \mu\text{m}$ behind the crack tip.

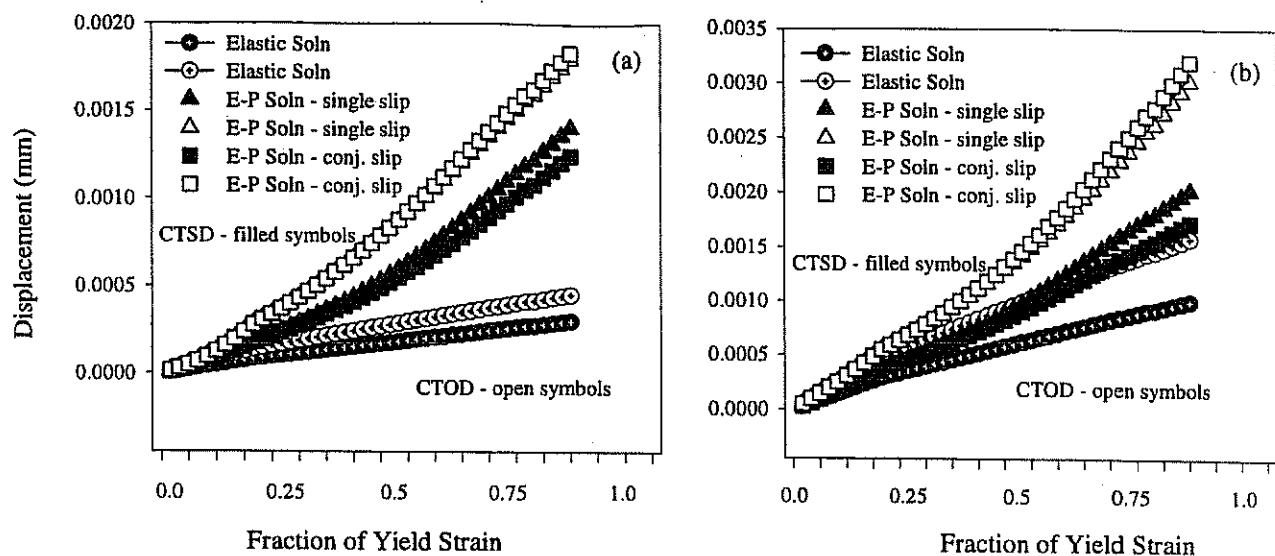
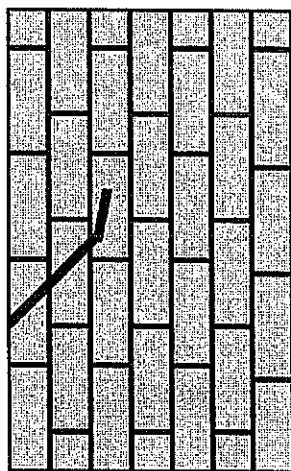
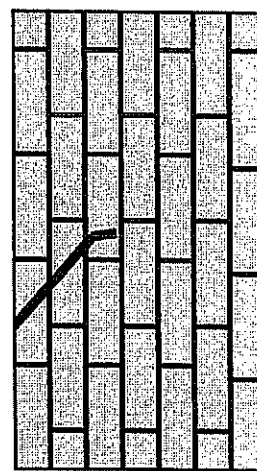


Figure IV.11 CTSD and CTOD as a function of applied polycrystal tensile strain for a surface crack ($a/d = 2.5$) in a favorably oriented grain with a range of nearest neighbor (Grain A) orientations evaluated (a) 2 μm and (b) 25 μm behind the crack tip.



Kinked-up (KU) crack



Kinked-down (KD) crack

Figure IV.12 Schematic of kinked-up (KU) and kinked-down (KD) crack configurations.

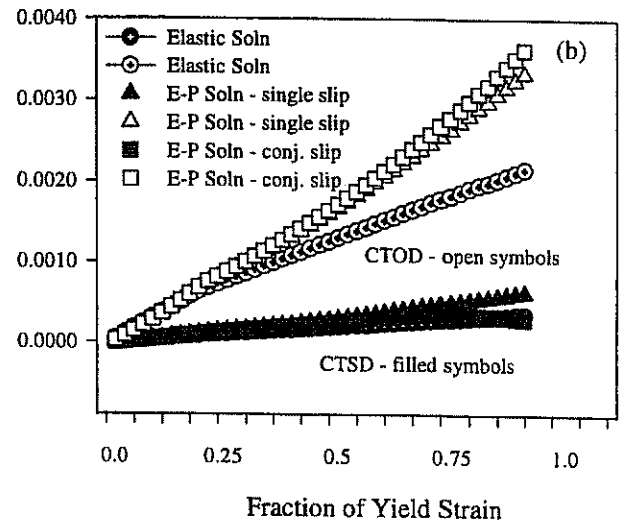
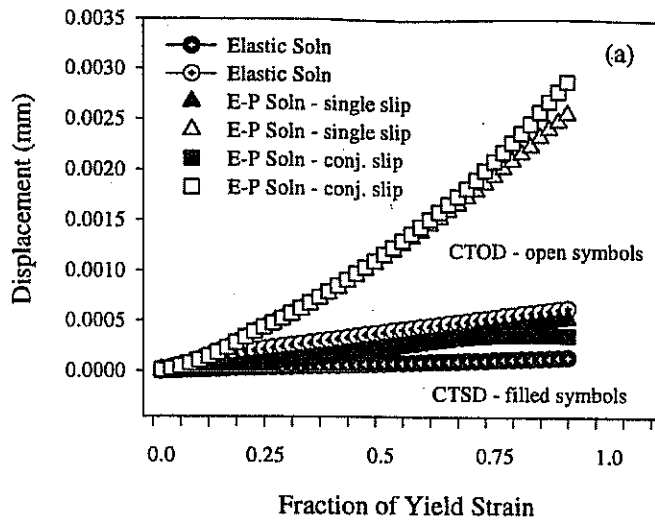


Figure IV.13 CTSD and CTOD as a function of applied polycrystal tensile strain for a surface crack ($a/d = 2.5$ - KD) in a favorably oriented grain with a range of nearest neighbor (Grain A) orientations evaluated (a) $2 \mu\text{m}$ and (b) $25 \mu\text{m}$ behind the crack tip.

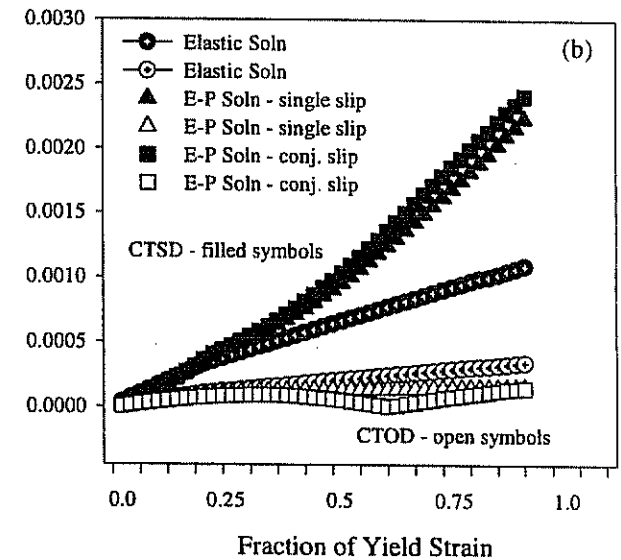
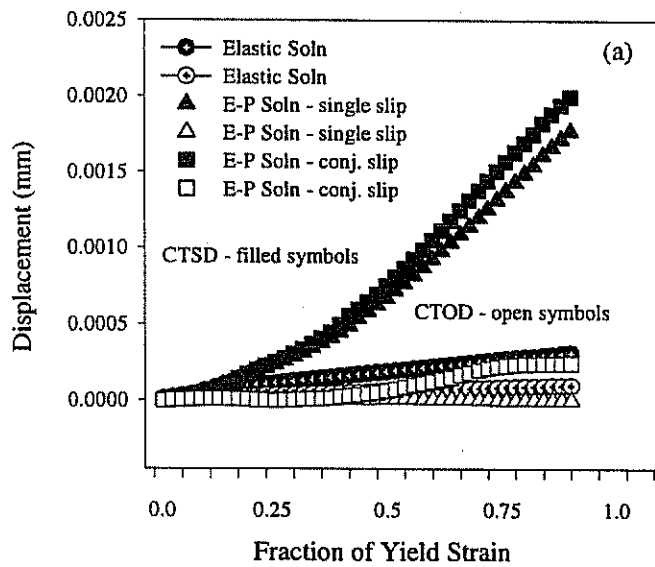


Figure IV.14 CTSD and CTOD as a function of applied polycrystal tensile strain for a surface crack ($a/d = 2.5$ - KU) in a favorably oriented grain with a range of nearest neighbor (Grain A) orientations evaluated (a) $2 \mu\text{m}$ and (b) $25 \mu\text{m}$ behind the crack tip.

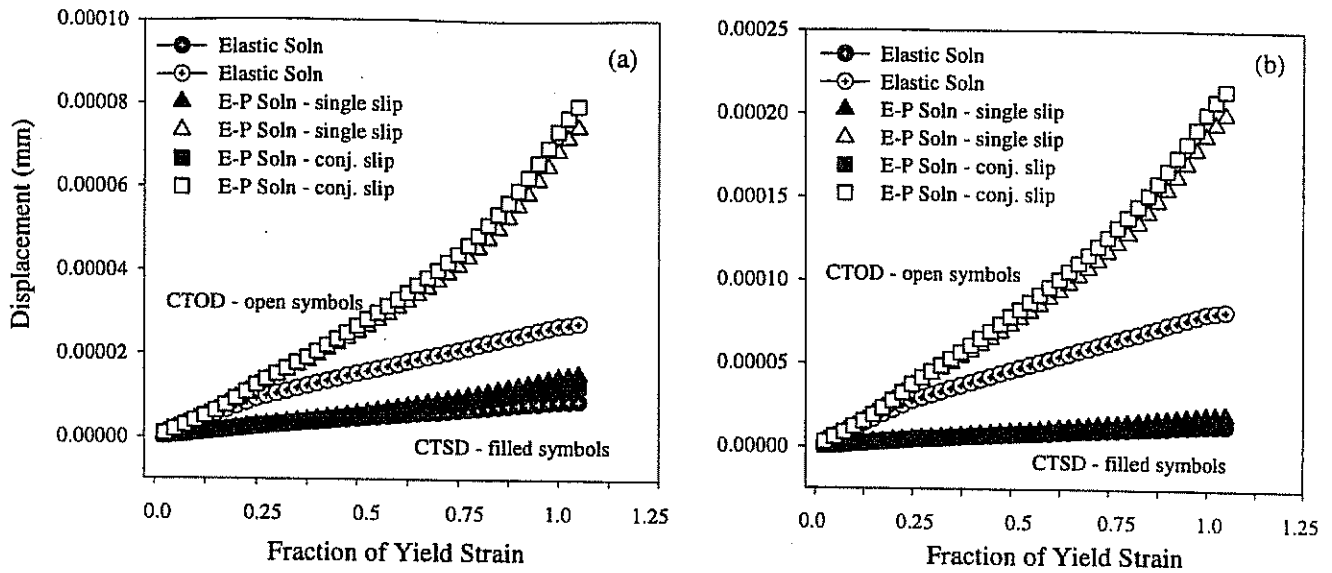


Figure IV.15 CTSD and CTOD as a function of applied polycrystal shear strain for a surface crack ($a/d = 0.25$) in a favorably oriented grain with a range of nearest neighbor (Grain A) orientations evaluated (a) $2 \mu\text{m}$ and (b) $18 \mu\text{m}$ behind the crack tip.

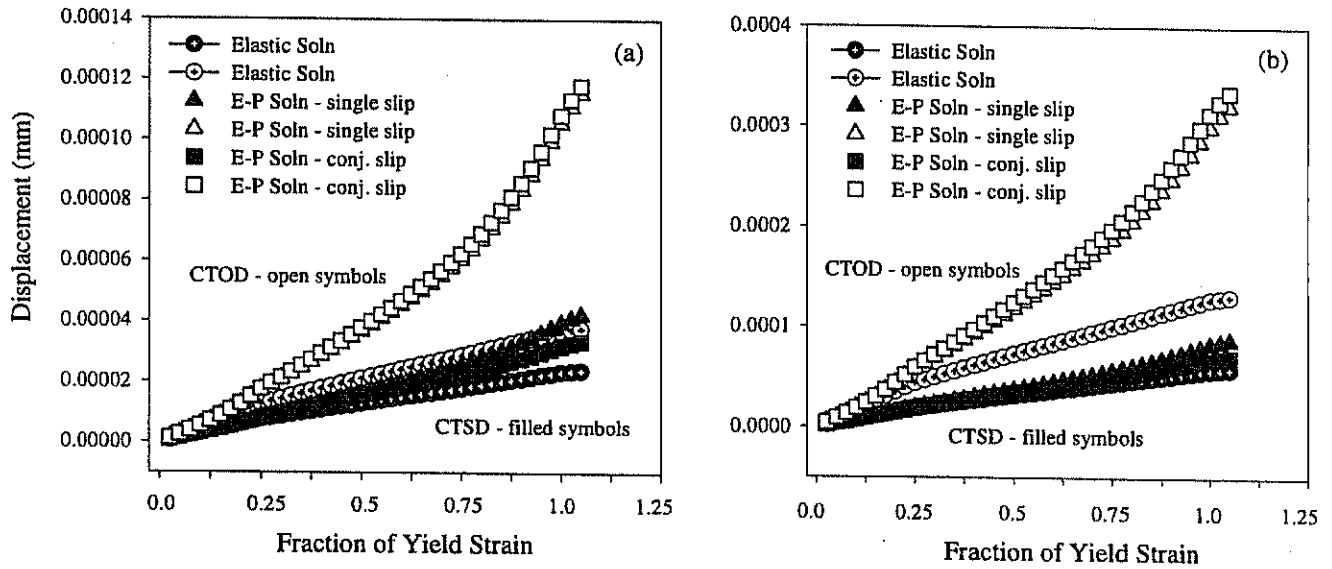
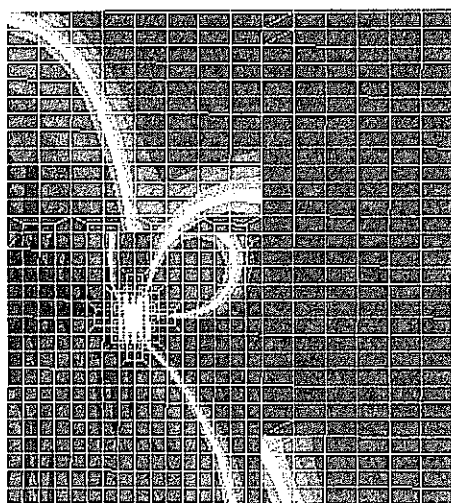
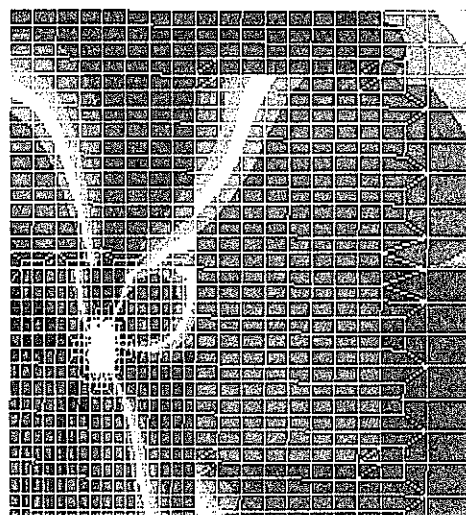


Figure IV.16 CTSD and CTOD as a function of applied polycrystal shear strain for a surface crack ($a/d = 0.5$) in a favorably oriented grain with a range of nearest neighbor (Grain A) orientations evaluated (a) $2 \mu\text{m}$ and (b) $25 \mu\text{m}$ behind the crack tip.



(a)



(b)

Figure IV.17 Contour plots of effective plastic strain for an applied shear strain of $0.9 \gamma_y$ for the two cases in Table IV.1b, $a/d = 0.5$; peak strain intensity has a threshold of 0.5% plastic strain for (a) single slip and (b) conjugate slip in the adjacent grain.

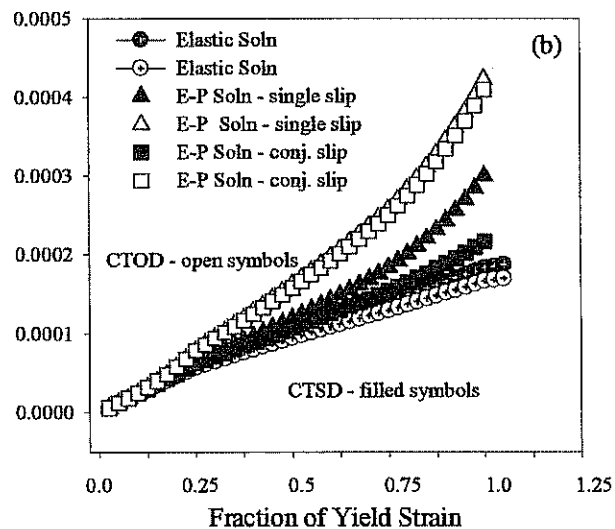
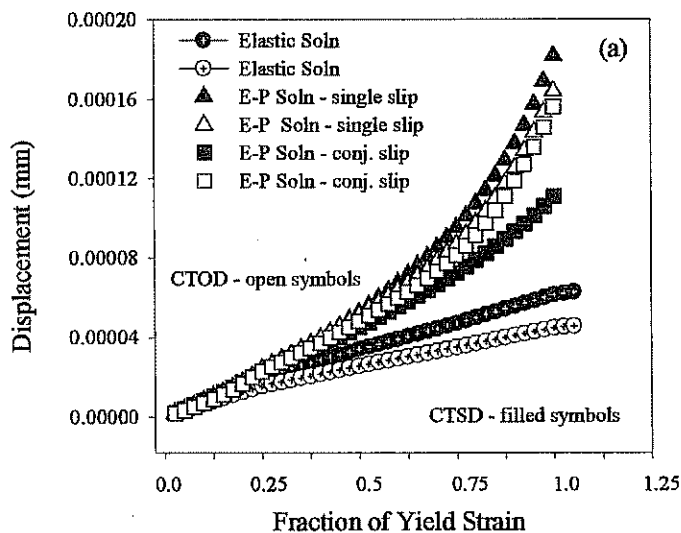


Figure IV.18 CTSD and CTOD as a function of applied polycrystal shear strain for a surface crack ($a/d = 0.97$) in a favorably oriented grain with a range of nearest neighbor (Grain A) orientations evaluated (a) $2 \mu\text{m}$ and (b) $25 \mu\text{m}$ behind the crack tip.

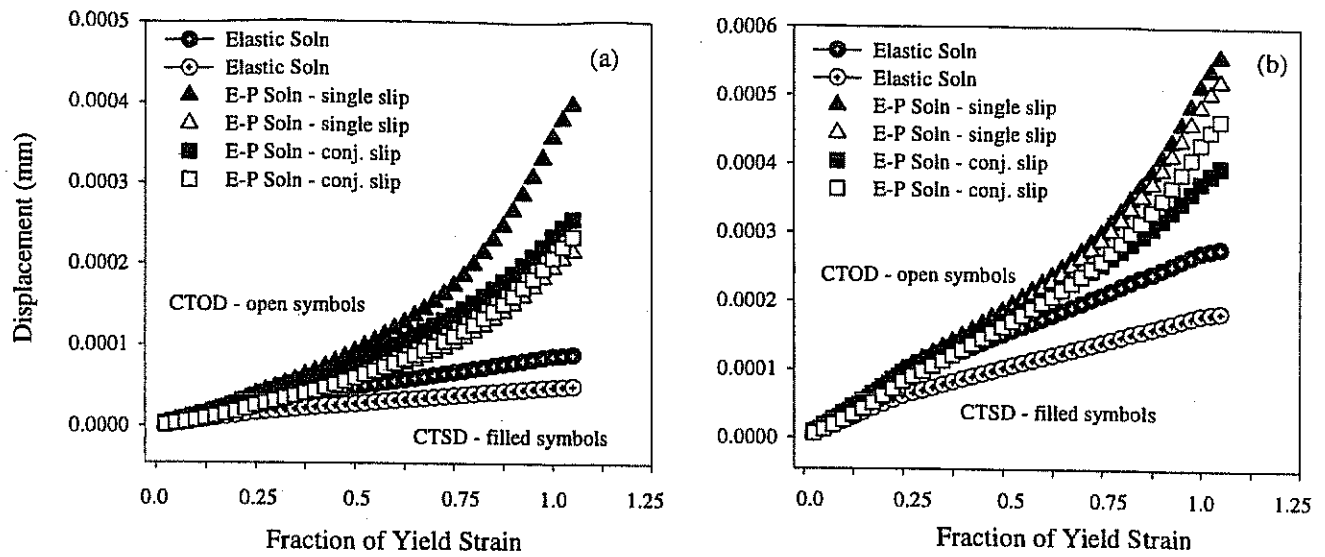


Figure IV.19 CTSD and CTOD as a function of applied polycrystal shear strain for a surface crack ($a/d = 1.25$) in a favorably oriented grain with a range of nearest neighbor (Grain A) orientations evaluated (a) $2\ \mu\text{m}$ and (b) $25\ \mu\text{m}$ behind the crack tip.

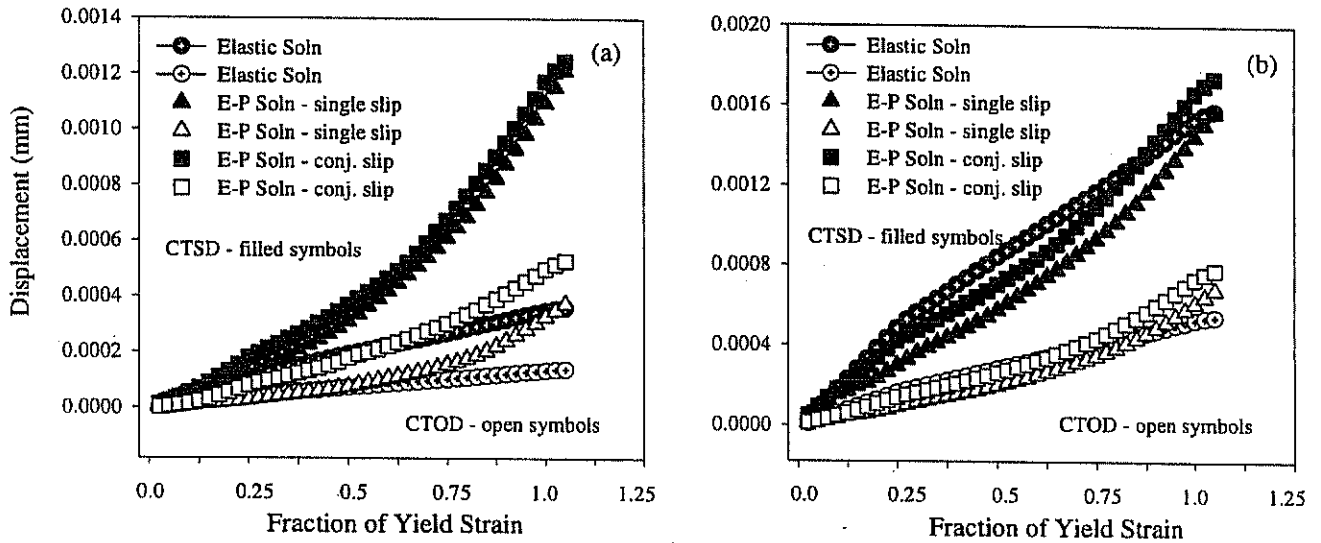


Figure IV.20 CTSD and CTOD as a function of applied polycrystal shear strain for a surface crack ($a/d = 1.97$) in a favorably oriented grain with a range of nearest neighbor (Grain A) orientations evaluated (a) $2\ \mu\text{m}$ and (b) $25\ \mu\text{m}$ behind the crack tip.

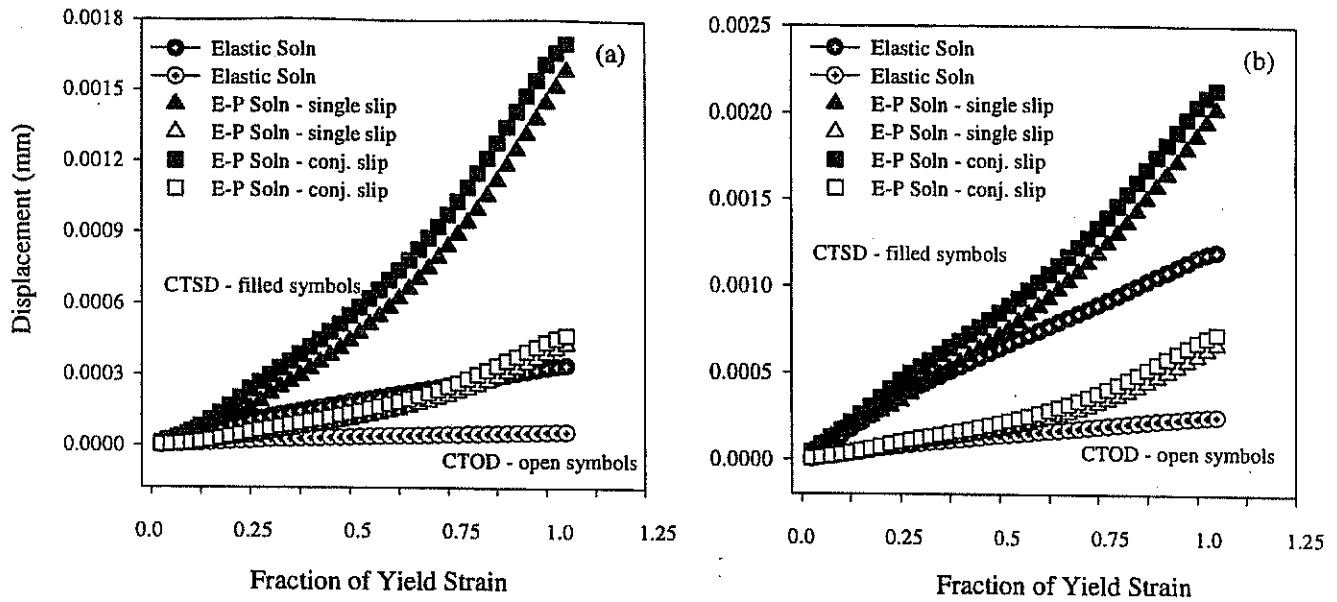


Figure IV.21 CTSD and CTOD as a function of applied polycrystal shear strain for a surface crack ($a/d = 2.5$) in a favorably oriented grain with a range of nearest neighbor (Grain A) orientations evaluated (a) 2 μm and (b) 25 μm behind the crack tip.

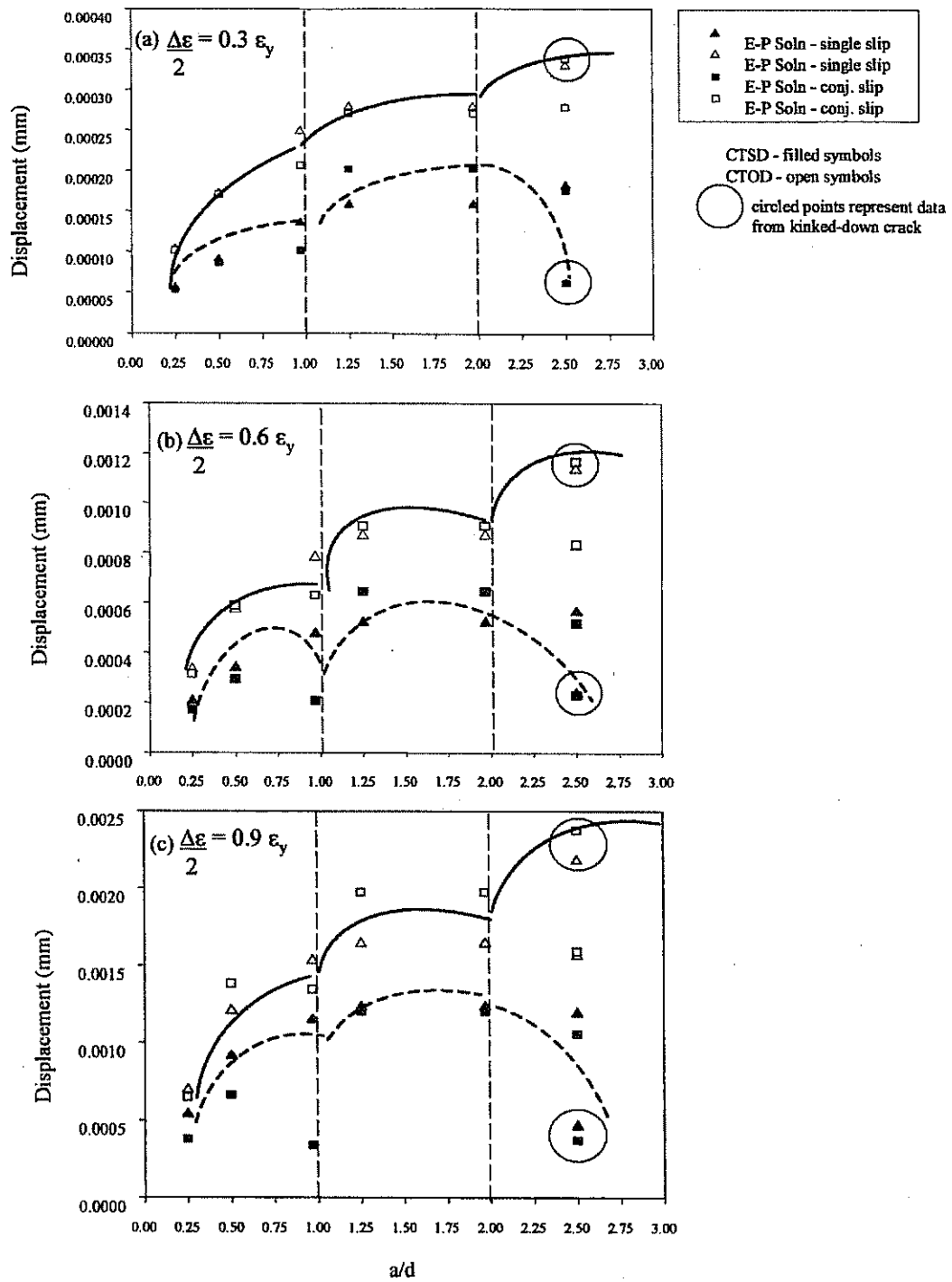


Figure IV.22 CTSD and CTOD for remote tensile loading case as a function of crack length ratio at $2 \mu\text{m}$ behind the crack tip for strain amplitudes of (a) $0.3 \epsilon_y$, (b) $0.6 \epsilon_y$, and (c) $0.9 \epsilon_y$.

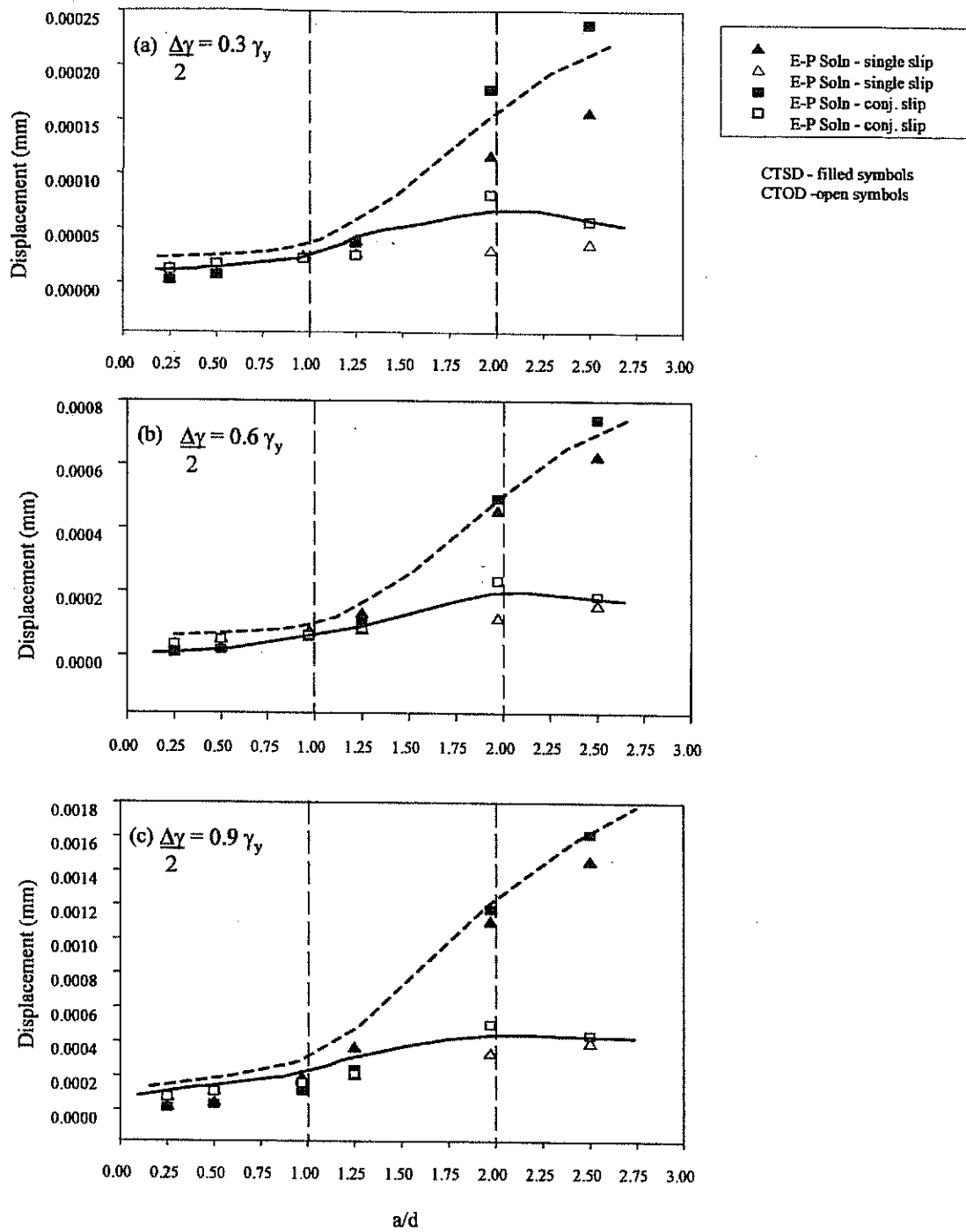


Figure IV.23 CTSD and CTOD for remote shear loading case as a function of crack length ratio at 2 μ m behind the crack tip for strain amplitudes of (a) $0.3\gamma_y$, (b) $0.6\gamma_y$, and (c) $0.9\gamma_y$.

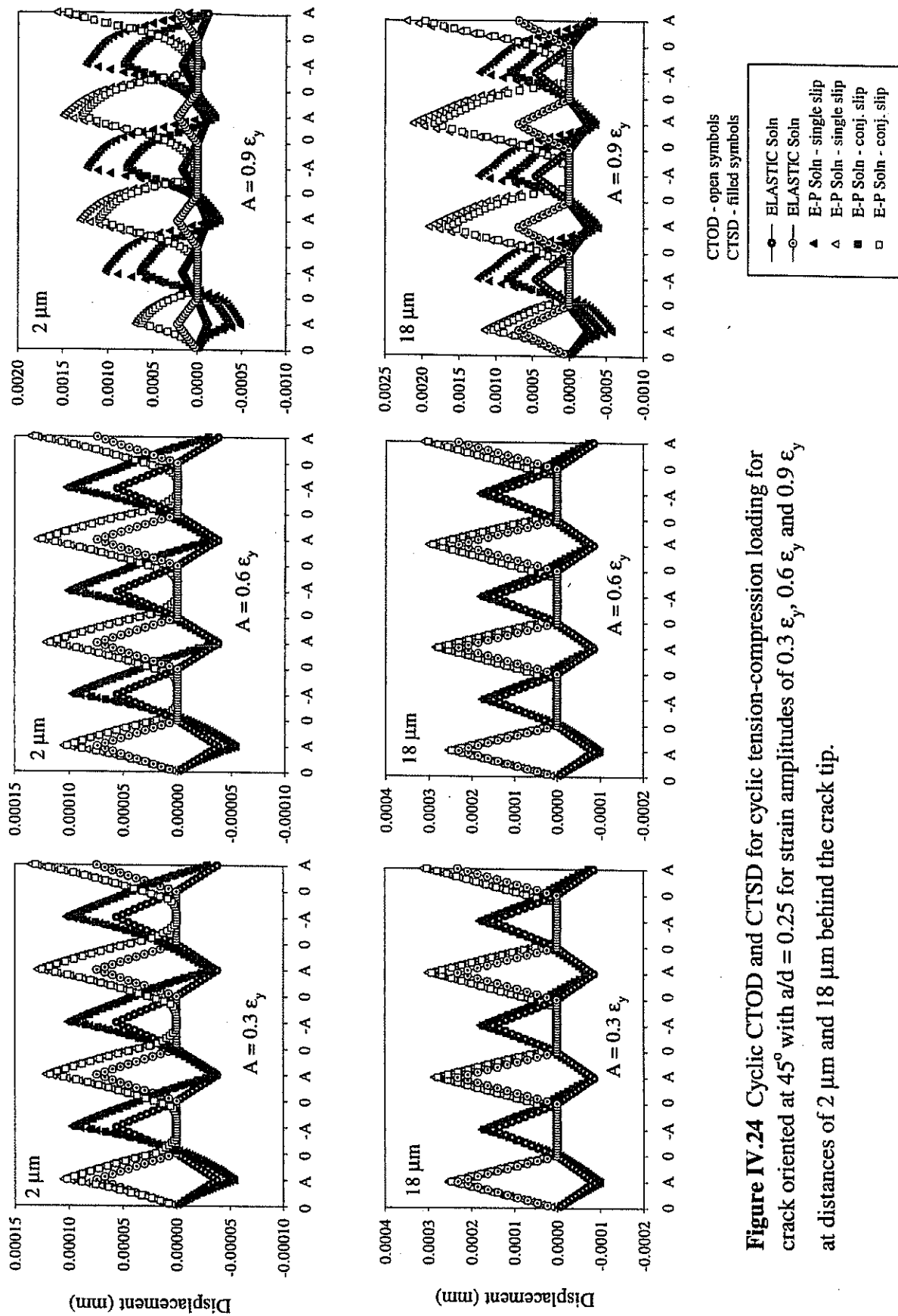


Figure IV.24 Cyclic CTOD and CTSD for cyclic tension-compression loading for crack oriented at 45° with $a/d = 0.25$ for strain amplitudes of $0.3 \epsilon_y$, $0.6 \epsilon_y$ and $0.9 \epsilon_y$ at distances of $2 \mu\text{m}$ and $18 \mu\text{m}$ behind the crack tip.

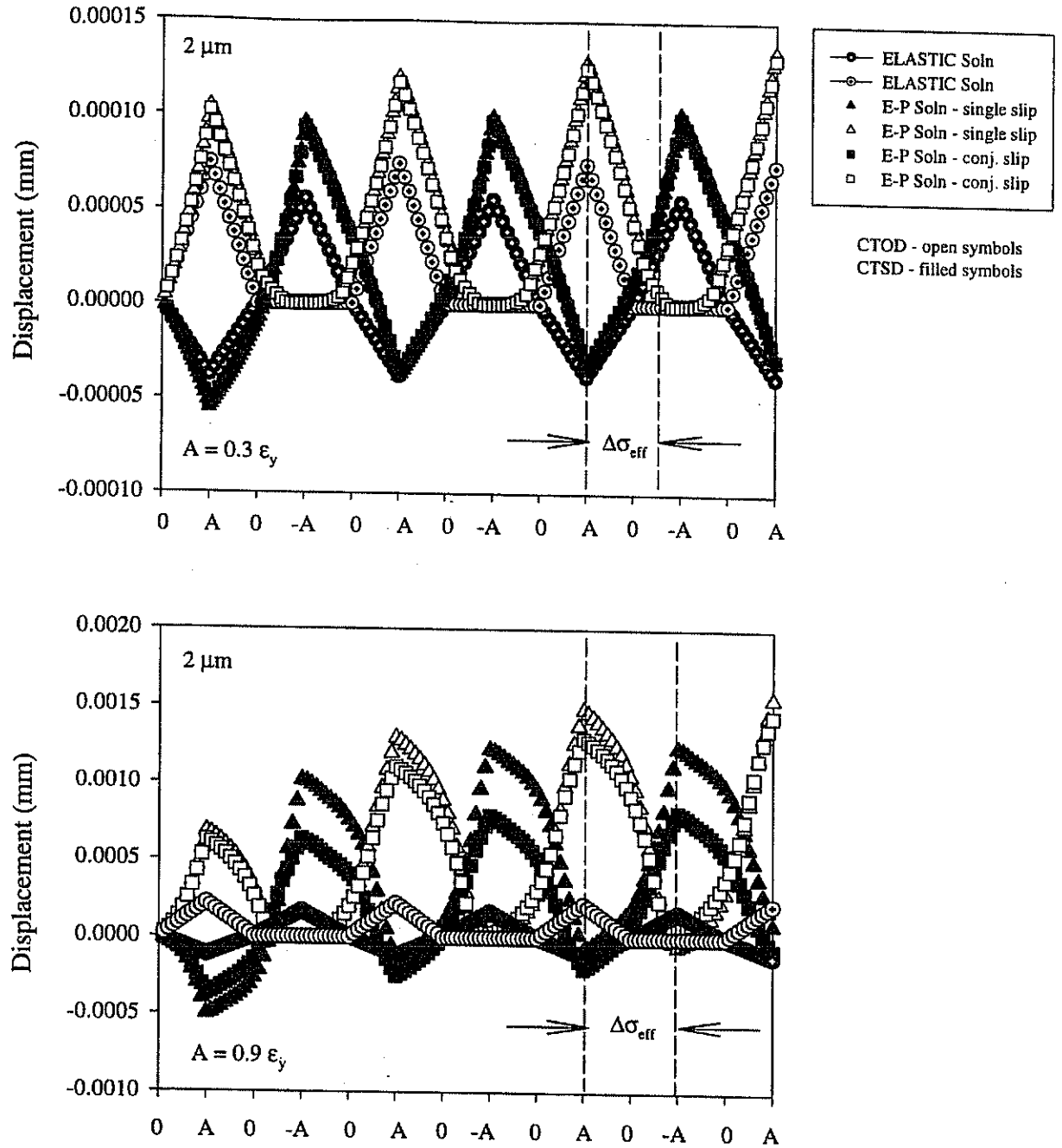


Figure IV.25 Cyclic CTOD and CTSD for cyclic tension-compression loading for crack oriented at 45° with $a/d = 0.25$ for strain amplitudes of $0.3 \epsilon_y$ and $0.9 \epsilon_y$ at a distance of $2 \mu\text{m}$ behind the crack tip showing the differences in the effective stress amplitude, $\Delta\sigma_{\text{eff}}$, due to plasticity-induced closure effects.

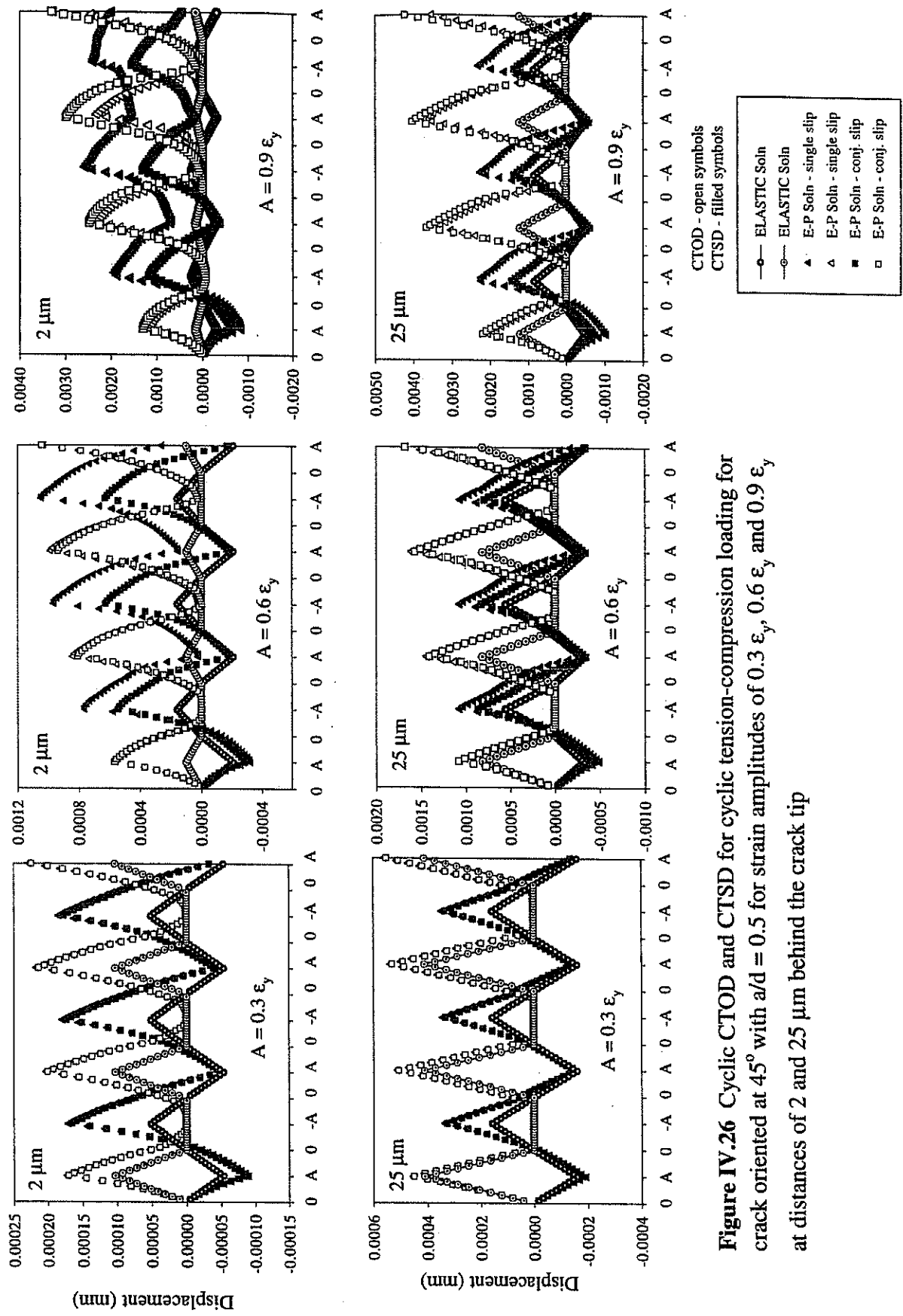
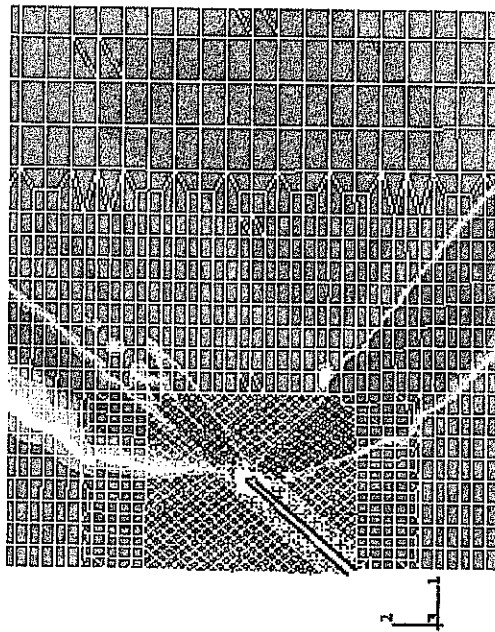
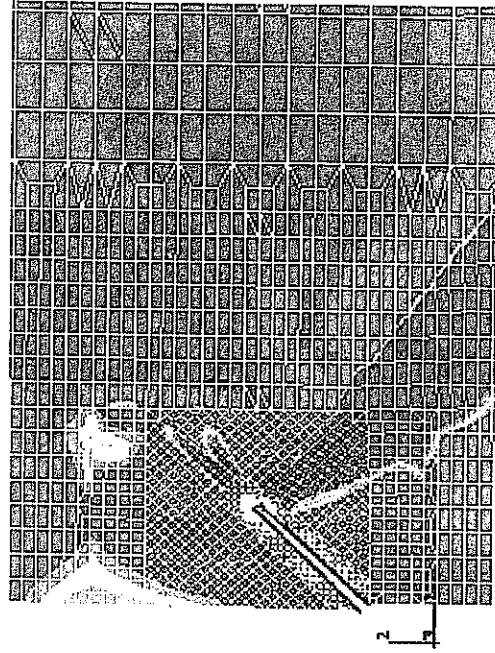


Figure IV.26 Cyclic CTOD and CTSD for cyclic tension-compression loading for crack oriented at 45° with $a/d = 0.5$ for strain amplitudes of $0.3 \epsilon_y$, $0.6 \epsilon_y$ and $0.9 \epsilon_y$ at distances of 2 and $25 \mu\text{m}$ behind the crack tip



(a)



(b)

Figure IV.27 Contour plots of effective plastic strain for a cyclic tension-compression with tensile strain of $0.9 \epsilon_y$ for the two cases, (a) single slip and (b) conjugate slip for $a/d = 0.5$; the peak strain intensity has a threshold of 1% plastic strain after 3 cycles and at the maximum load.

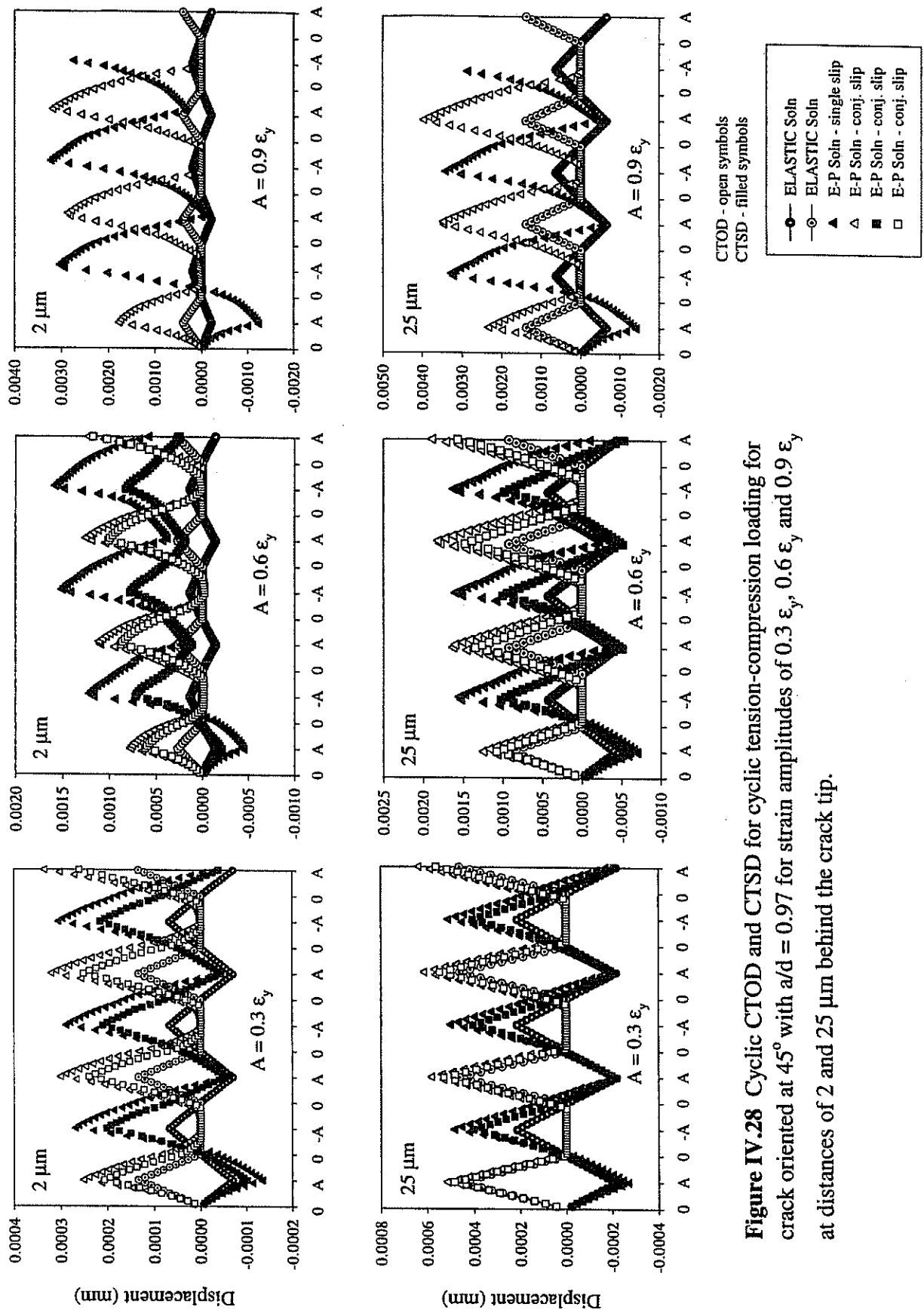


Figure IV.28 Cyclic CTOD and CTSD for cyclic tension-compression loading for crack oriented at 45° with $a/d = 0.97$ for strain amplitudes of $0.3 \epsilon_y$, $0.6 \epsilon_y$ and $0.9 \epsilon_y$ at distances of 2 and 25 μm behind the crack tip.

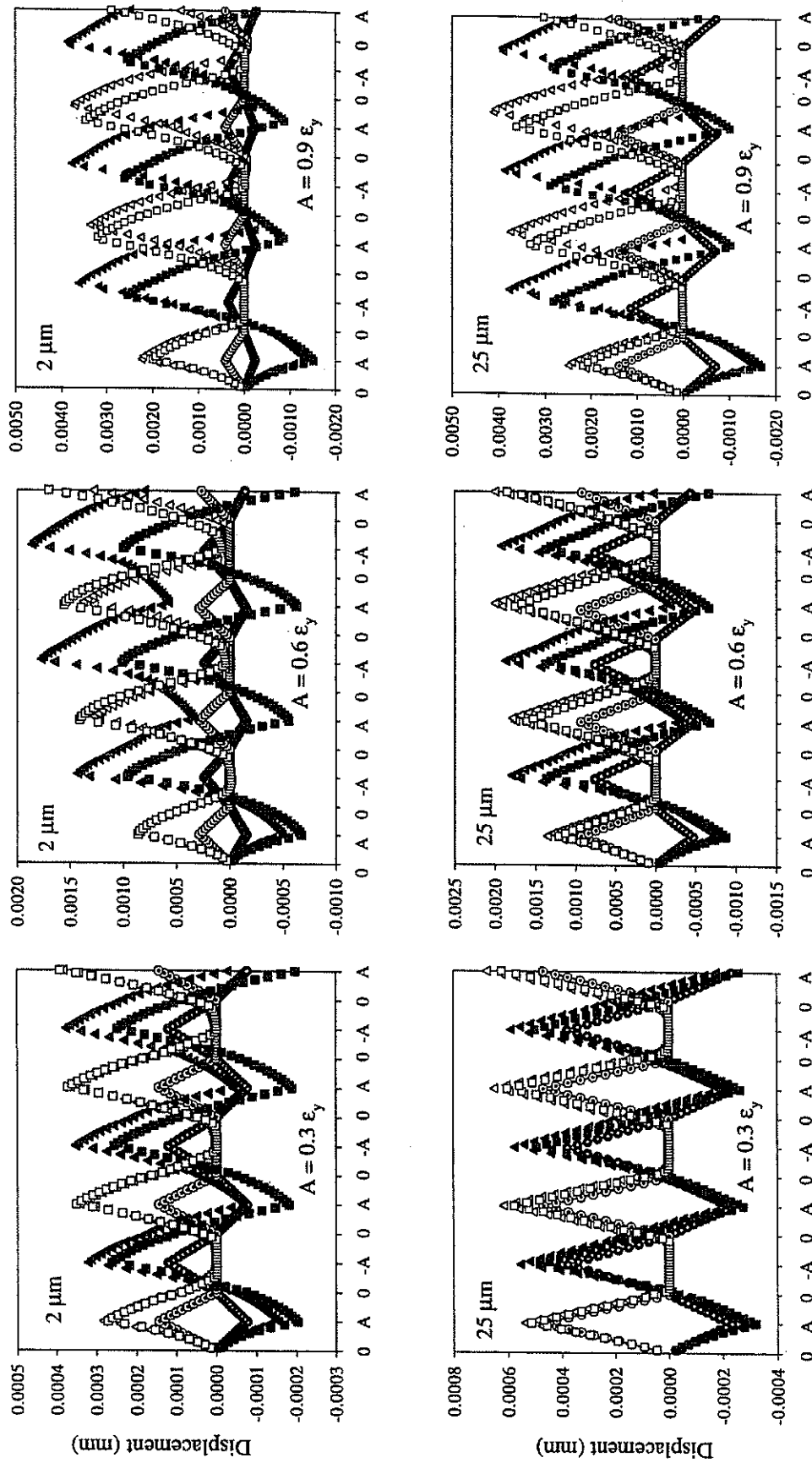


Figure IV.29 Cyclic CTOD and CTSD for cyclic tension-compression loading for crack oriented at 45° with $a/d = 1.25$ for strain amplitudes of $0.3 \epsilon_y$, $0.6 \epsilon_y$ and $0.9 \epsilon_y$ at distances of 2 and 25 μm behind the crack tip.

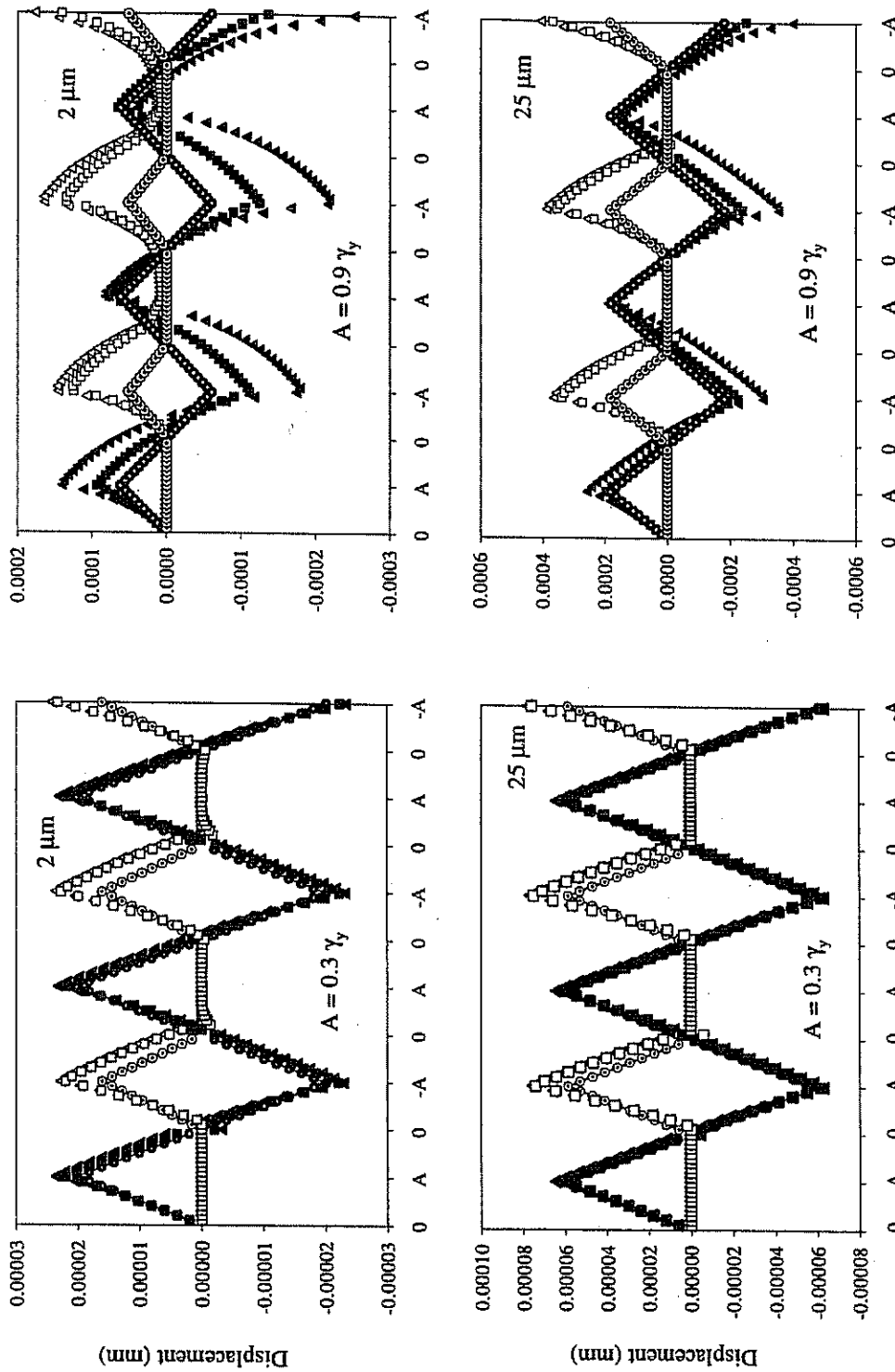
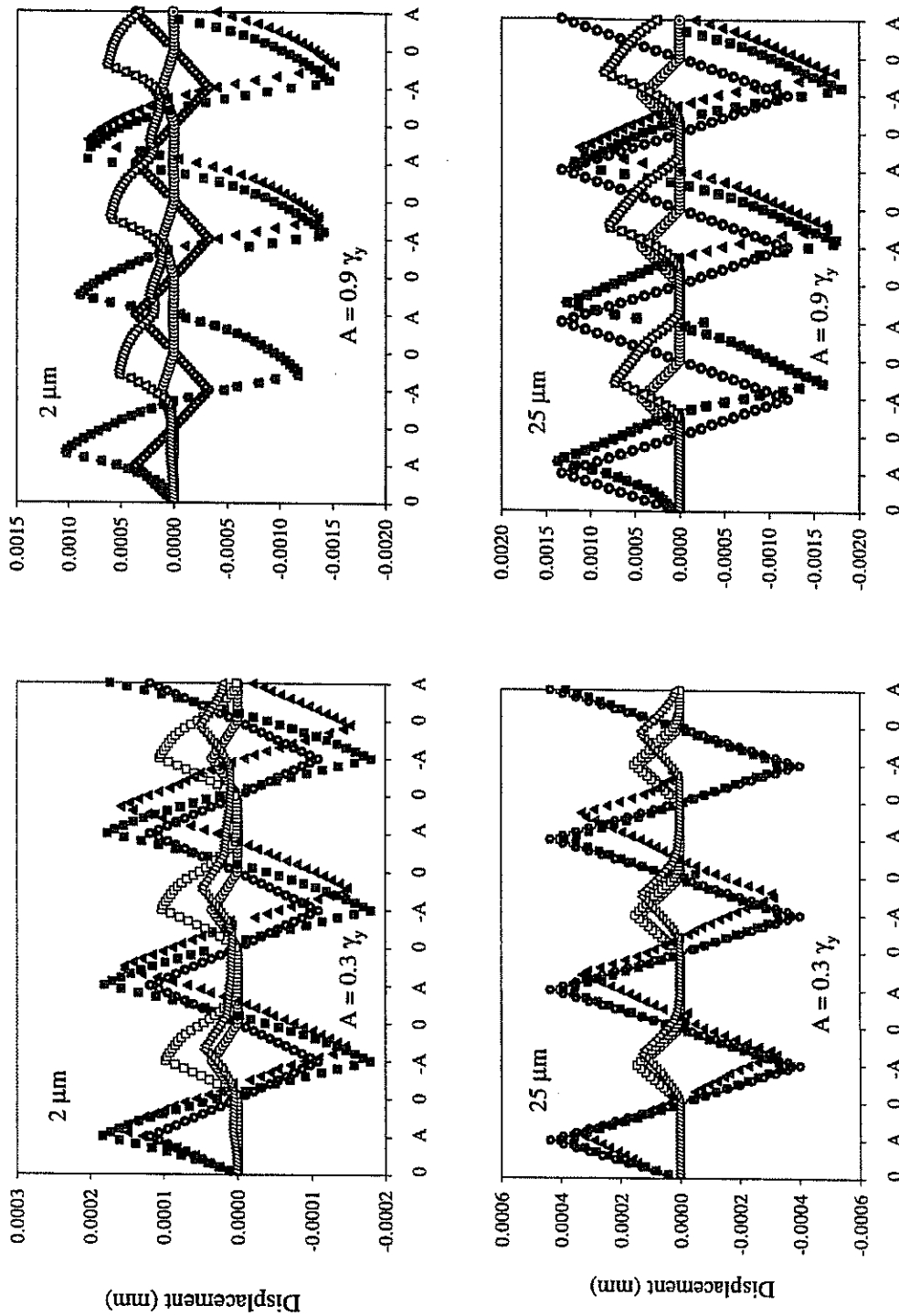


Figure IV.31 Cyclic CTOD and CTSD for cyclic shear loading for crack oriented at 90° with respect to the tensile axis with $a/d = 0.97$ for strain amplitudes of $0.3 \gamma_y$ and $0.9 \gamma_y$ at distances of 2 and 25 μm behind the crack tip.



CTOD - open symbols
CTSD - filled symbols

—○— ELASTIC Soln
—●— ELASTIC Soln
■ E-P Soln - conj. slip
□ E-P Soln - conj. slip
▲ E-P Soln - single slip
△ E-P Soln - single slip

Figure IV.32 Cyclic CTOD and CTSD for cyclic shear loading for crack oriented at 90° with respect to the tensile axis with $a/d = 1.97$ for strain amplitudes of $0.3 \gamma_y$ and $0.9 \gamma_y$ at distances of 2 and 25 μm behind the crack tip.

Table IV.1a: Assignment of Nearest-Neighbor Grain Misorientation for Remote Tension-Compression

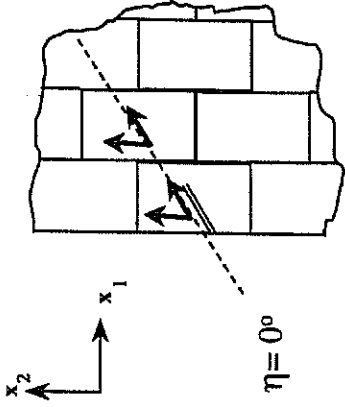
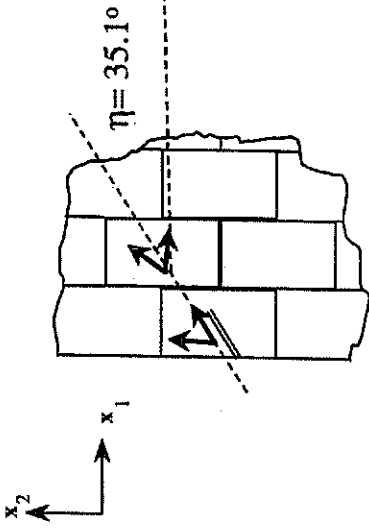
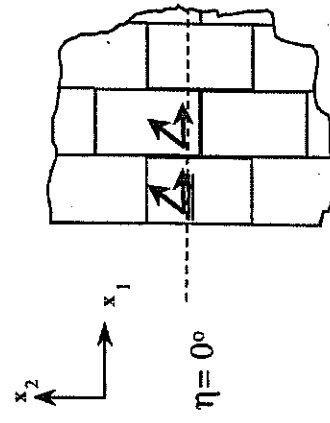
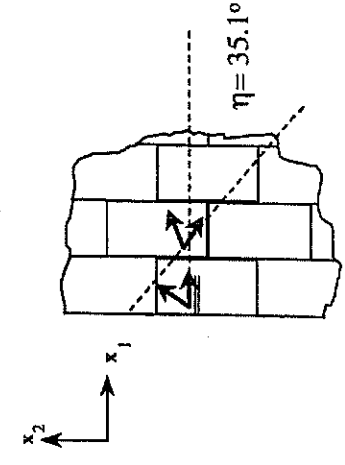
θ_1 : Orientation of Grain with Crack (degrees)	θ_2 : Bisector Orientation of Grain A (Adjacent to Crack) (degrees)	η : Minimum Misorientation (degrees)	Schematic of surface grains and orientations of adjacent grains
9.9	9.9 (single slip)	0	 <p>$\eta = 0^\circ$</p>
9.9	45 (conjugate slip)	35.1	 <p>$\eta = 35.1^\circ$</p>

Table IV.1b: Assignment of Nearest-Neighbor Grain Misorientation for Remote Shear

θ_1 : Orientation of Grain with Crack (degrees)	θ_2 : Bisector Orientation of Grain A (Adjacent to Crack) (degrees)	η : Minimum Misorientation (degrees)	Schematic of surface grains and orientations of adjacent grains
35.1	35.1 (single slip)	0	 <p>$\eta = 0^\circ$</p>
35.1	0 (conjugate slip)	35.1	 <p>$\eta = 35.1^\circ$</p>

CHAPTER V

IMPLICATIONS FOR SMALL CRACK GROWTH MODELS

This Chapter considers the micromechanical computations presented in Chapters III and IV and draws implications for more specific dependencies in small crack growth models. The uncracked polycrystal analyses (as presented in Chapter III) are used to address shakedown of cyclic microplasticity and nonpropagating crack threshold or limits. The micromechanical calculations for embedded cracks, although 2-D in nature, provide a means to qualitatively understand the nature of the mode-mixity observed in small fatigue cracks as a function of amplitude, stress-state, and crack length. In addition, first order effects studied in this work - periodic barrier interactions and lack of constraint due to the surface - are utilized to assist in suggesting improved models for small fatigue crack growth. The micromechanical computations provide insight into various aspects of heterogeneous microplasticity and small crack growth behavior that is not attainable by macroscopic observation. In addition, interpretations are given on the relationships of the sliding and opening displacements to crack length ratio, stress state and amplitude.

V.1 Shakedown Limits for Cyclic Microplasticity

Shakedown refers to the stress or strain level below which there is either a cessation (elastic shakedown) or stabilization (elastic-plastic shakedown) of the accumulation of cyclic microplasticity upon subsequent cycling. Elastic shakedown limits are important quantities because they have a close relationship to nonpropagating crack limits for small cracks. Study of shakedown requires examination of the relationship between the macroscopically applied stress and the local plasticity on the slip (micro) system. It is also important to compare the level of microplasticity with the average plastic strain of the aggregate.

For cyclic tension-compression and cyclic shear, the polycrystal model used in Chapter III was employed. As in Chapter III, cyclic tension-compression and cyclic shear loading was applied at several fractions of the yield strain (30%, 50%, 70%, 90%, in addition to 200%). Figure V.1 shows the relationship between the maximum shear stress amplitude (averaged over all grains) and the amplitude of plastic shear strain quantities for both loading cases. Figure V.1 reveals that the separation between the local maximum slip system shear strain (maximum among all grains) and the average maximum plastic shear strain (averaged over all grains) occurs at a higher maximum average shear stress level for tension-compression as compared to cyclic shear. Trend lines are also drawn which show the relative differences in the local and macroscopic shear strain levels. For both cyclic tension-compression and cyclic shear, there is a

definite nonlinear relationship (even more so for cyclic tension-compression) between the maximum shear stress amplitude (averaged over all grains) and the amplitude of both plastic shear strain quantities considered. This Figure seems to indicate that elastic shakedown of cyclic microplasticity occurs in cyclic shear at a lower maximum shear stress level (≈ 160 MPa) as compared to cyclic tension-compression (≈ 300 MPa). The applied strain amplitude that corresponds to this level for cyclic tension-compression is approximately $0.4 \epsilon_y$ (≈ 0.0026); this strain value is close to the smooth specimen fatigue limit in terms of strain for 4340 Steel (≈ 0.00274) (137).

In Figure V.2 (log scale), three measures of the shear strain are shown - the amplitude of the maximum plastic shear strain on the slip system (among all grains), the amplitude of the maximum plastic shear strain (averaged over all grains), and the amplitude of the maximum shear strain (averaged over all grains). Two features of these plots are discussed as well as the significance for determining shakedown limits. One feature is the difference in the intensification (denoted by I on Figures V.2a and V.2b) of the maximum plastic shear strain on a slip system and the maximum plastic shear strain amplitude for both loading cases. For cyclic tension-compression, the amplitude of the maximum plastic shear strain on the slip system is about 2 times higher than the average plastic shear strain amplitude for all shear stress amplitudes; for cyclic shear, the intensification ranges from 4 to 6. The intensification is a measure of enhanced local microplasticity as compared to the average bulk plastic shear strain. One possible explanation of the higher density of microcracks for cyclic shear as compared to cyclic

tension-compression is this rather higher degree of intensification at the local level. This could not be predicted using traditional macroscale cyclic plasticity models.

A second observation is the difference in the intersection of the macroscopic average shear strain and micro plastic shear strain amplitudes. For cyclic tension-compression, the intersection occurs at a maximum shear stress range of approximately 420 MPa, whereas for cyclic shear, the intersection occurs at 220 MPa. Both of these intersection points correspond to an applied strain amplitude of 90% of the cyclic yield strains for each loading cases. Table V.1 summarizes the strain levels and shear stress levels which are representative of the elastic shakedown limit and fully plastic limits of cyclic microplasticity. The elastic shakedown values for microplastic strain can be argued to correspond to one type of smooth specimen fatigue limit, i.e. lack of sufficient inelastic driving force to either nucleate cracks or possibly grow them within grains.

V.2 Evaluation of $\Delta CTSD/CTOD$, ΔCTD , $\Delta CTSD/\Delta CTOD$, and $\Delta CTOD$

After examining the uncracked polycrystalline aggregate to determine shakedown limits of cyclic microplasticity, it is important to next evaluate quantities which are directly related to the behavior at the crack tip and how amplitude, crack length ratio, and stress state play a role in that behavior. The analyses in Chapter IV provide the basis for these evaluations to shed light on the driving force parameter for small crack lengths ($a/d < 2$).

V.2.1 Ratio of | CTSD/CTOD |

For cyclic tension-compression, the ratio of | CTSD/CTOD | defined as R_{cc} is plotted for a/d ratios of 0.25, 0.5, 0.97, 1.25, and 1.97 (for amplitudes of $0.3 \epsilon_y$, $0.6 \epsilon_y$, and $0.9 \epsilon_y$); for cyclic shear loading, R_{cc} is plotted for a/d ratios of 0.25, 0.97, and 1.97 (for amplitudes of $0.3 \gamma_y$ and $0.9 \gamma_y$). For both loading cases, both the single and conjugate slip cases as well as the elastic solutions are also provided to show the relative differences as compared to the micromechanical solutions. The R_{cc} ratio is primarily shown for either the maximum or minimum amplitudes of the loading cycles.

V.2.1.1 Cyclic Tension-Compression

Figure V.3 ($a/d = 0.25$) shows that for the first cycle, the elastic solution and the crystal plasticity micromechanical solutions have quite comparable values for R_{cc} for all strain amplitudes, whereas for subsequent cycling, the ratios are quite distinct. Note that the “A” on the x-axis in these figures denotes the applied strain amplitude. For $a/d = 0.5$ in Figure V.4, amplitude and orientation dependencies are reflected in the R_{cc} at the two higher strain amplitudes ($0.6 \epsilon_y$ and $0.9 \epsilon_y$). The lowest strain amplitude of $0.3 \epsilon_y$ shows a similar result as for $a/d = 0.25$. Also note the differences in the R_{cc} for the single and conjugate slip cases. As discussed in Chapter IV, the single slip case promotes increased sliding displacements, especially at the higher strain amplitudes, as signified by its higher

R_{cc} values as compared to the conjugate slip case. For a/d ratios of 0.97 and 1.25 in Figures V.5 and V.6 respectively, even the first cycle shows differences in the R_{cc} values for the elastic and micromechanical solutions for all strain amplitudes. Subsequent cycling for the micromechanical solution produces R_{cc} values which shows distinctions for the single and conjugate slip cases.

These plots reveal important results: (i) the elastic solution will primarily show an R_{cc} of 0.5 for all a/d ratios and amplitudes (with $a/d = 0.5$ as the exception for $0.6 \epsilon_y$ and $0.9 \epsilon_y$) whereas the micromechanical solutions at the maximum and minimum load show R_{cc} at much lower values and (ii) the behavior over much of the cycle is dominated by opening behavior. Continued cycling, not just the initial cycle, shows that the opening displacements contribute significantly to the driving forces for small crack behavior.

V.2.1.2 Cyclic Shear

For cyclic shear, two strain amplitudes are considered ($0.3 \gamma_y$ and $0.9 \gamma_y$). For this loading case, $R_n = 0$ ($\Delta\tau_n/2/\Delta\gamma_n/2$) such that the product $\beta_e R_n = 0$ in Equations (I.6) and (I.7). Since β_e was defined as relating to the mode-mixity of sliding and opening displacements, cyclic shear would, therefore, yield little to no mode-mixity of the CTOD and CTSD. However, for small cracks, as the micromechanical calculations indicate, sliding *and* opening displacements are evident for cyclic shear loading. Figure V.7 shows the R_{cc} values for $a/d = 0.25$ and for both shear strain amplitudes. For this a/d ratio, the

R_{cc} values for the micromechanical solutions and the elastic solutions are nearly the same with an R_{cc} of approximately 0.3 at the maximum and minimum loads. For $a/d = 0.97$ in Figures V.8a and V.8b, the R_{cc} values are much higher because the sliding displacements are a much higher proportion of the opening displacements for cyclic shear, especially for larger a/d ratios and shear strain amplitudes. For $a/d = 1.97$ in Figures V.9a and V.9b, there are distinctions between the single and conjugate slip cases, especially for $0.3 \gamma_y$, with the single slip case promoting on the order of twice the amount of sliding displacements as the conjugate slip case. At the higher strain amplitude of $0.9 \gamma_y$, the R_{cc} values for the single and conjugate slip cases are quite comparable. The results for the R_{cc} cyclic shear loading case reveal that only at increased a/d ratios ($a/d > 0.97$) are sliding displacements significantly higher than the opening displacements. This also points to the constraints that the surface plays a significant role in the behavior of small cracks.

Another interesting feature exhibited in Figure V.9 is that R_{cc} for both single and conjugate slip cases is less than the elastic solution. This points to the effect of surrounding grains and their influence on the sliding and opening behavior at the crack tip. The elastic solution, which is completely homogeneous, shows an enhanced ratio due to the absence of constraint from surrounding grains. The cyclic tension-compression case also shows evidence of the elastic solution which yields higher R_{cc} values as compared to the crystal plasticity micromechanical solutions. An additional comparison between the two loading cases reveals that for the cyclic tension-compression case, the

R_{cc} ranges from 0.1 to 0.5, whereas for the cyclic shear case, R_{cc} ranges from 0.2 to 2.0. For the cyclic shear case, the sliding displacements become more dominant with increasing a/d ratios and applied strain, whereas for the cyclic tension-compression case, there is a greater contribution of the opening displacements.

V.2.2 ΔCTD

This calculation is made in order to understand the relative dependencies of crack length ratio and amplitude on ΔCTD for cyclic tension-compression and cyclic shear.

The ΔCTD is defined as

$$\Delta CTD = \sqrt{\Delta CTOD^2 + \Delta CTSD^2} \quad (V.1)$$

For these calculations, the $\Delta CTSD$ and $\Delta CTOD$ are the ranges of the sliding and opening displacements, respectively measured at $2 \mu m$ behind the crack tip at the end of the third cycle in the loading sequence. The ΔCTD calculated in this manner reflects the magnitude of the vector sum of the sliding and opening displacements. The following sections will explore the ΔCTD for both loading cases.

V.2.2.1 Cyclic Tension-Compression

Figure V.10 shows the Δ CTD over the third cycle of loading as a function of crack length ratio. Trend lines are also drawn for the different strain amplitudes. For cyclic tension-compression in Figure V.10a, the Δ CTD shows a strong dependence on amplitude and crack length. What is striking is the strong dependence of the Δ CTD on applied load for the elastic-plastic solutions reflected by the increasing slopes for $a/d < 1$ (given in Table V.2a). For the Δ CTD plot in Figure V.10a, the minima at the first grain boundary ($a/d = 0.97$) is the lowest as compared to the next grain boundary at $a/d = 1.97$.

The current micromechanical calculations differ from Li's (140) results. First, the Δ CTD found here (for $a/d < 1$) increases from zero (for $a/d = 0.25$) then reaches a maximum (around $a/d = 0.5$), then decreases (at $a/d = 0.97$). His results show a Δ CTD that begins at a maximum value (at $a/d \approx 0.25$) then decreases to nearly zero (at $a/d = 0.97$). This mainly occurs because of the constraints he imposes for the displacements along the crack plane and only allow for sliding along the crack plane which leads to severe blockage of the sliding displacements. Further, he has no means to account for a free surface, nor does any other continuously distributed dislocation band model which mimics Hall-Petch type behavior (cf. Navarro and de los Rios (82-83)).

Focusing on the behavior within the first grain, for each amplitude, there is a different slope which increases for increasing amplitude. The slopes, however, do not increase in proportion with the applied strain amplitude. The slopes and corresponding

amplitudes are given in Table V.2a. By doubling the strain amplitude from $0.3 \epsilon_y$ to $0.6 \epsilon_y$, the ΔCTD increases fivefold. By increasing the strain amplitude threefold, the ΔCTD increases by a factor of 13. This also points to the considerable lack of constraint afforded to small crack behavior due to the free surface. As the crack approaches the grain boundary, the ΔCTD parameter shows a pronounced decrease for increasing applied strains, especially for an adjacent grain which promotes conjugate slip. The crack length ratio and amplitude dependency of ΔCTD also persists into the next grain for strain amplitudes of $0.6 \epsilon_y$ and $0.9 \epsilon_y$. The driving forces for $0.3 \epsilon_y$ appear to be relatively constant throughout all applied strain amplitudes and crack length ratios, consistent with the elastic solutions for this dominantly displacement-controlled loading condition.

V.2.2.2 Cyclic Shear

For cyclic shear, the behavior is shown in Figure V.10b. Within the first grain and for the shear strain amplitudes considered, there is little to no crack length ratio or amplitude dependency of the ΔCTD . The slope is nearly the same for both shear strain amplitudes showing minimal effect of the crack length ratio for $a/d < 1$. For $a/d > 1$, there is a marked difference in the ΔCTD as a function of amplitude. For the 45° crack loaded in tension, the normal stress across the crack plane evidently has a greater effect on the mode mixity at the crack tip for $a/d < 1$ as compared to the cyclic shear case. The

Δ CTD for a strain amplitude of $0.3 \gamma_y$ shows a significant increase in the second grain as compared to the first grain, an approximate 50% increase in the Δ CTD. For $0.9 \gamma_y$, the Δ CTD increases by nearly a factor of 7 from an $a/d = 0.97$ to an $a/d = 1.97$.

Another interesting observation of the Δ CTD is that cyclic tension-compression has consistently higher values of the Δ CTD as compared to the cyclic shear case. One explanation, as alluded to earlier, has to do with the normal stress across the crack plane. This factor contributes significantly to enhancing the opening displacements which are produced at the crack tip. As the previous R_{cc} plots (cf. Figs. V.3 - V.9) revealed, there are proportionate contributions of the sliding and opening displacements for the cyclic tension-compression case, whereas for the cyclic shear case, the sliding displacements become dominant for increasing crack length ratios. It appears that although the sliding displacements do become dominant for cyclic shear, these displacements are not greater than the combined effect of the opening and sliding displacements that are produced for the cyclic tension-compression case.

V.2.3 Δ CTSD/ Δ CTOD

The ratio of the ranges of the CTSD and CTOD and is examined for these calculations to elucidate the understand relative changes as a function of stress state and amplitude.

V.2.3.1 Cyclic Tension-Compression

Figure V.11 shows the ratio of the range of the sliding and opening displacements for cyclic tension-compression over the third cycle of loading. For the smallest strain amplitude, $0.3 \epsilon_y$ (in Fig. V.11a) and within the first grain, the ratio is nearly unity. As the a/d ratio increases from 1.25 to 1.97, the range of the sliding displacements progresses from 10% to 40% higher than the range of the opening displacements. In Figures V.11b and V.11c for strain amplitudes of $0.6 \epsilon_y$ and $0.9 \epsilon_y$ respectively, the behavior in the first grain is much different than for $0.3 \epsilon_y$. As the first grain is approached, there is a steady decrease in the ratio which means that at this barrier, the range of the opening displacement is greater than the range of the sliding displacement. With increasing a/d ratios, the range of the sliding displacements recovers and increases from 10% to 40% higher than the range of the opening displacements for a/d ratios of 1.25 and 1.97. Of course, for long cracks, one would expect this ratio of the $\Delta CTSD$ and $\Delta CTOD$ to approach zero.

This behavior is markedly different from that commonly assumed for small cracks in the first grain based on pile-up typ solutions. These results show a dominance of the opening displacement for elastic-plastic cases, whereas the elastic solution is opposite in nature.

V.2.3.2 Cyclic Shear

Figure V.12 shows the change of the ratio of the range of the sliding and opening displacements for cyclic shear loading. These results differ substantially from the cyclic tension-compression case. For the cyclic shear case, the ratio increases approximately linearly throughout all a/d ratios considered. The elastic solution shows are fairly good estimate of the ratio for both strain amplitudes ($0.3 \gamma_y$ and $0.9 \gamma_y$), although for $0.3 \gamma_y$, the conjugate slip case shows an increased proportion of the range of the opening displacements. The results for the cyclic shear case appear to point to a minimal effect of the adjacent grain on this formulation of the driving force parameters since there is a linear increase in this quantity for both amplitudes and crack length ratios considered. Perhaps the driving force parameters are so high that the orientation of the surrounding and adjacent grains do not significantly affect the mixity.

V.3 ΔCTD as a Function of Parameter $\frac{\Delta\tau_n}{2} \frac{\Delta\gamma_n}{2}$

The evaluation of the ΔCTD as a function of the product $\frac{\Delta\tau_n}{2} \frac{\Delta\gamma_n}{2}$ for a given crack length ratio potentially provides a direct correlation between this critical plane quantity and the crack tip CTD. The quantity $\Delta\tau_n/2$ is the amplitude of the shear strain on the plane of the maximum range of shear strain and $\Delta\gamma_n/2$ is the amplitude of the shear

strain acting on the plane of the maximum range of shear strain. ΔCTD has been used for correlating crack growth behavior under EPFM conditions. This parameter has also been shown to scale with the J-Integral according to

$$\Delta J \propto \frac{\Delta\sigma}{2} \frac{\Delta\varepsilon}{2} a \quad (\text{V.2})$$

and as shown by McDowell and Berard

$$\Delta J = \psi \left(\frac{\Delta\sigma}{2} \frac{\Delta\varepsilon_e}{2} \right) a \quad (\text{V.3})$$

The following sections report the relationship between the range of the CTOD and the product $\frac{\Delta\tau_n}{2} \frac{\Delta\gamma_n}{2}$ for different a/d ratios and stress states.

V.3.1 Cyclic Tension-Compression

Figures V.13a - V.13e show the variation of the ΔCTOD over the third cycle for increasing values of the critical plane product. These plots reveal a linear relationship which signifies that for increasing applied loads, the driving force increases in proportion, as expected. What may not have been anticipated is the semblance of the slope of this linear relationship for all a/d ratios considered. The average slope is approximately

0.00166. It is also observed that both the single and conjugate slip cases have the same behavior.

V.3.2 Cyclic Shear

Figures V.14 a - V.14c show the relationship between the DCTOD and the critical plane product. For this loading case, there is also a linear relationship between the driving force and the applied load. The slope however, for this loading case is markedly different from the cyclic tension-compression case. For the cyclic shear case, the slope for $a/d = 0.25$ is the same for both the single and conjugate slip cases. For $a/d = 0.97$ to 1.97 , the slope increases by nearly a factor of three. The changing slope is possibly due to the increasing driving forces which build up at the crack tip. Since there is no normal stress across the crack plane for cyclic shear which may enhance or deter the CTSD or CTOD, the driving forces accumulate and produces increased dependencies on crack length ratio. For the cyclic tension-compression case, the driving force was independent of crack length ratio.

V.4 Conclusions

In evaluating the current form of the models for small crack growth, there appear to be several implications based on the crystal plasticity micromechanical analyses. First, the threshold regime was qualitatively evaluated using an uncracked polycrystal to determine the elastic shakedown limits of cyclic microplasticity. There was a nonlinear relationship between the maximum shear stress (averaged over all grains) and the local maximum plastic shear strain (averaged over all grains). From evaluating different relationships of the CTSD and CTOD, it was found that cyclic tension-compression showed a greater dependency on the amplitude and crack length ratio, whereas for the cyclic shear case, there was limited dependencies only for increased crack length ratios.

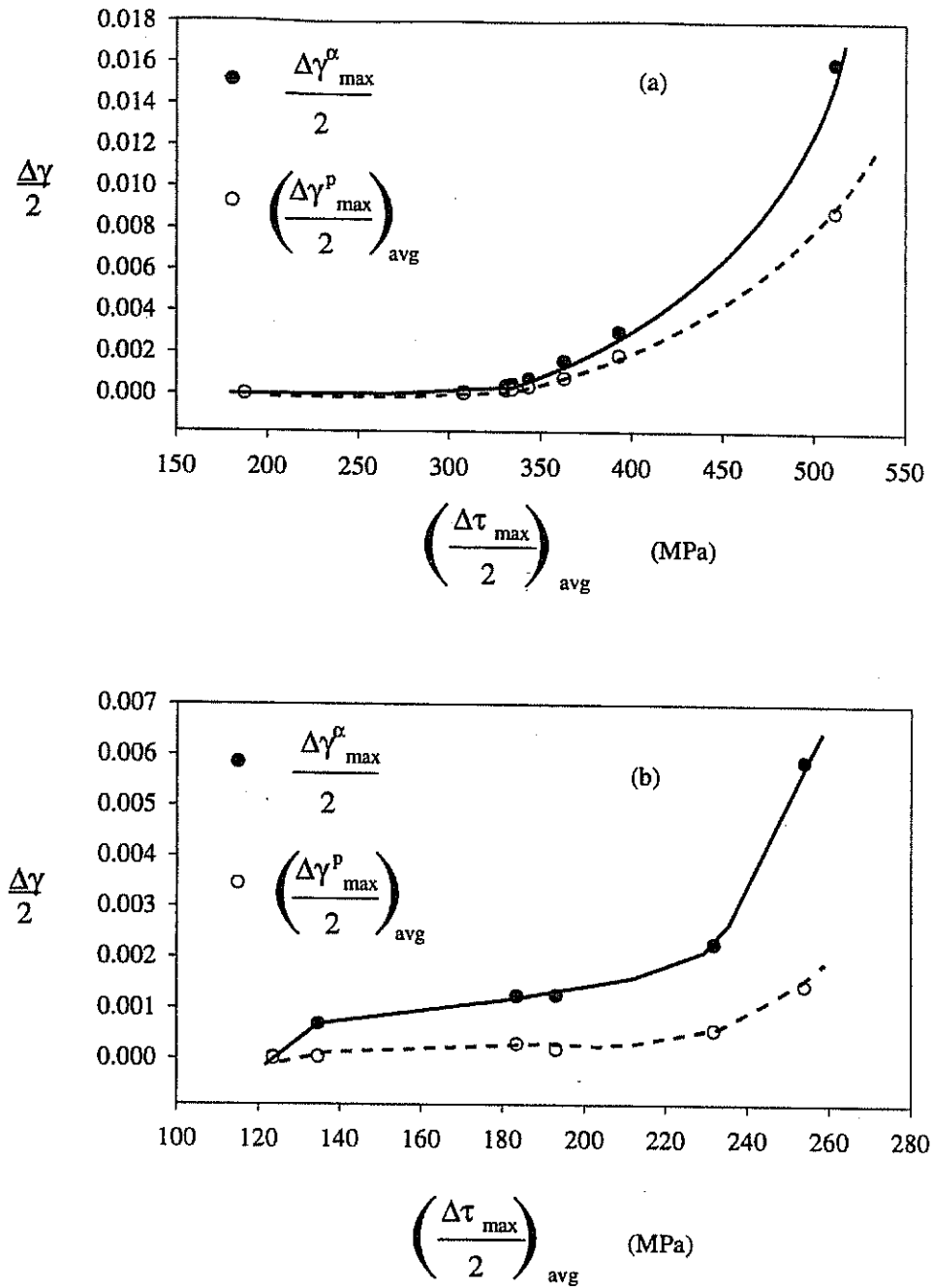


Figure V.1 Comparison of the maximum shear strain amplitude on a slip system and the maximum plastic shear strain amplitude (averaged over all grains) as a function of the average amplitude of the maximum shear stress for (a) cyclic tension-compression and (b) cyclic shear.

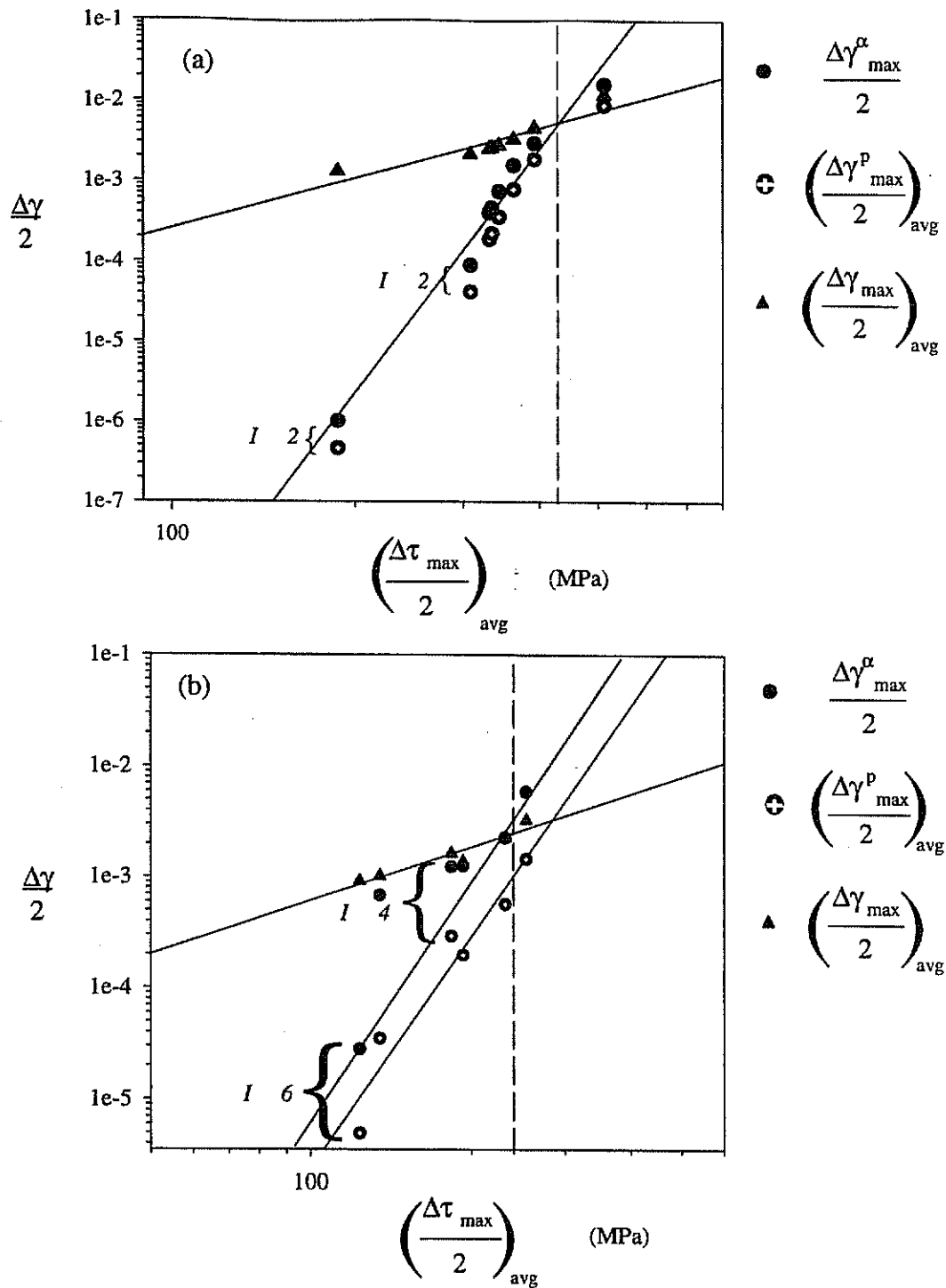


Figure V.2 Relationship between the amplitude of the maximum average shear stress and the shear strain amplitudes showing relative intensity between the maximum shear strain on a slip system and the maximum plastic shear strain (a) cyclic tension-compression and (b) cyclic shear.

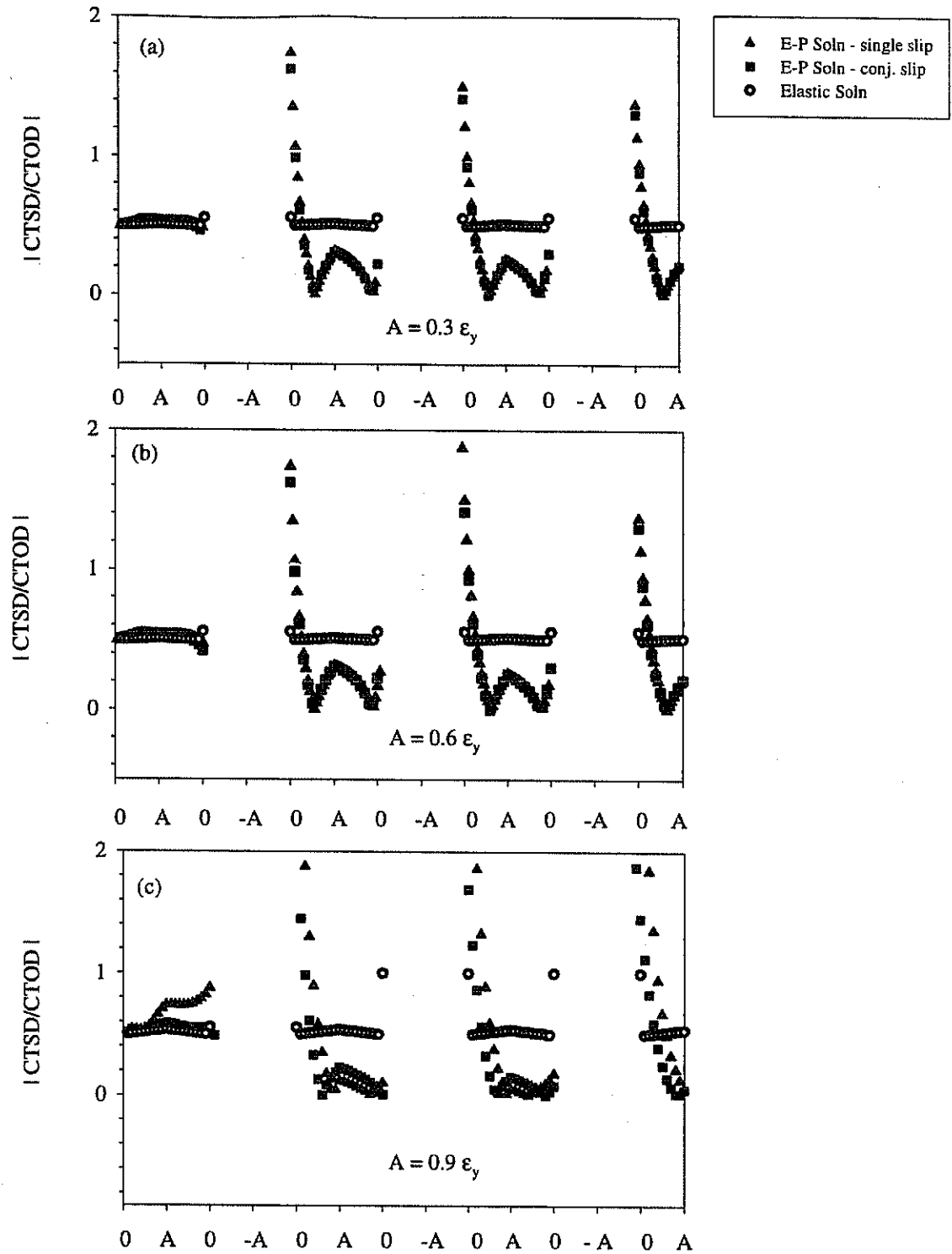


Figure V.3 Ratio of $|CTSD/CTOD|$ for cyclic tension-compression loading for a crack oriented at 45° with respect to the tensile axis with $a/d = 0.25$ for strain amplitudes of (a) $0.3 \epsilon_y$, (b) $0.6 \epsilon_y$, and (c) $0.9 \epsilon_y$ at a distance of $2 \mu\text{m}$ behind the crack tip.

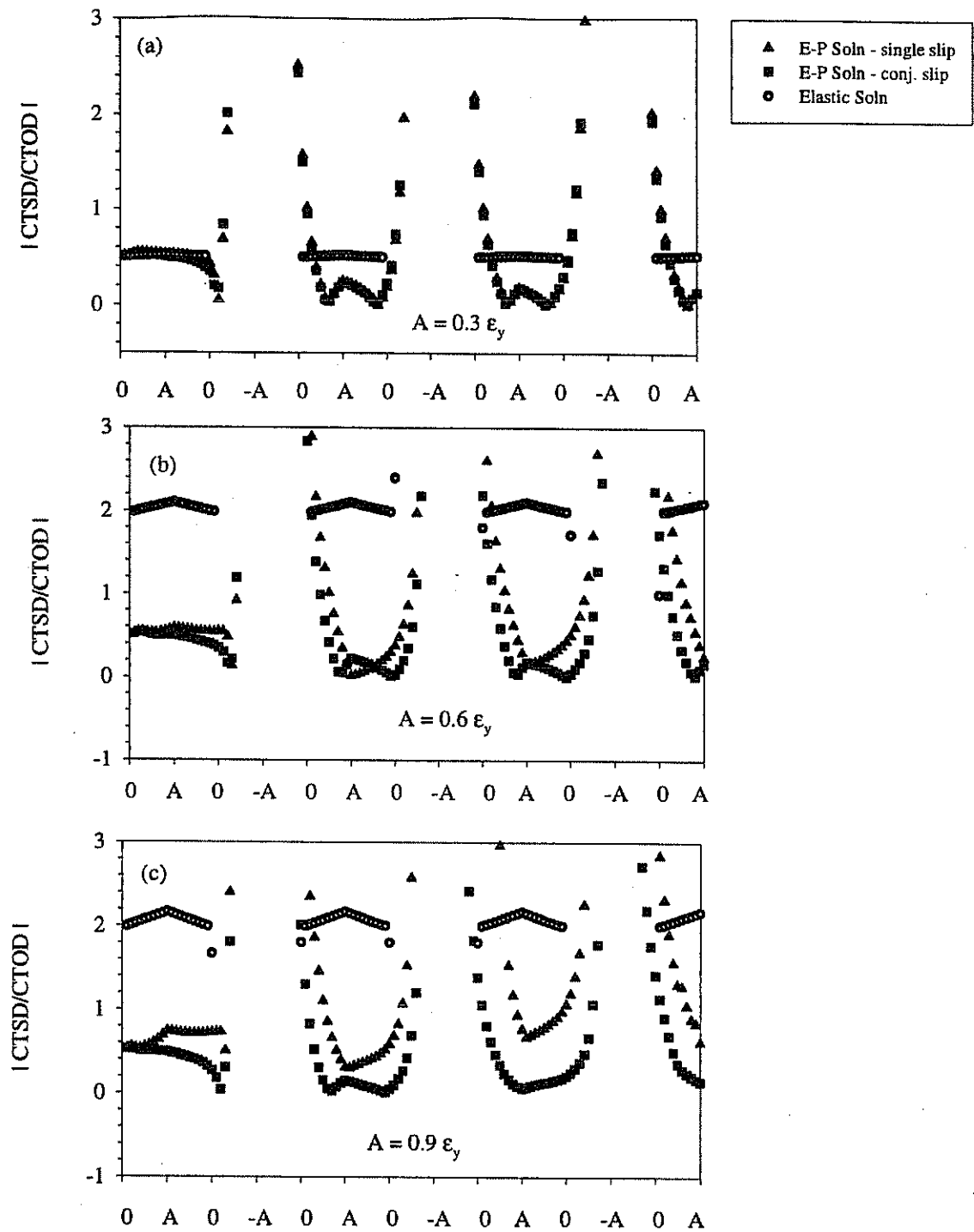


Figure V.4 Ratio of $|CTSD/CTOD|$ for cyclic tension-compression loading for a crack oriented at 45° with respect to the tensile axis with $a/d = 0.5$ for strain amplitudes of (a) $0.3 \epsilon_y$, (b) $0.6 \epsilon_y$, and (c) $0.9 \epsilon_y$ at a distance of $2 \mu\text{m}$ behind the crack tip.

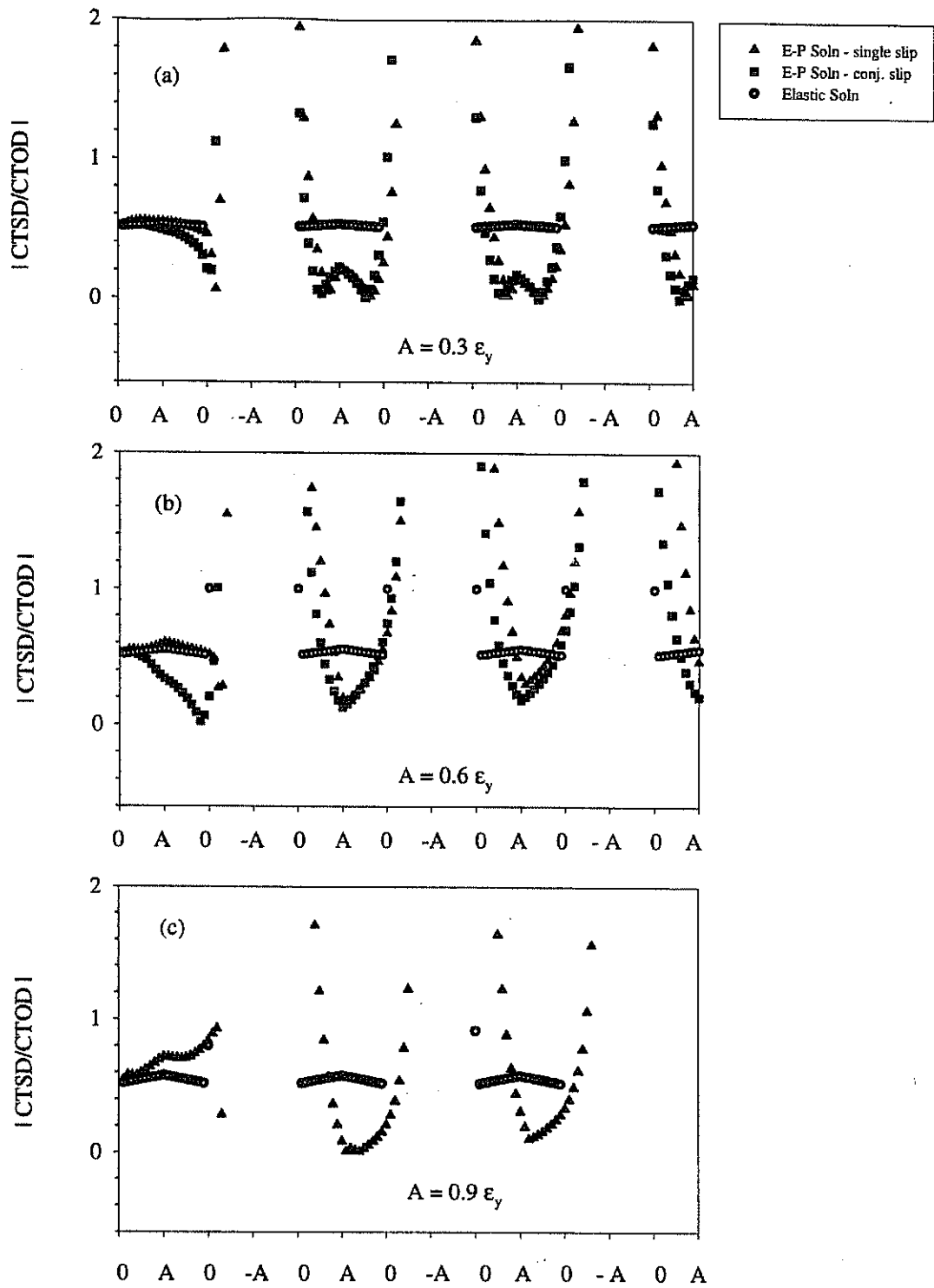


Figure V.5 Ratio of $|CTSD/CTOD|$ for cyclic tension-compression loading for a crack oriented at 45° with respect to the tensile axis with $a/d = 0.97$ for strain amplitudes of (a) $0.3 \epsilon_y$, (b) $0.6 \epsilon_y$, and (c) $0.9 \epsilon_y$ at a distance of $2 \mu\text{m}$ behind the crack tip.

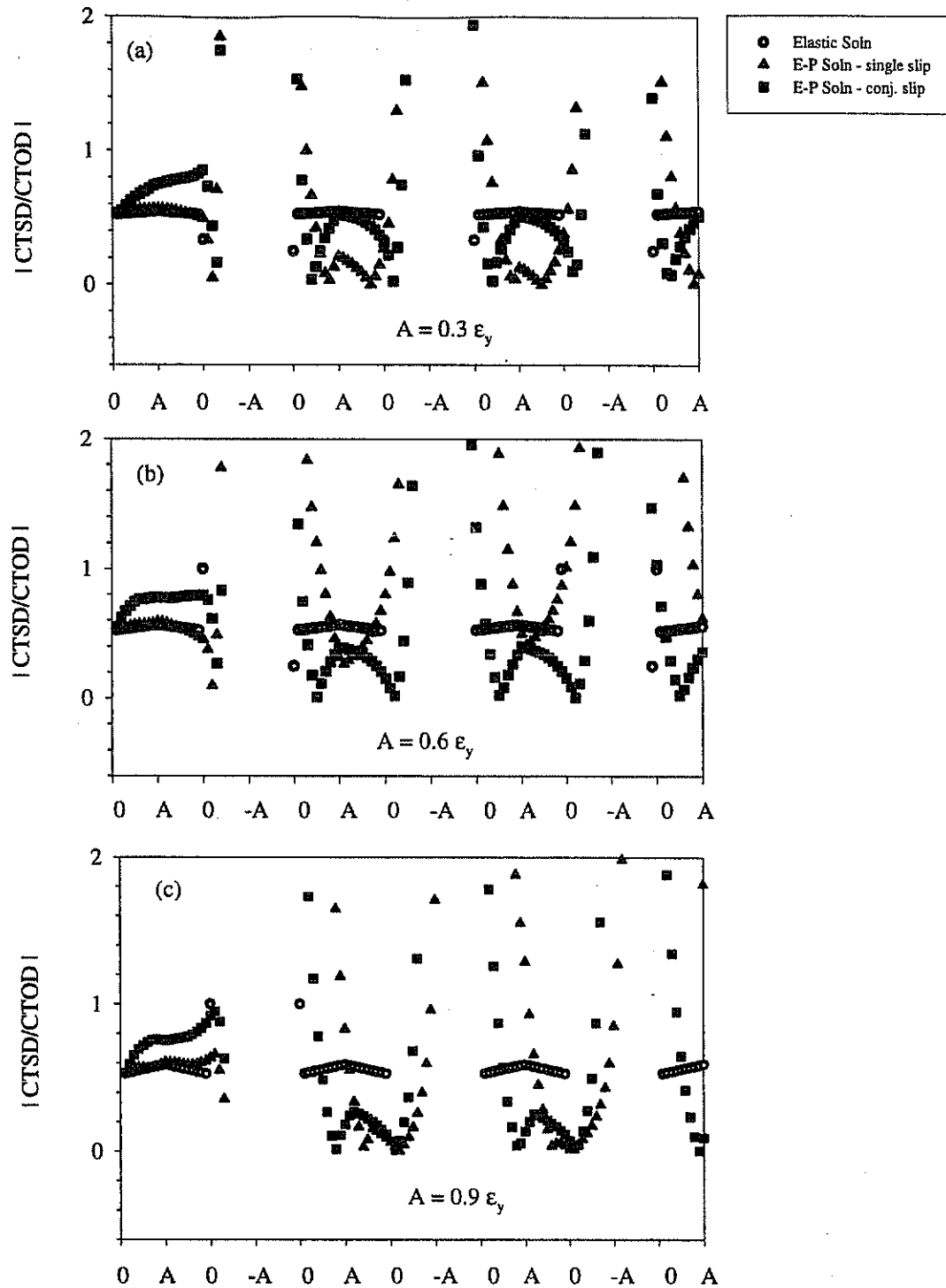


Figure V.6 Ratio of $|CTSD/CTOD|$ for cyclic tension-compression loading for a crack oriented at 45° with respect to the tensile axis with $a/d = 1.25$ for strain amplitudes of (a) $0.3 \epsilon_y$, (b) $0.6 \epsilon_y$, and (c) $0.9 \epsilon_y$ at a distance of $2 \mu\text{m}$ behind the crack tip.

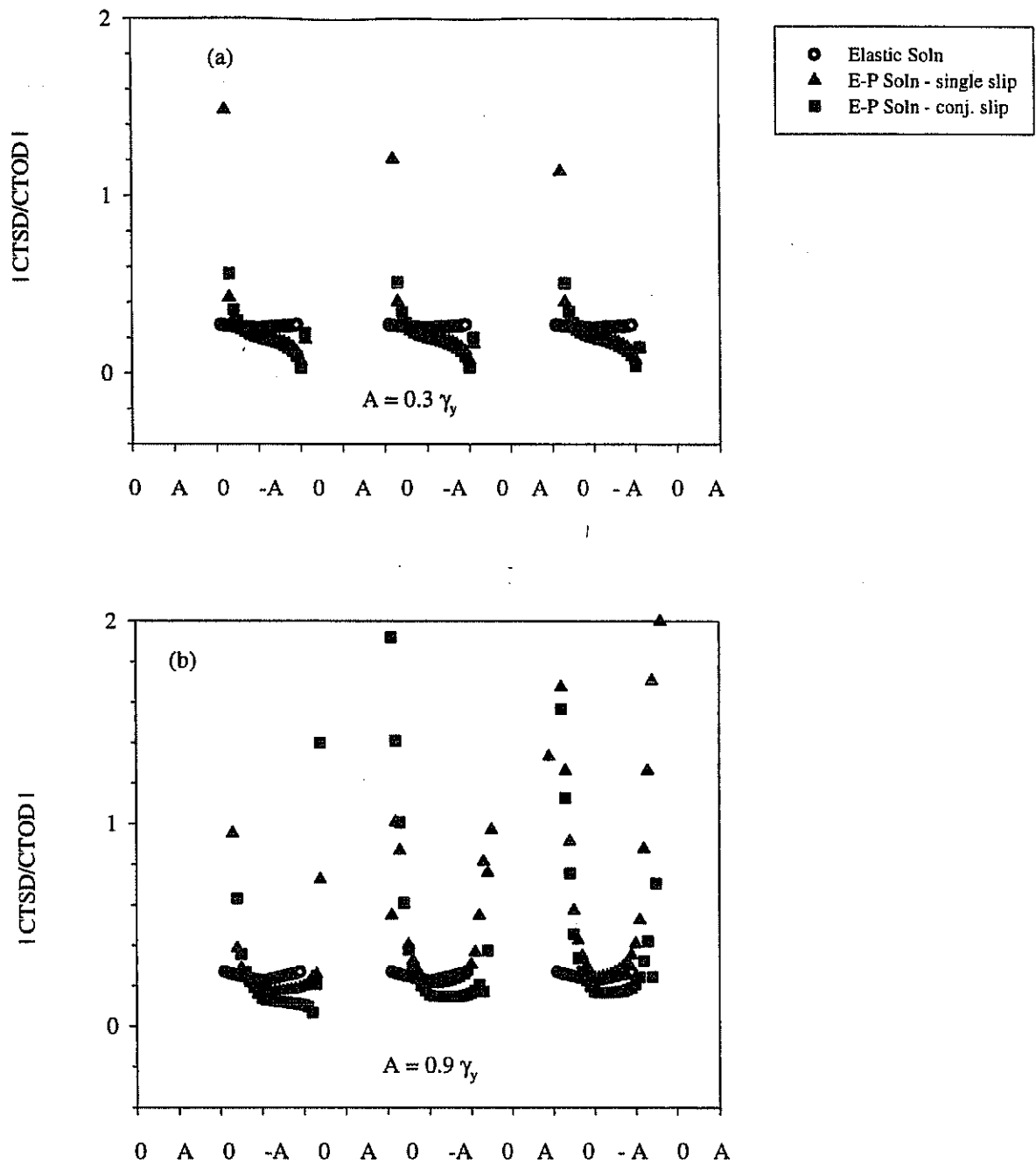


Figure V.7 Ratio of $|CTSD/CTOD|$ for cyclic shear loading for crack oriented at 90° with respect to tensile axis with $a/d = 0.25$ for strain amplitudes of (a) $0.3\gamma_y$ and (b) $0.9\gamma_y$ at a distance of $2 \mu\text{m}$ behind the crack tip.

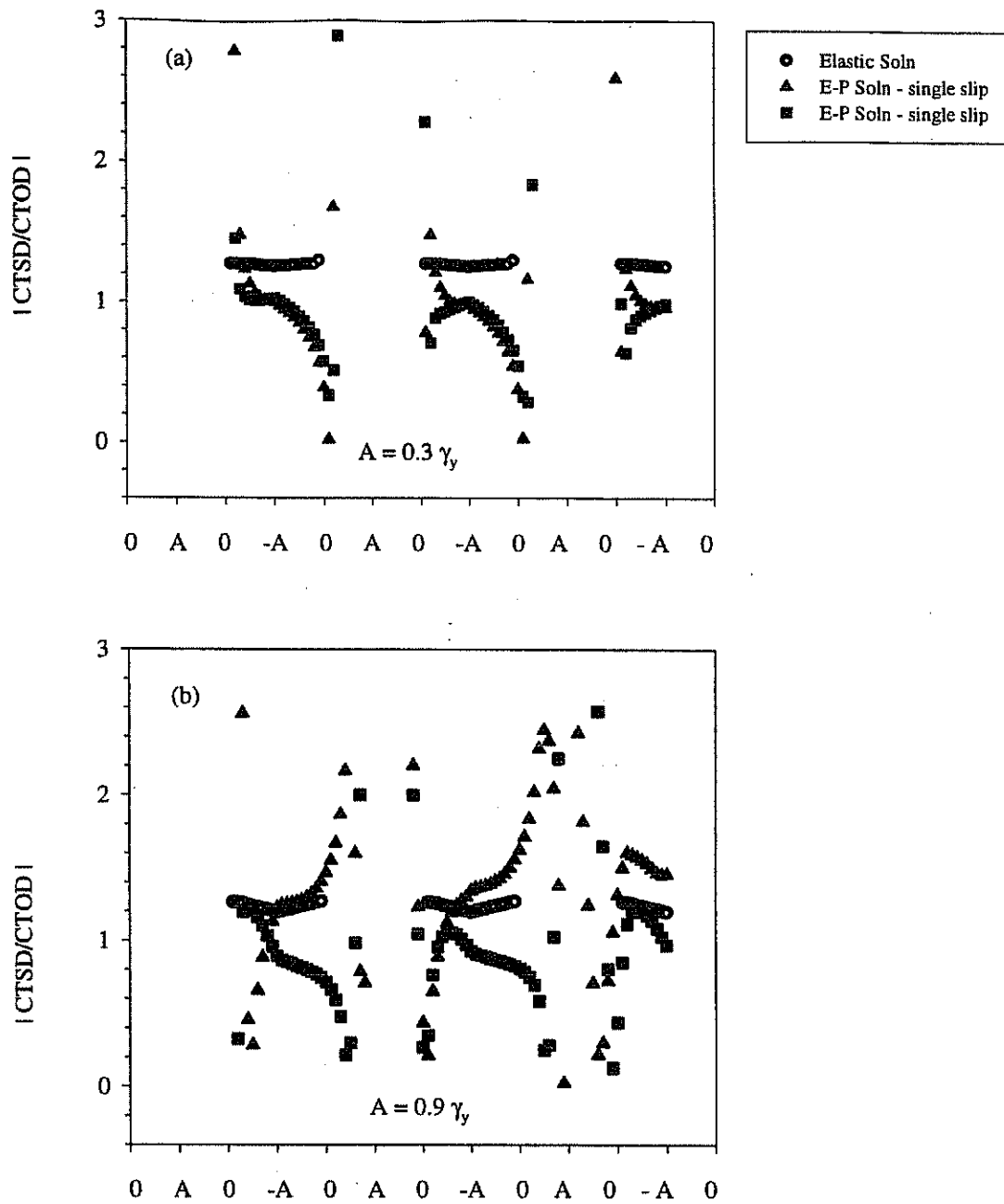


Figure V.8 Ratio of $|CTSD/CTOD|$ for cyclic shear loading for crack oriented at 90° with respect to tensile axis with $a/d = 0.97$ for strain amplitudes of (a) $0.3\gamma_y$ and (b) $0.9\gamma_y$ at a distance of $2 \mu\text{m}$ behind the crack tip.

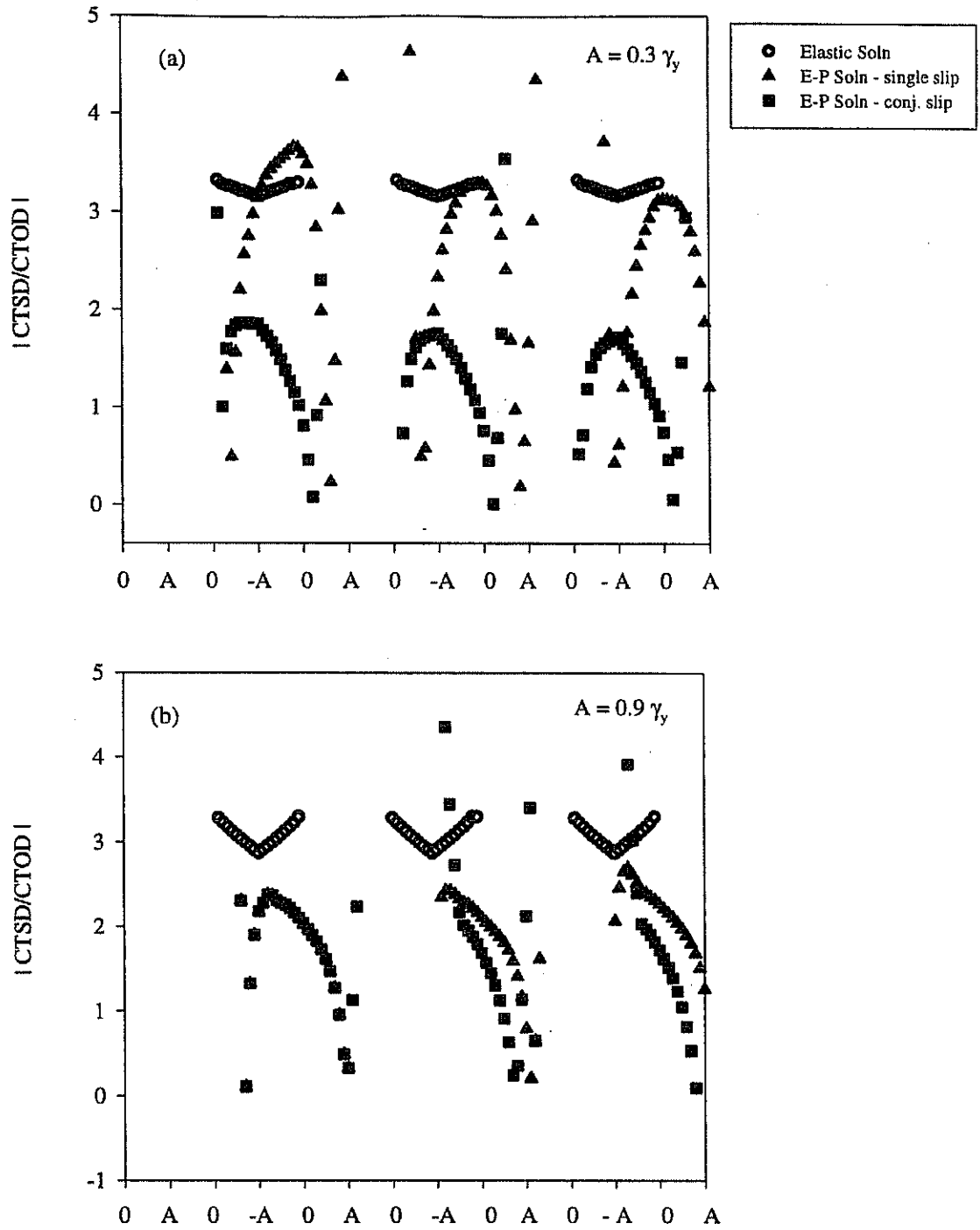


Figure V.9 Ratio of $|CTSD/CTOD|$ for cyclic shear loading for crack oriented at 90° with respect to tensile axis with $a/d = 1.97$ for strain amplitudes of (a) $0.3\gamma_y$ and (b) $0.9\gamma_y$ at a distance of $2 \mu\text{m}$ behind the crack tip.

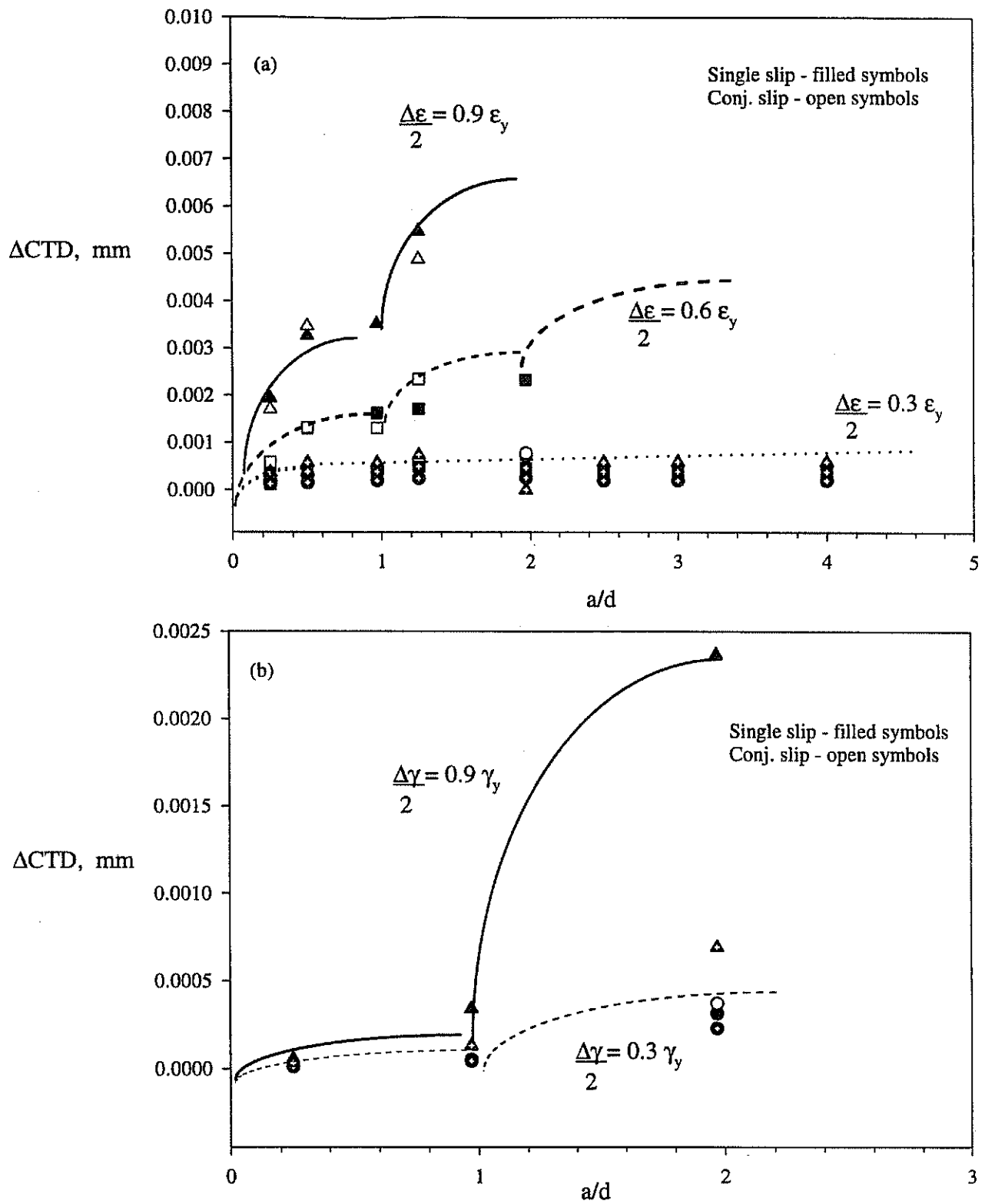


Figure V.10 ΔCTD as a function of crack length ratio at a distance of $2 \mu\text{m}$ behind the crack tip after 3 cycles of loading for (a) cyclic tension-compression and (b) cyclic shear.

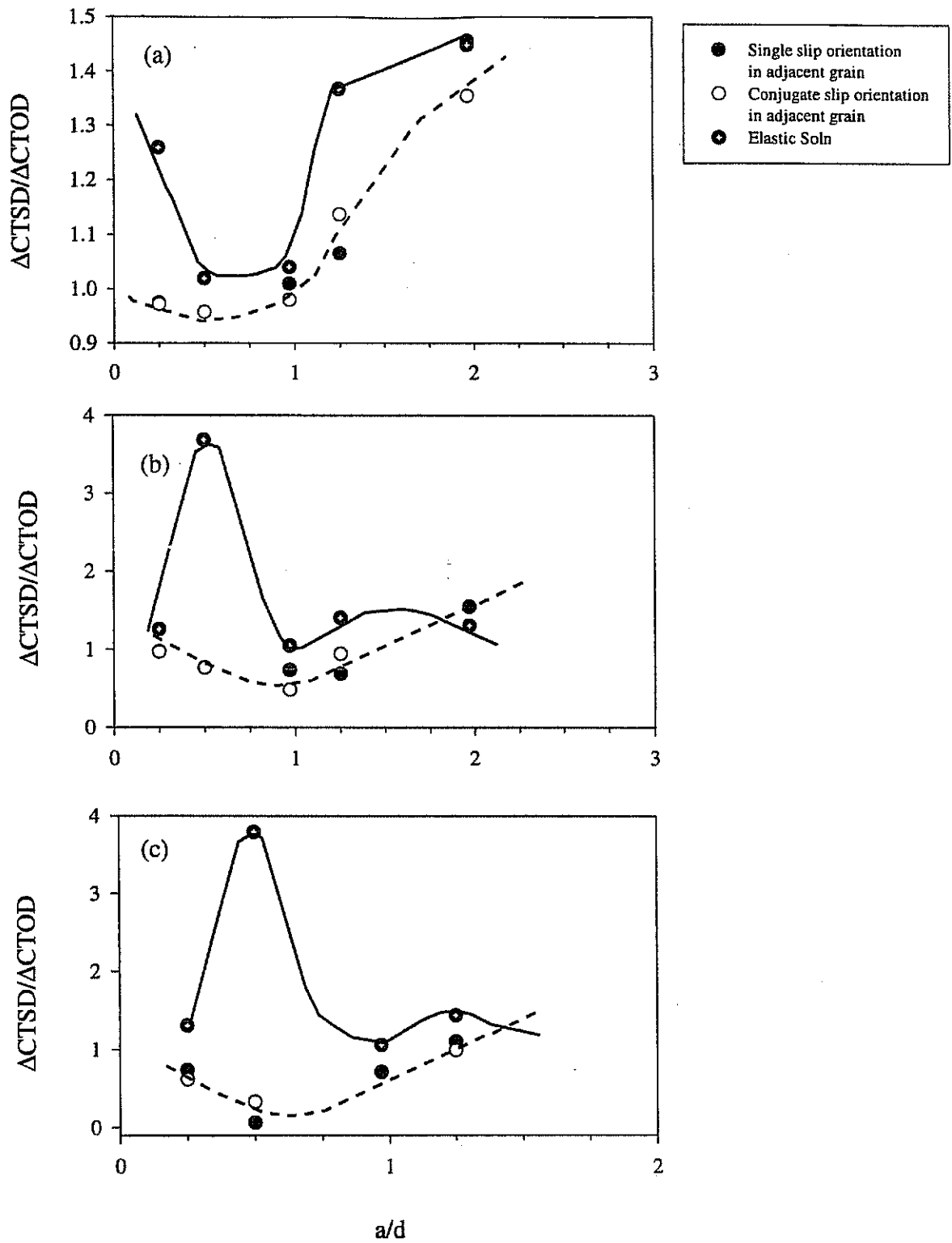


Figure V.11 $\Delta CTSD/\Delta CTOD$ as a function of crack length ratio for cyclic tension-compression and at $2 \mu\text{m}$ behind the crack tip over the 3rd cycle of loading for applied strain amplitudes of (a) $0.3 \epsilon_y$, (b) $0.6 \epsilon_y$, and (c) $0.9 \epsilon_y$.

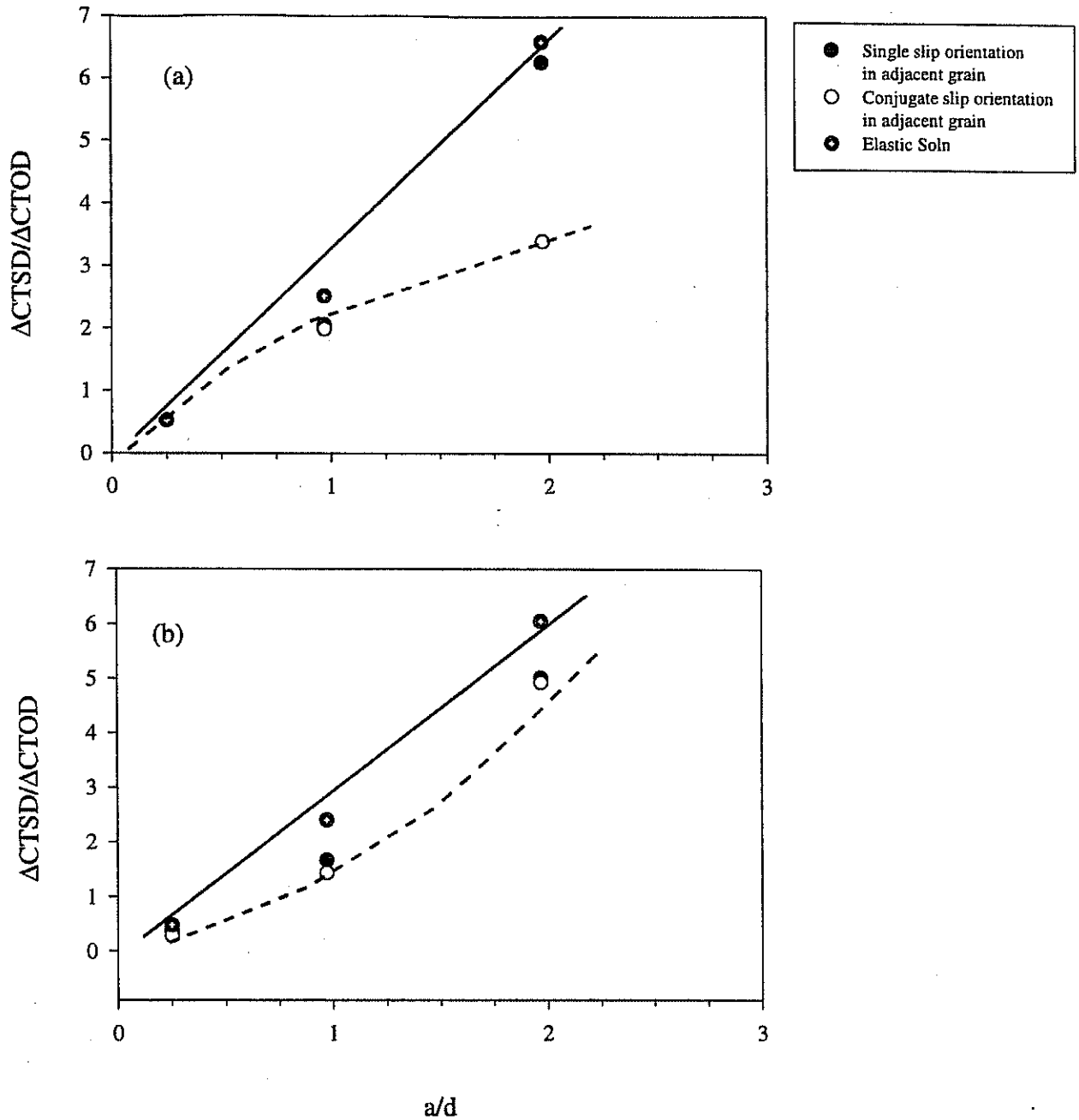


Figure V.12 $\Delta CTSD/\Delta CTOD$ as a function of crack length ratio for cyclic shear and at $2 \mu m$ behind the crack tip after 3 cycles of loading for applied strain amplitudes of (a) $0.3 \gamma_y$ and (b) $0.9 \gamma_y$.

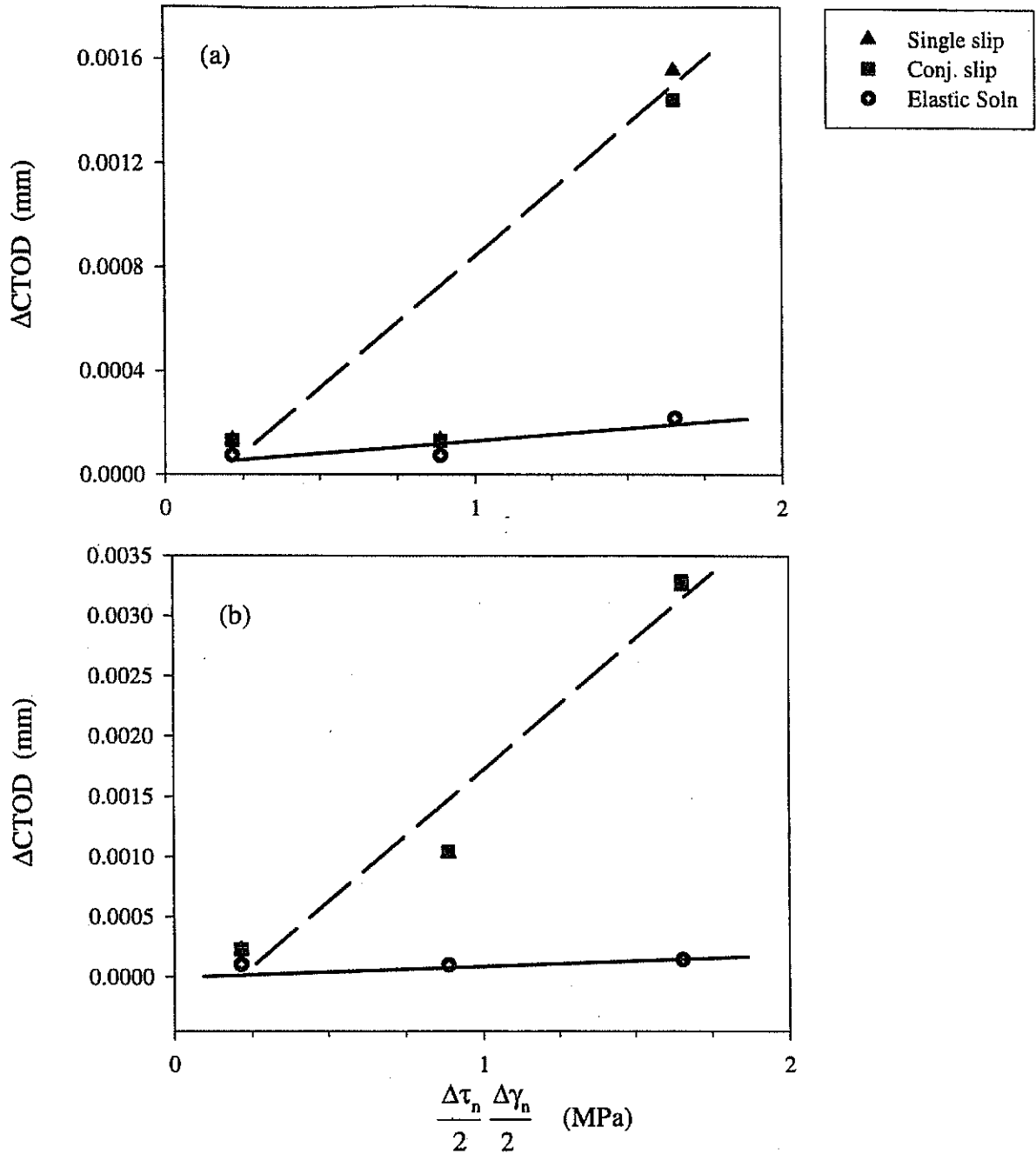
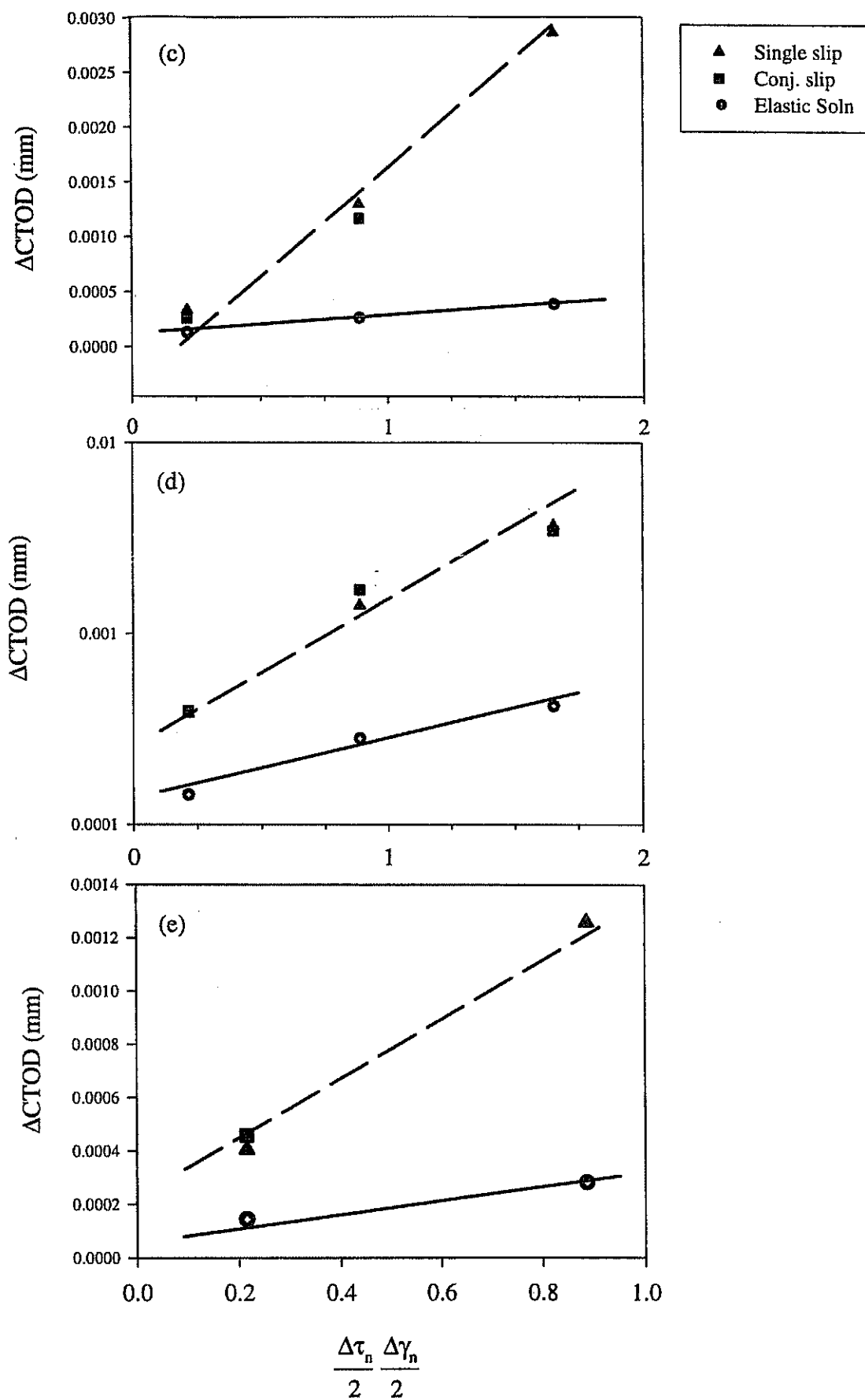


Figure V.13 $\Delta CTOD$ as a function of product of $\Delta \tau_n/2$ (amplitude of shear stress on the plane of maximum range of shear strain) and $\Delta \gamma_n/2$ (amplitude of the shear strain acting on the plane of maximum range of shear strain) for cyclic tension-compression at $2 \mu m$ behind the crack tip after 3 cycles of loading for crack length ratios of (a) 0.25, (b) 0.5, (c) 0.97, (d) 1.25, and (e) 1.97.



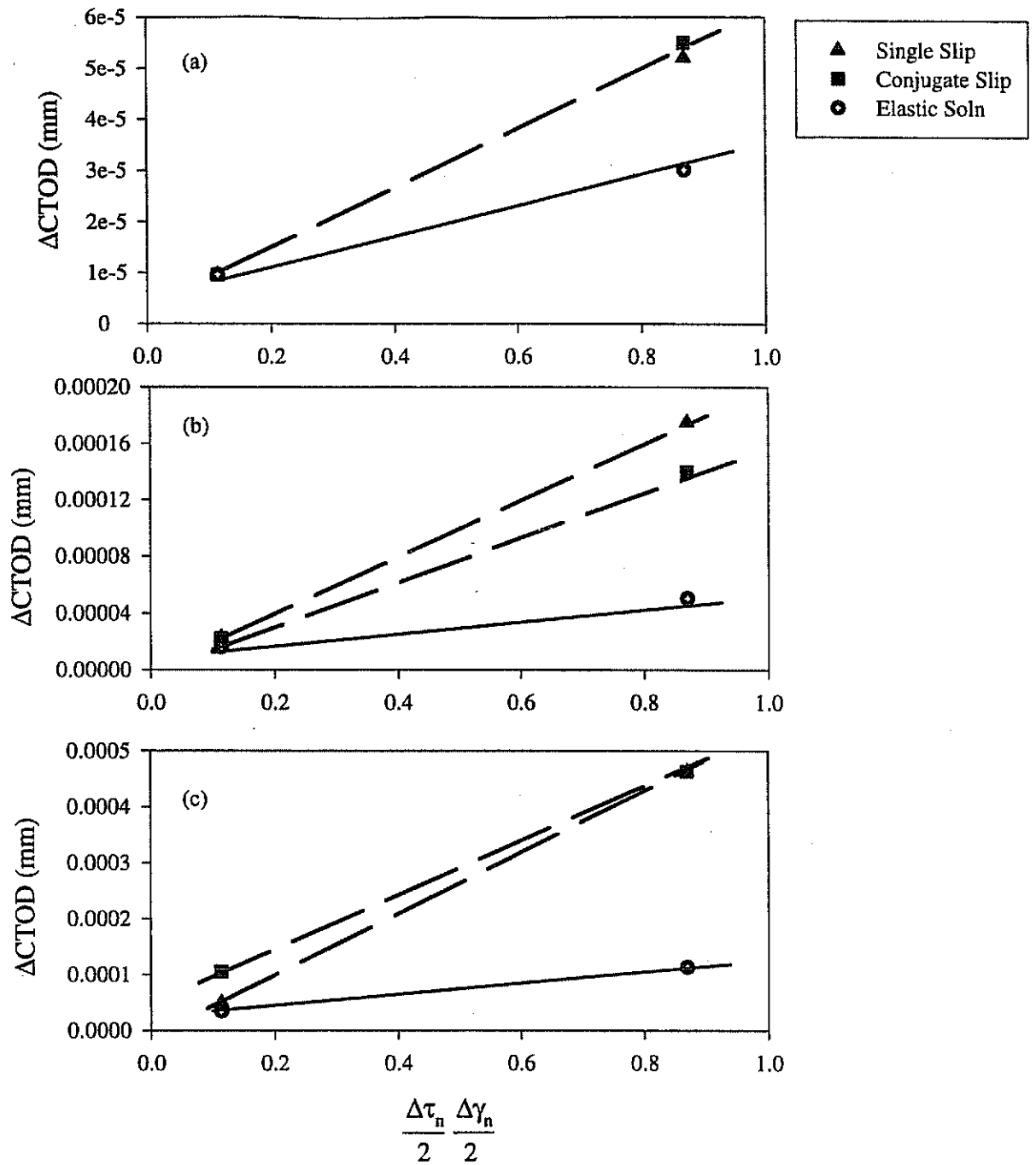


Figure V.14 $\Delta CTOD$ as a function of product of $\Delta\tau_n/2$ (amplitude of shear stress on the plane of maximum range of shear strain) and $\Delta\gamma_n/2$ (amplitude of the shear strain acting on the plane of maximum range of shear strain) for cyclic shear at $2 \mu m$ behind the crack tip after 3 cycles of loading for crack length ratios of (a) 0.25, (b) 0.97, and (c) 1.97.

**Table V.1 Estimates of Shakedown Limits based on
Micromechanical Solutions for 4340 Steel**

Loading Case	Elastic Shakedown		Fully Plastic Limits	
	$\frac{\Delta\tau_{\max}}{2}$	Strain Amplitude	$\frac{\Delta\tau_{\max}}{2}$	Strain Amplitude
Cyclic Tension-Compression	160 MPa	$0.4 \epsilon_y \approx 0.0026$	300 MPa	$0.9 \epsilon_y \approx 0.00585$
Cyclic Shear	220 MPa	$0.4 \gamma_y \approx 0.00168$	450 MPa	$0.9 \gamma_y \approx 0.00378$

**Table V.2a Relationship between the Applied Strain Amplitude and
the Initial Slope of the Δ CTD vs. a/d for $a/d < 1$ for Cyclic Tension-Compression**

Strain Amplitude	Approximate Slope (mm)
$0.3 \epsilon_y$	0.0005
$0.6 \epsilon_y$	0.0025
$0.9 \epsilon_y$	0.0066

**Table V.2b Relationship between the Applied Strain Amplitude and
the Initial Slope of the Δ CTD vs. a/d for $a/d < 1$ for Cyclic Shear**

Shear Strain Amplitude	Approximate Slope (mm)
$0.3 \gamma_y$	0.00001
$0.9 \gamma_y$	0.00001

**Table V.3a Slope, l , for Cyclic Tension-Compression
for different crack length ratios**

a/d	Slope, l
0.25	0.00101
0.5	0.00212
0.97	0.00176
1.25	0.00214
1.97	0.00127

Avg. Slope 0.00166

Table V.3b Slope, l , for Cyclic Shear for different crack length ratios

a/d	Slope, l	
	Single Slip	Conjugate Slip
0.25	0.00006	0.00006
0.97	0.000202	0.000156
1.97	0.000547	0.000474

CHAPTER VI

CONCLUSIONS AND RECOMMENDATIONS

VI.1 Conclusions

The problem of estimating the remaining life in components under HCF conditions is the limiting factor of properly assessing the small crack regime. Since small cracks may account for 50-90% of the total life of the component (for $N_f = 1$ mm), characterizing this regime with the correct dependencies is crucial. With many of the factors with affect small crack behavior such as the role of the free surface, microstructural barriers and inhomogeneities, surface roughness, and grain boundary blockage, developing and 'all-inclusive' small crack model is indeed a challenge. Although there have been many advances through the work of many researchers (18, 77), providing a mechanistic assessment of these factors has been lacking. This work is an effort to shed light on some of the first order effect such as the effect of the lack of constraint due to the free surface, effect of surrounding (not only adjacent) grains on the crack tip behavior, as well as the limits for cyclic microplasticity. A crystal plasticity micromechanical model embedded with a finite element context was used to assess these factors. This points to one of the advantages of using finite elements coupled with micromechanical concepts - no adhoc assumptions are made regarding grain-to-grain interactions. Using 2-D planar double slip crystal plasticity embedded in a finite element context allows for the assessment of heterogeneity effects

caused by plasticity within individual grains and the interactions among these grains. The primary goal of the proposed research is to address many of the outstanding issues which hinder development of a satisfactory theory for fatigue growth of small/short cracks in structures, including:

- (i) establishing a framework for correlation/prediction of fatigue crack growth of small fatigue cracks consistent with concepts of elastic-plastic fracture mechanics and critical plane theories of multiaxial fatigue, focusing on growth of microstructurally short cracks and physically short cracks;
- (ii) developing crack length-, amplitude- and stress state-dependent criteria for the transition from one regime to the next to denote limits of applicability of certain correlative forms: regimes include propagation of microstructurally small/short cracks where barriers control intermittent growth behavior, physically small/short cracks in Stage I shear-dominated growth under the weakening influence of microstructure, and Stage II normal stress-dominated growth of physically small/short cracks and long cracks;
- (iii) understanding the propagation behavior of microcracks as a function of stress state and amplitude and developing appropriate modeling concepts;
- (iv) introducing threshold conditions for cyclic microplasticity and nonpropagating cracks (i.e. fatigue limit) into the framework of a multiaxial HCF fatigue theory;
- (v) incorporating distribution attributes of microplasticity and microcracks (i.e.

orientation and crack density) to facilitate prediction of propagation of microcracks under variable stress state loading conditions.

The first set of analyses was determining the dependencies on the development of heterogeneity of the microstructure and its effect on the behavior of an uncracked polycrystal as well as small fatigue cracks. Understanding the nature of the heterogeneity of cyclic microplasticity and its effect on small crack behavior is an essential component in devising improved formulations for small fatigue crack growth laws ranging from the microstructurally small crack to the long crack regime. Although the micromechanical analyses mainly provide results which are qualitative in nature, analyses of this type are innovative in that they incorporate the effect of the free surface and the effect of nearest neighboring and surrounding grains. The outstanding issues addressed in this work are to fully incorporate the effects of periodic barrier interactions, non-propagating crack limits and shakedown of microplasticity.

The uncracked analysis were utilized to determine the distribution of three candidate fatigue initiation parameters to determine which one correlates more closely with the density and distribution of microcracks found experimentally. The Fatemi-Socie parameter produced distributions which were indicative of the nature of the accumulation of the cyclic microplasticity and it best correlated with fatigue data for nominally HCF conditions. Both elastic and elastic-plastic shakedown limits are qualitatively determined, where the elastic shakedown limit also corresponded with the smooth specimen fatigue limit for cyclic tension-compression. It was also found that there was an accentuation of the

maximum of the plastic shear strain amplitude above the average plastic shear strain for the aggregate.

A distinguishing feature of the cracked analysis performed is the inclusion of the effect of the surface and the contribution of the surrounding (not only adjacent) grains to the behavior at the crack tip as opposed to Li (137) in his bicrystal analyses. What had not been explored up to this point are the effects of the relative orientation of the adjacent grain on directly influencing the mode-mixity of the CTOD and CTSD. The cyclic tension-compression results showed that there is evidence of local ratchetting of the sliding and opening displacements, even though the applied strain level is completely reversed. Cyclic shear shows this behavior for $2 > a/d > 7$. The effects of plasticity-induced closure are readily demonstrated in the cyclic behavior of the CTOD and CTSD.

An evaluation of the mode mixity of the sliding and opening displacements for stress state, amplitude, and crack length ratio dependency was performed. Mode mixity and nonproportional CTSD and CTOD is reflected sooner for cyclic tension-compression as compared to the cyclic shear case; mode-mixity does occur for both stress states considered (tension-compression and shear). The formulation proposed has specific dependencies - crack length ratio, stress state and amplitude - which are more physically based.

In view of the strong amplitude and stress state dependence of crack growth in the first regime, the nonlinearity of crack length dependence in the growth law depends both on the strain range and the degree of biaxiality. The microcrack propagation law to be developed here is consistent with critical plane concepts for multiaxial stress states as

demonstrated previously by McDowell & Berard (1-2) as well as observations of fatigue crack growth behavior for short cracks (3-10). This is of practical significance since effective stress and strain concepts do not accurately correlate fatigue life, in general, over a wide range of stress states. The present approach offers treatment of nonlinear cumulative damage and sequence effects, similar to that of damage curve (11) and related continuum damage mechanics (12) approaches.

The modelling effort was aimed at providing a physically consistent format for propagation of microcracks as influenced by microstructural barriers, amplitude and stress state. Several principal areas require development:

1. The grain-to-grain variation of the amplitude and orientation of cyclic slip is expected to play an increasingly strong role in the distribution and growth rate of microcracks with decreasing stress amplitude. Under HCF conditions, a much less uniform field of microcracks is typically observed compared to LCF conditions. Accordingly, we will make use of continuum slip crystal plasticity theory to relate the macroscopic stress state and amplitude to a distribution of driving forces among grains. Such effects are expected to play a more significant role for cracks on the order of several grain sizes and below; as cracks lengthen in fatigue, they begin to significantly influence the local driving forces for propagation, with diminishing influence of microstructure. Calculations will be performed using a planar double slip idealization of crystal plasticity (17-18) for a random, initially isotropic ensemble of grains subject to a range of constant amplitude stress states to

understand the nature of the distribution of cyclic slip and normal stress to slip planes as a function of amplitude and stress state. Combined kinematic-isotropic hardening cyclic plasticity laws will be assumed at the slip system level (cf. (19)) to match the observed cyclic stress-strain response for the aggregate of grains. Moreover, the contribution of misorientation to blockage of fatigue crack growth under HCF conditions must be taken into account.

2. Using two dimensional finite element solutions based on planar double slip as an approximation of three-dimensional crystal plasticity, the cyclic stress and strain distribution in the vicinity of the crack tip will be determined for cracks with length ranging from sub-grain dimension to up to 10 grains in an equiaxed microstructure. It will be assumed that growth occurs in the orientation of one of the two slip systems in each grain (i.e. Stage I growth). Each grain will have one overall orientation of slip systems initially; to capture gradient effects of deformation within grains, it will be necessary to subdivide the grain into compatible elements with the same initial orientation which experience different degrees of slip.

The resulting information will be used to develop an approach for propagation of small cracks in the presence of microstructure interactions, including amplitude and stress state effects. Furthermore, since the grain size appears explicitly in the calculations, it may be possible for the first time to quantify the elusive conditions for transition from Stage I to Stage II in terms of the ratio of crack length to grain size, including possible additional effects of stress state and amplitude. These calculations should also shed additional insight

into mechanisms of arrest for sub-grain size cracks and the occurrence of a fatigue limit as a function of stress state. Furthermore, the basis for transition from nonlinear, perhaps oscillatory, crack length dependence to approximately linear crack length dependence observed for crack lengths in excess of 3-5 grain diameters might be understood from these calculations. By considering the cyclic crack tip opening as a function of crack length, amplitude and stress state, these calculations might also serve to improve on the isotropic continuum finite element calculations (cf. (20)) which presently serve as a basis for accounting for plasticity-induced crack closure effects.

VI.2 Recommendations

The recommendations for this work are concerned with expanding the description of the microstructure as well as including a simulated roughness-induced closure effect for small fatigue cracks. Qualitative analyses of this type are crucial in providing an understanding of the mechanisms which contribute to the anomalous behavior of small cracks as well as the changing role of the microstructure and its effect on the crack growth rate.

VI.2.1 Slip Intensification

In using 2-D planar double slip crystal plasticity concepts in simulating the microstructure, equal probability of slip on either slip system was assumed for all micromechanical analyses such that plasticity effects are only included in the model. For the crack analyses which align one of the two slip systems along the crack plane, additional analyses were performed such that the slip system that was aligned with the crack plane was modeled with a slip system resistance that was 20% lower than the resistance on the other slip system. This was done to determine if preferential softening along one slip system would have an effect on the amount of sliding and opening displacements as compared to the slip systems with equal resistance, G . In a similar work by Repetto and Ortiz (), they used planar double slip crystal plasticity to simulate the behavior of a persistent slip band such that a “band” of material was given properties which allowed material along that direction to experience preferential softening, thereby producing increased sliding displacements along that direction.

All cases considered for these analyses were performed at 90% of the yield strain and displacements were taken at $2\text{ }\mu\text{m}$ behind the crack tip. Figure VI.1 shows the cyclic CTSD and CTOD results for a crack oriented at 45° with respect to the tensile axis for $a/d = 0.25$. The sliding and opening displacements from the previous analyses with equal resistance on the slip systems are also plotted. The results show that at $2\text{ }\mu\text{m}$ behind the crack tip, there

is nearly a 12% increase in the opening and sliding displacements for both the single and conjugate slip cases with preferential softening as compared to the cases with equal slip resistance.

Figures VI.2-VI.4 show the cyclic CTSD and CTOD results for a crack oriented at 90° with respect to the tensile axis for $a/d = 0.25, 0.97$, and 1.97 , respectively. For the two highest strain amplitudes, there was no appreciable difference in the CTSD and CTOD for cases of preferential slip and equal slip resistance. One explanation is that the driving forces for remote shear loading and at the amplitude of $0.9 \gamma_y$ (for $a/d = 0.97$ and 1.97) are high enough such that the resistance to slip has a minimal effect on accentuating driving forces which are already elevated.

VI.2.2 Remeshing with Growing Small Crack

Studying the effects of differing crack paths is another consideration in understanding the effects of heterogeneity on the behavior of small fatigue cracks. In recent work by Gardner and Qu (), a remeshing technique in ABAQUS () has been formulated which uses a K criterion to grow a small surface crack in a 2-D field. The model correctly shows the fatigue growth (under cyclic tensile loading) of a small crack from Stage I to Stage II crack growth. By combining planar double slip crystal plasticity within a finite element mesh with a remeshing algorithm, more of a statistical aspect for small crack growth behavior may be obtained.

VI.2.3 Frictional Contact along the Crack Face

Since plasticity effects were considered for this work, a second order aspect of small crack growth is the consideration of frictional contact along the crack face. Friction would not only offer resistance to crack face motion, but would serve as a means to quantify roughness-induced closure effects for small fatigue cracks. A coefficient of friction of 0.4 was used for all cases.

VI.2.3.1 Cyclic Tension-Compression

In Figures IV.7 - IV.8 is the plot for friction along the crack face. The addition of friction along the crack face does effectively reduce the amount of sliding displacements with a limited effect on the opening displacements. At the amplitude of $0.9 \epsilon_y$, the sliding displacements are effectively reduced by one half upon entering the third cycle of loading.

VI.2.3.2 Cyclic Shear

In Figures IV.9 - IV.10 show the effect of friction for the cyclic shear case. For $a/d = 0.25$, there is minimal affect of the friction on the sliding and opening displacements. For a higher a/d value in Fig. IV.10, there is a marked difference in the sliding behavior,

especially for increased cycling.

VI.2.4 Numerical Simulations of Small Crack Growth

In determining the remaining life of components under HCF, there are many tools at the disposal of the researcher. One of the numerical tools that has recently been applied to model small crack growth is expert systems. Steadman *et al.* (141) applied a novel numerical algorithm - an expert system methodology - which captures the distortion effects associated with the small crack front including trapping (retardation) as well as eventual circumvention of each obstacle. For cyclic loading conditions, a history of crack front shapes and associated growth rates are simulated as the crack front advances. Expert system methodologies can be thought of as the next generation of Monte Carlo simulations (142) for they provide another layer of detail for the microstructure and growth simulation capabilities. Although this method has only been applied to one layer or one dimension of crack expansion, it can be readily expanded to simulate a more three-dimensional crack front. Some constraints to the numerical simulations are closure levels cannot be properly determined.

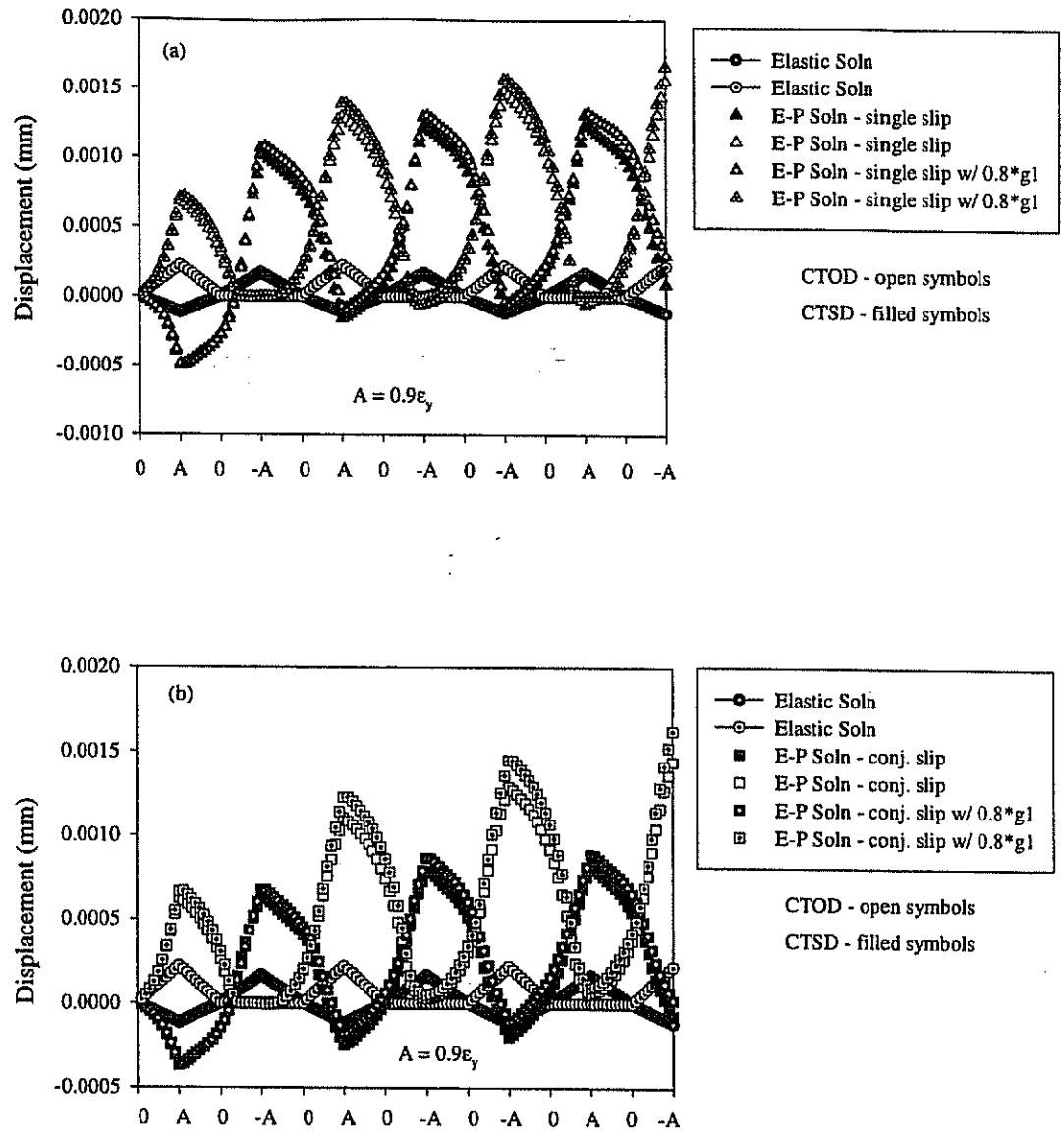


Figure VI.1 Cyclic CTOD and CTSD for cyclic tension-compression loading for crack oriented at 45° with $a/d = 0.25$ for a strain amplitudes of $0.9\epsilon_y$ with preferential softening of $0.8 \cdot g1$ (along slip direction aligned with the crack plane) at a distance of $2 \mu\text{m}$ behind crack tip for (a) single and (b) conjugate slip.

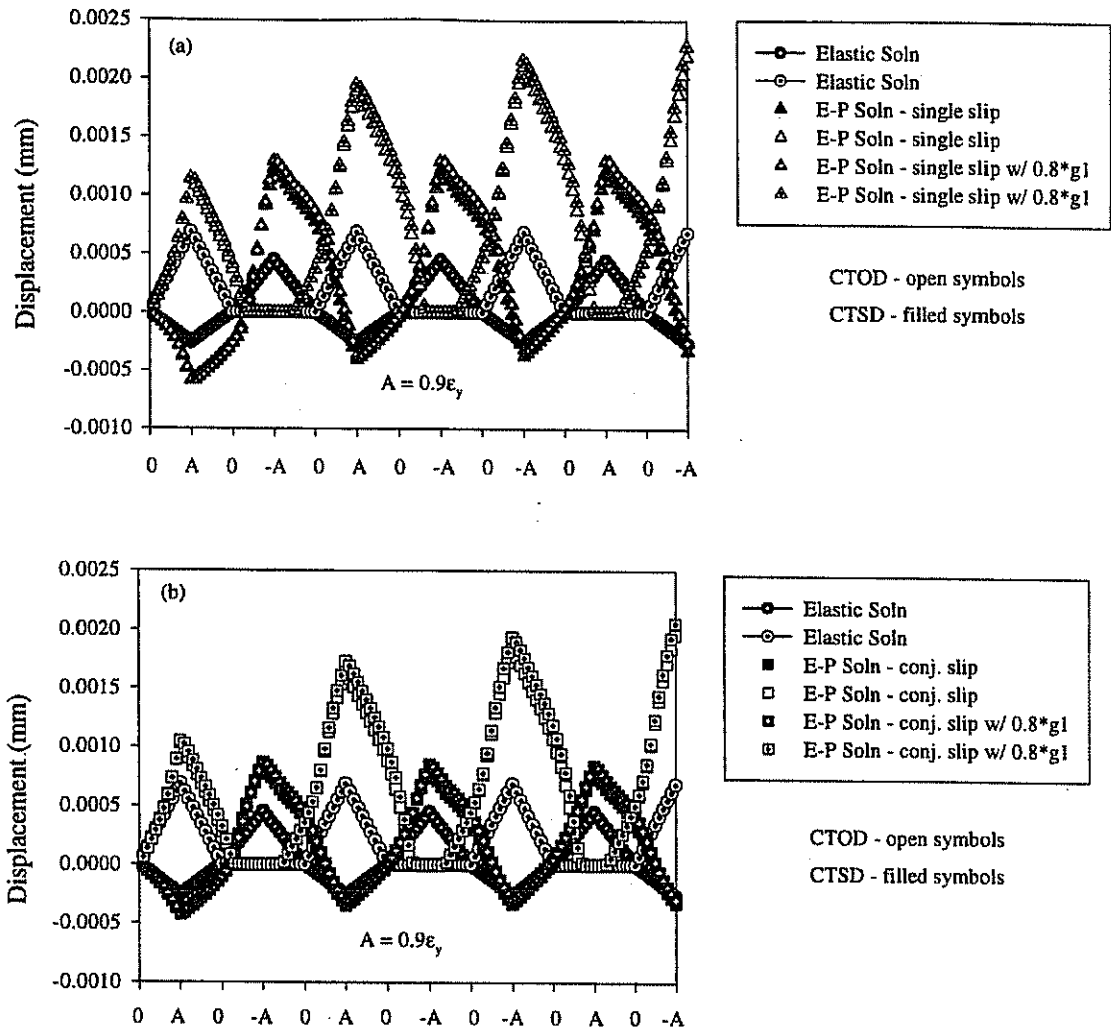


Figure VI.2 Cyclic CTOD and CTSD for cyclic tension-compression loading for crack oriented at 45° with $a/d = 0.25$ for a strain amplitudes of $0.9\epsilon_y$ with preferential softening of $0.8 \cdot g_1$ (along slip direction aligned with the crack plane) at a displacement of $18 \mu\text{m}$ behind crack tip for (a) single and (b) conjugate slip.

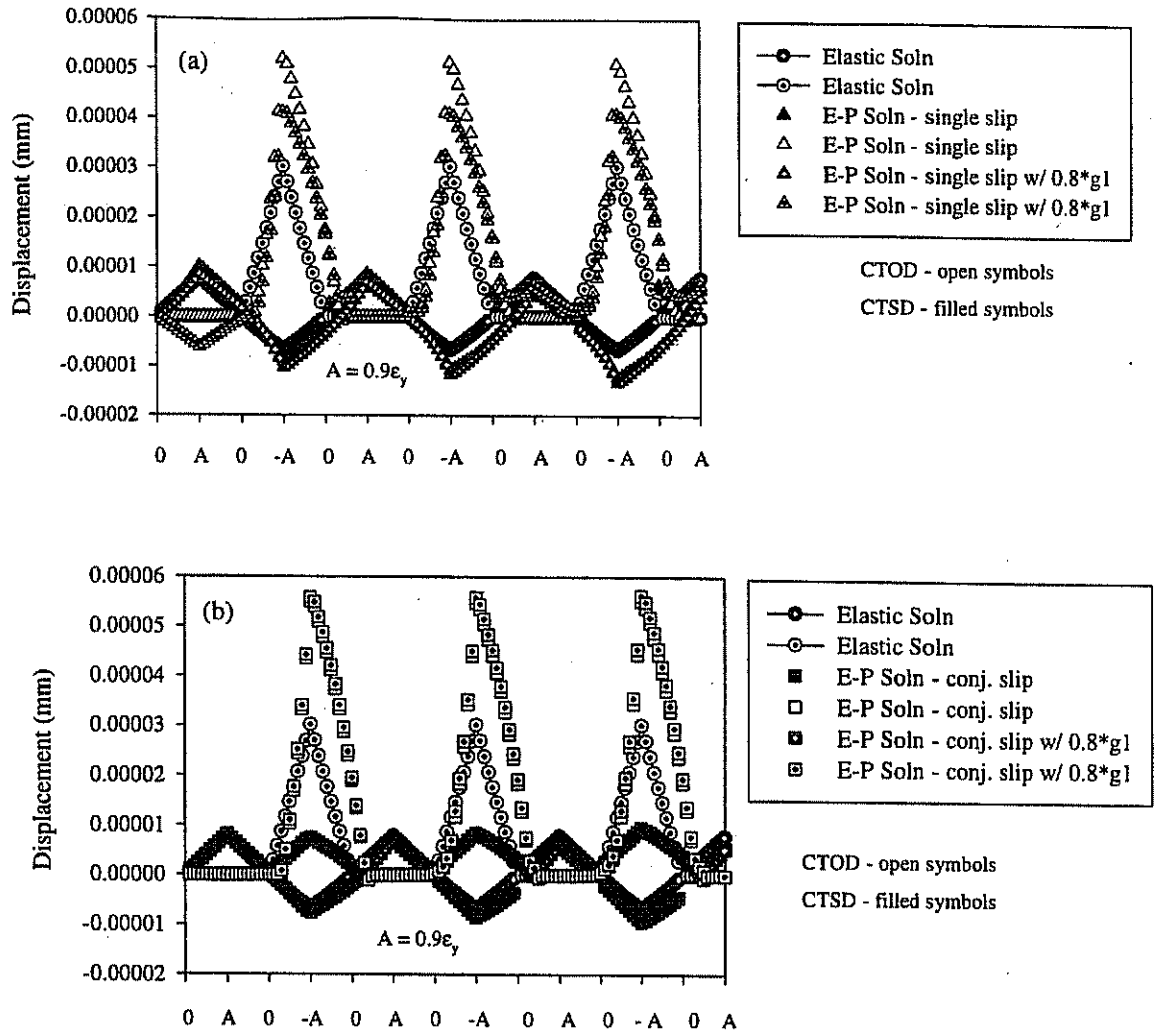


Figure VI.3 Cyclic CTOD and CTSD for cyclic tension-compression loading for crack oriented at 90° with $a/d = 0.25$ for a strain amplitudes of $0.9\gamma_y$ with preferential softening of $0.8 \cdot g1$ (along slip direction aligned with the crack plane) at a distance of $2 \mu\text{m}$ behind crack tip for (a) single and (b) conjugate slip.

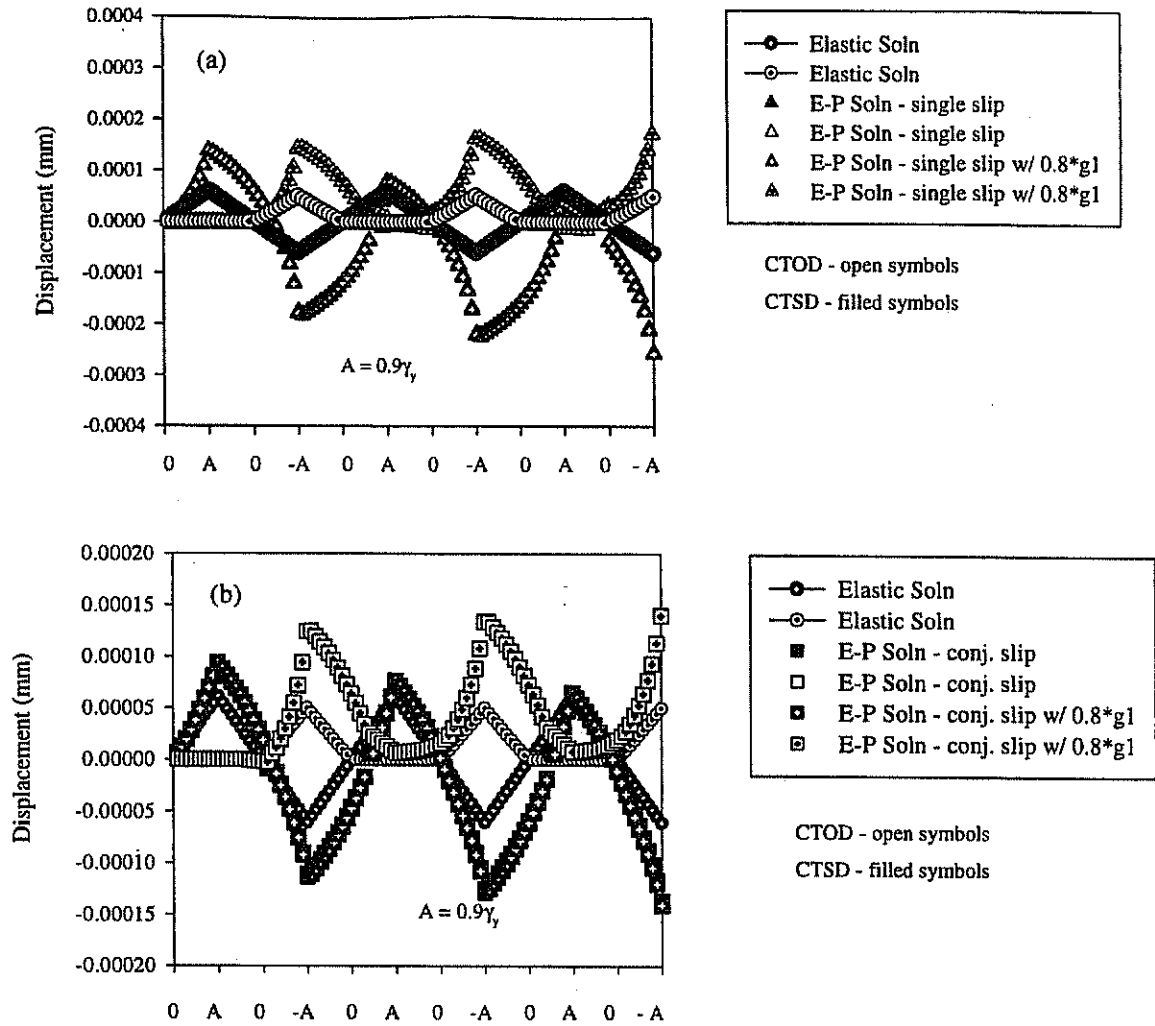


Figure VI.4 Cyclic CTOD and CTSD for cyclic shear loading for crack oriented at 90° with $a/d = 0.97$ for a strain amplitudes of $0.9\gamma_y$ with preferential softening of $0.8 \cdot g1$ (along slip direction aligned with the crack plane) at a distance of $2 \mu\text{m}$ behind crack tip for (a) single and (b) conjugate slip.

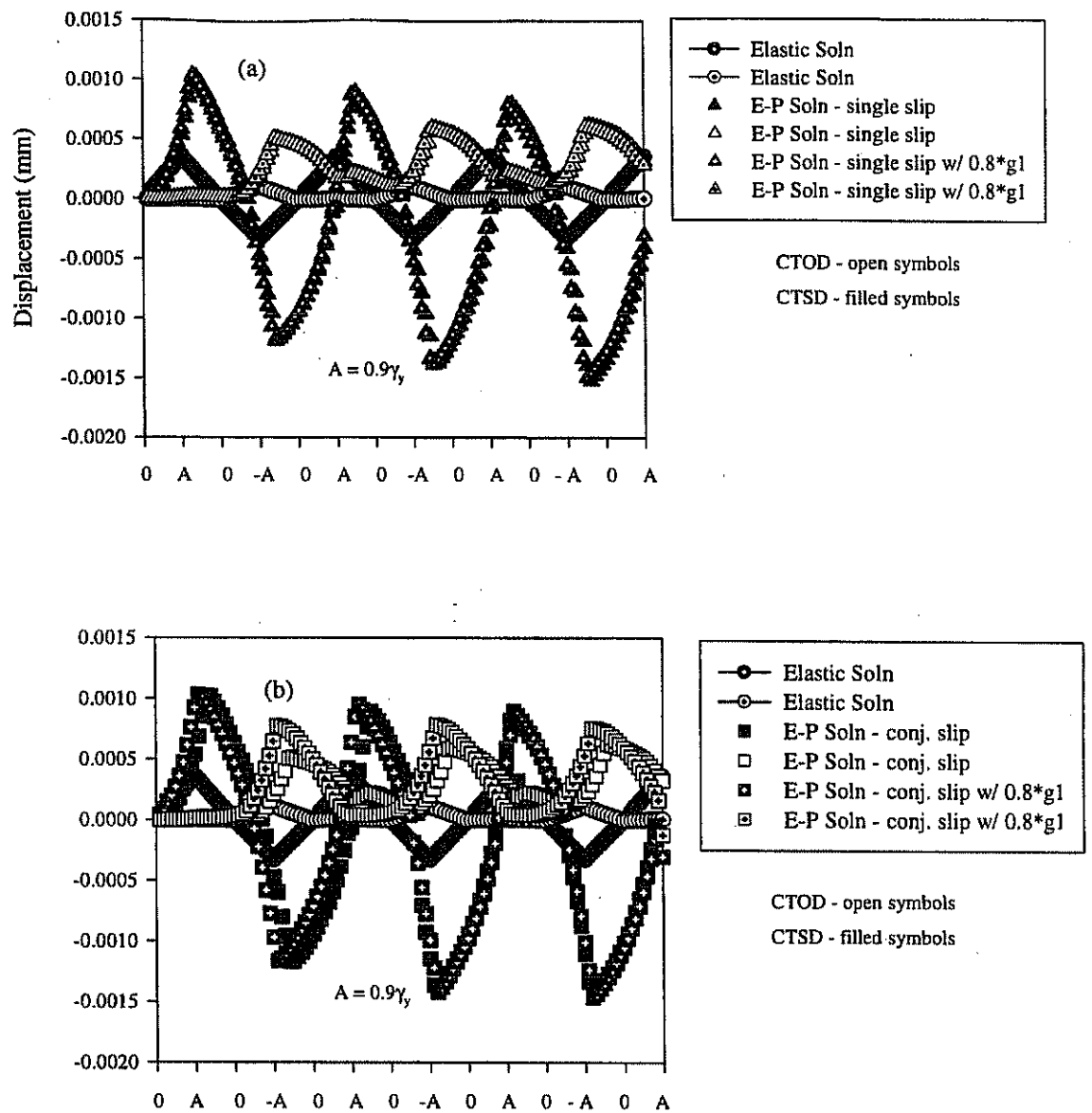


Figure VI.5 Cyclic CTOD and CTSD for cyclic shear loading for crack oriented at 90° with $a/d = 1.97$ for a strain amplitudes of $0.9\gamma_y$ with preferential softening of $0.8 \cdot g_1$ (along slip direction aligned with the crack plane) at a distance of $2 \mu\text{m}$ behind crack tip for (a) single and (b) conjugate slip.

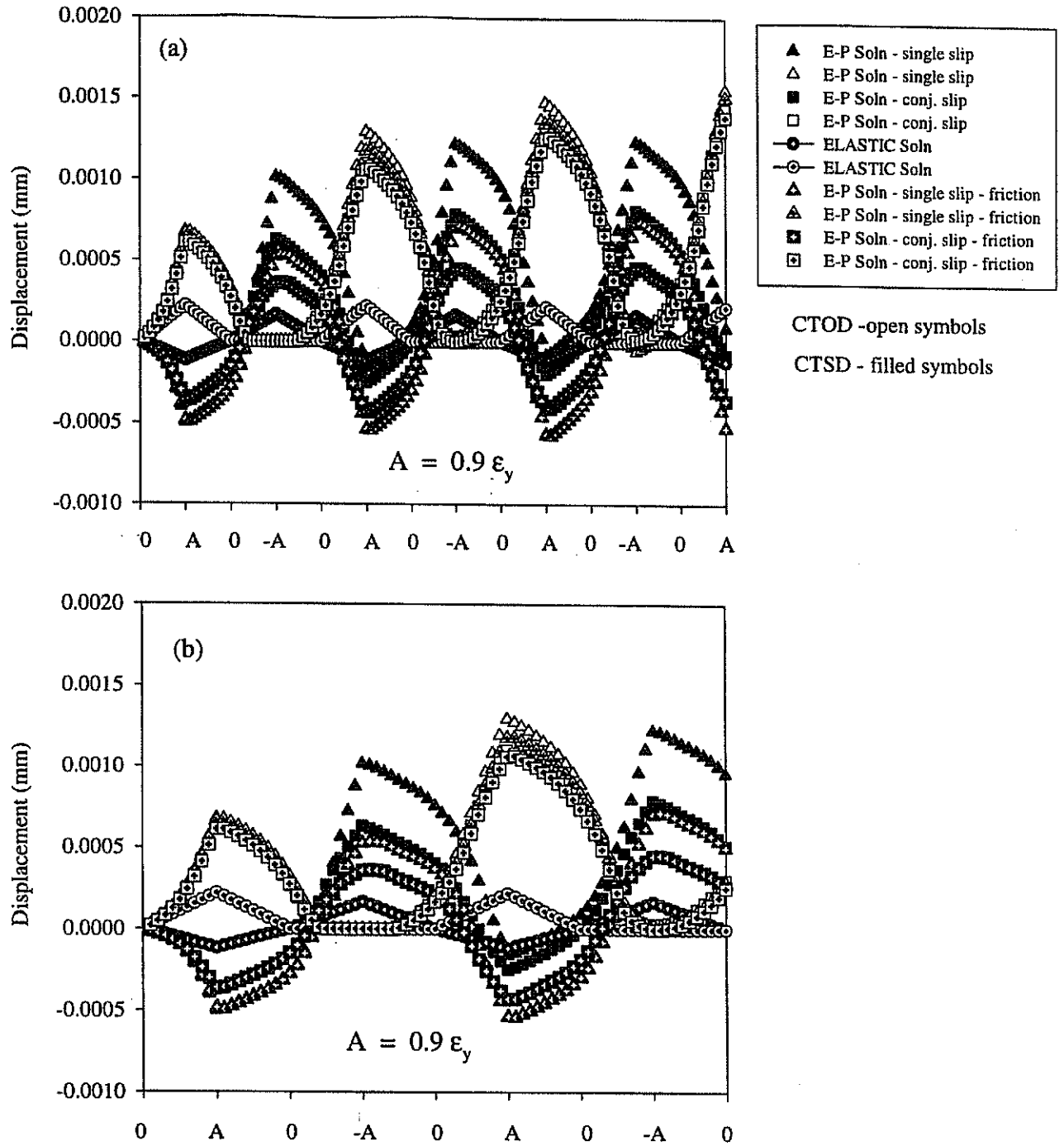


Figure VI.7 Cyclic CTSD and CTOD for cyclic tension-compression loading for crack oriented at 45° with $a/d = 0.25$ for a strain amplitude of $0.9 \epsilon_y$ with a coefficient of friction of 0.4 on the crack faces at a distance of $2 \mu\text{m}$ behind the crack tip for single and conjugate slip cases (a) for all three cycles and (b) exploded view of first two cycles.

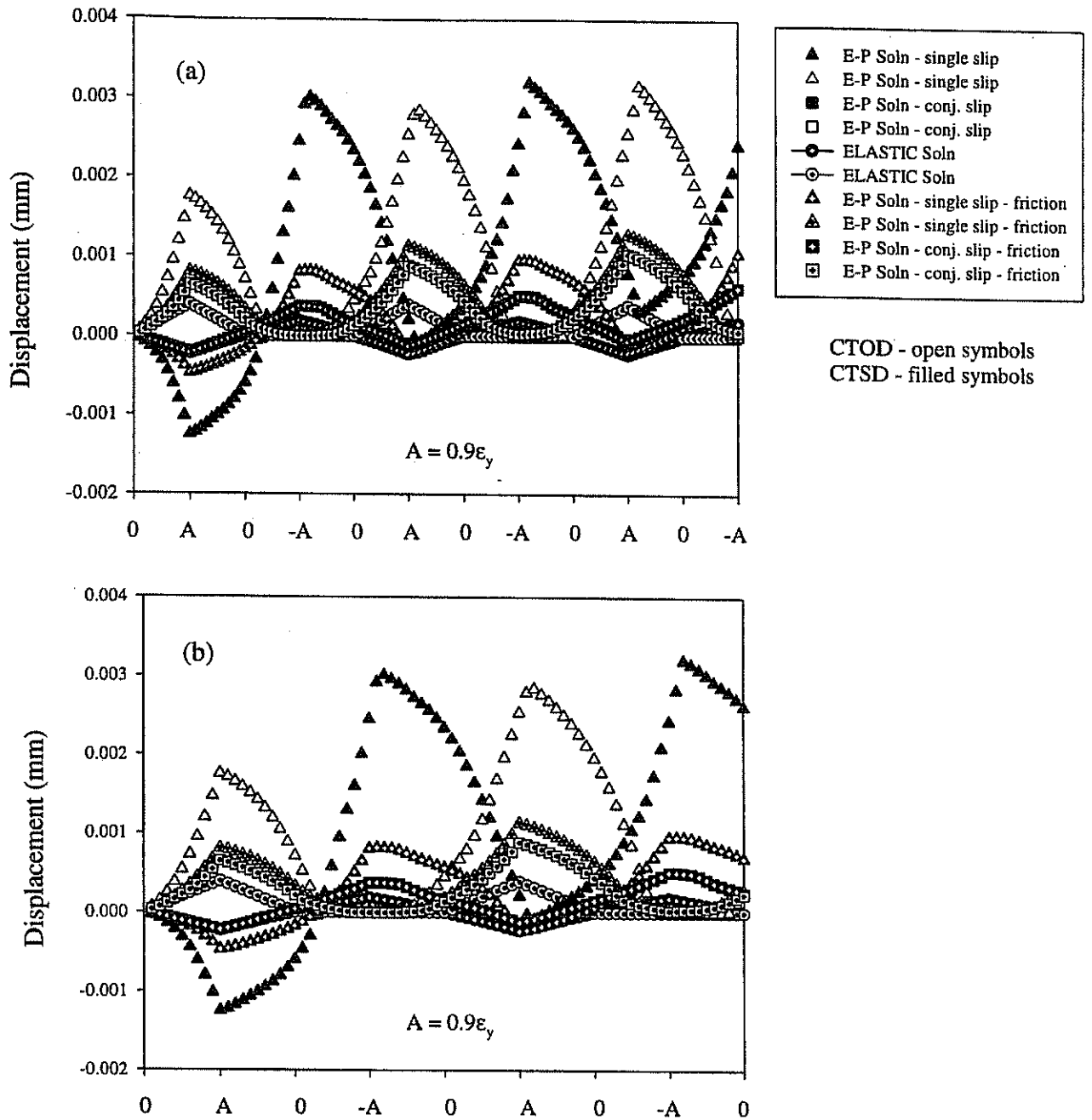


Figure VI.8 Cyclic CTSD and CTOD for cyclic tension-compression loading for crack oriented at 45° with $a/d = 0.97$ for a strain amplitude of $0.9 \epsilon_y$ with a coefficient of friction of 0.4 on the crack faces at a distance of $2 \mu\text{m}$ behind the crack tip for single and conjugate slip cases (a) for all three cycles and (b) exploded view of first two cycles.

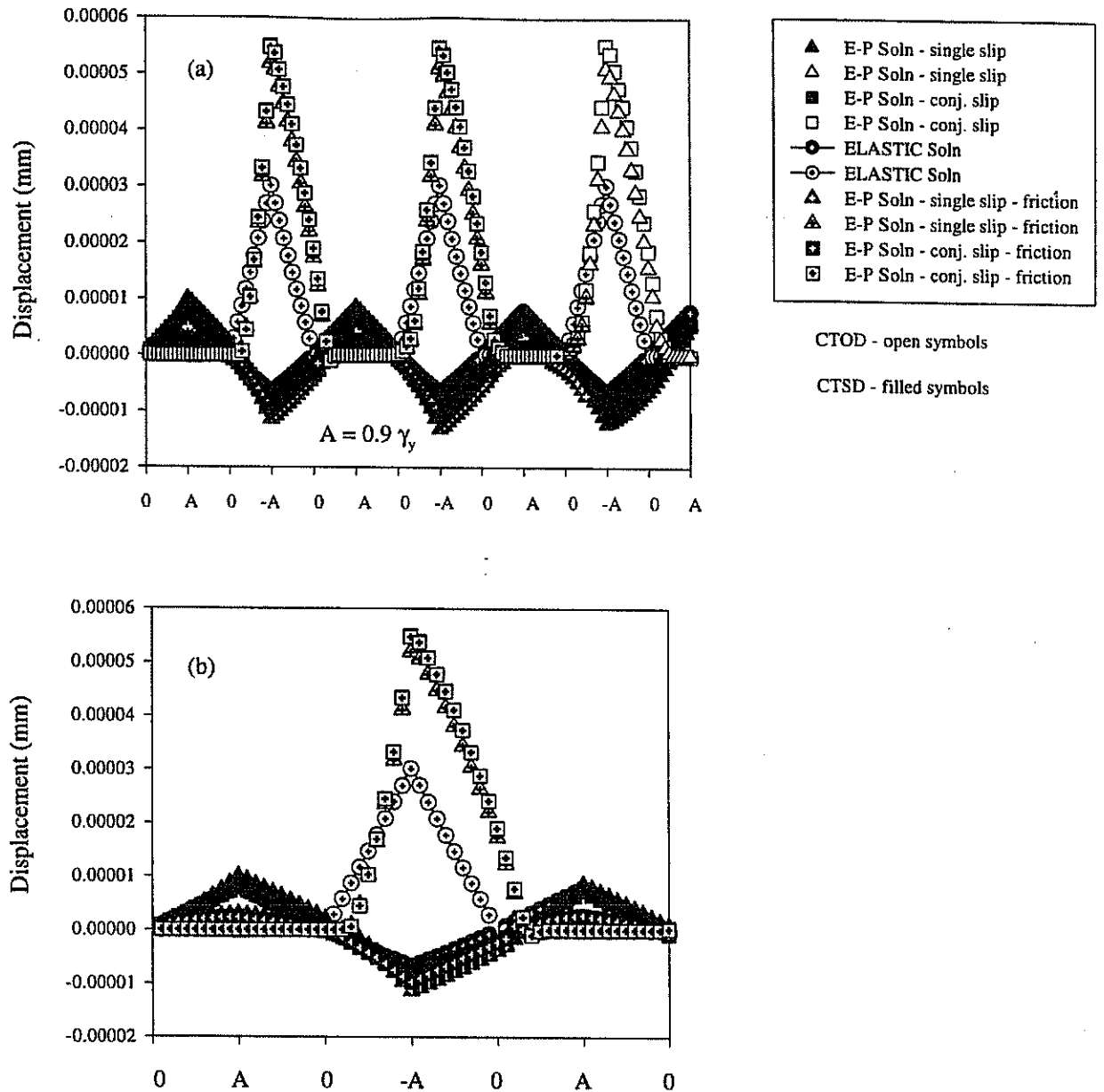


Figure VI.9 Cyclic CTSD and CTOD for cyclic tension-compression loading for crack oriented at 90° with respect to the tensile axis with $a/d = 0.25$ for a strain amplitude of $0.9 \gamma_y$ with a coefficient of friction of 0.4 on the crack faces at a distance of $2 \mu\text{m}$ behind the crack tip for single and conjugate slip cases (a) for all three cycles and (b) exploded view of first two cycles.

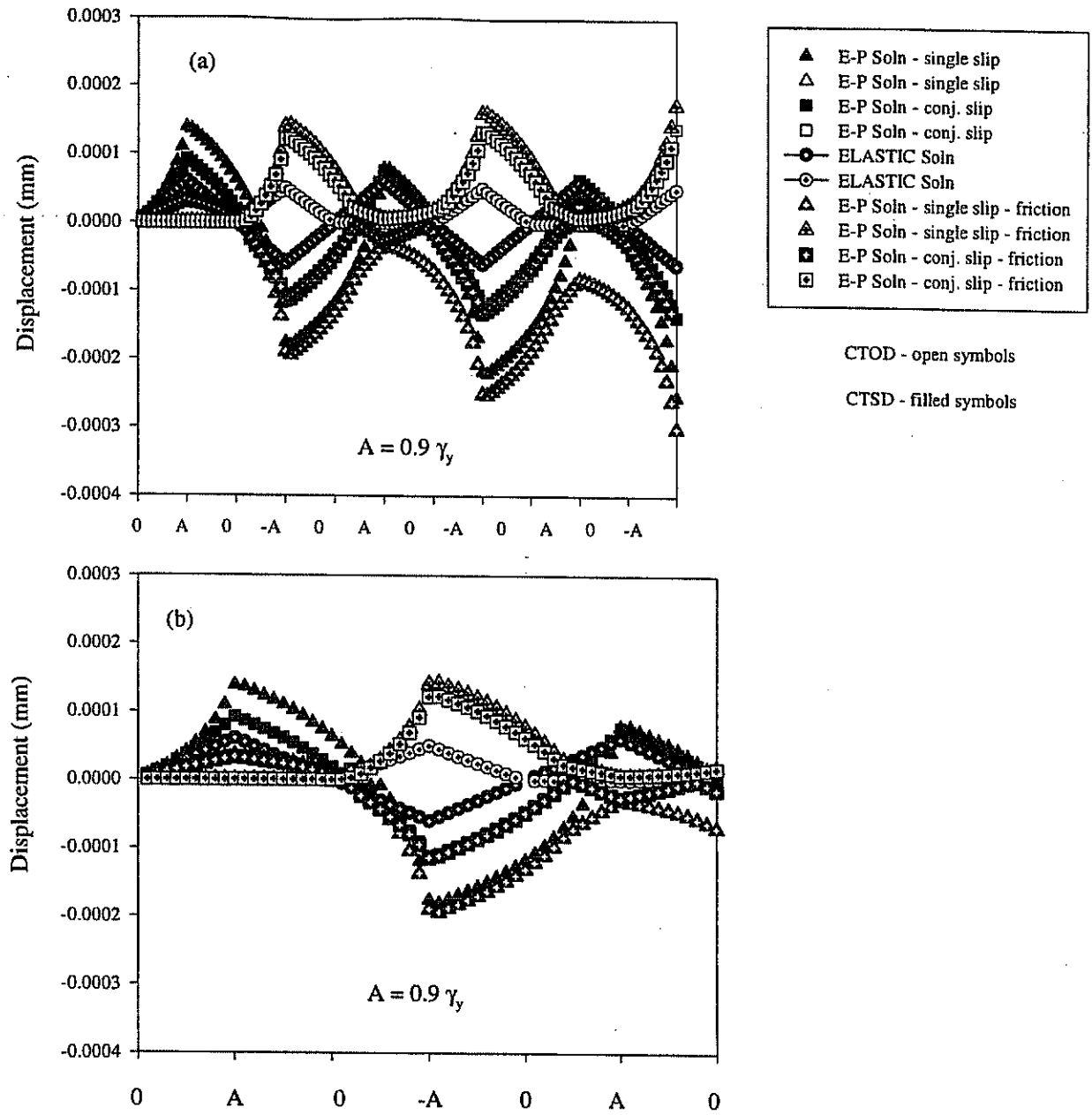


Figure VI.10 Cyclic CTSD and CTOD for cyclic tension-compression loading for crack oriented at 90° with respect to the tensile axis with $a/d = 0.97$ for a strain amplitude of $0.9 \gamma_y$ with a coefficient of friction of 0.4 on the crack faces at a distance of $2 \mu\text{m}$ behind the crack tip for single and conjugate slip cases (a) for all three cycles and (b) exploded view of first two cycles.

REFERENCES

- (1) Suresh, S., Fatigue of Materials, Cambridge University Press, Great Britain, 1991.
- (2) McDowell, D. L. and Berard, J.-Y., 1990, "A ΔJ -Based Approach to Biaxial Low-Cycle Fatigue of Shear Damaged Materials," in Fatigue Under Biaxial and Multiaxial Loading, ESIS10, K. Kussmaul, D. McDiarmid and D. Socie, Eds., Mechanical Engineering Publications, London, pp. 413-431.
- (3) McDowell, D. L. and Berard, J.-Y., 1992, "A ΔJ -Based Approach to Biaxial Fatigue," Fatigue and Fracture of Engineering Materials and Structures, Vol. 15, No. 8, pp. 719-741.
- (4) Socie, D. F., 1993, "Critical Plane Approaches for Multiaxial Fatigue Damage Assessment," in Advances in Multiaxial Fatigue, ASTM STP 1191, D. L. McDowell and R. Ellis, Eds., ASTM, Philadelphia, pp. 7-36.
- (5) Socie, D., 1987, "Multiaxial Fatigue Damage Models," ASME Journal of Engineering Materials and Technology, Vol. 109, pp. 293-298.
- (6) Brown, M. and Miller, K. J., 1973, "A Theory for Fatigue Failure Under Multiaxial Stress-Strain Conditions," Proceedings, Institution for Mechanical Engineers, London, Vol. 187, No. 65, pp. 745-755.
- (7) Brown, M. and Miller, K. J., 1982, "Two Decades of Progress in the Assessment of Multiaxial Low-Cycle Fatigue Life," in Low Cycle Fatigue and Life Prediction, ASTM STP 770, C. Amzallag, B. Leis, and P. Rabbe, Eds., ASTM, Philadelphia, pp. 482-499.
- (8) Hoshide, T. and Socie, D. F., 1987, "Mechanics of Mixed Mode Small Fatigue Crack Growth," Engineering Fracture Mechanics, Vol. 26, No. 6, pp. 842-850.
- (9) Dang-Van, K., 1993, "Macro-Micro Approach in High-Cyclic Multiaxial Fatigue," in Advances in Multiaxial Fatigue, ASTM STP 1191, D. L. McDowell and R. Ellis, Eds., ASTM, Philadelphia, pp. 120-130.
- (10) Miller, K. J., 1993, "The Two Thresholds of Fatigue Behavior," Fatigue and Fracture of Engineering Materials and Structures, Vol. 16, No. 9, pp. 931-939.

- (11) Miller, K. J., 1993, "Materials Science Perspective of Metal Fatigue Resistance," *Materials Science and Technology*, Vol. 9, pp. 453-462.
- (12) Tanaka, K., 1987, "Short-Crack Fracture Mechanics in Fatigue Conditions," in Current Research on Fatigue Cracks, T. Tanaka, M. Jono and K. Komai, Eds., *Current Japanese Materials Research*, Vol. 1, Elsevier, pp. 93-117.
- (13) Hoshide, T., Miyahara, M. and Inoue, T., 1988, "Elastic-Plastic Behavior of Short Fatigue Cracks in Smooth Specimens," in Basic Questions in Fatigue: Volume I, ASTM STP 924, J. T. Fong and R. J. Fields, Eds., ASTM, Philadelphia, pp. 312-322.
- (14) Chan, K., Lankford, J. and Davidson, D., 1986, "A Comparison of Crack-Tip Field Parameters for Large and Small Fatigue Cracks," *ASME Journal of Engineering Materials and Technology*, Vol. 108, pp. 206-213.
- (15) Berard, J.-Y., McDowell, D. L. and Antolovich, S. D., 1993, "Damage Observations of a Low-Carbon Steel Under Tension-Torsion Low-Cycle Fatigue," in Advances in Multiaxial Fatigue, ASTM STP 1191, D. L. McDowell and R. Ellis, Eds., ASTM, Philadelphia, pp. 326-344.
- (16) O'Connor, J., 1994, "Probabilistic Reliability Modeling of Fatigue on the H-46 Tie Bar," Master's Thesis, Naval Postgraduate School, Monterey, CA.
- (17) Bates, P. R., MH-53J Main Rotor Hub Crack Propagation Testing and Analysis, Georgia Tech Research Institute, Atlanta, 1990-1993, Projects A-8788 and A-8699.
- (18) McDowell, D. and Bennett, V., 1997, "Micromechanical Aspects of Small Multiaxial Fatigue Cracks," in *Proceedings, 5th International Conference on Biaxial/Multiaxial Fatigue and Fracture*, E. Macha and Z. Mróz, Eds., Poland, Sept. 8-12, 1997.
- (19) McClung, R. C., Chan, K. S., Hudak, S. J., Jr., and Davidson, D. L., 1994, "Analysis of Small Crack Behavior for Airframe Applications," NASA CP 3274, Part 1, pp. 463-479.
- (20) McDowell, D. L. and Poindexter, V., 1994, "Multiaxial Fatigue Modeling Based on Microcrack Propagation: Stress State and Amplitude Effects," in *Proceedings, 4th International Conference on Biaxial/Multiaxial Fatigue*, May 31-June 3, 1994, Paris, France.
- (21) Cahn, R. W., Haasen, P., and Kramer, E. J., Materials Science and Technology - A Comprehensive Treatment, Wiley-VCH, New York, 1998.

- (22) Plumbridge, W. J., 1972, "Review: Fatigue-Crack Propagation in Metallic and Polymeric Materials," *Journal of Materials Science*, Vol. 7, pp. 939-962.
- (23) Li, X. 1996, "Micromechanical Model of Stage I to Stage II Crack Growth Transition for Aluminum Alloys," *Theoretical and Applied Fracture Mechanics*, Vol. 24, pp. 217-231.
- (24) Pearson, S., 1975, "Initiation of Fatigue Cracks in Commercial Aluminum Alloys and the Subsequent Propagation of Very Short Cracks," *Engineering Fracture Mechanics*, Vol. 7, pp. 235-247.
- (25) Carlson, R. L., Dancila, D. S., and Kardomateas, G. A., 1996, "An Investigation of the Growth of Small Corner Cracks from Small Flaws in 6061-T651 Aluminum," *Proceedings of the 6th International Fatigue conference*, pp.
- (26) Bannantine, J. A., Comer, J. J., and Handrock, J. L., Fundamentals of Metal Fatigue Analysis, Prentice Hall, New Jersey, 1990.
- (27) Gdoutos, E. E., and Zacharopoulos, D. A., 1990, "A Damage Model for Crack Initiation and Growth," *Theoretical and Applied Fracture Mechanics*, Vol. 14, pp. 117-122.
- (28) Chow C. L., and Wei, Y., 1991, "A Damage Mechanics Model of Fatigue Crack Initiation in Notched Plates," *Theoretical and Applied Fracture Mechanics*, Vol. 16, pp. 123-133.
- (29) Wang, J., and Chow, C. L., 1989, "Mixed Mode Ductile Fracture Studies with Nonproportional Loading Based on Continuum Damage Mechanics," *ASME Journal of Engineering Materials and Technology*, Vol. 111, pp. 205-209.
- (30) Lemaitre, J., 1985, "A Continuous Damage Mechanics Model for Ductile Fracture," *ASME Journal of Engineering Materials and Technology*, Vol. 107, pp. 83-89.
- (31) Inoue, T., Hoshide, T., Yoshikawa, T., and Kimura, Y., 1986, "Slip Band Behavior and Crack Initiation in Polycrystalline Copper under Multiaxial Low-Cycle Fatigue-- A Damage Mechanics Approach," *Engineering Fracture Mechanics*, Vol. 25, Nos. 5/6, pp. 665-675.
- (32) Manson, S. S. and Halford, G. R., 1986, "Re-Examination of Cumulative Fatigue Damage Analysis -- An Engineering Perspective," *Engineering Fracture Mechanics*, Vol. 25, Nos. 5/6, pp. 539-571.

- (33) Manson, S. S. and Halford, G. R., 1981, "Practical Implementation of the Double Linear Damage Rule and Damage Curve Approach for Treating Cumulative Fatigue Damage," *International Journal of Fracture*, Vol. 17, No. 2, pp. 169-192.
- (34) Socie, D. F., Waill, L. A., and Dittmer, D. F., 1985, "Biaxial Fatigue of Inconel 718 Including Mean Stress Effects," in Multiaxial Fatigue, ASTM STP 853, K. J. Miller and M. W. Brown, Eds., ASTM, Philadelphia, pp. 463-481.
- (35) McDowell, D. L., 1996, "Multiaxial Fatigue Strength," *ASM Handbook*, Vol. 19, pp. 263-273.
- (36) Stulen, F. B. and Cummings, H. N., 1954, "A Failure Criterion for Multiaxial Fatigue Stresses," *Proceedings of the ASTM*, Vol. 54, pp. 822-835.
- (37) Findley, W. N., Coleman, J. J., and Handley, B. C., 1956, "Theory for Combined Bending and Torsion Fatigue with Data for 4340 Steel," in *Proceedings, International Conference on Fatigue of Metals*, The Institution of Mechanical Engineers, New York, pp. 150-157.
- (38) Findley, W. N., 1959, "A Theory for the Effect of Mean Stress on Fatigue of Metals Under Combined Torsion and Axial Load or Bending," *Journal of Engineering for Industry*, pp. 301-306.
- (39) Socie, D. F., Kurath, D., and Koch, J. L., 1985, "A Multiaxial Fatigue Damage Parameter," in *Proceedings, 2nd International Symposium on Multiaxial Fatigue*, Sheffield, UK, pp.
- (40) Fatemi, A. and Socie, D. F., 1988, "Critical Plane Approach to Multiaxial Fatigue Damage including Out-of-Phase Loading," *Fatigue and Fracture of Engineering Materials and Structures*, Vol. 11, No. 3, pp. 149-165.
- (41) Gough, H. J., Pollard, H. V., and Clenshaw, W. J., 1951, "Some Experiments on the Resistance of Metals under Combined Stress," *Ministry of Supply, Aeronautical Research Council Reports and Memoranda No. 2522*, HMSO, London.
- (42) Kurath, P. and Fatemi, A., 1990, "Cracking Mechanisms for Mean Stress/Strain Low-Cycle Multiaxial Fatigue Loading," in Quantitative Methods in Fractography, ASTM STP 1085, B. M. Strauss and S. K. Putatunda, Eds., ASTM, Philadelphia, pp. 123-143.

- (43) Wang, Y. and Pan, J., 1998, "Constraint Effects on Small Mixed-Mode Cracks and Fatigue Damage Parameter under Multiaxial Loading Conditions," in Fatigue, Fracture, and Residual Stresses, PVP-373, S. Rahman, Ed., ASME, pp.191-196.
- (44) Reddy, S. and Fatemi, A., 1992, "Small Crack Growth in Multiaxial Fatigue," in Advances in Fatigue Lifetime Predictive Techniques, ASTM STP 1122, M. R. Mitchell and R. W. Landgraf, Eds., ASTM Philadelphia, pp. 276-298.
- (45) Dowling, N. E. and Begley, J. A., 1976, "Fatigue Crack Growth During Gross Plasticity and the J-Integral" in Mechanics of Crack Growth, ASTM STP 590, J. R. Rice and P. C. Paris, Eds., ASTM, Philadelphia, pp. 82-103.
- (46) Ogata, T., Nitta, A. and Blass, J. J., 1993, "Propagation Behavior of Small Cracks in 304 Stainless Steel Under Biaxial Low-Cycle Fatigue at Elevated Temperature," in Advances in Multiaxial Fatigue, ASTM STP 1191, D.L. McDowell and R. Ellis, Eds., ASTM, Philadelphia, pp. 313-325.
- (47) Nisitani, H., 1987, "Behavior of Small Cracks in Fatigue and Relating Phenomena," in Current Research on Fatigue Cracks, T. Tanaka, M. Jono and K. Komai, Eds., Current Japanese Materials Research, Vol. 1, Elsevier, pp. 1-26.
- (48) Murakami, Y., 1988, "Correlation Between Strain Singularity at Crack Tip under Overall Plastic Deformation and the Exponent of the Coffin-Manson Law," in Low Cycle Fatigue, ASTM STP 942, H.D. Solomon, G.R. Halford, L.R. Kaisand, and B.N. Leis, Eds., ASTM, Philadelphia, pp. 1048-1065.
- (49) Lamba, H.S., 1975, "The J-Integral Applied to Cyclic Loading," Engineering Fracture Mechanics, Vol. 7, p. 693.
- (50) Tanaka, K., 1983, "The Cyclic J-Integral as a Criterion for Fatigue Crack Growth," International Journal of Fracture, Vol. 22, pp. 91-104.
- (51) Dowling, N.E., 1977, "Crack Growth During Low-Cycle Fatigue of Smooth Axial Specimens," in Cyclic Stress-Strain and Plastic Deformation Aspects of Fatigue Crack Growth, ASTM STP 637, L. F. Imperlizzeri, Ed., ASTM, Philadelphia, pp. 97-121.
- (52) Shih, C. F. and Hutchinson, J. W., 1976, "Fully Plastic Solutions and Large Scale Yielding Estimates for Planes Stress and Crack Problems," ASME Journal of Engineering Materials and Technology, Vol. 98, pp. 289-295.

- (53) Breat, J. L., Mudry, F., and Pineau, A., 1983, "Short Crack Propagation and Closure Effects in A508 Steel," *Fatigue of Engineering Materials and Structures*, Vol. 6, No. 4, pp. 349-358.
- (54) Hussain, K., de Los Rios, E. R., and Navarro, A., 1993, "A Two-Stage Micromechanics Model for Short Fatigue Cracks," *Engineering Fracture Mechanics*, Vol. 44, No. 3, pp. 425-436.
- (55) Forsyth, P. J. E., 1971, "A Two-Stage Process of Fatigue Crack Growth," in *Proceedings, Symposium on Crack Propagation*, Cranfield, pp. 76-94.
- (56) McDowell, D., 1997, "Multiaxial Small Fatigue Crack Growth in Metals," *International Journal of Fatigue*, Vol. 19, No. 1 Supplement, pp. S127-S135.
- (57) Cox, H. L. and Field, J. E., 1952, "The Initiation and Propagation of Fatigue Cracks in Mild Steel Pieces of Square Section," *Aeronautics Quarterly*, Vol. 4, pp. 1-19.
- (58) Swenson, D. O., 1969, "Transition Between Stage I and Stage II Modes of Fatigue Crack Growth," *Journal of Applied Physics*, Vol. 40, No. 9, pp. 3467-3475.
- (59) Tanaka, K. and Akinawa, Y., "Propagation and Non-propagation of Small Fatigue Cracks," in *Advances in Fracture Research*, Proc ICF7, Vol. 2, Houston, TX, (March 20-24, 1989), pp. 869-887.
- (60) Riemelmoser, F. O., Pippan, R., and Stüwe, H. P., 1998, "An Argument for a Cycle-By-Cycle Propagation of Fatigue Cracks at Small Stress Intensity Range," *Acta Materialia*, No. 46, No. 5, pp. 1793-1799.
- (61) Dang-Van, K., 1993, "Macro-Micro Approach in High-Cycle Multiaxial Fatigue," in *Advances in Multiaxial Fatigue*, ASTM STP 1191, Eds. D. L. McDowell and R. Ellis, ASTM, Philadelphia, pp. 120-130.
- (62) McDowell, D. L., 1996, "Basic Issues in the Mechanics of High Cycle Fatigue," *International Journal of Fracture*, Vol. 80, pp. 103-145.
- (63) Tong, J., Yates, J. R., and Brown, M. W., 1995, "A Model for Sliding Mode Crack Closure: Parts I & II," *Engineering Fracture Mechanics*, Vol. 52, No. 4, pp. 599-623.

- (64) Zhang, J. Z., Halliday, M. D., Poole, P., and Bowen, P., 1997, "Crack Closure in Small Fatigue Cracks - A Comparison of Finite Element Predictions with In-Situ Scanning Electron Microscope Measurements," *Fatigue and Fracture of Engineering Materials and Structures*, Vol. 20, No. 9, pp. 1279-1293.
- (65) James, M. R. and Morris, W. L., 1983, "Effect of Surface Roughness on Growth of Short Fatigue Cracks," *Metallurgical Transactions A*, Vol. 14A, pp. 153-155.
- (66) Harvey, S. E., Marsh, P. G., and Gerberich, W. W., 1994, "Atomic Force Microscopy and Modeling of Fatigue Crack Initiation in Metals," *Acta Metallurgica et Materialia*, Vol. 42, No. 10, pp. 3493-3502.
- (67) Tanaka, K. and Mura, T., 1981, "A Dislocation Model for Fatigue Crack Initiation," *Journal of Applied Mechanics*, Vol. 48, pp. 97-103.
- (68) Venkataraman, G., Chung, T., Nakasone, Y., and Mura, T., 1990, "Free-Energy Formulation of Fatigue Crack Initiation Along Persistent Slip Bands: Calculation of S-N Curves and Crack Depths," *Acta Metallurgica et Materialia*, Vol. 38, No. 1, pp. 31-40.
- (69) Venkataraman, G., Chung, T., and Mura, T., 1991, "Application of Minimum Energy Formalism in a Multiple Slip Band Model for Fatigue - I. Calculation of Slip Band Spacing," *Acta Metallurgica et Materialia*, Vol. 39, No. 11, pp. 2621-2629.
- (70) Venkataraman, G., Chung, T., and Mura, T., 1991, "Application of Minimum Energy Formalism in a Multiple Slip Band Model for Fatigue - II. Crack Nucleation and Derivation of a Generalized Coffin-Manson Law," *Acta Metallurgica et Materialia*, Vol. 39, No. 11, pp. 2631-2638.
- (71) Newman, Jr., J. C., Bigelow, C. A., and Shivakumar, K. N., 1993, "Three-Dimensional Elastic-Plastic Finite-Element Analyses of Constraint Variations in Cracked Bodies," *Engineering Fracture Mechanics*, Vol. 46, No. 1, pp. 1-13.
- (72) Chan, K. S. and Lankford, J., 1988, "The Role of Microstructural Dissimilitude in Fatigue and Fracture of Small Cracks," *Acta Metallurgica*, Vol. 36, No. 1, pp. 193-206.
- (73) Lankford, J., 1985, "The Influence of Microstructure on the Growth of Small Fatigue Cracks," *Fatigue and Fracture of Engineering Materials and Structures*, Vol. 8, No. 2, pp. 161-175.

- (74) Keller, R. and Gerberich, W. W., 1989, "Surface versus Bulk Deformation in Fatigue," *Scripta Metallurgica*, Vol. 23, pp. 1115-1120.
- (75) Lin, S. R. and Lin, T. H., 1983, "Initial Strain Field and Fatigue Crack Initiation Mechanics," *Journal of Applied Mechanics*, Vol. 50, pp. 367-372.
- (76) Chen, S. H., Katz, Y., and Gerberich, W. W., 1991, "Crack-tip Strain Fields and Fracture Microplasticity in hydrogen-induced cracking of Fe-3wt%Si Single Crystals," *Philosophical Magazine A*, Vol. 63, No. 1, pp. 131-155.
- (77) Zhang, Y. H. and Edwards, L., 1992, "Effect of Grain Boundaries on the Development of Plastic Deformation Ahead of Small Fatigue Cracks," *Scripta Metallurgica et Materialia*, Vol. 26, No. 12, pp. 1901-1906.
- (78) Tomkins, B., 1968, "Fatigue Crack Propagation - An Analysis," *Philosophical Magazine*, Vol. 18, pp. 1041-1066.
- (79) Hobson, P. B., Brown, M. W. Brown, and de los Rios, E. R., 1986, "Two Phases of Short Crack Growth in a Medium Carbon Steel," in *The Behavior of Short Fatigue Cracks*, K. J. Miller and E. R. de los Rios, Eds., EGF Publ. 1, Institution of Mechanical Engineers, London, pp. 441-459.
- (80) Hussain, K., de los Rios, E. R., and Navarro, A., 1993, "A Two-Stage Micromechanics Model for Short Fatigue Cracks," *Engineering Fracture Mechanics*, Vol. 44, No. 3, pp. 425-436.
- (81) Tanaka, K., Akinawa, Y., Nakai, Y., and Wei, R. P., 1986, "Modelling of Small Fatigue Crack Growth Interacting with Grain Boundary," *Engineering Fracture Mechanics*, Vol. 24, No. 6, pp. 803-819.
- (82) Navarro, A. and de los Rios, E. R., 1988, "An Alternative Model of the Blocking of Dislocations at Grain Boundaries," *Philosophical Magazine*, Vol. 57, pp. 37-50.
- (83) Navarro, A. and de los Rios, E. R., 1987, "A Model for Short Fatigue Crack Propagation With an Interpretation of the Short-Long Crack Transition," *Fatigue and Fracture of engineering materials and Structures*, Vol. 10, No. 2, pp. 169-186.
- (84) Sarfarazi, M. and Ghosh, S., 1987, "Microfracture in Polycrystalline Solids," *Engineering Fracture Mechanics*, Vol. 27, No. 3, pp. 257-267.

- (85) Newman, Jr., J. C., and Raju , I. S., 1984, "Prediction of Fatigue Crack-Growth Patterns and Lives in Three-Dimensional Cracked Bodies," in *Advances in Fracture Research*, Vol. 3, Proceedings, 6th International Conference on Fracture (ICF6), Eds., S. R. Valluri, D. M. R. Taplin, P. Rama Rao, J. F. Knott, and R. Dubey, pp. 1597-1608.
- (86) Trantina, G. G., deLorenzi, H. G., and Wildening, W. W., 1983, "Three-Dimensional Elastic-Plastic Finite Element Analysis of Small Surface Cracks," *Engineering Fracture Mechanics*, Vol. 18, No. 5, pp. 925-938.
- (87) Dawicke, D. S., Grandt, Jr., A. F., and Newman, Jr., J. C., 1990, "Three-Dimensional Crack Closure Behavior," *Engineering Fracture Mechanics*, Vol. 36, No. 1, pp. 111-121.
- (88) Newman, Jr., J. C., 1995, "Fatigue-Life Prediction Methodology Using a Crack-Closure Model," *Journal of Engineering Materials and Technology*, Vol. 117, pp. 433-439.
- (89) Wu, X. R., Newman, Jr., J. C., Zhao, W., Swain, M. H., Ding, C. F., and Phillips, E. P., 1998, "Small Crack Growth and Fatigue Life Predictions for High-Strength Aluminum Alloys: Part I - Experimental and Fracture Mechanics Analysis," *Fatigue and Fracture of Engineering Materials and Structures*, Vol. 21, pp. 1289-1306.
- (90) Carlson, R. L., Steadman, D. L., Dancila, D. S., and Kardomateas, G. A., 1997, "Fatigue Growth of Small Corner Cracks in Aluminum 6061-T651," *International Journal of Fatigue*, Vol. 19, Supplement No. 1, pp. S119-S125.
- (91) Newman, Jr., J. C., Phillips, E. P., and Swain, M. H., 1999, "Fatigue-Life Methodology Using Small-Crack Theory," *International Journal of Fatigue*, Vol. 21, pp. 109-119.
- (92) Rashid, M. M. and Nemat-Nasser, S., 1992, "A Constitutive Algorithm for Rate-Dependent Crystal Plasticity," *Computer Methods in Applied Mechanics and Engineering*, Vol. 94, pp. 201-228.
- (93) Horstemeyer, M., 1995, "Physically-Motivated Modeling of Deformation-Induced Anisotropy," PhD Thesis, Georgia Institute of Technology, Atlanta, GA.
- (94) Defalias, Y., 1993, "Planar Double-Slip Micromechanical Model for Polycrystal Plasticity," *ASCE Journal of Engineering Mechanics*, Vol. 119, No. 6, pp. 1260-1284.

- (95) Asaro, R. J., 1983, "Crystal Plasticity," ASME Journal of Applied Mechanics, Vol. 50, pp. 921-934.
- (96) Puškár, A., Microplasticity and Failure of Metallic Materials, Materials Science Monographs 56, Elsevier, Amsterdam, 1989.
- (97) Taylor, G. I., 1938, "Plastic Strain in Metal," Journal of the Institute of Metals, Vol. 62, pp. 307-324.
- (98) Pierce, D., Asaro, R. J., and Needleman, A., 1983, "Material Rate Dependence and Localized Deformation in Crystalline Solids," Acta Metallurgica, Vol. 31, No. 12, pp. 1951-1976.
- (99) Anand, L. and Kothari, M., 1996, "A Computational Procedure for Rate-Independent Crystal Plasticity," Journal of Mechanics and Physics of Solids, Vol. 44, No. 4, pp. 525-558.
- (100) Schroder, J. and Miehe, C., 1997, "Aspects of Computational Rate-Independent Crystal Plasticity," Computational Materials Science, Vol. 9, pp. 168-176.
- (101) Asaro, R. J., and Needleman, A., 1985, "Texture Development and Strain Hardening in Rate-Dependent Polycrystals," Acta Metallurgica, Vol. 33, No. 6, pp. 923-953.
- (102) Cuitiño, A. M. and Ortiz, M., 1992, "Computational Modeling of Single Crystals," Modeling and Simulation in Materials Science and Engineering, Vol. 1, pp. 225-263.
- (103) Bassani, J., "Plastic Flow of Crystals," in Advancers in Applied Mechanics, Vol. 30, pp. 191-256.
- (104) Moran, B., Ortiz, M., and Shih, C., 1990, "Formulation of Implicit Finite Element Methods for Multiplicative Finite Deformation Plasticity," International Journal for Numerical Methods in Engineering, Vol. 29, pp. 483-514.
- (105) Cailletaud, G., Doquet, V., and Pineau, A., 1991, "Cyclic Multiaxial Behavior of an Austenitic Stainless Steel: Microstructural Observations and Micromechanical Modeling" Fatigue under Biaxial and Multiaxial Loading,ESIS10 (Ed. by K. Kussmaul, D. McDiarmid, and D. Socie), Mechanical Engineering Publications, London, pp. 131-149.
- (106) Jordan, E. H., Shi, S., and Walker, K. P., 1993, "The Viscoplastic Behavior of Hastelloy-X Single Crystals," International Journal of Plasticity, Vol. 9, pp. 119-139.

- (107) Hoffman, J. D., Numerical Methods for Engineers and Scientists. McGraw-Hill, Inc., New York, 1992.
- (108) ABAQUS, 1998, Version 5.7, Hibbit, Karlsson, and Sorenson, Inc., Pawtucket, RI.
- (109) McGinty, R. M., Personal Communication, 1998.
- (110) Potra, F. A., and Shi, Y., 1995, "Efficient Line Search Algorithm for Unconstrained Optimization," *Journal of Optimization Theory and Applications*, Vol. 85, No. 3, pp. 677-704.
- (111) Nicholson, D. W., 1981, "On Stable Numerical Integration Methods of Maximum Time Step," *Acta Mechanica*, Vol. 38, Nos. 3/4, pp. 191-198.
- (112) Rashid, M. M., 1992, "Texture Evolution and Plastic Response of Two-Dimensional Polycrystals," *Mechanics and Physics of Solids*, Vol. 40, No. 5, pp. 1009-1029.
- (113) McHugh, P. E., Varias, A. G., Asaro, R. J., and Shih, C. F., 1989, "Computational Modeling of Microstructures," *Future Generation Computer Systems*, Vol. 5, pp. 295-318.
- (114) Dawson, P. R., Needleman, A., and Suresh. S., 1994, "Issues in the Finite Element Modeling of Polyphase Plasticity," *Materials Science and Engineering A*, Vol A175, Nos. 1-2, pp. 43-48.
- (115) Dawson, P. R., Beausoin, A. J., and Mathur, K. K., 1994, "Finite Element Modeling of Polycrystalline Solids," *Materials Science Forum*, Vol. 157-6, No. 2, pp. 1703-1712.
- (116) Jordan, E. H. and Walker, K. P., 1992, "A Viscoplastic Model for Single Crystals," *ASME Journal of Engineering Materials and Technology*, Vol. 114, pp. 19-26.
- (117) Gall, K., Sehitoglu, H., and Kadioglu, Y., 1997, "Methodology for Predicting Variability in Microstructurally Short Fatigue Crack Growth Rates," *Journal of Engineering Materials and Technology*, Vol.119, No. 2, pp. 171-179.
- (118) Sehitoglu, H., Gall, K., and García, A. M., 1997, "Fatigue Crack Growth - A Modeling Perspective," *Proc. High Cycle Fatigue of Structural Materials*, TMS Fall Meeting, Warrendale, PA, pp. 181-190.
- (119) García, A. M. and Sehitoglu, H., 1997, "Contact of Crack Surfaces During Fatigue:

- Part 1. Formulation of the Model," Metallurgical and Materials Transactions A, Vol. 28A, pp. 2263-2275.
- (120) García, A. M. and Sehitoglu, H., 1997, "Contact of Crack Surfaces During Fatigue: Part 2. Simulations," Metallurgical and Materials Transactions A, Vol. 28A, pp. 2277-2289.
 - (121) Li, C., Zhang, P., and Zhang, T., 1994, "On Crystallographic Crack Transfer Across Interfaces in Four Types of Aluminum Bicrystal," Materials Science and Engineering, Vol. A183, pp. 23-30.
 - (122) Papadopoulos, I. Y., 1995, "High Cycle Fatigue Criterion Applied in Biaxial and Triaxial Out-of-Phase Stress Conditions," Fatigue and Fracture of Engineering Materials and Structures, Vol. 18, No. 1, pp.79-91.
 - (123) Crisfield, M. A., 1987, "Plasticity Computations using the Mohr-Coulomb Yield Criterion," Engineering Computations, Vol. 4, pp. 300-308.
 - (124) Abdul-Latif, A. and Saanouni, K., 1994, "Damaged Anelastic Behavior of FCC Polycrystalline Metals with Micromechanical Approach," International Journal of Damage Mechanics, Vol. 3, pp. 237-259.
 - (125) Abdul-Latif, A. and Saanouni, K., 1997, "Effect of Some Parameters on the Plastic Fatigue Behavior with Micromechanical Approach," International Journal of Damage Mechanics, Vol. 6, pp. 433-452.
 - (126) Hoshide, T., and Socie, D. F., 1988, "Crack Nucleation and Growth Modeling in Biaxial Fatigue," Engineering Fracture Mechanics, Vol. 29, No. 3, pp. 287-299.
 - (127) Roven, H. J. and Nes, E., 1991, "Cyclic Deformation of Ferritic Steel - I. Stress Strain Response and Structure Evolution," Acta Metallurgica et Materialia, Vol. 39, No. 8, pp. 1719-1733.
 - (128) Sun, Z., de los Rios, E. R., and Miller, K. J., 1991, "Modeling Small Fatigue Cracks Interacting with Grain Boundaries," Fatigue and Fracture of Engineering Materials and Structures, Vol. 14, No. 2/3, pp. 277-291.
 - (129) Li, C., 1990, "Vector CTD Analysis for Crystallographic Crack Growth," Acta Metallurgica et Materialia, Vol. 38, No. 11, pp. 2129-2134.

- (130) Wang, C. H. and Miller, K. J., 1992, "The Effects of Mean and Alternating Shear Stresses on Short Fatigue Crack Growth Rates," *Fatigue and Fracture of Engineering Materials and Structures*, Vol. 15, No. 12, pp. 1223-1236.
- (131) Lankford, J. and Leverant, G. R., 1985, "Experimental Characterization of Fatigue Crack Tip Processes," *Journal of Metals*, pp. 54-57.
- (132) Li, C., 1990, "On the Interaction Among Stage I Short Crack, Slip Band and Grain Boundary: A FEM Analysis," *International Journal of Fracture*, Vol. 43, pp. 227-239.
- (133) Koss, D. A. and Chan, K. S., 1980, "Fracture Along Planar Slip Bands," *Acta Metallurgica*, Vol. 28, pp. 1245-1252.
- (134) Kocks, U. F., 1970, "The Relations Between Polycrystalline Metals and Single-Crystal Deformation," *Metallurgical Transactions*, Vol. 1A, pp. 1121-1142.
- (135) Li, C., 1992, "A Three-Dimensional Finite Element Analysis for Crystallographic Crack Near the Interface of an Incompatible Bicrystal," *Fatigue and Fracture of Engineering Materials and Structures*, Vol. 16, No. 1, pp. 21-35.
- (136) Newman, Jr., J. C., 1999, to appear in Mixed Mode Crack Behavior, ASTM STP 1359, Philadelphia, Eds., D. L. McDowell and K. J. Miller.
- (137) Baumel, A., Materials Data for Cyclic Loading. Supplement 1. Amsterdam; Elsevier, 1990.
- (138) Repetto, E. A. and Ortiz, M., 1997, "A Micromechanical Model of Cyclic Deformation and Fatigue-Crack Nucleation in f.c.c. Single Crystals," *Acta Materialia*, Vol. 45, No. 6, pp. 2577-2595.
- (139) Doquet, V., 1999, "Micromechanical Simulations of Microstructure-Sensitive Stage I Fatigue Crack Growth," *Fatigue and Fracture of Engineering Materials and Structures*, Vol. 22, pp. 215-233.
- (140) Gardner, B., Personal Communication, 1999.
- (141) Steadman, D. L., Carlson, R. L., and Kardomateas, G. A., 1998, "Expert System Model of Small Crack Growth," in *Proceedings, 39th AIAA/ASME/ASCE/AHS/ASC Structure, Structural Dynamics, and Materials Conference and Exhibit and AIAA/ASME/AHS Adaptive Structures Forum - Part 4, A Collection of Technical Papers, Proceedings, American Institute of Aeronautics and Astronautics*, pp. 3003-3013.

- (142) Cox, B. N. and Morris, W. L., 1988, "Monte Carlo Simulations of the Growth of Small Fatigue Cracks," *Engineering Fracture Mechanics*, Vol. 31, No. 4, pp. 591-610.

VITA

Valerie Poindexter Bennett was born in Atlanta, Georgia on November 14, 1969. She is the daughter of Lola Mae Poindexter and John William Poindexter, Jr. She graduated from Frederick Douglass High School in Atlanta, Georgia in 1987. Mrs. Bennett was awarded a dual degree - Bachelor of Engineering Degree in Mechanical Engineering and Bachelor of Science in Mathematics - in 1992 from Vanderbilt University. In 1993, she was awarded a Master of Science Degree in Mechanical Engineering from the Georgia Institute of Technology.

Valerie married Harold Vernelle Bennett in Atlanta, Georgia on August 20, 1994 and they have one child, Quinton JeJuan Bennett.